NUREG/CR-6831
ANL-03/17

Examination of Spent PWR Fuel Rods after 15 Years in Dry Storage

Argonne National Laboratory

U.S. Nuclear Regulatory Commission
Office of Nuclear Regulatory Research
Washington, DC 20555-0001

AVAILABILITY OF REFERENCE MATERIALS IN NRC PUBLICATIONS

NRC Reference Material

As of November 1999, you may electronically access NUREG-series publications and other NRC records at NRC's Public Electronic Reading Room at http://www.nrc.gov/reading-rm.html. Publicly released records include, to name a few, NUREG-series publications; *Federal Register* notices; applicant, licensee, and vendor documents and correspondence; NRC correspondence and internal memoranda; bulletins and information notices; inspection and investigative reports; licensee event reports; and Commission papers and their attachments.

NRC publications in the NUREG series, NRC regulations, and *Title 10, Energy*, in the Code of *Federal Regulations* may also be purchased from one of these two sources.

1. The Superintendent of Documents
   U.S. Government Printing Office
   Mail Stop SSOP
   Washington, DC 20402–0001
   Internet: bookstore.gpo.gov
   Telephone: 202-512-1800
   Fax: 202-512-2250
2. The National Technical Information Service
   Springfield, VA 22161–0002
   www.ntis.gov
   1–800–553–6847 or, locally, 703–605–6000

A single copy of each NRC draft report for comment is available free, to the extent of supply, upon written request as follows:

Address: Office of the Chief Information Officer,
Reproduction and Distribution
Services Section
U.S. Nuclear Regulatory Commission
Washington, DC 20555-0001
E-mail: DISTRIBUTION@nrc.gov
Facsimile: 301–415–2289

Some publications in the NUREG series that are posted at NRC's Web site address http://www.nrc.gov/reading-rm/doc-collections/nuregs are updated periodically and may differ from the last printed version. Although references to material found on a Web site bear the date the material was accessed, the material available on the date cited may subsequently be removed from the site.

Non-NRC Reference Material

Documents available from public and special technical libraries include all open literature items, such as books, journal articles, and transactions, *Federal Register* notices, Federal and State legislation, and congressional reports. Such documents as theses, dissertations, foreign reports and translations, and non-NRC conference proceedings may be purchased from their sponsoring organization.

Copies of industry codes and standards used in a substantive manner in the NRC regulatory process are maintained at—

The NRC Technical Library
Two White Flint North
11545 Rockville Pike
Rockville, MD 20852–2738

These standards are available in the library for reference use by the public. Codes and standards are usually copyrighted and may be purchased from the originating organization or, if they are American National Standards, from—

American National Standards Institute
11 West 42nd Street
New York, NY 10036–8002
www.ansi.org
212–642–4900

Legally binding regulatory requirements are stated only in laws; NRC regulations; licenses, including technical specifications; or orders, not in NUREG-series publications. The views expressed in contractor-prepared publications in this series are not necessarily those of the NRC.

The NUREG series comprises (1) technical and administrative reports and books prepared by the staff (NUREG–XXXX) or agency contractors (NUREG/CR–XXXX), (2) proceedings of conferences (NUREG/CP–XXXX), (3) reports resulting from international agreements (NUREG/IA–XXXX), (4) brochures (NUREG/BR–XXXX), and (5) compilations of legal decisions and orders of the Commission and Atomic and Safety Licensing Boards and of Directors' decisions under Section 2.206 of NRC's regulations (NUREG–0750).

DISCLAIMER: This report was prepared as an account of work sponsored by an agency of the U.S. Government. Neither the U.S. Government nor any agency thereof, nor any employee, makes any warranty, expressed or implied, or assumes any legal liability or responsibility for any third party's use, or the results of such use, of any information, apparatus, product, or process disclosed in this publication, or represents that its use by such third party would not infringe privately owned rights.

NUREG/CR-6831
ANL-03/17

Examination of Spent PWR Fuel Rods after 15 Years in Dry Storage

Manuscript Completed: August 2003
Date Published: September 2003

Prepared by
R.E. Einziger, H. Tsai, M.C. Billone, B.A. Hilton[*]

Argonne National Laboratory
9700 South Cass Avenue
Argonne, IL 60439

[*]Argonne National Laboratory-West
P.O. Box 2528
Idaho Falls, ID 83403

S. Basu, NRC Project Manager

Prepared for
Division of Systems Analysis and Regulatory Effectiveness
Office of Nuclear Regulatory Research
U.S. Nuclear Regulatory Commission
Washington, DC 20555-0001
NRC Job Code Y6248

EXAMINATION OF SPENT PWR FUEL RODS AFTER 15 YEARS IN DRY STORAGE

R. E. Einziger, H. Tsai, M. C. Billone, and B. A. Hilton

ABSTRACT

For ≈15 years 15 x 15 PWR fuel (35.7 GWd/MTU) was stored in a dry inert-atmosphere Castor V/21 cask as peak cladding temperatures decreased from ≈350 to 150°C. Before storage, the loaded cask was subjected to extensive thermal-benchmark tests, during which time the peak temperatures were >400°C. The cask was opened to examine the fuel rods for degradation and to determine if they were suitable for extended storage. In the central region of the fuel column, the measured hydrogen content of the cladding is consistent with the thickness of the oxide layer. At higher elevations, there is less hydrogen than would be expected from the oxide thickness. Migration of hydrogen to the cooler ends of the rod probably occurred during dry storage. The volume of hydrides varies azimuthally around the cladding but all of the hydrides appear to have retained a circumferential orientation. Little or no cladding creep occurred during thermal-benchmark testing and dry storage. Post-storage creep testing indicated that the cladding retains significant creep ductility after dry-cask storage. It is anticipated that the creep would not increase appreciably during additional storage because of the low temperature after 15 years. Based on the Surry fuel rod data, no deleterious effects of 15-years of dry cask storage were observed.

CONTENTS

Abstract iii

Executive Summary ix

Foreword xi

Acknowledgments xiii

Abbreviations xv

1 Introduction and Objectives 1

2 Test Conditions and Materials 3

  2.1 Storage Conditions 3

    2.1.1 Performance Testing 3

    2.1.2 Extended Dry Storage 4

  2.2 Fuel Description 5

  2.3 Characterization of Surry Fuel Prior to Storage 6

3 Poststorage Examinations 9

  3.1 Fuel Rod Selection and Sampling Locations 9

  3.2 Profilometry 11

  3.3 Fission Gas Analysis and Void Volume Determination 12

  3.4 Metallography and Hydrogen Analysis 12

    3.4.1 Fuel Pellet Condition 13

    3.4.2 Oxide Layers and Fuel-Cladding Gap 14

    3.4.3 Hydrogen Content, Distribution, and Orientation 15

3.5 Microhardness Measurements 18

3.6 Poststorage Thermal Creep Tests 18

3.6.1 Thermal Creep Apparatus 18

3.6.2 Thermal Creep Test Matrix and Summary of Results 19

3.6.3 Hoop Thermal Creep Strain vs. Time 21

4 Implications for Extended Dry Storage 25

4.1 Assessment of Creep during Pre-storage Tests and Long-Term Storage 25

4.1.1 Method 1: Baseline and Measurement Uncertainty 25

4.1.2 Method 2: Creep Code Calculations 26

4.1.3 Method 3: Comparison with Prestorage Turkey Point Diameters 27

4.1.4 Method 4: Comparison with Maximum Potential Creep-down 28

4.2 Fuel Rod Stress 29

4.3 Hydride Redistribution and Reorientation 29

4.3.1 Comparison of Surry Hydride Distribution with Other Fuels 30

4.3.2 Reorientation 31

4.4 Cladding Annealing 31

4.5 Post-storage Residual Creep Strain and Strain Rate 32

5 Conclusions and Recommendations 35

5.1 Conclusions 35

5.2 Recommendations 36

6 References 37

APPENDICES

A Fuel Rod Sectioning Diagrams A-1

B Profilometry B-1

B.1 Methodology B-3

B.2 Average Rod Diameter Profiles B-4

C Fuel Rod Gas Analysis Data C-1

C.1 Introduction C-3

C.2 Calibration and Testing Methodology C-5

D Metallographic Data D-1

E Baseline Comparative Data E-1

F Thermal Creep Test F-1

F.1 Test Apparatus F-4

F.2 Test Conduct F-10

F.3 Surry Post-Storage Thermal Creep Tests F-15

FIGURES

1. Estimated Temperature of Assembly T11 during Extended Dry-storage Period 5

2. Cutting Diagram for Metallographic, Microhardness, and Hydrogen Content Characterization of Rod H9 from Surry-2 Assembly T11 10

3. Averaged Outer-diameter Profile of Rod H9 (from Surry-2 Assembly T11) after Extensive Thermal Benchmark Testing and ≈15 years of Dry-cask Storage in He 11

4. Cross-sectional Mosaic of Rod H9: (A) ≈1000 mm above Midplane, (B) Approximate Midplane... 14

5. Cladding Outer-surface Oxide Layers of Rod H9 from Surry-2 Assembly T11 at: (A) Approximate Fuel Midplane, and (B) ≈1000 mm above Midplane 15

6. Hydride Structure in Fuel Rod Cladding of Assembly T11 at Two Elevations: (A) Midplane of Rod H9, (B) ≈500 mm above Midplane of Rod H9, (C) Approximate Midplane of Rod G6, and (D) ≈500 mm above Midplane of Rod G6 17

7. Thermal Creep Data for Irradiated and Dry-cask-stored Surry Cladding Sample C9

Tested at 400°C and 190-MPa Hoop Stress for 1873 h, Followed by 693 h at 250 MPa 23

8. Thermal Creep Data for Irradiated and Dry-cask-stored Surry Cladding Sample C8 Tested at 380°C and 220-MPa Engineering Hoop Stress for 2180 h 23

9. Thermal Creep Data for Irradiated and Dry-cask-stored Surry Cladding Sample C6 Tested at 380°C and 190-MPa Engineering Hoop Stress for 2348 h 24

10. Thermal Creep Data for Irradiated and Dry-cask-stored Surry Cladding Sample C3 Tested at 360°C and 220-MPa Engineering Hoop Stress for 3305 h 24

TABLES

1. Time/Temperature History of Assembly T11 from Castor-V/21 Cask 4

2. Sample Identification Matrix for Surry Rods after Extended Dry Storage 10

3. Rod Volume, Internal Pressure (at 27°C) and Fission Gas Release 13

4. Surry-2 Assembly T11 Cladding Outer Oxide Layer Thickness (µm) at 0, 500, and 1000 mm above the Fuel Midplane 15

5. Hydrogen Content (wppm) at ≈ 0, 500, and 1000 mm above the Fuel Midplane and Standard Deviation of Data for Surry Fuel Rod Cladding and Turkey Point 3-Cycle Fuel 18

6. Thermal Creep Test Matrix and Predicted Creep Strains for Test Times of Six, Nine and Twelve Calendar Months (Based on July 18, 2001 Sponsor/Peer Review Meeting) 20

7. Surry Cladding Thermal Creep Test Matrix and Summary of Results. 21

8. Variation of Averaged Rod Diameters from Assembly to Assembly and within an Assembly before Storage… 25

9. Predicted Creep Strains after Various Test and Storage Periods 26

10. Global and Average Rod Diameters -- Uncorrected for oxide growth -- at 2-3 m Elevation from Bottom of Rod 27

11. Summary of Storage Creep Estimates for Various Calculation Methods 29

EXECUTIVE SUMMARY

For ≈15 years Dominion Generation's Surry Nuclear Station 15 x 15 Westinghouse pressurized water reactor (PWR) fuel was stored in a dry inert-atmosphere Castor V/21 cask at the Idaho National Environmental and Engineering Laboratory (INEEL) at peak cladding temperatures that decreased from ≈350 to 150°C. The UO_2 fuel pellets had an initial enrichment of 3.11% and a nominal density of 95% theoretical. The cladding was cold-worked/stress-relieved Zircaloy-4. The rods were fabricated with an internal He pressure of 2.86 MPa at ≈300 K. Assembly T11, chosen for examination, was irradiated for three cycles to achieve an average burnup of 35.7 GWd/MTU and an assembly-averaged fast (E>1 MeV) neutron fluence that was calculated to be 6.38×10^{25} n/m^2. The fuel had cooled ≈1300 days before it was loaded into the cask. Before storage, the loaded cask was subjected to extensive thermal-benchmark tests, during which time the peak temperatures were >400°C. The cask was opened to examine the fuel rods for degradation and to determine if they were suitable for extended storage. No fuel rod breaches and no visible degradation or crud/oxide spallation from the fuel rod surface were observed.

Twelve rods were removed from the center of the T11 assembly and shipped from INEEL to Argonne-West for profilometric scans. Four of these rods were punctured to determine the fission gas release from the fuel matrix, internal pressure, and void volume in the rods. Three of the 4 rods were cut into 5 segments each, and then shipped to Argonne-East for detailed examination. The results from the profilometry (12 rods), gas release measurements (4 rods), metallographic examinations (5 samples from 2 rods), microhardness (3 samples from 1 rod), and hydrogen content determination (3 samples from 1 rod) are reported. Thermal creep tests on 4 samples from 2 rods have been completed. Creep strains and strain rates gathered to date are presented as a function of temperature, hoop stress, and time. The data indicate that the Surry cladding retains significant creep ductility after dry-cask storage.

Although only limited prestorage characterization is available, several conclusions can be drawn. Based on a comparison with characterization of Florida Power Turkey Point rods with similar characteristics (dates of service, assembly type, fuel manufacturer, approximate enrichment [2.56%], and burnup [≈28 GWd/MTU]), it appears that little or no fission gas was released from the fuel pellets during either the thermal-benchmark tests or the long-term storage. In the central region of the fuel column, where the axial temperature gradient in storage is small, the measured hydrogen content of the cladding is consistent with the thickness of the oxide layer. At ≈1 m above the fuel midplane, where a steep temperature gradient existed in the cask (with the temperature decreasing to a much lower value at the top of the rod), less hydrogen is present than would be expected from the oxide thickness that developed in-reactor. The volume of hydrides varies azimuthally around the cladding, and, at some elevations, the hydrides appear to be segregated somewhat to the inner and outer cladding surfaces. It is not possible, however, to determine if this segregation occurred in-reactor, during transportation, during the thermal-benchmark tests, or during the dry-storage period. Migration of hydrogen to the cooler ends of the rod during dry storage probably occurred and may signal a higher than expected concentration in those regions. It is most significant that all of the hydrides appear to have retained the circumferential orientation typical of prestorage PWR fuel rods.

The Surry cladding exhibits a residual creep strain of >1% for thermal creep test temperatures of 380°C (220 MPa) and 400°C (190 MPa). A residual creep strain of ≈6% was achieved in the 400°C sample after raising the stress level to 250 MPa for ≈700 h. Although the creep rate increased during the 700 h because of wall thinning, the deformation was uniform around the circumference of the cladding. Inasmuch as no symmetric or asymmetric bulging of the cladding was observed – a precursor to failure – the residual creep life of the 400°C sample is >6%. Secondary creep rates that span two orders of magnitude were measured for the five creep tests. These data are useful not only for code benchmarking, but also for determining the stress and temperature sensitivity of the creep rate.

Because prestorage diameter measurements on the actual test rods are lacking, four methods of analysis were undertaken to estimate that little or no cladding creep occurred during thermal-benchmark testing and dry storage. It is anticipated that the creep would not increase significantly during additional storage because of the low temperature after 15 years, continual decrease in temperature from the reduction in decay heat, and concurrent reductions in pressure and stress.

Based on the Surry data, no deleterious effects on fuel and cladding were observed after 15-years of dry cask storage.

FOREWORD

The original license and the certificate of compliance (CoC) for spent nuclear fuel dry storage casks are due to expire for many commercial nuclear power plants in the next few years. The Spent Fuel Project Office (SFPO) of the United States Nuclear Regulatory Commission (NRC) is developing revisions to interim staff guidance (ISGs) for review of technical documents to be submitted by licensees in support of their applications for renewal of licenses and CoCs. The renewal of licenses and CoCs for the existing casks would cover an additional period of 20 to 100 years and would require development of a technical basis for continued safe performance under the extended service conditions. Consistent with the above and the regulatory requirements of 10 CFR Part 72 for storage and handling of spent fuel, the acceptance criteria for spent fuel in storage casks in ISG-11 are being revised. Revision 2 of ISG-11 recognizes creep to be the dominant mechanism for cladding deformation under normal conditions of storage and recommends that the maximum cladding temperature during storage and for short-term vacuum drying and cask backfilling operations be limited to 400°C to assure that the extended storage does not result in gross rupture of fuel cladding.

The NRC Office of Nuclear Regulatory Research (RES) at NRC initiated an experimental research program in November 2000 to provide a technical basis for the aforementioned revision. Specifically, the program involved post-storage characterization and creep testing of representative pressurized water reactor (PWR) fuel rods from the Surry nuclear power plant, stored for over 15 years in CASTOR dry casks. The results indicate that significant residual creep capacity remains in fuel cladding after the initial storage period. With decreasing temperature and stress during the extended storage, the cladding is likely to experience a small amount of additional creep and will likely not result in gross rupture in the event of a cladding breach. Thus, the results support the recommendation of 400°C as the maximum allowable cladding temperature for extended storage, noting that it refers to the beginning of storage life. The recommended temperature also limits the amount of hydride reorientation in the radial direction during the extended storage. Hydrides, which result from clad oxidation during in-reactor operation, contribute to a loss of clad ductility if oriented radially in large quantities in cladding. The Surry PWR cladding did not exhibit any appreciable amount of radial reorientation.

The research results reported herein suggest the viability of spent fuel cladding to remain as a barrier to fission product release during extended storage up to 100 years in a dry cask environment. The results also suggest the likelihood of spent fuel cladding to retain sufficient structural integrity after the extended storage period for safe transfer to a final repository. Finally, the results provide a sound technical basis for granting an extension of cask licenses and CoCs, thereby reducing regulatory burden on licensees while maintaining safety of spent fuel storage. Note the results are valid for spent fuel with a burnup limit of 45 GWd/MTU. RES is currently conducting a similar experimental program for high burnup spent fuel cladding (burnup in excess of 45 GWd/MTU). The results from the high burnup program will be reported separately in the future.

Farouk Eltawila, Director
Division of Systems Analysis and Regulatory Effectiveness

ACKNOWLEDGEMENTS

The authors acknowledge the support of the U.S. Nuclear Regulatory Commission (R. Kenneally, S. Basu, H. Scott, K. Gruss, and C. Interrante), the Electric Power Research Institute (J. Kessler, A. Machiels), the U.S. Department of Energy (J. Price), and of BSC (P. Pasupathi, D. Stahl and E. Siegmann). The staff of the Idaho National Environmental and Engineering Laboratory (INEEL) test area north (TAN) facility is acknowledged for retrieving the fuel. Particularly valuable to the success of this project were the thermal-creep modeling predictions provided by C. Beyer of the Pacific Northwest National Laboratory (PNNL), P. Bouffioux (EdF), J. Rashid (ANATECH Corp.) and E. Siegmann (BSC).

ABBREVIATIONS

AGHCF	Alpha Gamma Hot Cell Facility
ANL-E	Argonne National Laboratory, East
ANL-W	Argonne National Laboratory, West
ASTM	American Society for Testing and Materials
ATM	Approved Test Material
BMI	Battelle Memorial Institute
BSC	Bechtel SAIC Company
CC	Calvert Cliffs
DOE	U.S. Department of Energy
DOE-RW	U.S. Department of Energy –Radioactive Waste
DPH	Diamond Pyramid Hardness
ECP	Element Contact Profilometer
EdF	Electricite de France
EPRI	Electric Power Research Institute
GASR	Gas Assay Sample and Recharge
GWd/MTU	Gigawatt days per metric ton of Uranium
HFEF	Hot Fuel Examination Facility
INEEL	Idaho National Environmental and Engineering Laboratory
LWR	Light Water Reactor
MPa	Megapascal
NIST	National Institute of Standards and Technology
NRC	U. S. Nuclear Regulatory Commission
NRC-NMSS	U. S. Nuclear Regulatory Commission – Nuclear Materials Safety and Safeguards
PBR	Pilling-Bedworth Ratio
PNNL	Pacific Northwest National Laboratory
psi	Pounds per square inch (a = absolute, g = gauge)
PWR	Pressurized Water Reactor
TAN	Test Area North
TP	Turkey Point
YMP	Yucca Mountain Project

1 INTRODUCTION AND OBJECTIVES

Some of the original licenses issued by the U.S. Nuclear Regulatory Commission (NRC) for 20 years of dry storage of light water reactor (LWR) fuel are coming up for renewal soon. Because the opening of a deep geological repository may be delayed, consideration is being given to interim dry storage of perhaps up to 100 years. Material-related issues exist with respect to the potential long-term behavior of the dry-cask storage system (cask, basket, seals, fuel, etc.). The principal fuel issues are whether spent-fuel cladding remains a viable barrier to fission product release and, if not, to what extent the fuel itself may provide a degree of fission product retention in the cask storage environment. A corollary issue is whether the fuel rods will retain sufficient integrity after 20+ years of dry storage to be safely transferred to a final repository.

An Electric Power Research Institute (EPRI) report, "Data Needs for Long-Term Dry Storage of LWR Fuel" (Ref. 1), identified several specific questions about fuel rod behavior. These include:

1. Has there been a change in the mechanical properties, especially the ductility, of the cladding?
2. What is the extent of cladding creep under storage conditions?
3. Has detrimental hydrogen pickup or hydride reorientation occurred in the cladding?
4. How much cladding annealing has occurred?
5. Has gas release from the fuel to the plenum been enhanced?
6. Has release of volatile fission products been enhanced?

Questions 1-4 are germane to maintaining cladding integrity during storage, subsequent handling during transfers, and off-normal events that may occur in the lifetime of the cask. Questions 5 and 6 are germane to environmental effects within the cask and the impacts these effects will have on subsequent safe handling. The mechanical properties of the cladding are most relevant in addressing the issue of integrity. Environmental effects will be more relevant and important if the mechanical properties have degraded significantly or if degradation phenomena have been enhanced because of the environment.

In the mid-1980s, the U.S. Department of Energy (DOE) procured a Castor V/21 dry-storage cask for testing at the Idaho National Environmental and Engineering Laboratory (INEEL). The primary purpose of the testing was to benchmark modeling codes by measuring the thermal and radiological characteristics of the cask; it was not intended to examine fundamental fuel behavior. Therefore, prior to the tests, the fuel had undergone only minimal characterization: visual examination of the outside of the assemblies and ultrasonic examination to ensure that no breached rods would be included. The cask was loaded with as-irradiated assemblies from the Surry Nuclear Station and then tested in a series of configurations under various cover gases. During the tests, the temperature within several fuel assemblies was monitored with a thermocouple probe inserted into a guide tube, and the cover gas was periodically analyzed to determine if any rod leaks had developed. No leaks were found. The details of these tests have been reported in several documents (Refs. 2-4). The cask remained on the storage pad at INEEL for ≈15 years, with the fuel in an essentially inert atmosphere (He/<1% air).

In an effort to determine if any degradation had occurred during the storage period, the NRC, EPRI, and DOE jointly funded a project to open the Castor cask, visually inspect the fuel and cask internals, and conduct both nondestructive and destructive examinations of the fuel rods that had undergone prototypical long-term storage (Ref. 5).

In-cask observations of the fuel consisted of visual examinations and crud evaluation. The fuel rods appeared to be unchanged by the long storage duration and the preceding thermal-benchmark testing. No evidence of appreciable cladding creep or rod bow was observed. Some crud/oxide was still adhering to the rods; no crud appeared to have fallen into either the spacers or cask bottom. No deleterious behavior (e.g., rod bulging or cracking) was observed that would indicate that continued long-term storage would not be safe (Ref. 6)

Any changes in fuel rod characteristics after irradiation, such as cladding creep, hydride precipitation, oxide growth, and fission gas release, would be a result of integrated time-at-temperature-dependent kinetic processes that occur during the rod's residence in the storage cask as well as during prior handing (cask loading, drying, transportation, etc.). Based on temperature alone, the center assembly in the Castor cask would be the choice for further examination. This assembly has an average burnup of 31.5 GWd/MTU and experienced a peak temperature during thermal-benchmark testing of 425°C, whereas the burnup in the T11 assembly in the adjacent location was higher (35.7 GWd/MTU). Based on the measurements made in the He atmosphere and the vertical orientation of the cask during the performance-testing phase, the difference in temperature between the positions was only 10°C. Therefore the higher burnup assembly T11 was chosen for further examination.

Twelve rods, selected on the basis of their ease of removal, were extracted for further characterization and testing. This report describes the results of the fuel and cladding characterization, as well as the implications of these results for long-term (i.e., beyond 20 years) dry-cask storage. Supporting documentation on methods and results appears in Appendices A-F.

2 TEST CONDITIONS AND MATERIALS

2.1 Storage Conditions

The behavior of the spent fuel is governed by its time at temperature and the storage atmosphere. The Surry rods underwent two types of storage, which contributed to the overall fuel and cladding condition. The rods were initially part of a thermal-performance-testing program, during which they were stored for short periods of time under various atmospheres (He, N_2, and vacuum) in horizontal and vertical orientations. Each combination produced a different maximum temperature and temperature profile. After this testing, the rods were stored vertically in the Castor V/21 cask, outdoors, on a concrete pad for 14.2 years, in a He atmosphere with <1% air, under conditions of decreasing temperature due to decreasing decay heat. After the cask was initially opened, the fuel rods spent another six months in the cask in an air atmosphere.

2.1.1 Performance Testing

The Castor cask was monitored with thermocouple probes during the thermal-benchmarking testing phase to determine the temperature profiles as a function of axial elevation and radial position within the cask. In an upright orientation, the hottest fuel occurred in the center five assemblies (Ref. 2). In addition, there was a thermal gradient along the fuel rods. The hottest elevation was typically near the cask midplane. The temperature dropped off significantly toward the top and bottom of the cask (Ref. 4).

Before complete loading, the fuel rods spent ≈200 h in air at a significantly reduced temperature. During the cask performance tests (Refs. 2-4), the fuel rods were in He, N_2 and vacuum atmospheres in both horizontal and vertical configurations. The peak cladding temperature, adjusted for the position of Assembly T11 in the cask, varied in each configuration (Ref. 3), as indicated in Table 1. At the completion of the cask performance tests, the fuel spent ≈2880 h vertically in a 70%-He/30%-air atmosphere (Ref. 3). The temperature was not measured during this time but is assumed to be the weighted average of the temperatures maintained in the vertical orientation with the partial He and N_2 atmospheres during the performance-testing runs. Following thermal-performance testing, the cask was filled with a He/<1% air atmosphere.

Cover gas samples were taken periodically throughout the performance-testing period and storage duration to look for cask leaks and fuel rod breaches (Ref. 3). In all cases, the intended atmospheres were maintained (Table 1). The moisture level in the cask was <0.03 vol. % in all cases.

Table 1. Time/Temperature History of Assembly T11 from Castor-V/21 Cask (Ref. 3)

Configuration	Cover Gas	Peak Cladding T, °C	≈Duration, h
Vertical	Air	Reduced T	200
Vertical	He	344	119
Vertical	N_2	359	43
Vertical	Vacuum	415	72
Horizontal	He	357	93
Horizontal	N_2	398	72
Vertical	70% He/30% Air	348	2880
Vertical	He/<1% Air[a]	344 → 155	1.3×10^5

[a] After the cask was initially opened at 14.2 years, the fuel was left in the cask for the last 6 months in a hot cell air atmosphere.

2.1.2 Extended Dry Storage

During storage, temperature decreases were consistent with the reduction in decay heat. Because the time between the end of the performance testing and the start of the extended dry storage was short, the initial temperature for the extended storage should be nearly the same as that measured during the performance testing in the same configuration, with the same cover gas (He), i.e., ≈344°C. (If one compares the measured temperatures in the vertical configuration with He and N_2 and makes a linear interpolation, one can see that the <1% air in the cask-storage atmosphere has an insignificant effect on the thermal conductivity of the gas mixture and, hence, on the temperature.) Temperature was not measured during the extended storage. However, when the cask was opened after ≈14.2 years, with the lid off and the cask containing air from the hot cell, a thermocouple probe inserted into the assembly a few feet down to the hot spot measured a temperature of 155°C (Ref. 6). In all likelihood, this temperature was below the temperature expected in the closed cask. The HYDRA thermal-hydraulic code, which was verified during the performance-testing period, is no longer readily available to calculate better time/temperature profiles after storage. The use of other verified codes such as COBRA-SFS would require additional work outside the scope of this study.

Two methods were used to develop a temperature profile, which could be used to calculate creep deformation for the storage period. In the first method, the profile was pinned at 344°C at the start of extended storage and 155°C at 14.8 years, when some fuel rods were removed from the cask. The ambient temperature, which was set at 38°C to represent the summer hot month in Idaho Falls, was expected to occur by 100 years. The actual temperature at 14.8 years was probably higher because the temperature was measured with the cask open and the fuel subjected to additional conductive and convective cooling. Hence, the actual temperature profile is probably higher, and this approximation represents a lower temperature bound. The following temperature profile was obtained:

$$T(t) = 308 \exp(-0.064\, t) + 309, \qquad (1)$$

where T is in K and t is in years.

In the second method, it was assumed that the temperature would be proportional to the exponentially decreasing decay heat until, eventually, the ambient temperature dominated. The main sources of decay heat are Cs-137 (half-life = 30.17 years) and Sr-90 (half-life = 28.8 years). Inasmuch as the half-lives are sufficiently close, the half-life of the Cs-137 was used. The initial temperature was fixed at 344°C and the long-term ambient temperature was set to 38°C. At the start of storage, Sr-90 makes up 40% of the major heat producers. We are representing it with the longer half-life of the Cs-137 so we will be overestimating, as a function of time, the amount of remaining heat in the system and hence overestimating the actual temperature by this method. With the decay fixed to the half-life of Cs-137, the profile is given by:

$$T(t) = 308 \exp(-0.023\, t) + 309. \qquad (2)$$

The two temperature profiles are shown in Fig. 1. The upper curve (Method 2) is based on Eq. 2, whereas the lower curve (Method 1) is based on Eq. 1. As indicated above, these two profiles should form a bound on the actual temperature profile experienced in the cask during the extended storage period.

2.2 Fuel Description

The Castor cask contained 21 15 x 15 Westinghouse fuel assemblies (Ref. 3) that had been irradiated in the Surry Reactor. Assembly T11, which had been stored close to the hottest part of the cask and had the highest burnup, was chosen for evaluation. The initial enrichment of the UO_2 fuel pellets was 3.11% and their nominal density was 95% of theoretical. The nominal as-fabricated outside diameter of the cold-worked/stress-relieved Zircaloy-4 cladding was 10.71 mm, with a wall thickness of 0.62 mm. The rods were pre-pressurized with He to 2.86 MPa at $\approx$300K (Ref. 4).

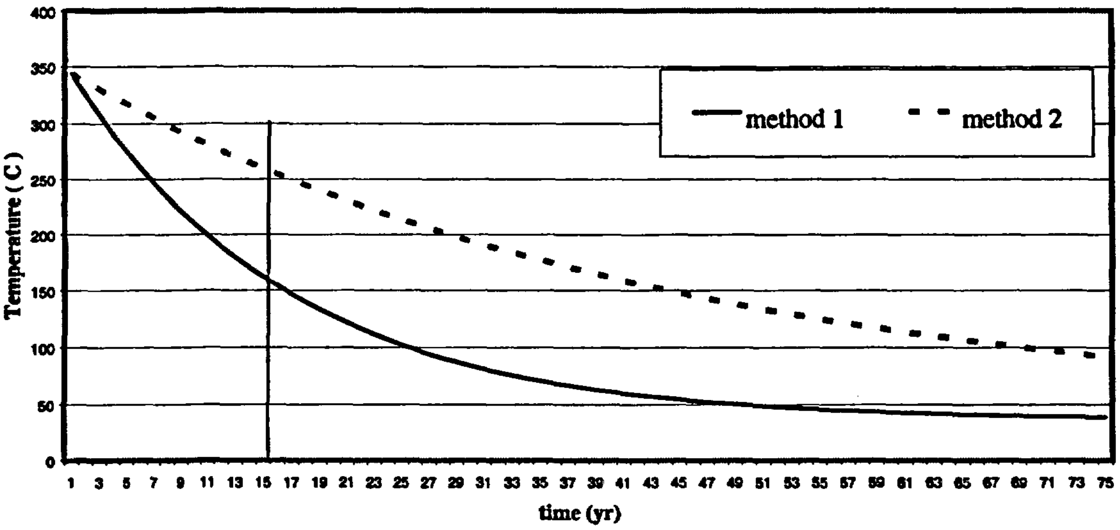

Fig. 1. Estimated temperature of Assembly T11 during extended dry-storage period. Vertical line indicates 14.8-year cask storage period.

The assembly was irradiated for three cycles and achieved an assembly-average burnup of 35.7 GWd/MTU. The assembly-averaged fast neutron fluence (E>1 MeV) was calculated to be 6.38×10^{25} n/m^2 (Ref. 7). (Note: the fast fluence within the axial test section regions is ≈8% higher.) The assembly, discharged in November 1981, was in wet storage until it was transported to INEEL and loaded into the Castor cask in July 1985, with a decay heat of 1.1 kW. Because rod-to-rod temperature profiles were not available, the center 12 rods in the assembly were assumed to be the hottest rods and were chosen for examination because of their ease of extraction from the assembly.

2.3 Characterization of Surry Fuel Prior to Dry Storage

Ideally, one would extensively characterize the fuel rods before storage to provide a baseline for determining changes that might occur; nondestructive profilometry on the actual test rods and gas analysis, ceramography, metallography, hydride analysis, and mechanical-property testing on adjacent sibling rods would be conducted. However, because the original purpose of the prestorage tests was to determine the thermal characteristics of the cask systems and not the long-term performance of the rods, only limited characterization was conducted on the Surry rods or assemblies prior to the initial cask performance testing (Refs. 4 and 8).

Because post-irradiation destructive examination data on exact sibling Surry rods is lacking, post-storage data will be compared with the data in the open literature the are relevant to PWR fuel rods, and, more specifically, with the post-irradiation data available for the Turkey Point rods (Refs. 9 and 10). Westinghouse 15 x 15 rods, manufactured to similar specifications as the Surry rods, were irradiated in the Turkey Point reactor for three cycles under conditions similar to those experienced by the Surry rods, but to a lower burnup of ≈26-28 GWd/MTU. The Turkey Point rods were extensively examined (Refs. 9 and 10), and their postirradiation characteristics are expected to be similar to those of the Surry rods.

Turkey Point cladding attributes of importance to the current evaluation include oxide layer thickness, hydrogen content, hydride distribution and orientation, and microhardness. The as-fabricated cladding thickness was nominally 0.617 mm, with a low of 0.597 mm and a high of 0.643 mm. The hydrogen content in the cladding ranges from 40±10 wppm at 610 mm from the rod bottom to 90±5 wppm at the 3050-mm elevation. The hydrides are circumferentially oriented. The oxide thickness varies both azimuthally and axially on a single rod. A difference of as much as a factor of two in oxide thickness at the same axial location was noted between two rods. Cladding oxide thickness and hydrogen uptake should be greater for the Surry rods because of their longer in-reactor residence time (≈1190 days for Surry vs. ≈850 days for Turkey Point).

Five rods from two 3-cycle Turkey Point assemblies were destructively analyzed (Ref. 10). All of the rods have the same isotopic distribution of fission gas and a fission gas release of ≈0.22%. The in-reactor gas release of the Surry rods might be slightly higher due to the higher burnup, but it is still expected to be ≤1% and well within the scatter of fission-gas-release data found for the general population of PWR rods in this burnup range.

All Surry rods had been ultrasonically examined for leaks at the plant site; no leaks were found. Full-length black-and-white videos of Assembly T11 and seven other assemblies, and color still pictures of all four sides of two assemblies (V05 and V27), were taken at INEEL. The videos provided little information about the condition of the rods. The photos showed an orange/reddish crud, thought to be Fe_2O_3, on Assembly V05 (Ref. 4). This is somewhat unusual because typical crud on PWR rods is a gray Fe_3O_4 magnetite. Videos and color stills of the same assemblies were taken after the Castor-V/21 performance tests, just before the commencement of long-term storage.

Under a rod consolidation project also conducted at INEEL, linear profilometry at 90° orientations was performed on selected rods from 36 similar Surry assemblies. The maximum, minimum, and average diameters along the two orientations for each of the 36 assemblies have been reported (Ref. 8). The difference between the maximum and minimum rod outer diameter for any one Surry assembly ranged between 0.03 and 0.06 mm (0.3 and 0.6% of the as-fabricated rod diameter). The average rod diameter for the set of assemblies varied by as much as 0.06 mm or 0.6%.

3 POSTSTORAGE EXAMINATIONS

3.1 Fuel Rod Selection and Sampling Locations

Twelve Surry rods taken from the Castor V/21 cask were transferred from the INEEL Test Area North (TAN) facility to the Argonne National Laboratory-West (ANL-W) Hot Fuel Examination Facility (HFEF), where profilometry was performed to help determine if any creep had occurred during dry storage. All 12 rods exhibited similar cladding diameter profiles (uncorrected for in-reactor oxide growth). Four rods with marginally higher diameters were chosen for fission gas release, internal pressure, and void volume determinations. These data are needed to determine the cladding stress, which is the driving force for creep. Choosing the rods with the largest diameters was intended to lead to the selection of those rods that might have experienced some thermal creep during postirradiation performance testing and dry storage. In reality, the differences found in the profilometry proved to be insignificant relative to experimental uncertainty. Thus, the selection of Rods H9, G6, H7, and G9 for gas analysis was somewhat arbitrary. Similarly, the internal gas pressures for the four rods were too close to allow discrimination in choosing three of the four rods for detailed characterization.

The three rods with the highest measured internal pressure, H9, G6, and H7, were sectioned into five segments (≈0.84 m each) per rod for transport to the Alpha Gamma Hot Cell Facility (AGHCF) at Argonne National Laboratory-East (ANL-E). Starting from the bottom of the rod, the first four segments (identified as E, D, C, and B by ANL-E) are each ≈840 mm long and the fifth segment (identified as A), which contains the plenum region, is ≈530-mm long. Paint marks were placed by ANL-W near the top of each segment to uniquely define its orientation. The segments were placed by ANL-W in shipping tubes supplied by ANL-E. These tubes were engraved with the following information: Surry, rod number, and A/G Number (Alpha Gamma Hot Cell number used to track specimens). Detailed instructions for segmentation, labeling and shipment were provided in hot cell instructions IPS-368-00-00 (H. C. Tsai, November 27, 2000). Thus, the tubes for rods H9 and G6 are labeled (591-A, 591-B, 591-C, 591-D and 591-E), and (592-A, 592-B, 592-C, 592-D, and 592-E), respectively.

The rod segments from two of the three rods with the largest diameters and highest gas pressures, H9 and G6, were sectioned to obtain specimens for creep testing, hydrogen determination, and metallographic examination for oxide thickness, cladding thickness, hardness, and hydride analysis. A few sections were also prepared for tensile testing. Limited ceramographic examination of the fuel was conducted because the rods were not breached and no change in the structure of the irradiated fuel was expected at the storage temperatures. When selecting specific locations for samples, we considered uniformity of burnup and fast fluence, proximity to the axial regions from which the creep samples were to be prepared, significant outer-surface oxidation, and the highest temperatures experienced during thermal-performance testing and storage. The sample identification matrix is given in the Table 2.

Table 2. Sample Identification Matrix for Surry Rods after Extended Dry Storage

Test Type	Number of Rods	Rod H9			Rod G6	
		0^a	500^a	1000^a	0^a	500^a
Profilometry	12	-	-	-	-	-
Gas analysis	4	-	-	-	-	-
Ceramography	-	591C-C4	591C-C12	591B-B2	592C-C4	592C-C12
Oxide thickness	-	591C-C4	591C-C12	591B-B2	592C-C4	592C-C12
Hydride orientation	-	591C-C4	591C-C12	591B-B2	592C-C4	592C-C12
Hydrogen content	-	591C-C5	591C-C13	591B-B3	-	-
Microhardness	-	591C-C4	591C-C12	591B-B2	-	-

^{a}Nominal distance (mm) of metallographic samples above fuel midplane.

The fuel midplane is at 1847 mm from the bottom of the rod. Sample C4 is at ≈5-18 mm above the fuel midplane and Sample C5 is at ≈19-32 mm above the fuel midplane. Samples C12 and C13 are ≈530-543 mm and ≈544-557 mm, respectively, above the fuel midplane. The cutting diagram for Rod H9 segment 591C is shown in Figure. 2. Cutting diagrams for Rod Segments 591B and 592C are shown in Appendix A.

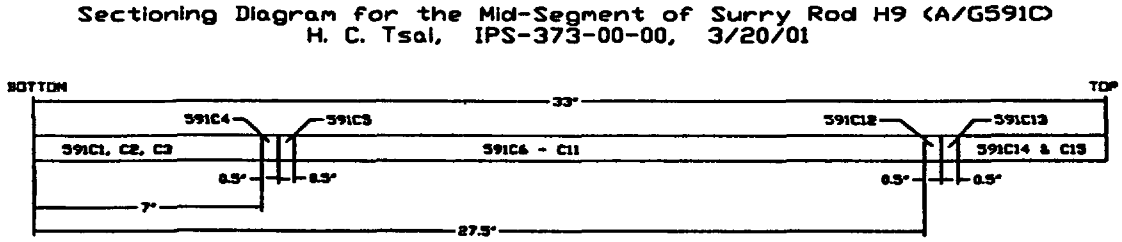

Sectioning Diagram for the Mid-Segment of Surry Rod H9 (A/G591C)
H. C. Tsai, IPS-373-00-00, 3/20/01

Fig. 2. Cutting diagram for metallographic, microhardness, and hydrogen analysis characterization of Rod H9 from Surry-2 Assembly T11. Samples C4 (metallography and microhardness) and C5 (hydrogen analysis) are at approximately the fuel midplane. Samples C12 (metallography and microhardness) and C13 (hydrogen analysis) are ≈500 mm above the fuel midplane

3.2 Profilometry

Linear profilometry traces of each rod were obtained at 0, 45, 90, and 135° relative orientations at ≈2.5-mm intervals along the length, starting at ≈330 mm from the top of the rod. The cladding diameter was measured to an accuracy of 2.5 x 10^{-3} mm. Averaging the four linear traces generated the cladding outer-diameter profile for Rod H9 (Fig. 3). Although not apparent in the individual traces, the averaged profile reveals discernible, albeit small, dips associated with the grid spacers of the assembly. Similar profiles were obtained for all 12 rods (see Appendix B). The average decrease in cladding diameter of the 12 rods 1 m from the bottom of the rod is ≈0.06±0.01 mm relative to the nominal as-fabricated diameter of 10.71 mm. This creepdown (≈0.6%) is typical for PWR rods with the Surry fuel cladding gap and a burnup of ≈36 GWd/MTU (Ref. 9).

Some of the profiles show an increase in diameter along the upper half of the rod relative to the lower half of the rod. Based on creepdown alone, one would expect the profile of the rod in an as-irradiated state to be reasonably flat in the middle 2.5 m of the fuel column, where the fast fluence is relatively uniform. The diameter increase in the upper half of the rods, measured after storage, is probably due to the increase in oxide layer thickness with axial location.

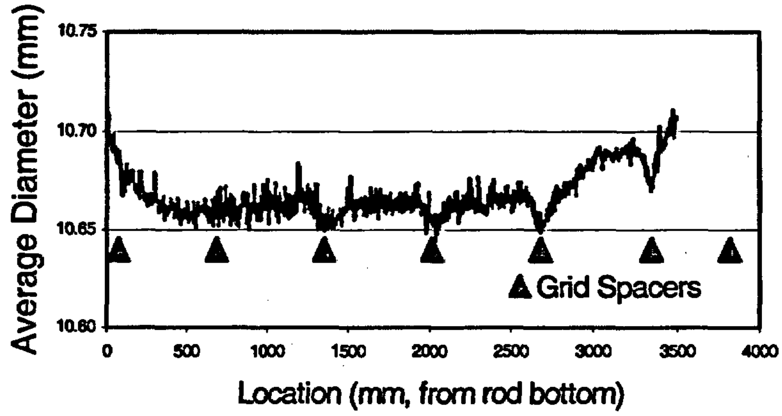

Fig. 3. Averaged outer-diameter profile of Rod H9 (from Surry-2 Assembly T11) after extensive thermal benchmark testing (≈350- 415°C) and ≈15 years of dry cask storage in He (≈344 → ≈155°C). The nominal as-fabricated cladding outer diameter is 10.71 mm.

When the cladding oxidizes in the reactor, the thickness of the oxide formed is greater than the metal layer that is oxidized. To compare the as-measured postirradiation diameter profile with a preirradiation profile or to compare the diametral growth from various locations on the same rod where differing rates of oxidation may have occurred, the as-measured postirradiation diameter profile must be corrected for oxide growth. The oxide layer thickness is divided by the Pilling-Bedworth ratio (PBR) to determine the effective thickness of Zircaloy that had oxidized. For this cladding, a PBR of 1.75 (Ref. 11), which accounts for the ≈10% porosity in the oxide layer, was used. The measured outer diameter of the cladding is then corrected by subtracting twice the difference between the oxide and metal thickness. The oxide thickness was measured at selected locations on the upper half of Rods H9 and G6. When the correction for the oxide layer was made, a relatively uniform creepdown of 0.6% was obtained for the middle 2.5 m of the fuel column.

3.3 Fission Gas Analysis and Void Volume Determination

Cladding creep during storage is driven by the stress induced by the rod internal gas pressure. This pressure is due primarily to the initial He fill gas and, to a lesser extent, the fission gas released from the fuel into the rod void volume. The void volume, gas composition and inventory, and fission gas isotopic composition were measured on four of the rods to determine internal rod pressure and to estimate the extent of maximum possible fission gas release during the storage period.

The measured internal gas pressures ranged from 3.43 to 3.61 MPa at 27°C, which is ≈0.7 MPa higher than the initial preirradiation gas pressure (see Table 3). The void volumes ranged from 19.53 to 20.39 x 10^{-6} m^3, which is typical for Westinghouse 15 x 15 rods. The decrease in void volume with burnup is caused by a combination of cladding creepdown and fuel swelling. The relative measurement errors of the void volumes and of the gas pressures are <3%. The internal gas composition in all four rods is essentially the same: 96-98% He fill gas with small amounts of O_2 (<0.01%) and N_2 (<0.03%). The poststorage isotopic composition of Xe and Kr are, within experimental error, the same as the postirradiation ratios for the Turkey Point fuel rods. The fission gas release values ranged from 0.4 to 1.1%, which is larger than the postirradiation fission gas release measured (0.22%) for the lower-burnup Turkey Point rods, but well within the range reported in the literature for rods of this type and burnup. Complete isotopic and chemical composition of the internal rod gases are given in Appendix C.

3.4 Metallography and Hydrogen Analysis

The procedures for sample cutting, preparation, and examination for both metallography and hydrogen analysis are documented in the AGHCF Operations Manual (AGHCF-PROG-204, 205, 206, and 207, August 2001). Etching of the sample is used to bring out certain features, such as hydrides in the cladding. For hydrides, an acid etch (45 ml H_2O_2 + 45 ml HNO_3 + 10 ml HF) is applied for 3 s. For the Surry cladding, the samples were re-etched for an additional 3 s, and no change in the hydride imaging was observed. Generally, a 50-75X photomosaic is prepared for the fuel rod cross-section observed on the Leitz-MM5RT Metallograph. Higher magnifications are used to image the cladding oxide thickness and the hydride morphology.

Table 3. Rod Volume, Internal Pressure (at 27°C) and Fission Gas Release

Rod	Void Volume, $m^3 \times 10^6$	Internal Gas Pressure, MPa	Fission Gas Release, %	Fission Gas Contribution to Void Pressure, %	Fission Gas Partial Pressure, MPa
T11-H9	19.76	3.61	1.08	3.61	0.129
T11-G6	19.53	3.51	0.39	1.36	0.047
T11-H7	20.29	3.43	0.88	3.01	0.102
T11-G9	20.02	3.44	0.49	1.65	0.056
Turkey Point	22 ± 1	3.5 ± 0.1	0.22 ± 0.01	0.50	0.017

Generally, oxide thickness photomicrographs are taken at eight evenly spaced locations around the cladding, covering a total of ≈45% of the cladding circumference. A similar procedure is used for the hydride morphology photomicrographs. The magnification of the metallograph is calibrated semiannually and/or after maintenance. A traceable 25-mm stage micrometer standard (KR-812) is used. The calibration is needed to put the correct scale markers on the photomicrographs.

For the cladding hydrogen analysis, the fuel is removed chemically through the use of a nitric acid bath. Depending on the anticipated hydrogen content, the cladding is subdivided by transverse and radial cuts so that each sample is small enough to preclude detector overload. Eight such measurements of the hydrogen content are performed with the Leco Model RH-404 hydrogen determinator. These measurements are then averaged to obtain the hydrogen content of the sample (e.g., C5) in wppm. The determinator is calibrated before each set of measurements. A titanium standard is provided by the manufacturer for calibration. The procedure for measuring the hydrogen content of Zircaloy cladding is based on the manufacturer's instruction manual and specific methods recommended for refractory metals (ASTM E-1447, Standard Test Method for Determination of Hydrogen in Titanium and Titanium Alloys by the Inert Gas Fusion Thermal Conductivity Method).

3.4.1 Fuel Pellet Condition

Changes in the condition of the fuel pellets were not expected because there was no cladding breach, and the temperature of the fuel during storage was lower than the temperature of the fuel during reactor operation. Transverse ceramographic samples were taken from Rod H9 at the rod midplane, ≈500 mm above the midplane, and ≈1000 mm above the midplane. Samples were taken from Rod G6 at 0 and 500 mm above the midplane. Cross-sectional mosaics (see Fig. 4) depict a pellet with multiple cracks, which is prototypical of this medium-burnup PWR fuel. Because of the extensive cracking, which occurred during reactor operation, several fuel fragments fell out of the cladding during the sectioning, leaving irregularly shaped voids (dark areas). The central region of the fuel ($r/r_0 < 0.5$) at the higher elevation contained a greater density of fission gas bubbles; hence the darker appearance. No such porous central region was apparent in samples from the lower-elevation C4 and C12, possibly because of their lower operating temperatures. The porous region at the higher elevation is nearly centered, indicating a symmetric temperature distribution, which is consistent with the fact that the rod was in the central region of the host assembly during the irradiation. As expected, no appreciable rim effect is observed in this medium-burnup rod.

3.4.2 Oxide Layers and Fuel-Cladding Gap

The thickness of the oxide layer on the cladding outer surface (see Fig. 5 and Table 4) was measured at eight azimuthal locations, evenly spaced around the cladding and covering ≈45% of the cladding circumference. At the higher elevation, consistent with a higher in-reactor temperature, the oxide layer is thicker. This is also larger than observed on the Turkey Point "D" rods at the same elevation, but well within the range of oxide thickness (5-40 μm) for this medium-burnup fuel (Ref. 12). Some fine circumferentially oriented microvoids were observed in the oxide layer (see Appendix D). Extremely limited and isolated spallation of the oxide was also observed, apparently due to the linkage of the microvoids (see Appendix D). Because the oxide layer is thin and considered non-load-bearing in the stress calculation, the isolated spallation would have no significant impact on fuel rod performance during dry storage. The oxide morphology was consistent with the observations made on the Turkey Point rods. A fuel/cladding gap was observed around the inner cladding circumference, probably formed during cooldown. Small (<10 μm), discontinuous oxide layers were observed on the cladding inner surface, but there was no evidence of fuel/cladding chemical interaction. Once again, this is typical behavior for rods at this burnup.

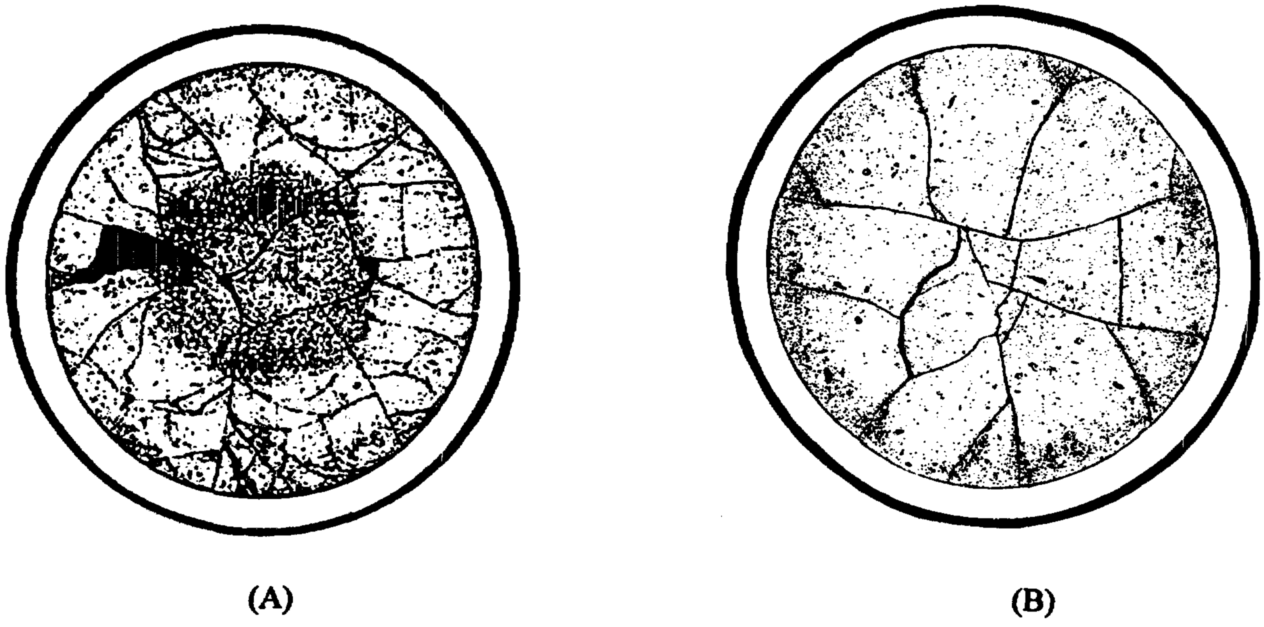
(A) (B)

Fig. 4. Cross-sectional mosaics of Rod H9: (A) ≈1000 mm above midplane, (B) approximate midplane.

Table 4. Surry-2 Assembly T11 Cladding Outer Oxide Layer Thickness (μm) at 0, 500, and 1000 mm above the fuel centerline

Rod	0 mm		500 mm		1000 mm	
	Oxide	Metal[a]	Oxide	Metal	Oxide	Metal
H9	24 ± 4	14 ± 2	33 ± 8	19 ± 4	40 ± 5	23 ± 3
G6	22 ± 6	13 ± 3	26 ± 3	15 ± 2	NM[b]	NM
TP-D[c] range	4 - 7	2.5 ± 1	5 - 8	3.7± 1	8 - 12	5.7 ± 1

[a] Based on oxide/metal thickness ratio = 1.75

[b] NM = not measured

[c] TP-D = Turkey Point D assemblies

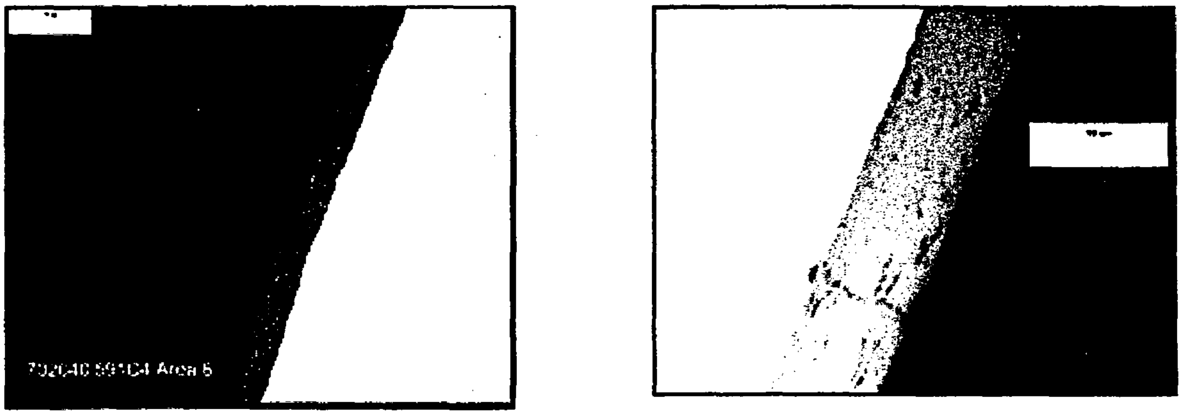

(A) (B)

Fig. 5. Cladding outer-surface oxide layer of Surry-2 Rod H9 from assembly T11 at: (A) approximate fuel midplane, and (B) ≈1000 mm above midplane. Scale = 50 μm.

3.4.3 Hydrogen Content, Distribution, and Orientation

Eight determinations of hydrogen content were made at each elevation using Leco fusion extraction analysis. The results are given in Table 5. Van Swam et al. (Ref. 11) indicates that the hydrogen pickup factor decreases with increased oxide thickness. For the range of oxide thicknesses measured on the Surry rods, the pickup factor is reasonably constant between 16 and 24%. For the Turkey Point rods, the factor is between 20 and 30%. The H_2 content was calculated for the measured oxide thickness using the average pickup factors. Within measurement uncertainty of the oxide thickness and pickup factor, good agreement was observed between the measured and calculated hydrogen content of Rod H9 axial locations. In the central region of the fuel column, where the axial temperature gradient in storage is small, the measured hydrogen content of the cladding is consistent with the thickness of the oxide layer. At ≈1 m above the fuel midplane, where the axial temperature gradient toward the end of the rod is steeply decreasing, there is less hydrogen than would be expected from the oxide thickness that developed in-reactor.

Adjacent cladding samples were etched to characterize hydride distributions. Six to eight azimuthal regions were imaged at the approximate fuel rod midplane, ≈500 mm above midplane, and ≈1000 mm above midplane along Rod H9 and at the approximate fuel rod midplane and ≈500 mm above the midplane along Rod G6. The density and radial location of hydrides varied both axially and azimuthally (see Appendix D and Fig. 6).

Hydrides at the midplane of Rod H9 are predominately in the inner and outer cladding surface regions. At progressively higher elevations, hydrides start to appear in the central part of the cladding as well. At 1 m above the midplane, the hydrides tend to be evenly distributed across the cladding width. The hydrides in the cladding of Rod G6 are also predominately in the inner and outer cladding surface regions at the rod midplane. Unlike Rod H9, the hydrides remain in the inner and outer cladding surface regions at the 500-mm elevation. Without baseline photomicrographs of the Surry cladding after reactor discharge, it is difficult to determine from metallographic images if radial or axial redistribution of hydrogen was a result of the prestorage testing ($T \leq \approx 414°C$) and/or dry-cask storage ($T \leq 350°C$).

When the concentration of hydrogen in solid solution in the Zircaloy matrix exceeds the solubility limit, the excess hydrogen precipitates as hydrides. Cladding is manufactured with a texture such that the hydrides precipitate in a circumferential direction upon reactor cooldown. At 414°C, almost all (220 - 250 wppm) of the hydrogen measured at the fuel midplane would have been in solid solution (Ref. 13). As the temperature decreased over time, the hydrogen in solid solution would eventually precipitate as hydrides according to the hydrogen precipitation solvus (Ref. 14). At the initial dry-cask-storage temperature (≈350°C), ≈100 wppm of the 250 wppm would have re-precipitated as hydrides. For the end-of-storage conditions, i.e., temperature of ≈150°C, essentially all of the hydrogen would have re-precipitated as hydrides.

The hydrides are in the form of long circumferential stringers. Although no radial hydrides are observed near the oxide/cladding interface, it is clear that small segments of the hydrides are oriented at angles between 0 and 90° from the cladding radius. This also holds true for the hydrides within the inner cladding region. These are only very small hydrides, and there is no evidence of significant reorientation. At a few of the azimuthal orientations ≈500 mm above the midplane on Rod G6, some of the long hydrides are surrounded by very small, randomly orientated precipitates.

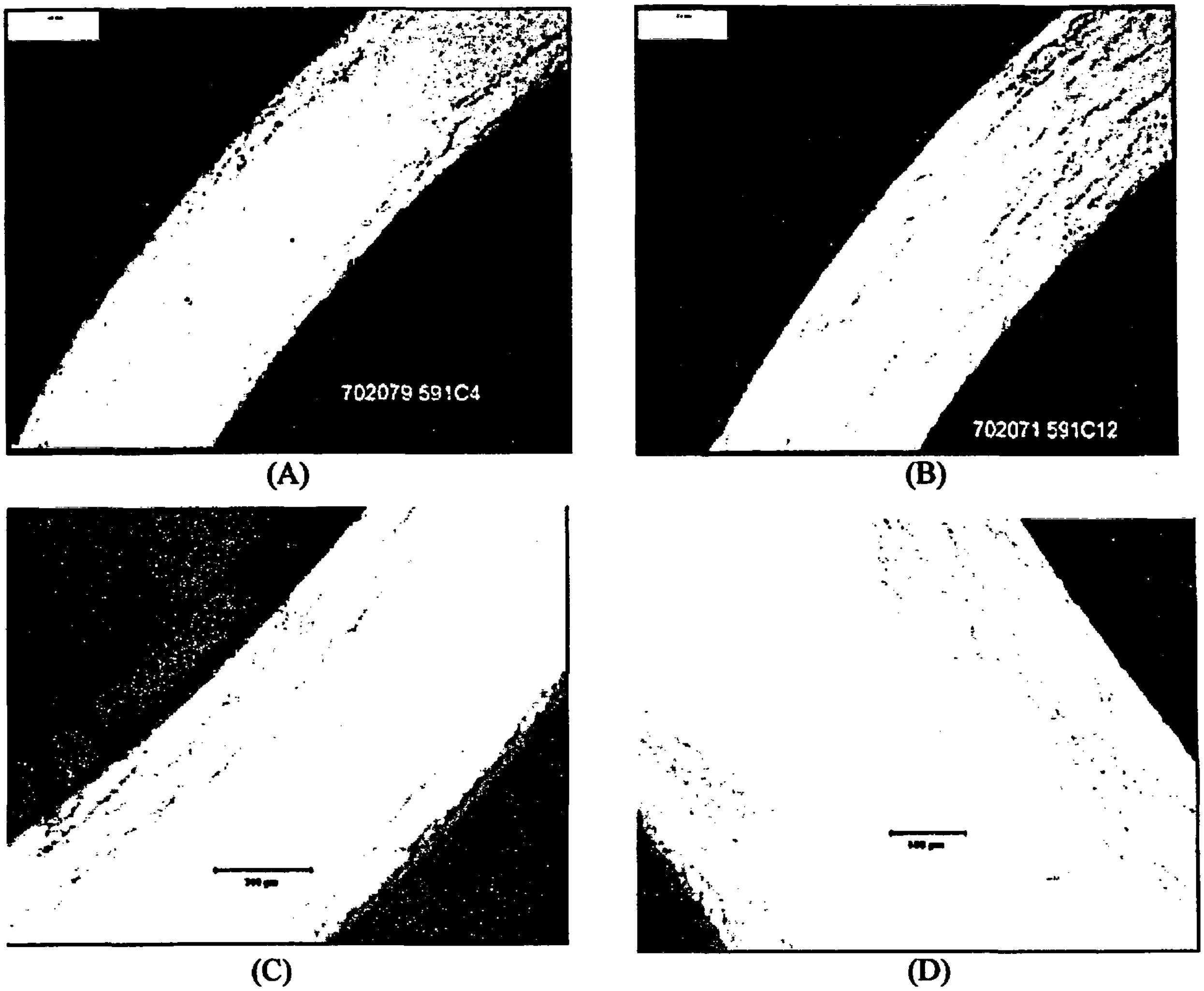

(A)

(B)

(C)

(D)

Fig. 6. Hydride structure in fuel rod cladding of Assembly T11 at two elevations: (A) approximate midplane of Rod H9, (B) ≈500 mm above midplane of Rod H9, (C) approximate midplane of Rod G6, and (D) ≈500 mm above midplane of Rod G6.

Table 5. Hydrogen Content (wppm) at ≈0, 500, 1000 mm above the Fuel Midplane and Standard Deviation data for Surry Fuel Rod Cladding and Turkey Point (TP) 3-cycle Cladding

Rod ID	0 mm		500 mm		1000 mm	
	Measured	Calculated[a]	Measured	Calculated	Measured	Calculated
H9	250 ± 40	200 ± 70	300 ± 25	270 ± 100	255± 14	330 ± 100
G6	NM	180 ± 70	NM[b]	210 ± 60	NM	NM
TP-D01/04	40-60	40 -85	50-70	40 - 100	75-90	65 – 150

[a] Calculated valued based on measured oxide thickness of adjacent sample and hydrogen pickup in Van Swam et al. (Ref. 11), assuming no axial migration;
[b] NM = not measured

3.5 Microhardness Measurements

Cladding microhardness was measured across the radius of the cladding at three axial locations of the H9 rod using a 200-g Vickers indenter (see Appendix D). Seven to nine measurements were performed at four azimuthal locations (≈90° apart) at each axial location. As seen in Appendix D, no discernable radial, azimuthal, or axial variation in hardness was observed. For the three H9 axial locations, the hardness values are 234±18, 239±5, and 236±10 dph, respectively. No comparative hardness data are available for the as-irradiated Surry cladding, but some data are available for the Turkey Point cladding. These two data sets are compared in Section 4.4.

3.6 Poststorage Thermal Creep Tests

Evaluation of creep ductility of the Surry cladding after dry-cask storage is an important part of this program. Thermal creep tests were conducted following storage to determine if the residual creep strain of the cladding was ≥1%, which would suggest that it would have survived bounding stresses and temperatures during storage, and retain residual creep strain for possible creep during transportation, reconsolidation, and final repository conditions. As data for these tests were collected as a function of time, the tests results also provided valuable data for the secondary creep rate of irradiated Zircaloy-4 cladding.

3.6.1 Thermal Creep Apparatus

The thermal creep apparatus is described in Appendix F. The system consists of three furnaces: two with a one-sample capacity and one with a three-sample capacity. The furnaces have a built-in thermocouple at the bottom for temperature feedback and control. In addition, in the test chambers that hold the specimens, two or three thermocouples are suspended near the midplane of the sample to monitor the sample temperature. With such control, tests are run at constant temperature vs. time and with very small axial temperature gradients. Each sample has its own pressurization system. Each system is equipped with controller/regulator units to maintain constant pressure within the sample. Should there be a sudden drop in pressure due to rupture, a solenoid valve in the system would isolate the breached sample from the pressure supply.

3.6.2 Thermal Creep Test Matrix and Summary of Results

Based on the October 2000 sponsor/peer-review meeting at Pacific Northwest National Laboratory (PNNL), eight tests were to be conducted in the temperature range of 360-400°C and the stress range of 120-190 MPa. At the July 2001 sponsor/peer review meeting at ANL, two additional tests (at 320°C) were suggested by DOE-RW and Yucca Mountain Project (YMP) representatives. The matrix and predicted creep strains for these 10 tests are presented in Table 6.

In November 2001, the first Surry creep test (S2.1 test with Sample C9) was initiated at an engineering stress of 190 MPa and a constant temperature of 400°C. Based on early test results, it became clear that the Surry cladding creep strain was a factor of 2-3 lower than predicted by the EdF model (December 2000) used to generate the test matrix predictions. This result was somewhat surprising because the cladding type, fast fluence, hydrogen content, stress, and temperature were all within the range of materials and test conditions that generated the data for the EdF creep model. Thus, although 5 of the 10 tests were designed to achieve ≥ 1% strain, it was evident that none would reach such strains unless they were run for longer times and/or under conditions of higher stress and/or temperature. The stress range for the remaining tests was increased from 120-190 MPa to 160-220 MPa. Although the temperature could have also been increased for the remaining tests, this would introduce the complication of evaluating the effects of annealing and the added difficulty of interpreting the data for benchmarking creep models and correlations.

The test matrix that evolved, given in Table 7, is based on the experience gained during the first test and on sponsor/peer interactions. Of the 10 tests planned, only five were conducted: the three tests requested by DOE-RW were; one test (380°C/160 MPa) was not conducted because it would generate very little strain; and one test (400°C/220 MPa) was not conducted due to problems with specimen preparation. Of the tests conducted, the initial 400°C/190 MPa test achieved 1% creep strain in 1873 h. This sample was reinserted at a higher stress of 250 MPa to achieve significantly higher strains during the available test time. Other tests were conducted at 380°C and both 220 and 190 MPa and at 360°C and 220 MPa. The creep strains and secondary creep rates determined from the five tests are also summarized in Table 7.

Table 6. Thermal Creep Test Matrix and Predicted Creep Strains for Test Times of Six, Nine and Twelve Calendar Months (based on July 18, 2001 Sponsor/Peer Review Meeting)

Primary Test Purpose[a]	ID #	T °C	Hoop Stress, MPa	Time, hours	Predicted Creep Strain, % (EdF Correlation, 12-00)		
					6 Months	9 Months	12 Months
RCS	1.1	380	190	≥3900	2.1	3.2	4.2
RCS	1.2	380	160	≥3900	1.1	1.5	2.1
PSC	1.3	380	120	≥3900	0.4	0.6	0.8
RCS	2.1	400	190	1300	2.6	---	---
RCS	2.2	400	160	1100	1.2	---	---
PSC	2.3	400	120	≥1300	0.5	1.2	1.8
RCS	3.1	360	250	1450	1.0	---	---
CB	3.2	360	120	≥2450	0.10	0.15	0.15
CB	4.1	320	190	≥4300	0.06	0.08	0.09
CB	4.2	320	120	≥4300	0.017	0.021	0.024

[a] Residual creep strain (RCS), primary-secondary creep (PSC), code benchmarking (CB)

Table 7. Surry Cladding Thermal Creep Test Matrix and Summary of Results[a]

Test ID	Sample ID	T, °C	Hoop Stress, MPa	Total Time, hours	Initiation Date	Accumulated Hoop Strain, %	Secondary Creep Rate, 10^{-4} %/h
1.1	C8	380	220	2180	03-02	1.10	4.5
1.2	C6	380	190	2348	03-02	0.35	0.88
1.3	---	380	160	---	---	---	---
2.1	C9	400	190	1873	11-01	1.04	4.9
2.2	---	400	220	---	---	---	---
2.3	C9	400	250	693	05-02	5.83	>49
3.1	C3	360	220	3305	02-02	0.22	0.42
3.2	---	360	TBD[b]	TBD	TBD	---	---
4.1	---	320	TBD	TBD	TBD	---	---
4.2	---	320	TBD	TBD	TBD	---	---

[a] All tests were terminated by August 1, 2002.
[b] To be determined

3.6.3 Hoop Thermal Creep Strain vs. Time

Hoop strains due to creep are determined from periodic measurements of the average outer diameter of the cladding sample vs. time. These measurements are made off-line at room temperature by first depressurizing the sample, to avoid the potential for hydride reorientation, and then cooling it. A laser profilometer is used to measure the azimuthal and axial variation of the 76-mm-long cladding tubing. The azimuthal values are averaged at each axial location. The five azimuthally-averaged values within the middle ≈40 mm of the sample are then averaged to obtain the average diameter of the cladding sample for conversion to creep strain. Details of the specimen design and the azimuthal and axial variations of sample diameter are presented in Appendix F.

The hoop creep strain at the sample outer surface is determined by the average change in diameter, normalized to the initial diameter ($\Delta D/D_o$). The 25-30-µm outer diameter oxide layer is assumed to have no resistance to creep. Also, the creep strain within the base metal is assumed to lead to no volume change, to be isotropic, and in a plane-strain state (i.e., no creep in the axial direction). These standard assumptions lead to a creep strain distribution across the wall that varies inversely with the square of the radial position. Correcting for the oxide layer thickness -- a very small correction -- and averaging the creep strain across the cladding wall leads to the following relationship for the wall-averaged hoop strain ($\varepsilon_{\theta c}$) for the Surry cladding:

$$\varepsilon_{\theta c} = 1.13\ (\Delta D/D_o) \qquad (3)$$

Figure 7 shows the time variation of both $\varepsilon_{\theta c}$ and $\Delta D/D_o$ for Sample C9, which was subjected to 400°C and 190 MPa hoop stress for 1873 h, followed by 693 h at 400°C and the elevated engineering hoop stress of 250 MPa. The wall-averaged creep strain and secondary creep rate at the end of the 1873 h were 1.04% and 4.9×10^{-4} %/h, respectively. The creep stain rate during the period of elevated stress was $> \approx 50 \times 10^{-4}$ %/h, with the total accumulated creep strain = 5.83%.

Figure 8 shows the time history of the creep strain for Sample C8 at 380°C and 220 MPa engineering hoop stress. It appears that secondary creep has been obtained. After 2180 h, the wall-averaged hoop creep strain is 1.10% and the secondary creep rate is 4.5×10^{-4} %/h. In comparing the creep strain of C8 with that of C9, (see Figs. 7 and 8) it is noted that the strain histories are similar for the two samples. This similarity suggests that a 20°C drop in temperature is compensated by a 30 MPa increase in hoop stress.

Figure 9 shows the time history of the creep strain for Sample C6 at 380°C and 190 MPa engineering hoop stress. It appears that this sample is also in the secondary creep regime after 2348 h at a wall-averaged hoop strain of 0.35%. The secondary creep rate is 8.8×10^{-5} %/h.

Figure 10 shows the time history of the creep strain for Sample C3 at 360°C and 220-MPa engineering hoop stress. The cladding is very creep resistant at this temperature level. Sample C3 appears to be in secondary creep regime after 3305 h at an average hoop strain of 0.22%. The secondary creep rate is $\leq 4.2 \times 10^{-5}$ %/h.

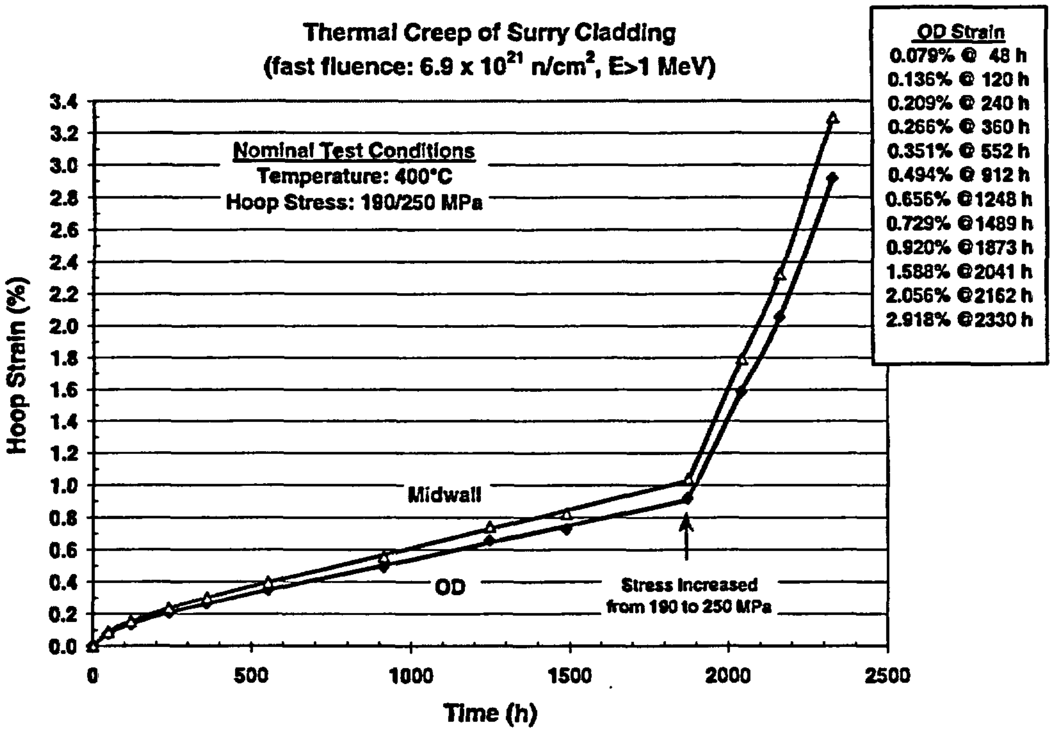

Fig. 7. Thermal creep data for irradiated, dry-cask-stored Surry cladding Sample C9 tested at 400°C and 190 MPa hoop stress for 1873 h, followed by 693 h at 250 MPa. Diamonds: OD measurements; triangles: calculated wall-average strain.

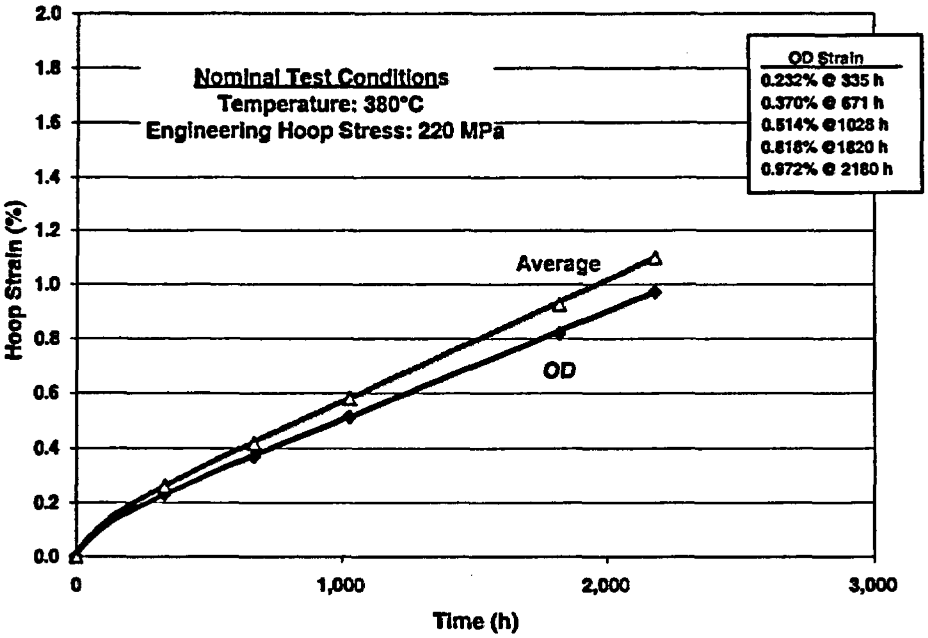

Fig. 8. Thermal creep data for irradiated, dry-cask-stored Surry cladding Sample C8 tested at 380°C and 220 MPa engineering hoop stress for 2180 h. Diamonds: OD measurements; triangles: calculated wall-averaged strain.

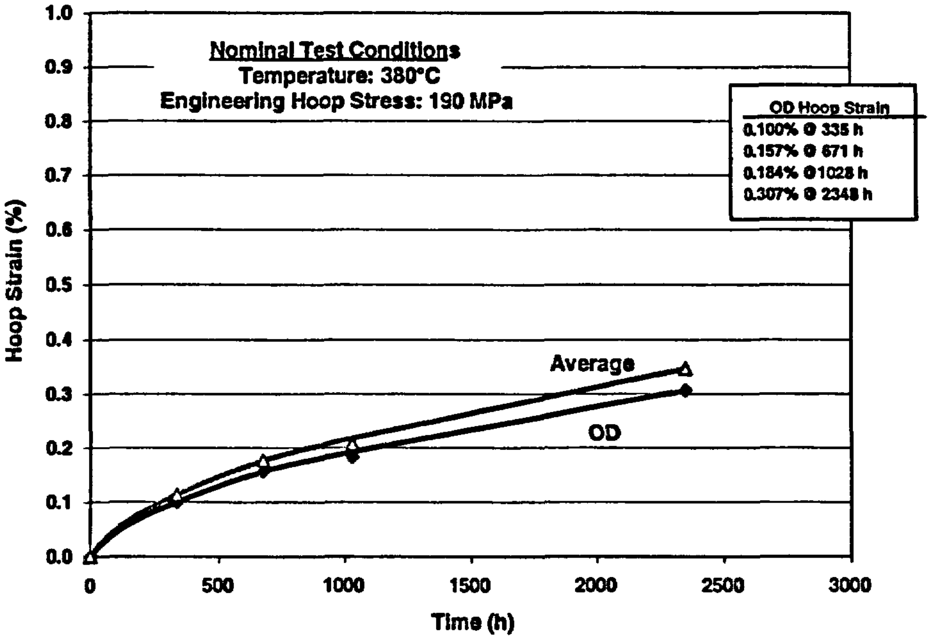

Fig. 9. Thermal creep data for irradiated and dry-cask-stored Surry cladding sample C6 tested at 380°C and 190 MPa engineering hoop stress for 2348 h. Diamonds: OD measurements; triangles: calculated wall-averaged strain.

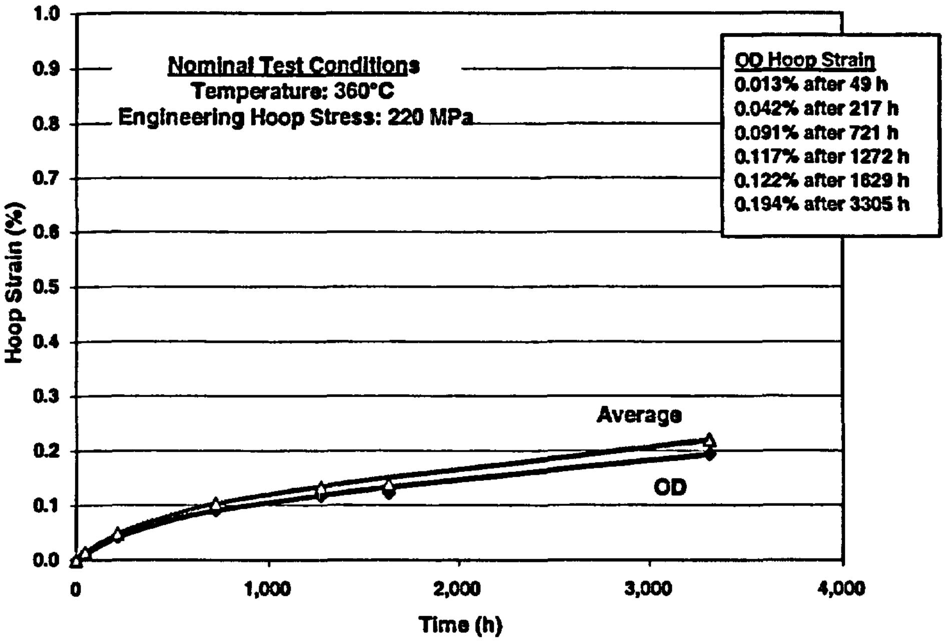

Fig. 10. Thermal creep data for irradiated, dry-cask-stored Surry cladding sample C3 tested at 360°C and 220 MPa engineering hoop stress for 3305 h. Diamonds: OD measurements; triangles: calculated wall-averaged strain.

4 IMPLICATIONS FOR EXTENDED DRY STORAGE

The original prestorage tests were not planned to provide long-term dry-storage-performance data. Therefore, temperature monitoring was terminated and post-performance testing characterization was very limited. The implications that can be drawn for extended dry storage are not as strong as they might otherwise have been. However, based on data trends, dry storage had no observed effects on the Surry rods.

4.1 Assessment of Creep during Prestorage Tests and Long-Term Storage

Ideally, one would like to compare individual rod profiles before and after storage to determine the amount of creep that occurred. Such a comparison would eliminate correction factors like oxide growth, crud variability, and systematic measurement error. In this particular situation, no prestorage profiles are available for the 12 Assembly T11 rods used in this study. Four methods were used to estimate the amount of creep that may have occurred during storage.

4.1.1 Method 1: Baseline and Measurement Uncertainty

Profilometry data from sister Surry rods taken during rod consolidation and from Turkey Point rods were used for comparative purposes. Measurements on the Turkey Point rods were obtained at the Battelle Memorial Institute (BMI) before shipment, at INEEL, and again during rod consolidation. The use of these diameter measurements as a baseline introduces a considerable degree of uncertainty to the creep estimation.

When these measurements, taken on the same Turkey Point rods at BMI and INEEL, are compared, a variation of ±0.2% is observed. This observation may be a result of differing measurement techniques and/or accuracy levels. Vinjamuri (Ref. 8) gives the maximum, minimum, and average diameters for the Surry and Turkey Point rods used in the consolidation project. The percentage variations are given in Table 8. (See Appendix E for Turkey Point, and Appendix B for Surry rod measured diameters.)

Table 8. Variation (%) of Averaged Rod Diameters from Assembly to Assembly and within an Assembly before Storage

Reactor	Assembly-to-assembly	Within an assembly
Surry (Ref. 8)	0.62	0.62
Turkey Point (Ref. 9)	0.31	0.46

Inasmuch as measurements were made in different facilities and the rods lacked tracking numbers through these tests, it is impossible to know which rod or assembly to use as a baseline. Thus creep strains based on any profile chosen for a basis of comparison may be as much as ± 0.6-0.9% different from the actual creep strains. In other words, > 0.9% creep strain would have to occur before it could be concluded with reasonable certainty that any thermal creep had occurred during performance testing and storage.

4.1.2 Method 2: Creep Code Calculations

Thermal creep predictions, which use the YMP creep code (Ref. 15), were made using the performance testing temperatures in Table 1 and the two long-term temperature profiles developed earlier. The stress calculation was based on measured parameters of an outside rod diameter = 10.71 – (0.06 ± 0.01) mm, internal rod pressure at room temperature = 3.5 ± 0.1 MPa, and cladding thickness (without oxide) = 0.596 mm. Based on the hardness measurements, it is assumed that no significant irradiation annealing of the cladding had taken place. Table 9 gives the calculated creep after various times.

Depending on the assumed temperature profile, 30 and 50% of any creep would have occurred during the long-term storage (0.03 and 0.08 % creep strain). Considering that this and other creep correlations predicted cumulative creep strain two to three times higher than measured (as reported above), one would expect that significantly less than 0.16% creep occurred during the prestorage thermal-benchmark tests and the long-term storage of this fuel.

Table 9. Predicted Creep Strains after Various Test and Storage Periods

Temperature °C	Duration h	Cumulative Creep Strain after Total Duration %	Creep during Duration %
344	119	0.012	0.012
359	43	0.015	0.003
415	72	0.032	0.017
357	93	0.037	0.005
398	72	0.047	0.010
348	2880	0.081	0.034
344 - 155	1.3×10^5	0.113[a]	0.032[a]
344 - 155	1.3×10^5	0.164[b]	0.083[b]

[a] Temperature profile for Method 1 in Fig. 1.

[b] Temperature profile for Method 2 in Fig. 1.

If the ratio of the creep during performance testing and extended dry storage calculated by Method 2 is reasonable, between 0.03 and 0.08% creep may have taken place during the extended storage period. This is further reduced to 0.01 - 0.04% creep if one takes into account the fact that the predictive creep equations were a factor of 2-3 high when compared with the creep measurements presented in this report for the same Surry cladding.

4.1.3 Method 3: Comparison with Prestorage Turkey Point Diameters

An estimate of the maximum creep can be obtained by comparing the after-storage diameters with the minimum diameter that may have existed before storage. The diameters of 20 Turkey Point rods were measured by spiral profilometry after irradiation and water storage (transportation in a water-filled cask) before dry storage. Average profile plots are available (Ref. 8) with error limits indicative of the rod ovality. The hottest region in the vertical storage cask with a He atmosphere was between 2 and 3 m from the bottom of the fuel. This elevation is where one would expect the maximum creep strain to occur during storage. With the estimates from the plots as a basis, the maximum, minimum, and average diameter for each rod in the 2-3 m elevation was tabulated (see Appendix E for Turkey Point, Appendix B for Surry). The global (worst case for a collection of rods) and average values over the set of rods in these tables are summarized in Table 10.

The worst case would be a comparison of the global maximum from the Surry rods with the global minimum from the Turkey Point rods, which is 0.6%. If we compare the average Surry maximum with the average Turkey Point minimum, this drops to 0.3%. When corrected for the difference between oxide growth in the Surry and Turkey point rods, this estimated worst-case creep strain is reduced to 0.4 and 0.1%, respectively. Comparison of the averages implies that no creep occurred during performance testing and storage. The uncertainty in the baseline, as shown above, indicates that these values are all essentially zero.

Table 10. Global and Average Rod Diameters -- Uncorrected for Oxide Growth -- at 2-3-m Elevation from Bottom of Rod

Assembly	Maximum Raw Diameter mm	Average Raw Diameter mm	Minimum Raw Diameter mm
Turkey Point global[a]	10.765	Not Applicable	10.638
Turkey Point average[a]	10.721	10.678	10.650
Surry global[b]	10.700	Not Applicable	10.645
Surry average[b]	10.679	10.670	10.656

[a] Turkey Point rod diameters measured prior to storage.

[b] Surry rod diameters measured after 15 years storage.

4.1.4 Method 4: Comparison with Maximum Potential Creepdown

Another way to evaluate thermal creep that may have occurred after reactor discharge is to compare the after-storage profiles with the minimum diameter that could have occurred due to in-reactor creepdown. During irradiation at a radially averaged fuel temperature of ≈780°C (Ref. 16), the diameter of the as-fabricated pellet, 9.385 mm (Surry drawings), would have increased ≈0.7% due to thermal expansion (Ref. 17). If the pellet formed a mandrel for the cladding, the outer cladding diameter (not accounting for oxide growth and pellet ridges) would be the diameter of this pellet plus two times the cladding thickness (0.617 mm) or 10.685 mm. Depending on whether this value is compared with the global or average maximum Surry diameters (see Table 10), the maximum creep would be between 0 and 0.13%.

The estimated maximum creep is further reduced if the expansion due to oxide growth is taken into account. This correction was made at the three locations where the oxide thickness was measured on the upper half of Surry Rods H9 and G6 (see Table 4). The oxide layer thickness was divided by a PBR of 1.75 (Ref. 11), which accounts for the ≈10% porosity in the oxide, to determine the effective thickness of Zircaloy that had been oxidized. The measured outer diameter of the cladding was then reduced by twice the difference between the oxide that had formed and the oxidized metal. As expected, the corrected diameters exhibit a reasonably flat profile. When the corrected diameters, with uncertainty (minimum metal oxidized), are compared with an initial in-reactor creepdown diameter of 10.685 mm, within experimental error, no creep occurred during dry storage.

The creep strain estimates shown in Table 11 are well below 1%. If any thermal creep occurred, it was probably during either the performance testing phase or the initial storage years when the temperature was hottest and the stress highest. The current storage temperature in the Castor cask is substantially lower then the initial storage temperature and will continue to drop during extended storage.

Table 11. Summary of Storage Creep Estimates for Various Calculation Methods

Method	Maximum Creep, %	Minimum Creep, %
1[a]	0.9	0
4[b]	0	0
2[c]	0.08	0.03
2a[d]	0.04	0.01
3[e]	0.4	0.1

[a] Baseline and measurement uncertainty.

[b] Comparison with maximum potential creepdown.

[c] Creep code calculations.

[d] Same as method2 except it has a correction to the creep correlation.

[e] Comparison with Turkey Point diameters measured before storage.

4.2 Fuel Rod Stress

Stress on the cladding due to the rod internal pressure is the driving force for cladding creep. For the Surry rods, most of the internal pressure is due to the He fill gas. It is not possible to partition the amount of fission gas released during in-reactor operation and during dry storage. The release occurs both by a diffusive process driven by the temperature gradient across the fuel and by cracking/rehealing during in-reactor startups and shutdowns. In-reactor, the temperature gradient is greater and the temperature is higher; hence, the diffusion coefficient is higher. The measured fission gas release in the Surry rods is within the range expected for the in-reactor release of fission gas. In all likelihood, all of the release occurred in-reactor. Any further release that may have occurred during storage would be substantially lower because of the lower diffusion constants and would have an insignificant effect on internal pressure and cladding stress. Thus, the stress on the cladding would decrease with time as the internal pressure decreases with temperature.

4.3 Hydride Redistribution and Reorientation

As the cladding is heated during drying of the cask and initial storage at higher temperatures, much of the hydrogen introduced into the cladding during irradiation goes into solid solution in the Zircaloy matrix. As the cladding cools during storage, hydrogen in solid solution will precipitate as hydrides as the solubility limit is exceeded. Depending on the stress levels in the cladding, the cladding texture and cooling rates, these hydrides may be circumferential or radial. Excessive hydrogen content or radially oriented hydrides may degrade the mechanical properties of the cladding.

The Castor V/21 cask initially supports a large axial temperature gradient at the top and bottom of the fuel rods. The measured hydrogen content of the cladding in the and bottom of the fuel rods. The measured hydrogen content of the cladding in the center of the fuel column, where the axial temperature gradient is small, agrees with the hydrogen level expected from the generation of the measured oxide layer. The hydrogen content of a region of the rod that was in the steep in-cask temperature gradient was less than expected from the thickness of the oxide layer that formed in-reactor. This finding indicates that hydrogen may have migrated during dry storage into the cooler ends of the rods. This migration probably took place early in storage when both the temperature and the temperature gradient were the largest.

This migration has not been confirmed by measurement. However, it would be relatively straightforward to measure the hydrogen level at 1.5 m and in the cooler plenum region to determine the extent of axial hydrogen migration in Rod H9. The effect of the re-precipitation of this excess hydrogen as the rods cool further during storage has not been evaluated.

4.3.1 Comparison of Surry Hydride Distribution with Other Fuels

Because no postirradiation or prestorage information is available about the hydrides in the Surry cladding, two similar PWR fuels that bracket the burnup of the Surry fuel are used as a comparative baseline. Metallographic examination of the Turkey Point PWR cladding, which is of the same design as Surry but at lower burnup (≈28 GWd/MTU) and hydrogen content (<100 wppm), reveals a very small fraction of hydrides branched in the radial direction following reactor discharge and cooling (Ref. 10). For this fuel, at similar axial elevations to the metallographic specimens taken on the Surry cladding, the hydrides were uniformly distributed, and appeared much shorter than those found in the Surry rods. Both Surry rods contained approximately five times as much hydrogen as the Turkey Point rods at the same elevation. This is due to the higher burnup (i.e., longer in-reactor residence time) of the Surry rods.

A standard 14 x 14 Combustion Engineering 4-cycle Calvert Cliffs (CC) PWR assembly (ATM-106) with a peak burnup of 46 GWd/MTU (Ref. 18) was used for comparative purposes. The peak burnup was ≈10 GWd/MTU higher than that of the Surry rods. The cladding of the CC rod was Sandvik Zircaloy-4, but the initial condition of the cladding was not given. At ≈1 m above the fuel midplane, both the Surry and CC rods showed circumferential hydrides rather evenly distributed across the cladding wall. The hydrides were in the range of 500 µm long in both cases. It is difficult to quantitatively measure the amount of hydrides. It did appear that the CC rods contained more hydrides than the Surry rods at this elevation. In neither case was there any evidence of radial hydrides.

No metallographic specimens are available for the CC rods that correspond to the metallographic samples taken on the Surry rods at 500 mm above fuel midplane. CC samples, which are ≈280 mm above and 410 mm below the midplane, are very similar and probably represent the midplane hydride structure. At these locations, at least an order of magnitude fewer hydrides are present in the CC rods than in the Surry rods. The hydrides are much shorter, possibly concentrated a little more in the center of the cladding, with very few and very small radial hydrides present. This is considerably different from the midplane hydride structure seen on the Surry rods.

Although the hydrides in the Turkey Point and Calvert Cliffs claddings after irradiation, and the Surry cladding after storage differ in appearance, without baseline micrographs of the Surry cladding after reactor discharge it is difficult to determine if radial and circumferential redistribution of hydrogen occurred after the period in vacuum (T ≈ 414°C) and/or after dry-cask storage (T ≤ 350°C). The H-distributions appear benign with regard to cladding integrity.

4.3.2 Reorientation

After years of storage, very few, if any, radial hydrides are found in the Surry fuel rods. The hoop stress needed for hydride reorientation in unirradiated Zircaloy is not well defined (35-40 MPa at 300-400°C) and depends on such things as fabrication history, basal pole texture, hydrogen content, and temperature. These parameters are briefly reviewed by Einziger and Kohli (Ref. 12). Recent unpublished evaluations of reorientation work in quenching-type experiments (cooling rates much faster than expected in dry storage) on irradiated cladding indicate that the stress threshold is temperature dependent and higher than in unirradiated material.[1] These later evaluations are not sufficiently conclusive to determine if significant reorientation of hydrides during cooling should have occurred under the low hoop stresses (<62 MPa at <415°C) present in the cladding of the Surry rods.

The stress required for reorientation appears to increase with decreasing temperature, and the stress in the fuel rods decreases with decreasing temperature. Because cooling from 355°C to ≈155°C precipitated hydrides that are circumferential, any additional hydride formation during further cooling should also be circumferential.

4.4 Cladding Annealing

Knoop hardness measurements with a 200-g weight were taken on as-irradiated Type "B" and Type "D" Turkey Point cladding and cladding of those two types annealed at 571, 482, and 323°C (Ref. 10). As with the Surry cladding, no variation in hardness was found across the Turkey Point cladding wall under the test conditions. The Knoop hardness of both as-irradiated cladding samples and all samples annealed at 323°C for 2100 h was 270±20. The hardness of the cladding annealed at 571°C for 740 h and at 482°C for 4656 h was 185±5. The agreement between the as-irradiated and as-annealed-at-323°C hardness results, as well as the agreement with the values in the literature (Ref. 19 and 20), suggests that little annealing should take place at 323°C for 2100 h. The values obtained also agree with the literature on the point that significant annealing of irradiation damage should occur in a short time (100 to 10000 h) above 400°C (Ref. 21).

When a 200-g weight is used, at least for stainless steel, the Vickers hardness is ≈ 5% lower than the Knoop hardness (Ref. 22). With the 5% correction between hardness scales, the Surry cladding hardness (≈250 Knoop), based on three samples from Rod H9, is slightly lower than the Turkey Point as-irradiated cladding, indicating that, at most, slight annealing may have occurred. If one assumes a linear relationship between hardness and indentation number, the amount of recovery is estimated to be <20%. According to Bouffioux's (Ref. 20) review of the Zircaloy annealing data, the only time that the cladding was at a high enough

---

[1] Based on unpublished analysis of reorientation experiment performed independently by K. Gruss (NRC) and Eric Siegmann (Framatome).

temperature for a long enough time for any annealing to occur was in vacuum when the temperature excursion to 415°C occurred. Even in that situation, the annealing would be expected to be small because the duration was short. However, without baseline data on the hardness of the specific H9 Surry cladding after reactor discharge, it is difficult to assess annealing by comparing the hardness of the H9 Surry cladding with cladding irradiated to lower neutron damage levels and possibly at lower in-reactor temperatures.

If each temperature profile proposed earlier were bounded by an isothermal period at 344°C until the temperature dropped to 325°C and then stayed at 325°C for the remainder of the 15 years of storage, Bouffioux's plot (Ref. 20) would still predict no recovery during the duration of the extended dry storage. Any recovery that may have occurred was probably during the performance testing, when the temperature reached as high as 415°C for 72 h, and not during the extended storage. At the even lower temperatures expected for continued storage (<150°C), no additional recovery is expected. Perhaps the strongest argument in favor of the idea that little, if any, annealing occurred is that the cladding hardness values are relatively uniform from midplane to ≈1 m above midplane.

4.5 Post-storage Residual Creep Strain and Strain Rate

The primary purpose of the post-storage thermal creep tests was to demonstrate that the Surry cladding would have adequate residual creep strain to survive upperbound dry-cask storage conditions (≤400°C, <150 MPa) and upperbound repository conditions. Inasmuch as creep data were recorded vs. time, valuable data were also generated to establish primary creep strains and secondary creep rates. However, because both the primary creep strain and the secondary creep rates of the poststored Surry cladding were factors of 2-3 below most model predictions, residual post-storage strains ≥ 1% were achieved in only three of the tests, whereas secondary creep appeared to be achieved in all five tests.

A hoop creep strain of 1% and a secondary creep rate of (4.8×10^{-4} %/h) were achieved after 1873 h at 400°C and 190 MPa engineering hoop stress. After reinserting the sample at 400°C and a significantly higher engineering hoop stress (250 MPa) for 693 h, the total hoop strain for this sample was ≈6% without failure at a secondary creep rate of ≈50×10^{-4} %/h, followed by an increase in creep rate due to wall thinning. This wall thinning was uniform around the circumference of the cladding, suggesting that local instability, which would be a precursor to failure, had not yet occurred. Such a creep strain would be more than adequate for upper bound dry-cask-storage and final-repository conditions. However, these results do not address the possibility of lower thermal creep strain life at lower temperatures (e.g., ≤ 360°C). A second sample tested at 380°C and 220 MPa, also achieved 1% thermal creep strain and secondary creep (4.5×10^{-4} %/h) within the test duration of 2180 h. This result is encouraging because both the temperature and the stress values are reasonable upper bounds for dry-cask-storage conditions.

The other two tests, at 380°C/190-MPa and 360°C/220-MPa, achieved strains of only 0.35% at 2348 h and 0.22% at 3305 h, respectively. These samples appear to have achieved secondary creep with creep rates of 0.88×10^{-4} %/h for the 380°C/190-MPa test and 0.42×10^{-4} %/h for the test at 360°C and 220-MPa. Additional data points, closer together in time, would be needed to determine the secondary creep rate more precisely. However, for these low-strain tests, it was not cost-effective to increase the number of data points per test. Both of these results are useful for validating models and correlations for predicting creep during dry-cask storage. Because NRC-SFPO ISG-11 Rev. 2 (Ref. 23) recommends 400°C as an upper temperature limit for vacuum drying, transfer, and dry storage, additional tests at 400°C (160 MPa and 220 MPa) are planned.

5 CONCLUSIONS AND RECOMMENDATIONS

5.1 Conclusions

Surry reactor PWR fuel rods (35.7 GWd/MTU) that were stored for ≈15 years at an initial temperature of ≈350°C (with temperatures reaching as high as 415°C during ≤72 h of performance testing) in a Castor-V/21 cask have been evaluated. After visual examination, the diametral profiles of 12 rods were measured and the gas inside four rods was analyzed for pressure, volume, composition, and isotopic content. Based on the results of the profilometry and gas analysis, three rods were sectioned and shipped to ANL-E for more detailed characterization. Metallography, microhardness, and hydrogen determination have been completed at three axial locations of Rod H9 and metallography has been completed at two locations of Rod G6. The main conclusions are:

1) It appears that the Surry rods experienced very little thermal creep during thermal-benchmark testing and dry-cask storage. The creep would not increase significantly during additional storage because of the low temperature after 15 years, the continual decrease in temperature due to the reduction in decay heat, and the concurrent reduction in pressure and stress. Comparing post-storage Surry rod diameters with the range of diameters measured for Surry and Turkey Point rods prior to storage introduces considerable uncertainty in the attempt to quantify thermal creep that may have accumulated during storage. Predictions from a best-estimate model suggest that the thermal creep during storage should be <0.1%. This prediction is supported when a correction is made for oxide layer thickness and when the diameter readings along a single Surry Rod (H9) are compared.

2) Within experimental uncertainty, no additional fission gas appears to have been released during the storage period.

3) No evidence of hydrogen pickup or hydride reorientation is noted during the storage period. The limited hydrogen-content data (3 axial locations of Rod H9) suggest that hydrogen may have migrated axially from above the fuel midplane to the cooler upper ends of the rods. At least two additional hydrogen measurements, e.g., at 1.5 m and in the plenum region, would be needed to confirm this hypothesis. The effects of such migration on the long-term stability of the rods in dry storage are undetermined.

4) Little, if any, cladding annealing occurred during the prestorage performance period or extended-storage period.

5) The Surry cladding has residual creep strain >1% for thermal creep test temperatures of 380°C (220 MPa) and 400°C (190 MPa). A residual creep strain of ≈6% was achieved in the 400°C sample after raising the stress level to 250 MPa for ≈700 h. Although the creep rate increased during the 700 h due to wall thinning, the deformation was

uniform around the circumference of the cladding. Inasmuch as no symmetric or asymmetric bulging of the cladding was observed – a precursor to failure – the residual creep strain of the 400°C sample is >6%. Secondary creep rates that span two orders of magnitude were measured for the five creep tests. These data are useful not only for code benchmarking, but for determining the temperature and stress sensitivity of the creep rate.

5.2 Recommendations

During the course of this research, additional work has been identified that would support both the criteria for dry cask storage licensing and the applications for dry cask storage license renewal. These areas include: generating additional creep data at 400°C, investigating possible axial migration of hydrogen during dry cask storage, investigating the degree of hydride reorientation that may occur during cooldown under stress, and performing post-creep ductility/toughness tests.

It would be very useful to generate more creep data at 400°C to supplement the data at 190 MPa and 250 MPa. To support the ISG-11 Rev 2 (Ref.23) recommendation of 400°C as an upper temperature limit for vacuum drying, transfer and storage, It is recommended that new creep tests at 400°C and 160 and 220 MPa be conducted.

Hydrogen content measurements were made on Rod H9 cladding samples at ≈0, 0.5 and 1.0 m above the midplane. Although the 1.0-m location had a thicker oxide layer, the cladding contained less hydrogen. Additional hydrogen measurements of the as-received Surry Rod H9 cladding should be taken at 1.5 m above midplane and the in plenum region. Both of these locations would have lower storage temperatures than the midplane and 0.5-m-above-midplane positions. If the trend of decreasing hydrogen content with axial elevation continued, this would strongly support the axial migration of hydrogen during storage.

Although all of the current creep samples are routinely depressurized prior to cooling, hydride reorientation could be investigated by cooling some of the creep samples while maintaining the internal pressure. Samples C2 and C6 tested at 360°C/220-MPa and 380°C/190-MPa would be ideal for this purpose, as neither sample has accumulated very much creep strain. Following cooldown under these stresses, metallographic analysis should be performed at the specimen midplane to determine the degree of hydride reorientation.

Three point bend tests have been proposed to measure the ductility/toughness of the Surry cladding prior to and after creep testing. Creep sample C8 (380°C/220-MPa) has achieved 1% creep strain and would be a good candidate for post-creep ductility testing. One of the new 400°C samples (220 MPa) will achieve greater than 1% creep strain in a reasonable time frame. It should be used as the second post-creep sample to be subjected to the three-point bend ductility test.

6 REFERENCES

1. Einziger, R. E., D. L. Baldwin, and S. G. Pitman. "Interim report. Data Needs for Long-Term Dry Storage of LWR Fuel." TR-108757, Electric Power Research Institute: Palo Alto, CA. April 1998.

2. McKinnon, M. A. and V. A. Deloach. "Spent Nuclear Fuel Storage – Performance Tests and Demonstrations." PNL-8451, Pacific Northwest Laboratory: Richland, WA. April 1993

3. McKinnon, M. A., and A. L. Doherty. "Spent Nuclear Fuel Integrity during Dry Storage – Performance Tests and Demonstrations." PNNL-11576, Pacific Northwest National Laboratory: Richland, WA. June 1997

4. Dziadosz, D., et al. "The CASTOR-V/21 PWR Spent-Fuel Storage Cask: Testing and Analysis." EPRI NP-4887/ PNL-5917, Electric Power Research Institute: Palo Alto, CA. November 1986

5. Kenneally, R. M. and J. H. Kessler. "Cooperative Research Program on Dry Cask Storage Characterization." Proc. ICONE 8, 8th International Conference on Nuclear Engineering: Baltimore, MD. April 2, 2000

6. "Dry Cask Storage Characterization Project: Interim Progress Report – October 2001." EPRI report 1003010. Electric Power Research Institute: Palo Alto, CA. October 2001

7. Moore, Ernie. V. <ernie_moore@dom.com> "T11 Fluence Calculation," July 13, 2001, [personal e-mail], (July 13, 2001)

8. Vinjamuri, K., M., et al. "Dry Rod Consolidation Technology Project at the INEEL." EGG-WM—8059. Idaho Falls, ID. April 1988

9. Davis, R. B. "Pre-Test Nondestructive Examination Data Summary Report on Turkey Point Spent Fuel Assemblies D01, D04, and D06 for the Climax – Spent Fuel Test." HEDL-TME 80-83, UC-70, Hanford Engineering Development Laboratory: Richland, WA. January 1981

10. Atkin, S. D. "Destructive Examination of 3-Cycle LWR Fuel Rods from Turkey Point Unit 3 for the Climax – Spent Fuel Test." HEDL-TME 80-89, UC-70, Hanford Engineering Development Laboratory: Richland, WA. June 1981

11. Van Swam, L. F. et al. "Behavior of Zircaloy-4 and Zirconium Liner Zircaloy-4 Cladding at High Burnup." Proc. International Topical Meeting on LWR Fuel Performance, Portland Oregon. P. 421. American Nuclear Society: LaGrange Park, IL. March 1997

12. Einziger, R. E., and R. Kohli. "Low-Temperature Rupture Behavior of Zircaloy-Clad PWR Spent Fuel Rods Under Dry Storage Conditions," *Nucl. Technol.* Vol. 67. p. 107. Oct. 1984

13. Kearns, J. J. "Terminal Solubility and Partitioning of Hydrogen in the Alpha Phase of Zirconium, Zircaloy-2 and Zircaloy-4." *J. Nucl. Mater.* Vol. 22. pp. 292-303. 1967

14. Kammenzind, B.F., et al. "Hydrogen Pickup and Redistribution in Alpha-Annealed Zircaloy-4," Zirconium in the Nuclear Industry: Proc. Eleventh International Symposium, ASTM STP 1295, E. R. Bradley and G. P. Sabol, Eds., American Society for Testing and Materials: Conschocken, PA. pp. 338-370. 1996.

15. Commercial Radioactive Waste Management System M & O 2000c. "Clad Degradation - Summary and Abstraction." ANL-WIS-MD-000007 REV 00 ICN 01. Las Vegas, Nevada: CRWMS M&O. ACC: MOL.20001024.0229, Dec 2000.

16. O'Donnell, G. M., H. H. Scott, and R. O. Meyer. "A New Comparative Analysis of LWR Fuel Designs." NUREG-1754. Nuclear Regulatory Commission: Washington, DC. Dec. 2001

17. Fink, J. K., M. C. Chasnov, and L. L. Leibowitz. "Thermodynamic Properties of UO_2." ANL-CEN-RSD-80-3. Argonne National Laboratory: Argonne, IL. April 1981

18. Guenther, R. J., et al. "Characterization of Spent Fuel Approved Testing Material—ATM-106." PNL-5109-106, Pacific Northwest Laboratory: Richland, WA. Oct. 1988.

19. Northwood, D. O. and U. Kosasih. "Hydride and Delayed Hydrogen Cracking in Zirconium and its Alloys." *Inter. Met. Rev.* Vol. 28. No.2. p. 92. 1983.

20. Bouffioux, P. and L Lefras. "Effect of Hydriding on the Residual Cold Work Recovery and Creep of Zircaloy 4 Cladding Tubes." Proc. LWR Fuel Performance Meeting, Park City, Utah. American Nuclear Society: LaGrange Park, IL. April 10, 2000.

21. Adamson, R. B. "Irradiation Growth of Zircaloy," Proc. 3rd Int. Conf. Zircaloy in the Nuclear Industry, Quebec City, Canada, August 10-12, 1976, ASTM STP 633, p. 326, A. L. Lowe and G. W. Parry, Eds., American Society for Testing and Materials: Conschocken, PA. 1977

22. Tate, D. R. *Trans. Am. Soc. Met..* Vol. 35. 1945.

23. Nuclear Regulatory Commission (U.S.), Spent Fuel Project Office. "Interim Staff Guidance - 11, Rev. 2 - Cladding Considerations for the Transportation and Storage of Spent Fuel." Washington, D.C. August 2002.

APPENDIX A

FUEL ROD SECTIONING DIAGRAMS

Figures

A.1 Cutting Diagram for the Characterization of Mid-Segment of Rod H9 from Surry-2 Assembly T11 .... A-3

A.2 Cutting Diagram for the Characterization of Second-from-Top Segment of Rod H9 from Surry-2 Assembly T11 .... A-4

A.3 Cutting Diagram for the Characterization of Mid-Segment of Rod G6 from Surry-2 Assembly T11 .... A-4

A.4 Cutting Diagram for the Characterization of Second-from-Top Segment of Rod G6 from Surry-2 Assembly T11 .... A-5

Each of the three fuel rods was cut into five segments at ANL-W and shipped to ANL-E for further fuel and cladding characterization, as well as creep testing. The cutting diagrams for characterization of rods H9 and G6 are shown in Figs. A.1 to A.4 (dimensions given in inches). For Figs. A.1 and A.3, the fuel column midplane is 178 mm (7 in.) from the segment bottom and grid spacer 4 is 330 mm (13 in.) from the segment bottom. Therefore, these segments represent the top 330 mm (13 in.) of Grid Span 3 and the bottom 580 mm (23 in.) of Grid Span 4. The segments shown in Figs. A.2 and A.4 contain the rest of Grid Span 4 (≈100 mm) and all of Grid Span 5. The metallography and hardness are from samples C4 (near midplane) and C12 (≈500 mm or 20 in. above midplane). The hydrogen analyses are from samples (C5 and C13) next to these. The metallography and hardness sample B2 (≈1000 mm or 40 in. above the midplane) is from Section 591C. The hydrogen analyses sample B3, is adjacent to sample B2. The same characterization cutting diagrams have been established for the middle (592C) and second-from-top (592B) segments of Rod G6.

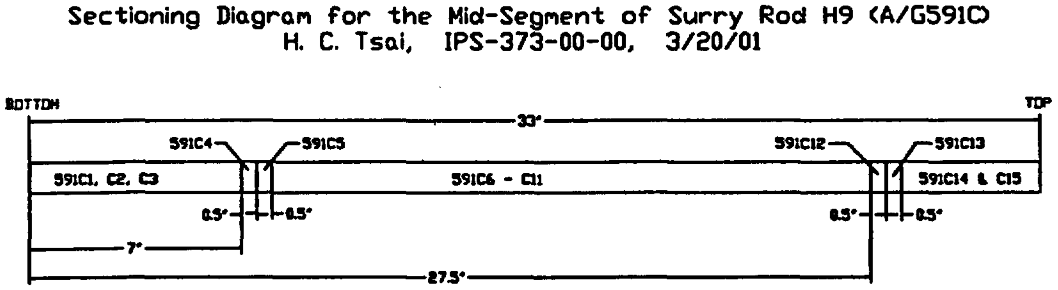

Fig. A.1 Cutting Diagram for the Characterization of Mid-Segment of Rod H9 from Surry-2 Assembly T11. C4 (metallography and microhardness) and C5 (hydrogen analysis) are located at about the core midplane within Grid Span 3. C12 (metallography and microhardness) and C13 (hydrogen analysis) are located ≈500 mm above the fuel midplane within Grid Span 4.

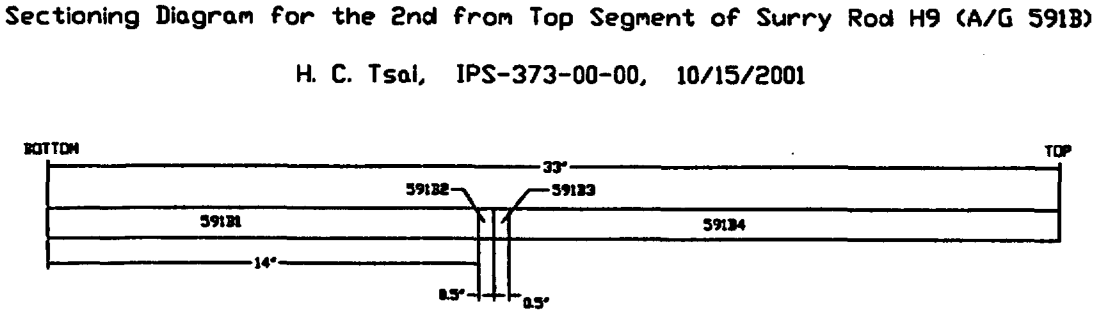

Fig. A.2 Cutting Diagram for the Characterization of Second-from-Top Segment of Rod H9 from Surry-2 Assembly T11. B2 (metallography and microhardness) and B3 (hydrogen analysis) are located at ≈1000 mm above the fuel midplane within Grid Span 5.

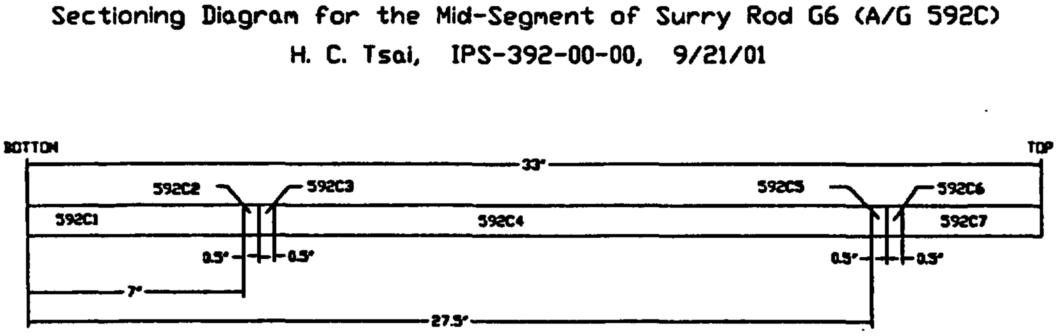

Fig. A.3 Cutting Diagram for the Characterization of Mid-Segment of Rod G6 from Surry-2 Assembly T11. C2 (metallography and microhardness) and C3 (hydrogen analysis) are located at about the core midplane within Grid Span 3. C5 (metallography and microhardness) and C6 (hydrogen analysis) are located ≈500 mm above the fuel midplane within Grid Span 4.

Sectioning Diagram for the 2nd from Top Segment of Surry Rod G6 (A/G 592B)
H. C. Tsai, IPS-373-00-00, 9/24/01

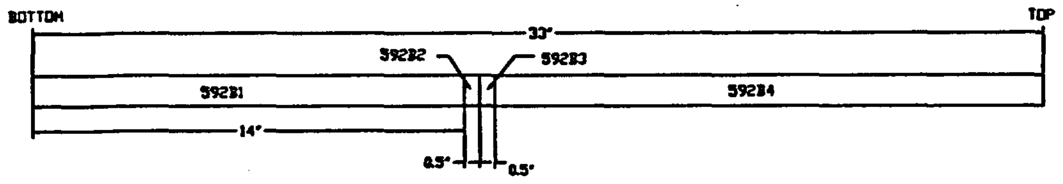

Fig. A.4 Cutting Diagram for the Characterization of Second-from-Top Segment of Rod G6 from Surry-2 Assembly T11. B2 (metallography and microhardness) and B3 (hydrogen analysis) are located at ≈1000 mm above the fuel midplane within Grid Span 5.

APPENDIX B

PROFILOMETRY

B.1 Methodology.. B-3

B.2 Average Rod Diameter Profiles.. B-4

Table

B.1 Diameter (mm) of Surry Rods Taken from Data at 2-3 m and at 1 m from the Bottom of the Rods.. B-4

Figures

B.1 Average Diameter Profile of Surry Unit No. 2 Rod T11-F7.................. B-5

B.2 Average Diameter Profile of Surry Unit No. 2 Rod T11-F8.................. B-5

B.3 Average Diameter Profile of Surry Unit No. 2 Rod T11-F9.................. B-6

B.4 Average Diameter Profile of Surry Unit No. 2 Rod T11-G6.................. B-6

B.5 Average Diameter Profile of Surry Unit No. 2 Rod T11-G7.................. B-7

B.6 Average Diameter Profile of Surry Unit No. 2 Rod T11-G9.................. B-7

B.7 Average Diameter Profile of Surry Unit No. 2 Rod T11-H7.................. B-8

B.8 Average Diameter Profile of Surry Unit No. 2 Rod T11-H9.................. B-8

B.9 Average Diameter Profile of Surry Unit No. 2 Rod T11-I8.................. B-9

B.10 Average Diameter Profile of Surry Unit No. 2 Rod T11-I9.................. B-9

B.11 Average Diameter Profile of Surry Unit No. 2 Rod T11-I10.................. B-10

B.12 Average Diameter Profile of Surry Unit No. 2 Rod T11-J8.................. B-10

B.1 Methodology

The profile of a rod is simply the distribution of its apparent diameter as a function of axial position at a given angle of rotation. The profile of an as-fabricated rod would be nearly uniform; however, irradiation will cause distortions in the profile. This is true even if the profile changes are quite small, on the order of only tens of microns. The process of measuring the profile of a rod is called profilometry, and the device used is called a profilometer. At ANL-West an Element Contact Profilometer (ECP) is used. For the Surry rods, the ECP was conducted at four azimuthal angles (0, 45, 90, and 135°) with multiple axial scans to determine the outer diameter axial profiles and to quantify ovality. The scans were performed over an axial region from ≈3.1 m axial height to the bottom of the rod at axial intervals not coarser than 2.5 mm. The ECP was calibrated at the beginning and end of every day of use to a NIST-traceable standard such that the error is within ±0.0051 mm. Because of other factors associated with the overall ECP process, HFEF prefers to set error bands of ±0.013 mm on the ECP data for full-length LWR rods.

The HFEF ECP generates a profile by allowing a horizontally opposed pair of precision linear transducers to lightly touch the outer surface of the rod. Each transducer is tipped with a precision-ground sapphire rod (about 3.18-mm diameter by 19-mm long) whose longitudinal axis is perpendicular to the axis of the rod, creating a tangential point of contact. Two pairs of notched spring-loaded guide rollers (one 76 mm above and one 76 mm below the measurement point) position the rod correctly with respect to the line of action of the transducers. Small bows in the direction of the line of action of the transducers are accommodated by displacement of the virtual center of the transducer pair, and small bows in the direction of the longitudinal axis of the parallel sapphires are accommodated by the 19-mm length of the sapphires. Symmetrical placement of the guide rollers about the measurement point minimizes any profile error caused by inclination of the rod's longitudinal centerline with the line of action of the transducers.

A profile is obtained by pulling the rod vertically through the gauging system and recording the difference between the opposing transducer signals. When calibrated with certified plug-gauge standards, an accurate measure of profile vs. axial and azimuthal position is obtained. No attempt is made to translate the axial measurement coordinate (stage z) to a reference on the rod itself. Such a translation must be inferred by examining the profile data for landmark features, such as profile changes at capsule-to-end-plug welds. All profilometry data are logged on a dedicated computer and are distributed as electronic files.

The ECP is installed on a standard HFEF examination stage (located at station 5M), which provides all the necessary motions and in-cell support services. The profilometer system is co-located with the bow and length measurement system on a common platform mounted to the vertical column of the stage. Only one type of measurement may be performed at a time.

B.2 Average Rod Diameter Profiles

The profilometry traces at 0, 45, 90, and 135° were averaged to generate the plots shown in Figs. B.1 to B.12. Further averaging was done to determine the minimum, average, and maximum diameters over the axial region 2-3 m from the bottom of the fuel rod (Table B.1). Also given is the average at 1 m from the bottom.

Table B.1 Diameter (mm) of Surry Rods Taken from Data at 2-3 m and at 1 m from the Bottom of the Rods

Rod	Maximum (2-3 m) mm	Average (2-3 m) mm	Minimum (2-3 m) mm	Average at 1-m Evaluation mm
J8	10.675	10.672	10.657	10.650
I10	10.680	10.673	10.655	10.650
I9	10.677	10.662	10.645	10.642
I8	10.682	10.675	10.653	10.650
H9	10.672	10.667	10.652	10.660
H7	10.680	10.671	10.655	10.660
G9	10.700	10.690	10.677	10.665
F8	10.675	10.663	10.652	10.645
F9	10.676	10.669	10.656	10.650
G6	10.683	10.671	10.658	10.660
G7	10.678	10.671	10.660	10.652
F7	10.672	10.665	10.654	10.635
Global	10.700	--	10.645	--
Average	10.679	10.670	10.656	10.651

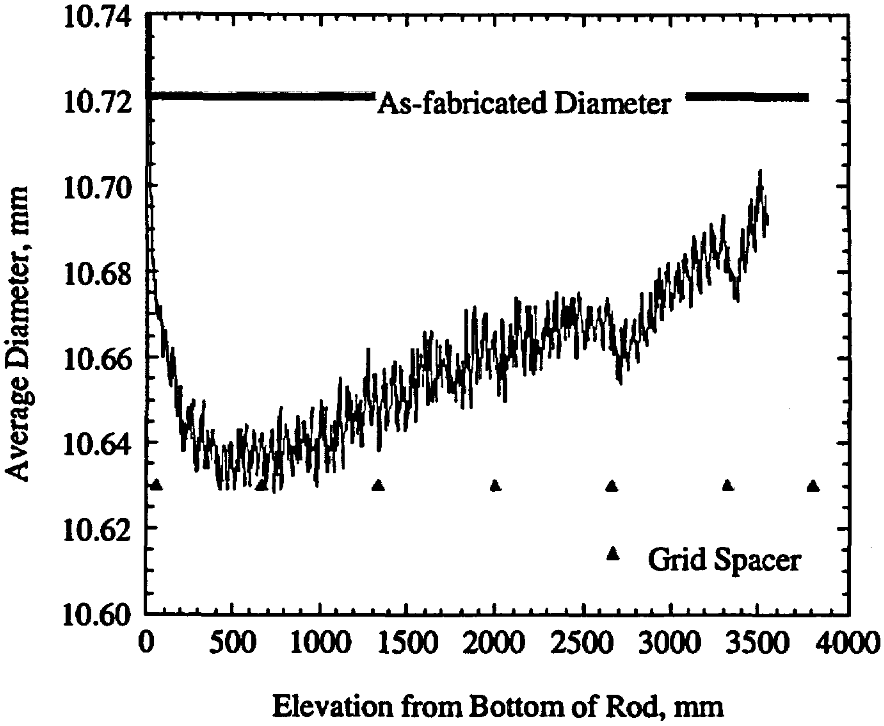

Fig. B.1 Average Diameter Profile of Surry Unit No. 2 Rod T11-F7

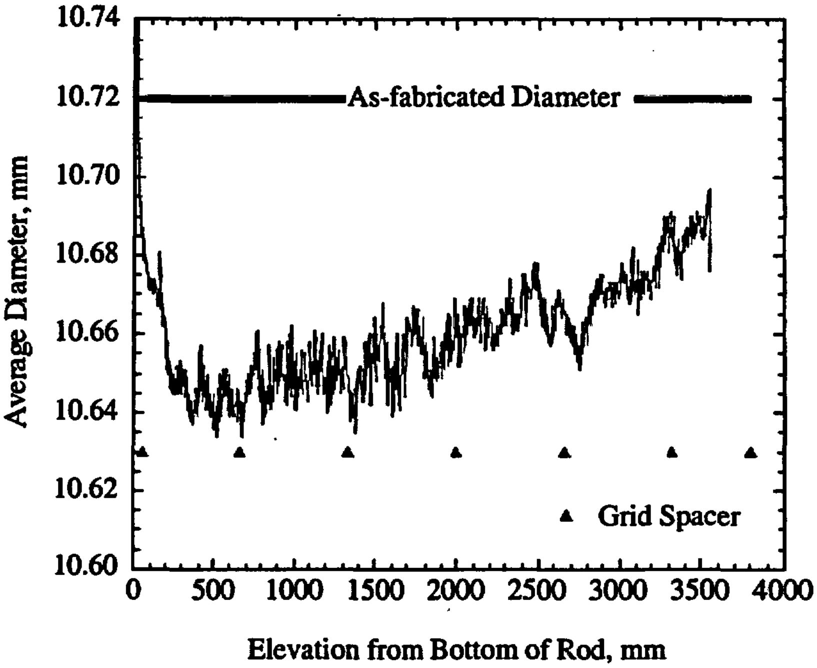

Fig. B.2 Average Diameter Profile of Surry Unit No. 2 Rod T11-F8

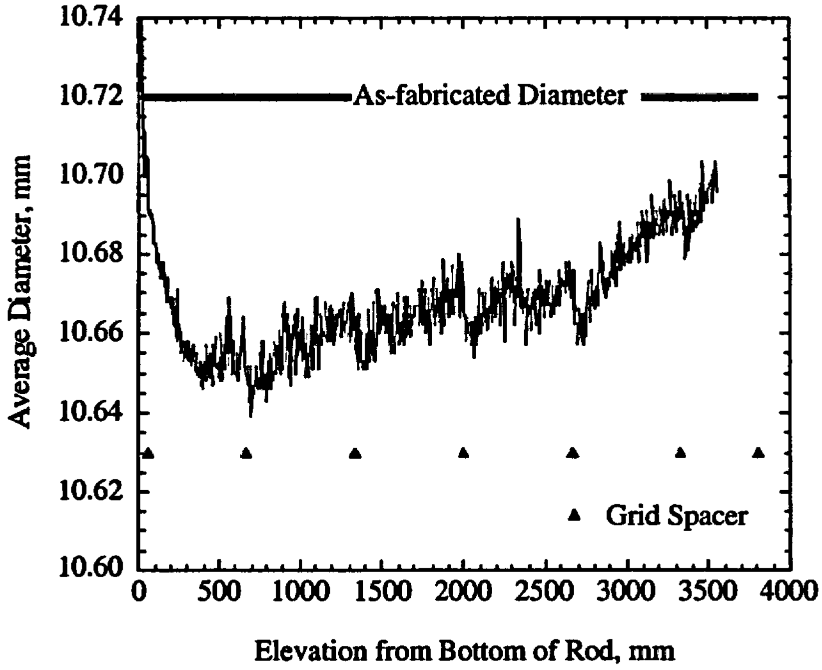

Fig. B.3 Average Diameter Profile of Surry Unit No. 2 Rod T11-F9

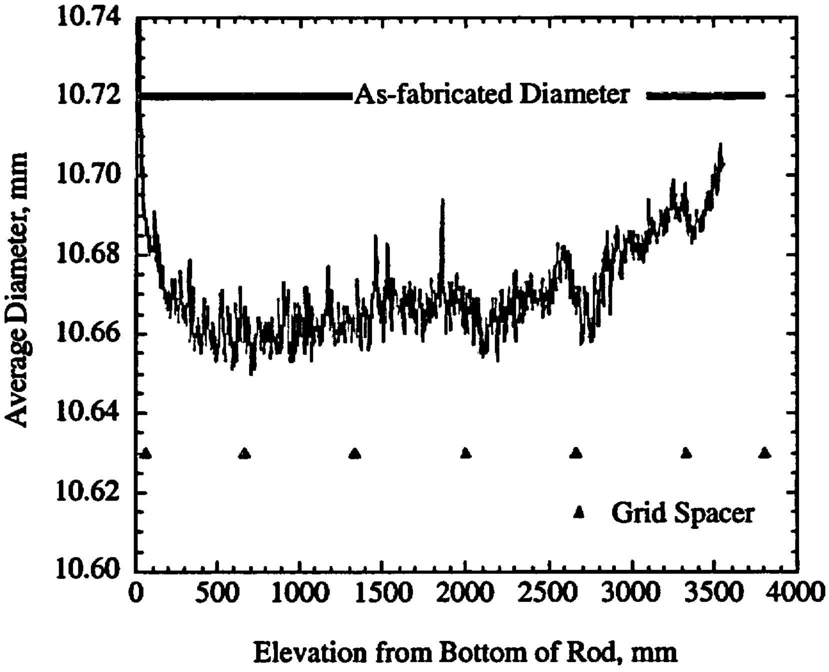

Fig. B.4 Average Diameter Profile of Surry Unit No. 2 Rod T11-G6

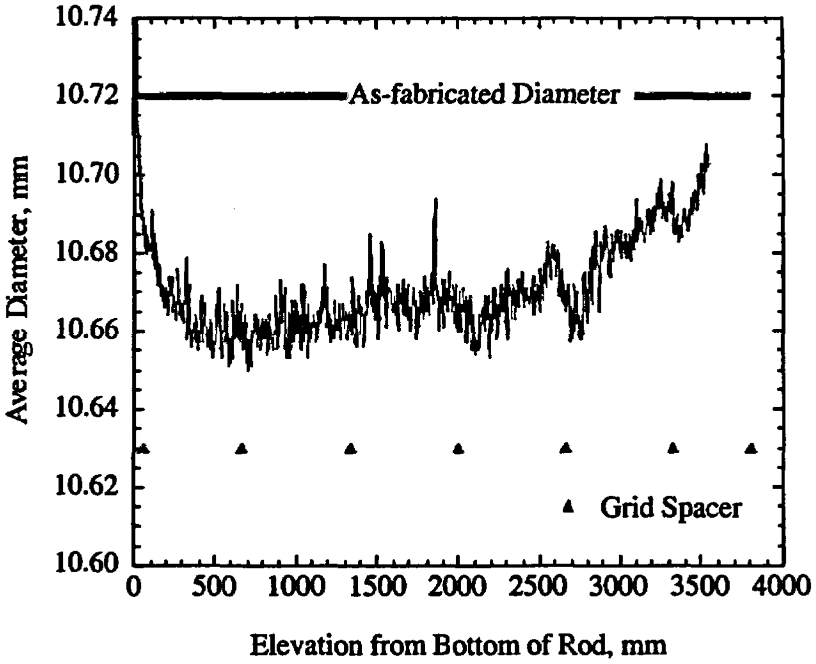

Fig. B.5 Average Diameter Profile of Surry Unit No. 2 Rod T11-G7

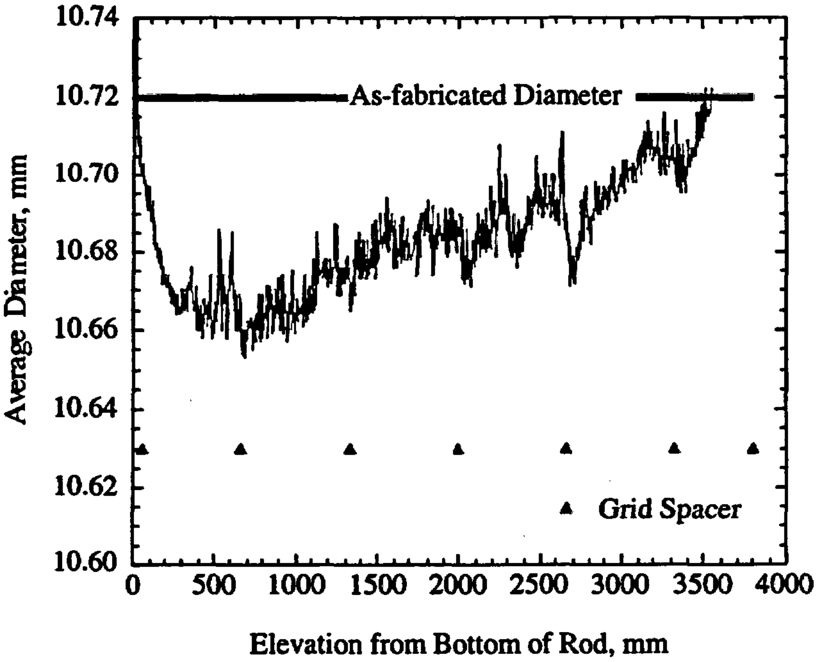

Fig. B.6 Average Diameter Profile of Surry Unit No. 2 Rod T11-G9

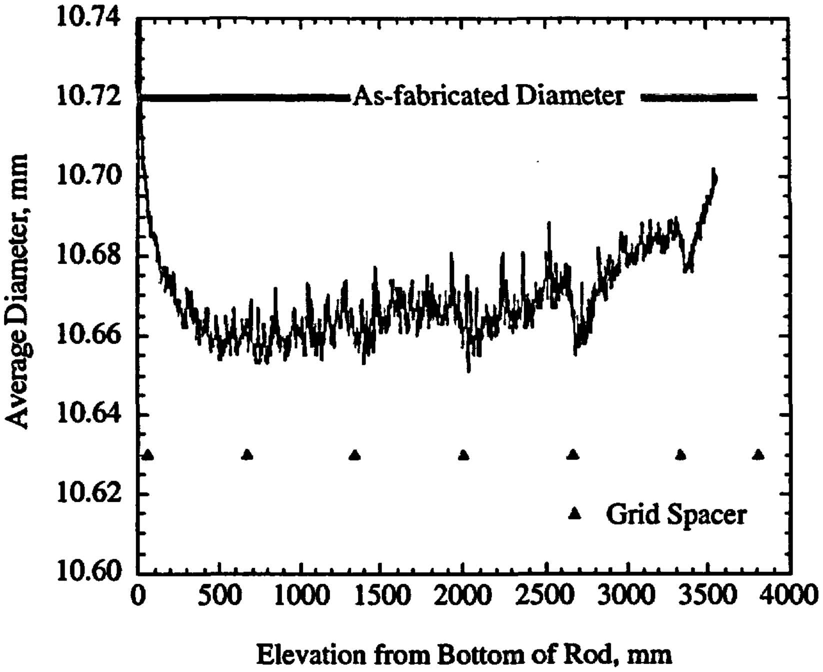

Fig. B.7 Average Diameter Profile of Surry Unit No. 2 Rod T11-H7

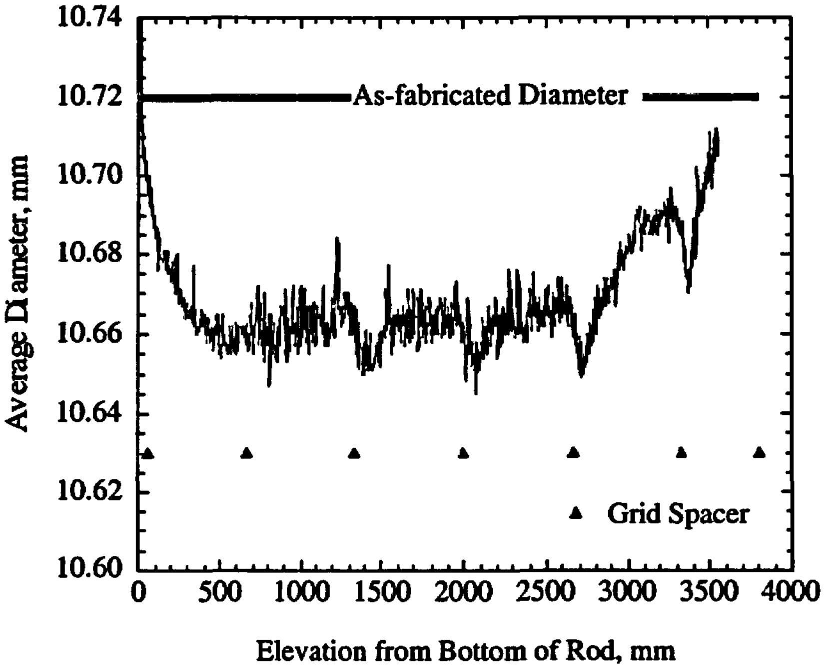

Fig. B.8 Average Diameter Profile of Surry Unit No. 2 Rod T11-H9

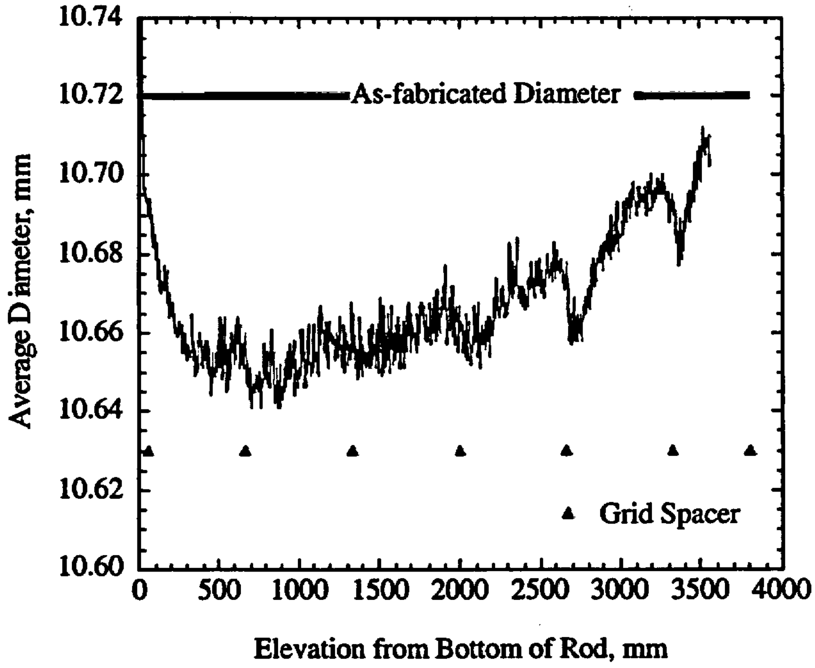

Fig. B.9 Average Diameter Profile of Surry Unit No. 2 Rod T11-I8

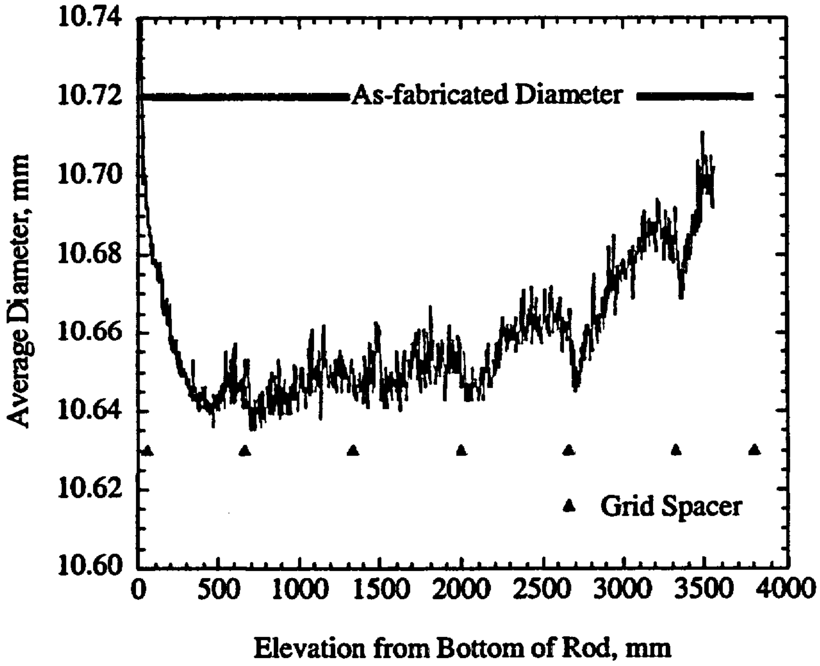

Fig. B.10 Average Diameter Profile of Surry Unit No. 2 Rod T11-I9

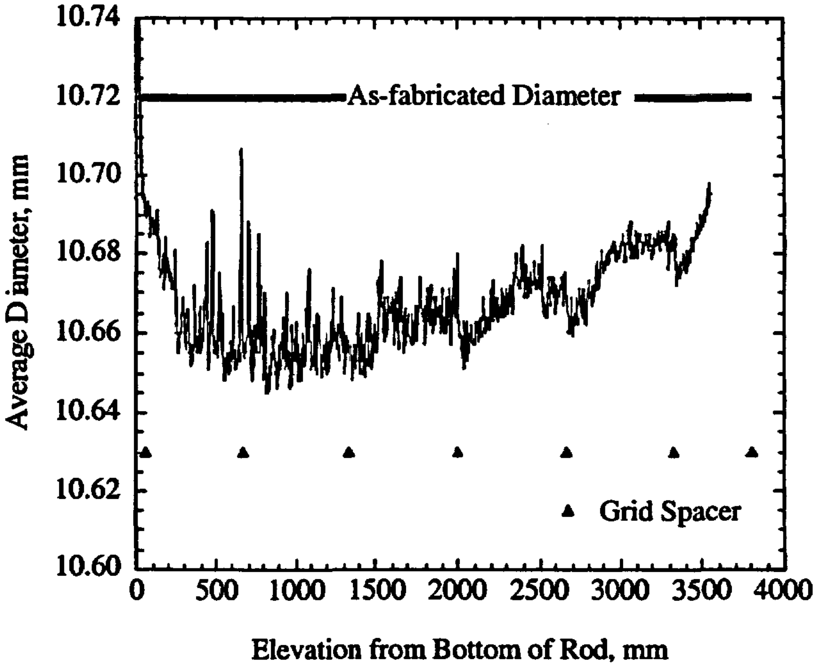

Fig. B.11 Average Diameter Profile of Surry Unit No. 2 Rod T11-I10

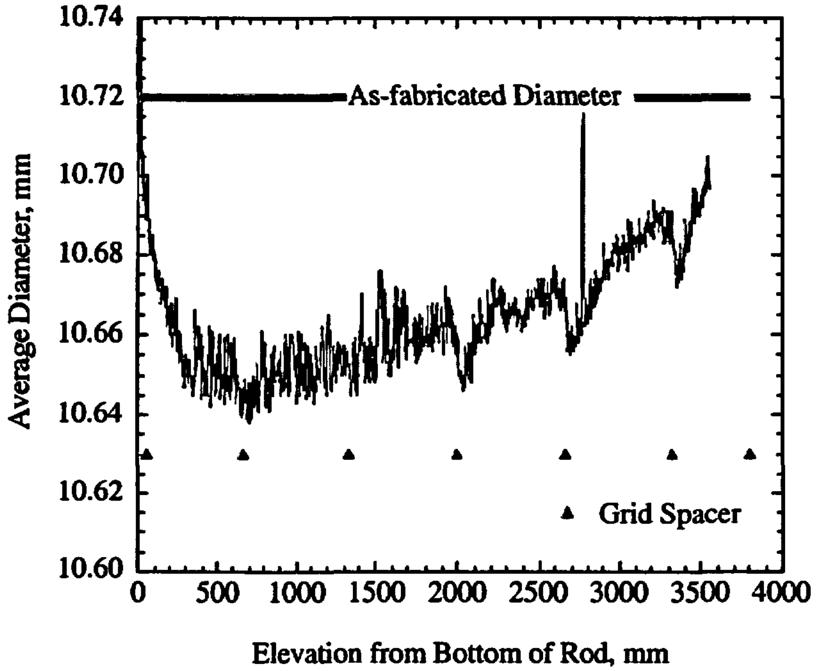

Fig. B.12 Average Diameter Profile of Surry Unit No. 2 Rod T11-J8

APPENDIX C

FUEL ROD GAS ANALYSIS DATA

C.1 Introduction.. C-3

C.2 Calibration and Testing Methodology.. C-5

Tables

C.1 Void Volume, Internal Gas Pressure and Fission Gas Release of Surry Unit 2 Fuel Rods Irradiated to 35.7 GWd/tU Burnup and Stored for 15 Years in Dry Cask Storage.................................... C-4

C.2 Internal Gas Chemical Composition (mol %) of Surry Unit 2 Fuel Rods Irradiated to 35.7 GWd/tU Burnup and Stored for 15 Years in Dry Cask Storage...C-4

C.3 Internal Fission Gas Isotopic Composition (at. %) of Surry Unit 2 Fuel Rods Irradiated to 35.7 GWd/tU Burnup and Stored for 15 years in Dry Cask Storage..C-5

C.1 INTRODUCTION

The void volumes and internal gas pressures determined by Gas Assay Sample and Recharge (GASR)[1] are summarized in Table C.1. The void volumes and the internal gas pressures of the four fuel rods examined are essentially the same. The void volumes range from 19.53 to 20.39 cm^3 (1.192-1.244 in.^{3}), and the internal gas pressures range from 3.39 to 3.56 MPa (498-523 psia). The relative errors (i.e., the standard deviation of the mean divided by the mean) of the void volumes and of the gas pressures are less than 3%. The internal gas pressures are approximately 0.6 MPa higher than the as-fabricated gas pressure. The increase in internal gas pressure is similar to that reported for PWR fuel rods of the same design and burnup at the time of reactor discharge. Hence, it appears that no significant release of fission gas from the fuel occurred during the dry storage period.

The chemical and fission gas isotopic compositions are presented in Tables C.2 and C.3, respectively. The Xe composition is between 1.5 and 3.2 mol%, and the Kr fraction is between 0.11 and 0.37 mol%. The Xe/Kr ratio ranges from 9.0 to 11.4 for the four fuel rods. The fission gas compositions are within the range of values reported for PWR fuel rods irradiated to similar burnup, indicating that no significant amount of fission gas was released from the fuel during the dry storage period.

The fission gas inventory of fuel rods H9 (FA-434) and H7 (FA-512) was approximately a factor of two higher compared to that of fuel rods G6 (FA-467) and G9 (FA-719). The isotopic fractions are similar for the four rods examined and are within the expected distribution for fuel rods with this burnup.

The fission gas release, for the four fuel rods examined, was calculated from the measured void volume, internal gas pressure, and gas chemical composition and from the calculated average assembly burnup (see Table C.1). The fission gas release corresponds with the fission gas inventory, being two times as high for fuel rods H9 (FA-434) and H7 (FA-512) as compared to fuel rods G6 (FA-467) and G9 (FA-719). The fission gas releases for these two sets of rods are ≈1% and ≈0.5%, respectively, which is within the range of data reported in the literature.

---

[1] R. S. Wisner, "Hot Fuel Examination Facility North (HFEF/NORTH) Fuel Element Plenum Puncturing and Gas Sampling System," Proceedings of the 36th Conference on Remote Systems Technology, Vol. 2, American Nuclear Society, 1988.

Table C.1 Void Volume, Internal Gas Pressure,[a,b] and Fission Gas Release of Surry Unit 2 Fuel Rods Irradiated to 35.7 GWd/tU Burnup[c] and Stored for 15 Years in Dry Cask Storage

Fuel Rod ID No.	Void Volume		Internal Gas Pressure[d]		Fission Gas Release[e]
	cm³	in.³	MPa	psia	%
T11-H9 (FA-434)	19.76	1.206	3.56	523	1.08
T11-G6 (FA-467)	19.53	1.192	3.46	509	0.39
T11-H7 (FA-512)	20.29	1.238	3.39	498	0.88
T11-G9 (FA-719)	20.39	1.244	3.40	499	0.49

[a] Void volume and internal gas pressure measurements were obtained at a system temperature of 300±1 K.

[b] Relative error (standard deviation of mean divided by the mean) of void volume and internal gas pressure measurements was less than 3%.

[c] Average assembly burnup as calculated by Dominion Generation.

[d] As-fabricated internal gas pressure was 2.83 MPa (415 psia).

[e] Fission gas release was derived from the measured void volume, internal gas pressure, fission gas composition, and from the calculated assembly average burnup.

Table C.2 Internal Gas Chemical Composition[a] (mol %) of Surry Unit 2 Fuel Rods Irradiated to 35.7 GWd/tU Burnup[b] and Stored for 15 Years in Dry Cask Storage

Fuel Rod ID No.	H_2	He	N_2	O_2	Ar	CO_2	Xe	Kr	Xe/Kr Ratio
T11-H9 (FA-434)	0.01[c]	96.1	0.01	ND	0.26	0.01	3.25	0.36	9.0
T11-G6 (FA-467)	0.01	98.3	0.02	ND	0.33	0.01	1.25	0.11	11.4
T11-H7 (FA-512)	ND[d]	96.7	0.03	ND	0.27	0.01	2.72	0.29	9.4
T11-G9 (FA-719)	0.01	98.1	0.02	0.01	0.25	0.01	1.50	0.15	10.0

[a] The relative error (standard deviation of mean divided by the mean) of the chemical composition was <8%, except at very low mole percentage (i.e., ≤0.03%), for which the relative error was 15%.

[b] Average assembly burnup as calculated by Dominion Generation.

[c] Composition was <0.01 mol% based on the resolution limit of instrument.

[d] ND = not detected

Table C.3 Internal Fission Gas Isotopic Composition[a,b] (at.%) of Surry Unit 2 Fuel Rods Irradiated to 35.7 GWd/tU Burnup[c] and Stored for 15 years in Dry Cask Storage

Fuel Rod ID No.	Krypton					Xenon					
	82	83	84	85	86	128	130	131	132	134	136
T11-H9 (FA-434)	0.39	11.0	33.5	1.99	53.1	0.09	0.30	7.14	22.0	28.5	42.0
T11-G6 (FA-467)	ND[d]	11.5	33.6	2.06	52.8	ND	0.22	7.51	21.8	28.2	42.2
T11-H7 (FA-512)	ND[d]	11.0	33.4	2.10	53.5	0.08	0.27	7.06	22.1	28.5	42.0
T11-G9 (FA-719)	ND[d]	11.2	33.3	2.16	53.3	ND	0.22	7.46	21.8	28.4	42.1

[a] The relative error (standard deviation of mean divided by the mean) of the isotopic composition was ≤10%, except at very low atom percentage (i.e., ≤0.03%) for which the relative error was 15%.

[b] Isotopic composition was <0.01 at% based on the resolution limit of instrument. Kr-78, Kr-80, Xe-124, and Xe-126 were not detected.

[c] Average assembly burnup as calculated by Dominion Generation

[d] ND = Not detected

C.2 CALIBRATION AND TESTING METHODOLOGY

The accuracies of the GASR and gas chemical composition results were verified by independent methods. The fuel rod internal gas pressure and void volume, determined by the GASR instrument, are derived measurements that depend on the component volumes in the GASR system. The system component volumes were verified by an independent, series-expansion procedure. The accuracy of the gas chemical analyses was verified by comparison of instrument analyses results with two reference gas mixtures.

The system volumes of the GASR, which are reported in the ANL-W Operating Procedure, were determined by an independent method using a NIST-traceable reference volume and a NIST-traceable pressure gauge. The differences between the system volumes reported in the ANL-W Operating Procedure and the system volumes determined by the independent method were less than the stated uncertainty of the measurements, which verified the accuracy of the GASR results.

Therefore, the system volumes reported in the ANL-W Operating Procedure were used for data reduction of the gas assay sample analysis.

The accuracy of the gas chemical analyses was verified by comparison of instrument analysis results with the NIST-certified composition of two reference gas mixtures. The gas mixtures were selected to bracket the range of fission gas compositions expected for a PWR fuel rod similar in design and burnup to the Surry fuel rods that were examined. The compositions were nominally 4.0%Xe-0.4%Kr-bal He and 0.4%Xe-0.004%Kr-bal He. The gas chemical analyses were within the stated uncertainty of the measurements, which verified the accuracy of the mass spectrometry results.

APPENDIX D

METALLOGRAPHIC DATA

Tables

D.1 Summary of Hydrogen Content for Surry Rod H9 Cladding....................D-3

D.2 Summary of Hardness Data for Surry Rod H9 Cladding......................D-4

Figures

Transverse Micrographs of the Fuel

D.1 through D.3 – Cross sections for H9 fuel and cladding at approximately the fuel midplane, a location ≈500 mm above the fuel midplane, and a location ≈1000 mm above the fuel midplane................................D-5

D.4 and D.5 – Cross sections for G6 fuel and cladding at approximately the fuel midplane and at a location ≈500 mm above the fuel midplane..............D-8

Cladding

Inner-surface Oxide Micrographs[1]

D.6 Inner-surface oxide layer at the fuel-cladding interface at one approximate midplane circumferential location for Rod H9.....................D-10

D.7 and D.8 - Inner surface oxide layer at four circumferential locations at ≈500 mm above the fuel midplane for Rod H9........................D-11

D.9 Inner surface oxide layer at two circumferential locations at ≈1000 mm above the fuel midplane for Rod H9...................................D-13

D.10 and D.11 - Inner surface oxide layer at four circumferential locations at approximately the fuel midplane for Rod G6.........................D-14

D.12 and D.13 - Inner surface oxide layer at four circumferential locations at ≈500 mm above the fuel midplane for Rod G6........................D-16

---

[1] For both outer-surface cladding oxide layer and hydrides, there are between two and eight locations around the circumference that are imaged for each axial location. These are designated Area 1 through 8

Outer-surface Oxide Micrographs[1]

D.14 through D.21 - Cladding outer-surface oxide layer at the H9 approximate fuel midplane for eight azimuthal positions........................D-18

D.22 through D.24 - Oxide layer vs. eight azimuthal positions for Rod H9 at ≈500 mm above the fuel midplane..D-26

D.25 through D.32 - Oxide layer vs. eight azimuthal positions for Rod H9 at ≈1000 mm above the fuel midplane..D-29

D.33 through D.40 - Oxide layer vs. eight azimuthal positions for Rod G6 at the approximate fuel midplane..D-35

D.41 through D.48 - Oxide layer vs. eight azimuthal positions for Rod G6 at ≈500 mm above the fuel midplane..D-39

Cladding Hydride Micrographs[1]

D.49 through D.56 - Cladding hydride morphology for Rod H9 at approximate fuel midplane and eight azimuthal areas..............................D-44

D.57 through D.64 - Cladding hydride morphology for Rod H9 at eight azimuthal positions at ≈500 mm above the fuel midplane..................................D-52

D.65 through D.70 - Cladding hydride morphology for Rod H9 at six azimuthal positions at ≈1000 mm above the fuel midplane..................................D-60

D.71 through D.78 - Cladding hydride morphology for Rod G6 fuel (approximate) midplane and eight azimuthal areas..............................D-66

D.79 Hydrides at three radial locations in the cladding at the approximate fuel midplane of Rod G6 under high magnification.................D-74

D.80 and D.87 - Cladding hydride morphology for Rod G6 at eight azimuthal positions at ≈500 mm above the fuel midplane..................................D-77

D.88 and D.89 - Hydrides at two radial locations at two azimuthal locations in the cladding of Rod G6 under high magnification.................D-85

Table D.1 Summary of Hydrogen Content (wppm) for Surry Rod H9 Cladding

	Sample 591C-C5 (≈25 mm above fuel midplane) Oxide = 24 µm	Sample 591C-C13 (≈530 mm above fuel midplane) Oxide = 33 µm	Sample 591B-B3 (≈1020 mm above fuel midplane) Oxide = 40 µm
	334	345	252
	237	294	261
	237	284	233
	238	304	273
	233	319	262
	221	276	251
	242	294	249
	240	283	246
			240
			272
			246
			270
Average =	248	300	255
Std Dev =	35	23	13

Table D.2 Summary of Hardness Data for Surry Rod H9 Cladding

591C4 Vickers Hardness (DPH)

	0°	90°	180°	270°
Inside edge	232	240	236	244
	236	238	242	234
	240	240	243	244
	237	234	238	233
	240	247	244	238
	233	233	233	248
	236	245	241	233
Outside edge	237		240	238
			250	
Avg	236	240	241	239
Std Deviation	3	5	5	6

Overall Avg.	239
Overall SD	5

591C12 Vickers Hardness (DPH)

	0°	90°	180°	270°
Inside edge	221	221	232	211
	244	244	240	230
	233	243	240	221
	244	239	230	222
	250	248	249	230
	245	237	228	222
	240	237	245	233
Outside edge	238		255	233
	238		239	
Avg	239	238	240	225
Std Deviation	8	9	9	8

Overall Avg.	236
Overall SD	10

591B2 Vickers Hardness (DPH)

	0°	90°	180°	270°
Inside edge	2212	240	213	246
	237	225	206	233
	234	246	199	238
	245	248	216	249
	250	248	249	230
	240	246	202	244
	243	264	198	240
Outside edge	245			253
Avg	238	245	212	243
Std Deviation	8	13	7	7

Overall Avg.	234
Overall SD	18

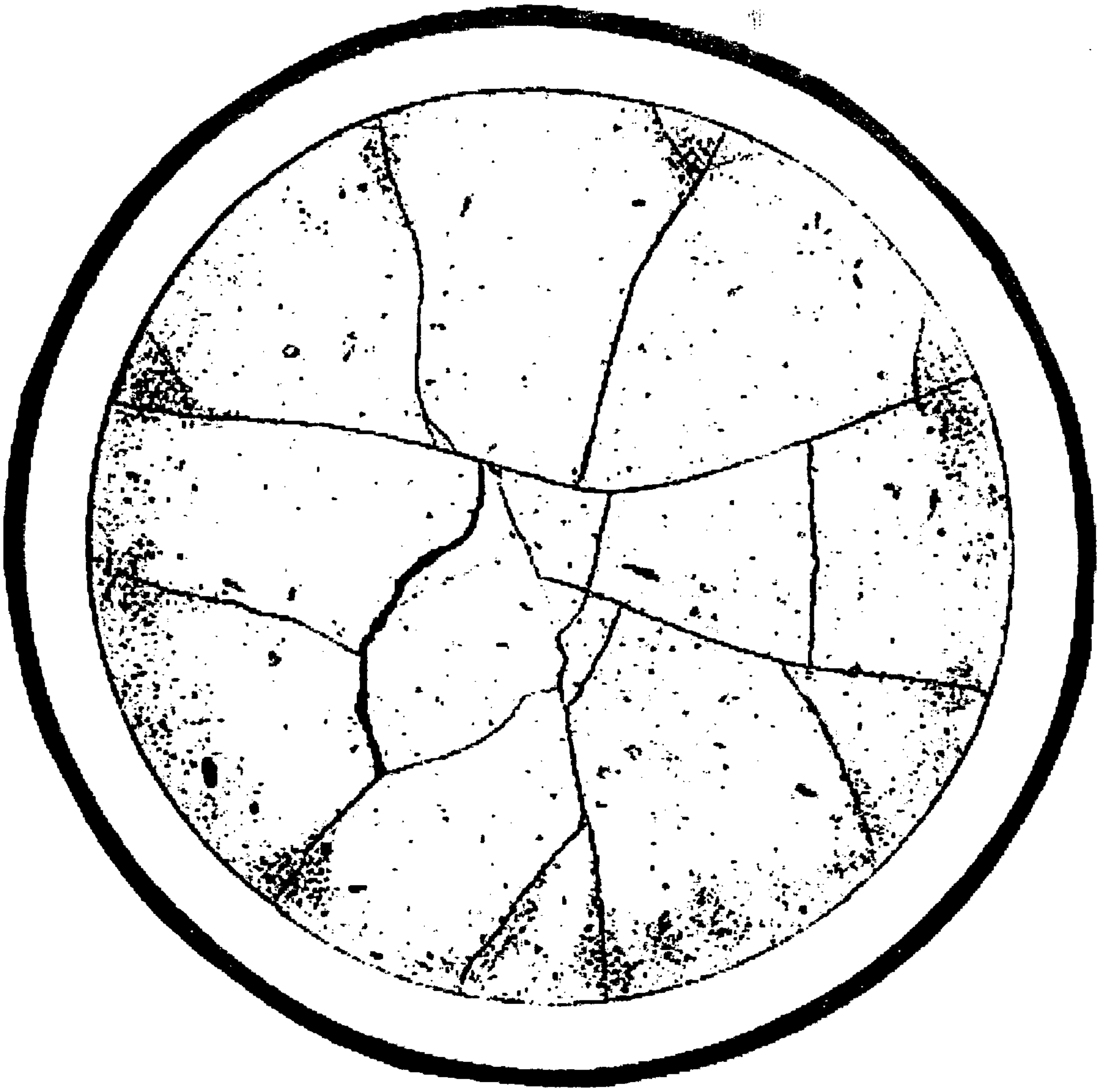

Fig. D.1 Cross-sectional mosaic of Rod H9 at the approximate fuel midplane.
JPG file = 591C4 Fuel Mosaic.

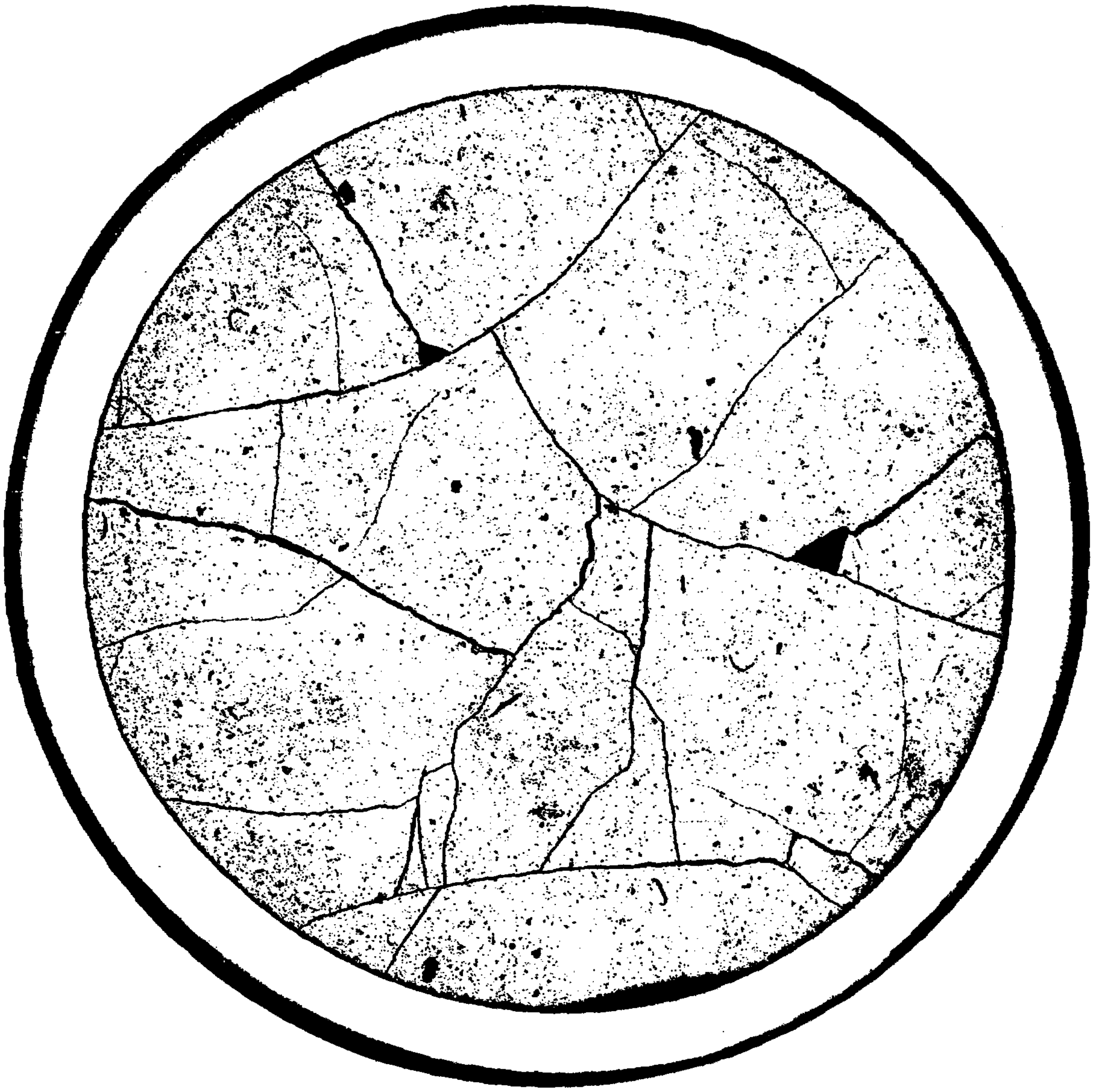

Fig. D.2 Cross-sectional mosaic of Rod H9 at ≈500 mm above the fuel midplane.
JPG file = 591C12 Fuel Mosaic.

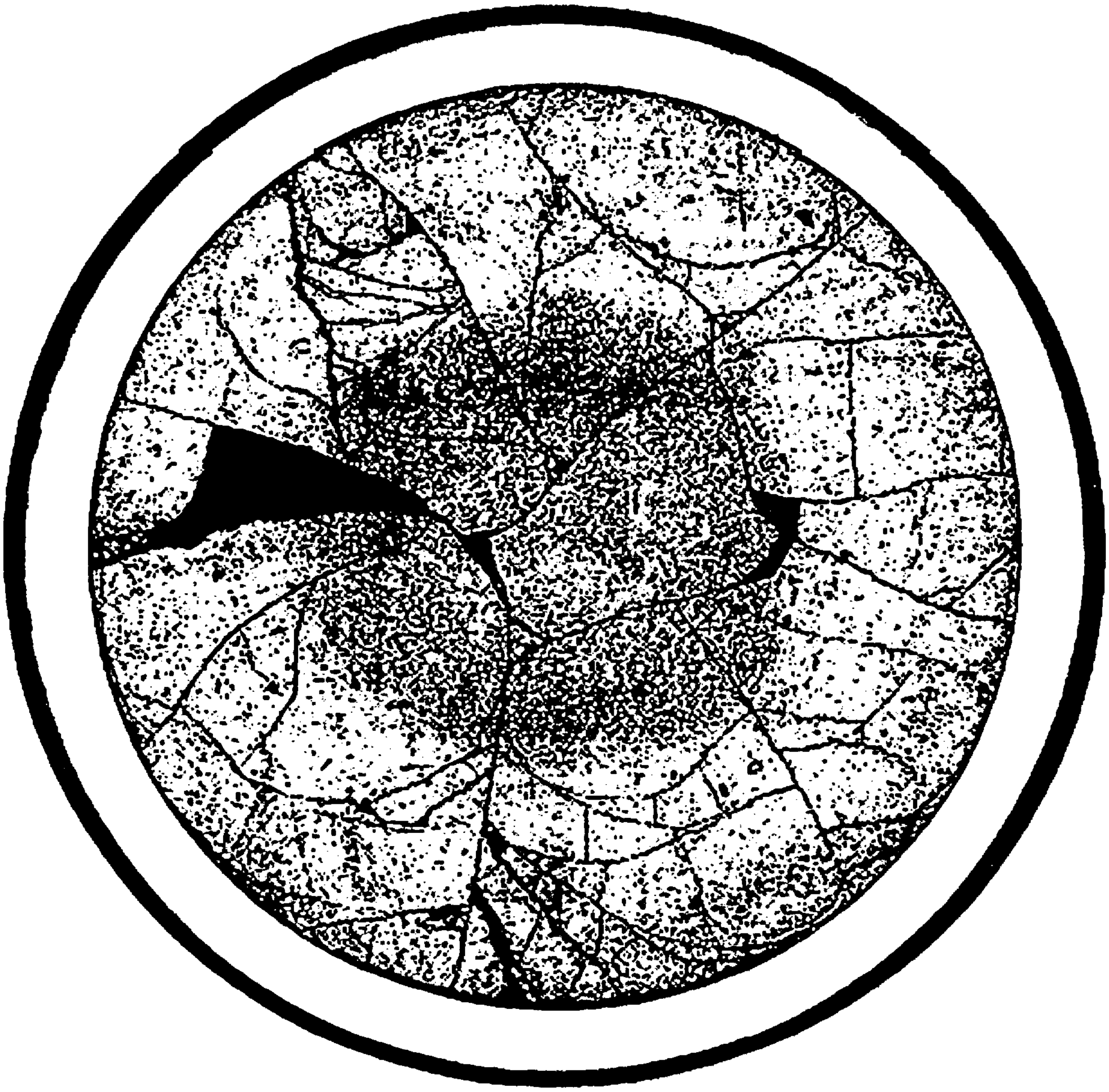

Fig. D.3 Cross-sectional mosaic of Rod H9 at ≈1000 mm above the fuel midplane.
JPG file = 591B2 Fuel Mosaic.

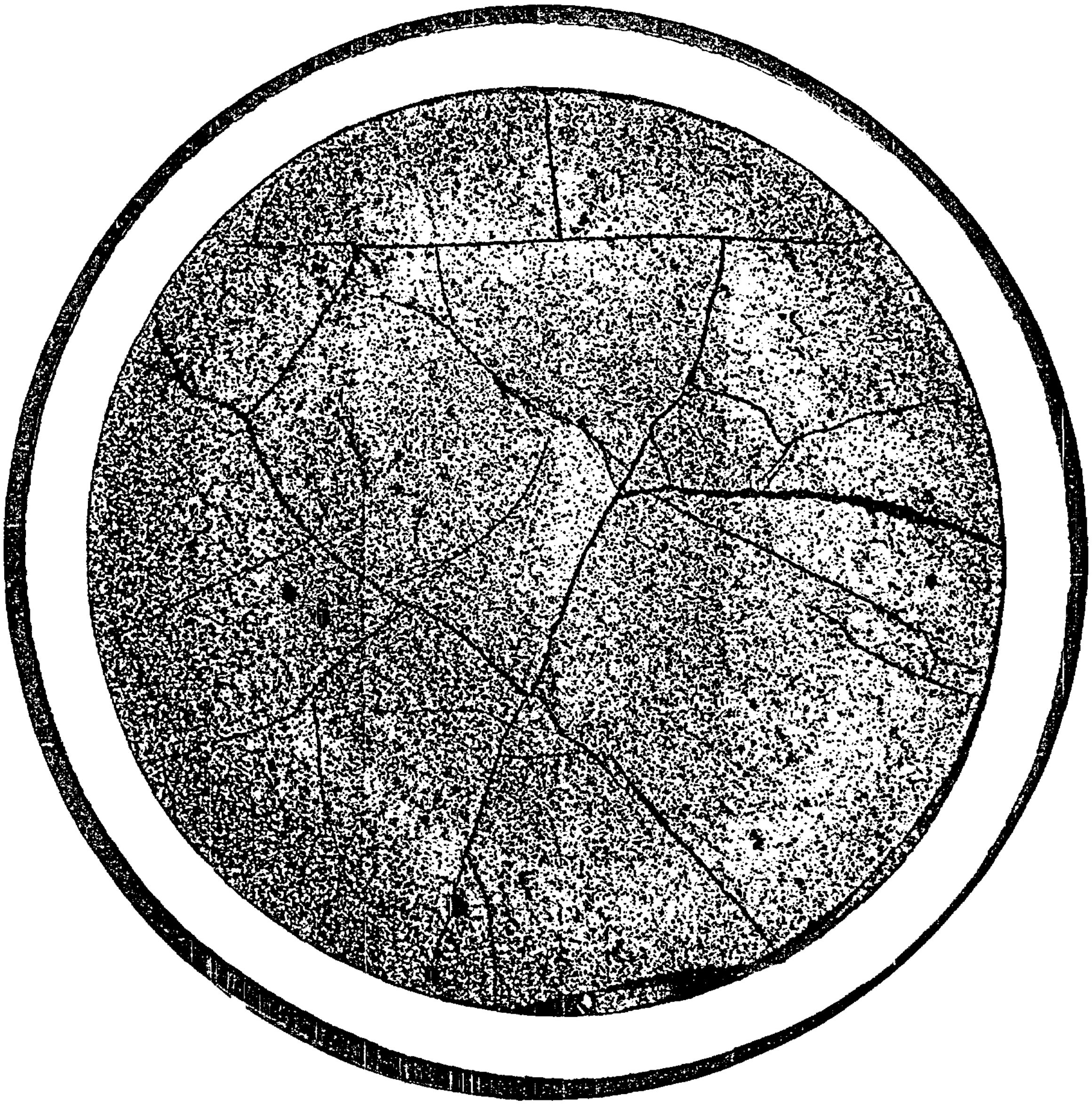

Fig. D.4 Cross-sectional mosaic of Rod G6 at the approximate fuel midplane.
JPG file = 592C4 Fuel Mosaic. 703341

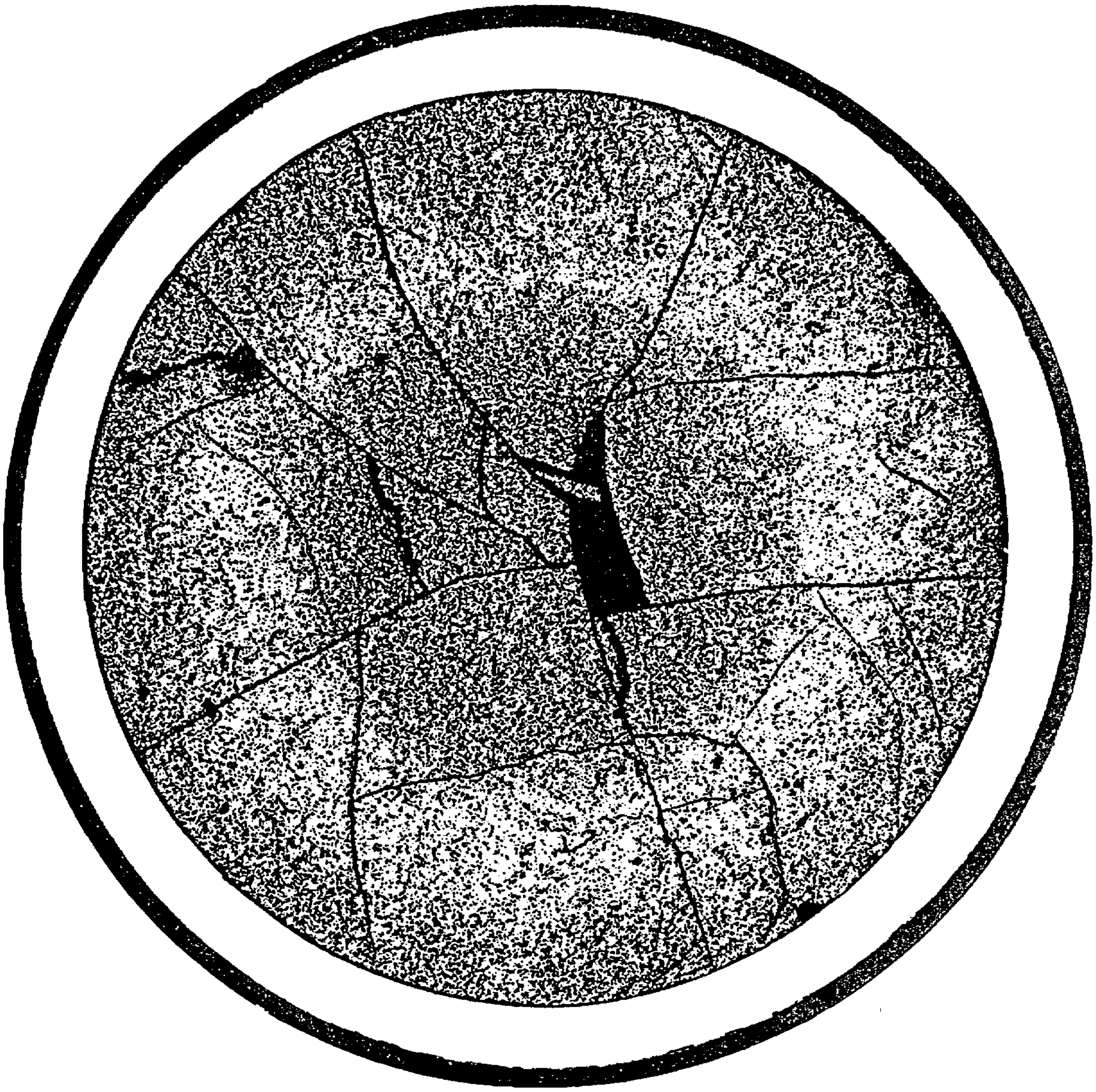

Fig. D.5 Cross-sectional mosaic of Rod G6 at ≈500 mm above the fuel midplane.
JPG file = 592C12 Fuel Mosaic. ET7043342

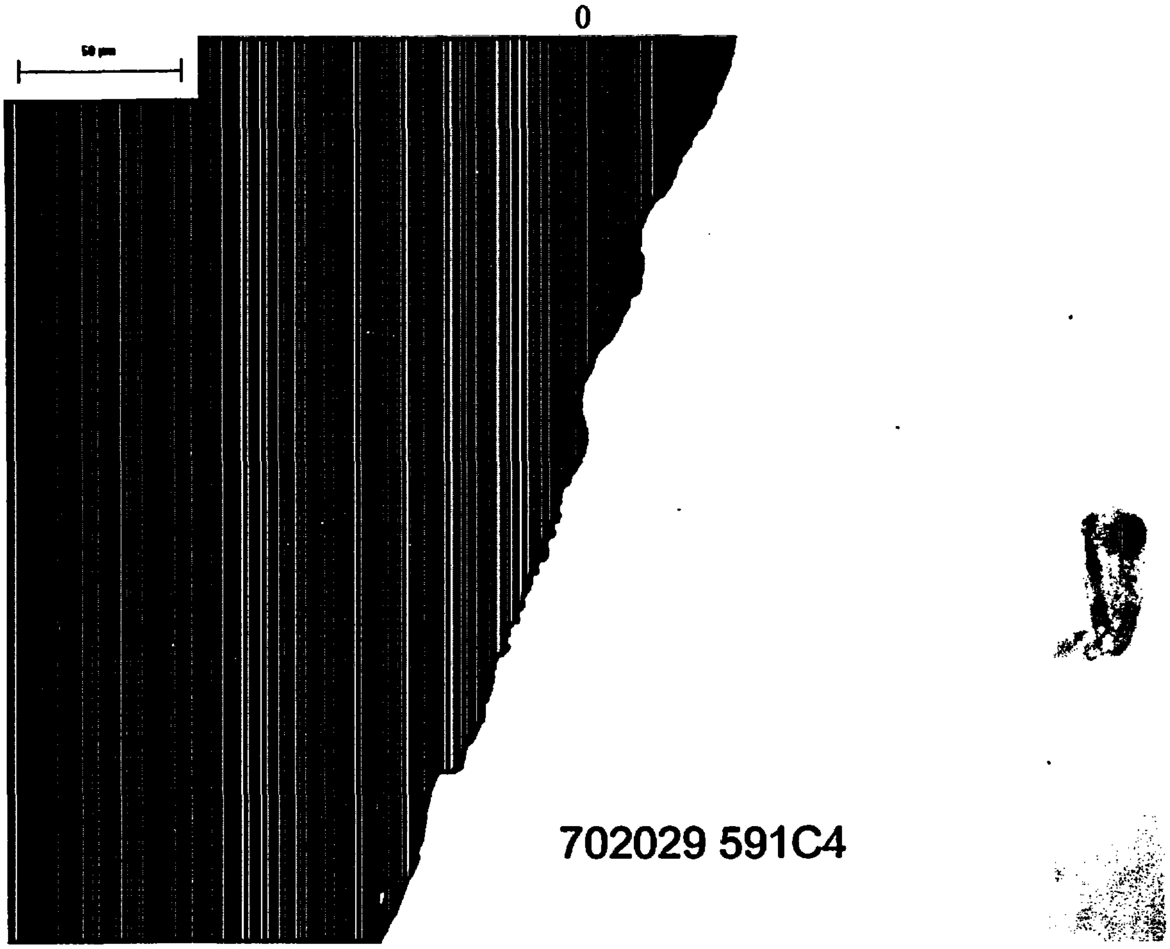

Fig. D.6 Cross-sectional view of Rod H9 fuel-cladding interface and cladding inner-surface oxide layer located at about the midplane (area 4). Scale marker = 50 µm. JPG file = 591C4 ID Oxide.

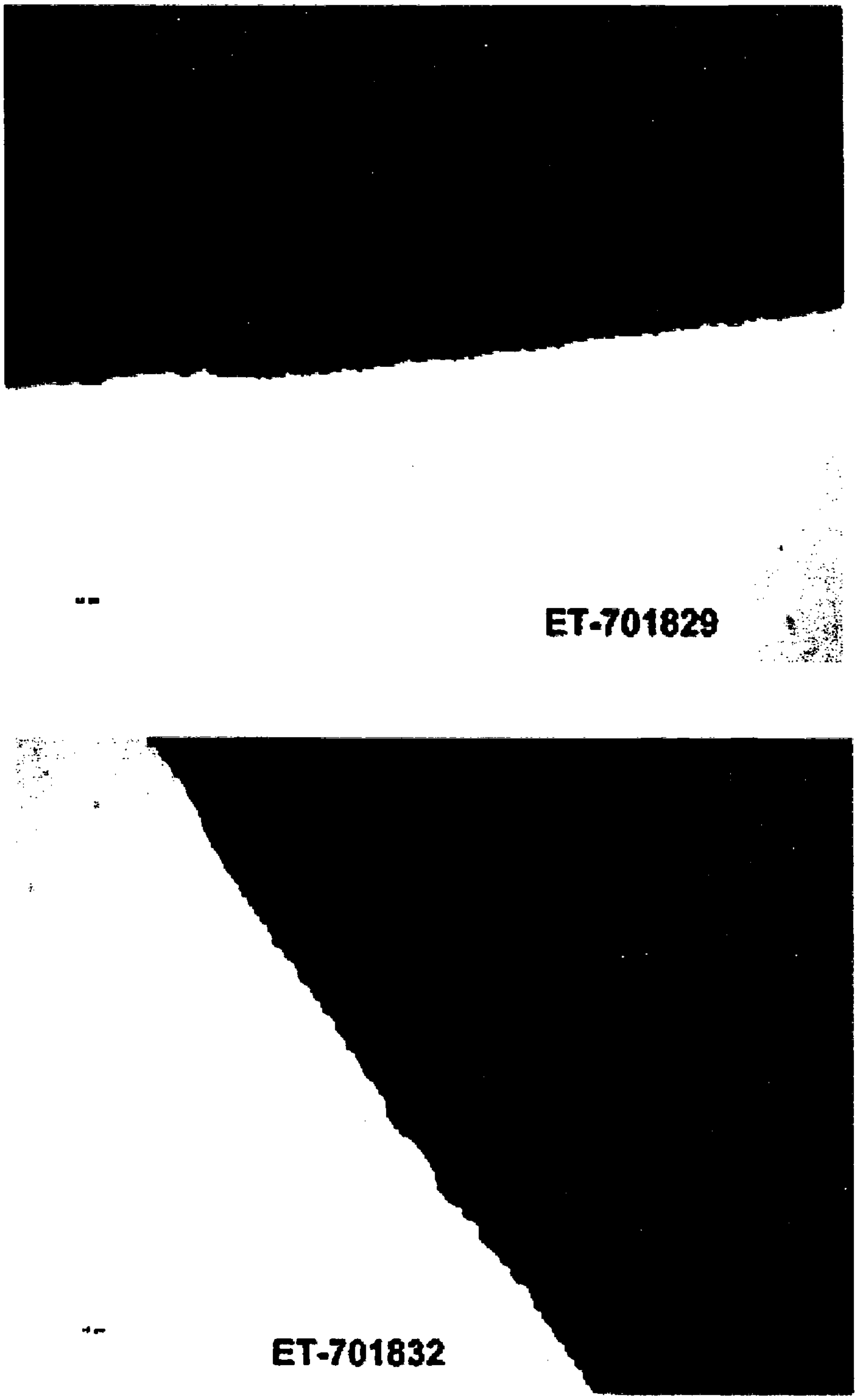

Fig. D.7 Cross-sectional view of Rod H9 fuel-cladding interface and cladding inner-surface oxide layer at two azimuthal positions located at ≈500 mm above the fuel midplane (areas 1-2). Scale marker = 50 μm. JPG file = 591C12 Areas 1-2.

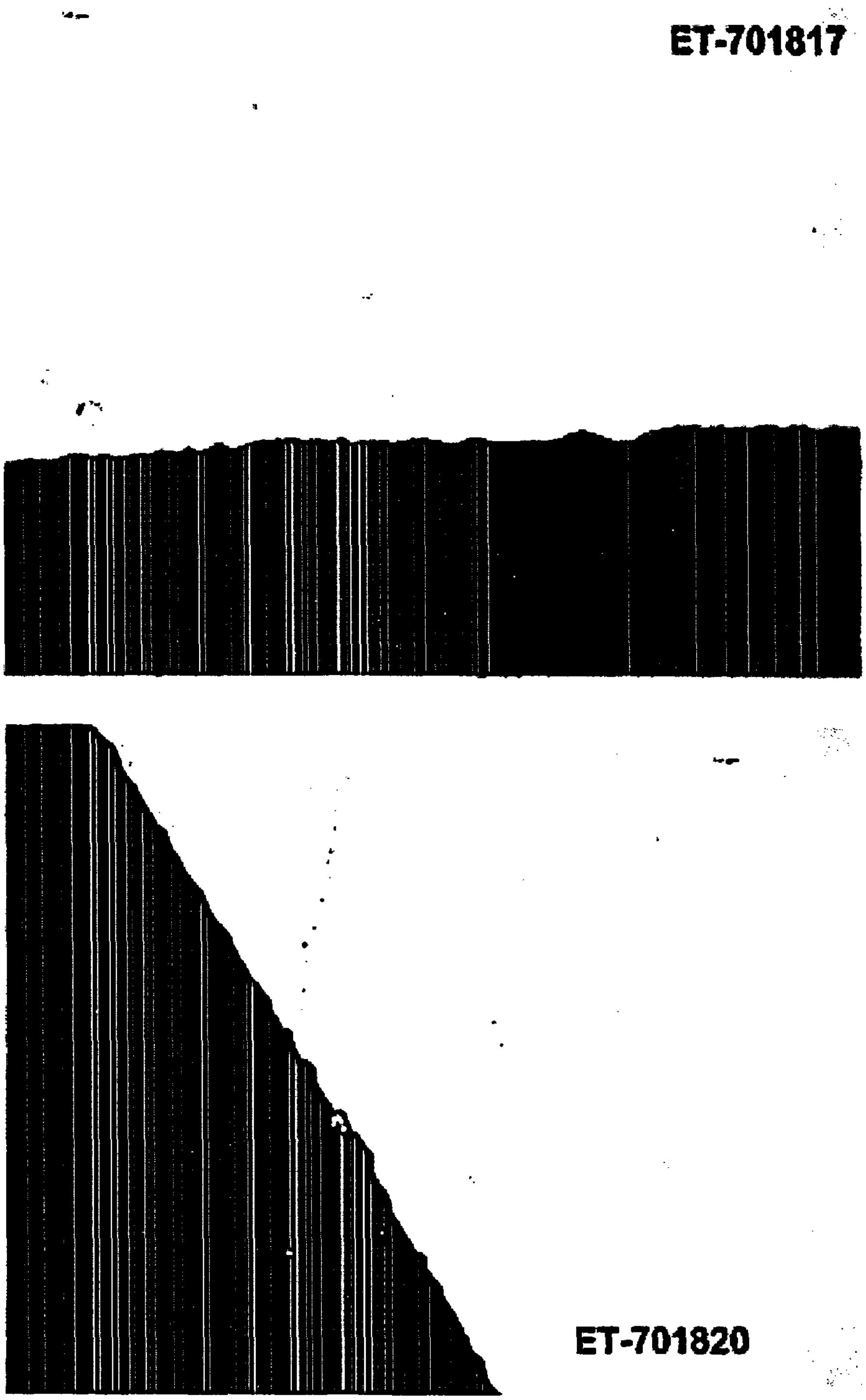

Fig. D.8 Cross-sectional view of H9 fuel-cladding interface at two azimuthal positions located at ≈500 mm above the fuel midplane (areas 3-4). Scale marker = 50 μm. JPG file = 591C12 ID Oxide Areas 3-4.

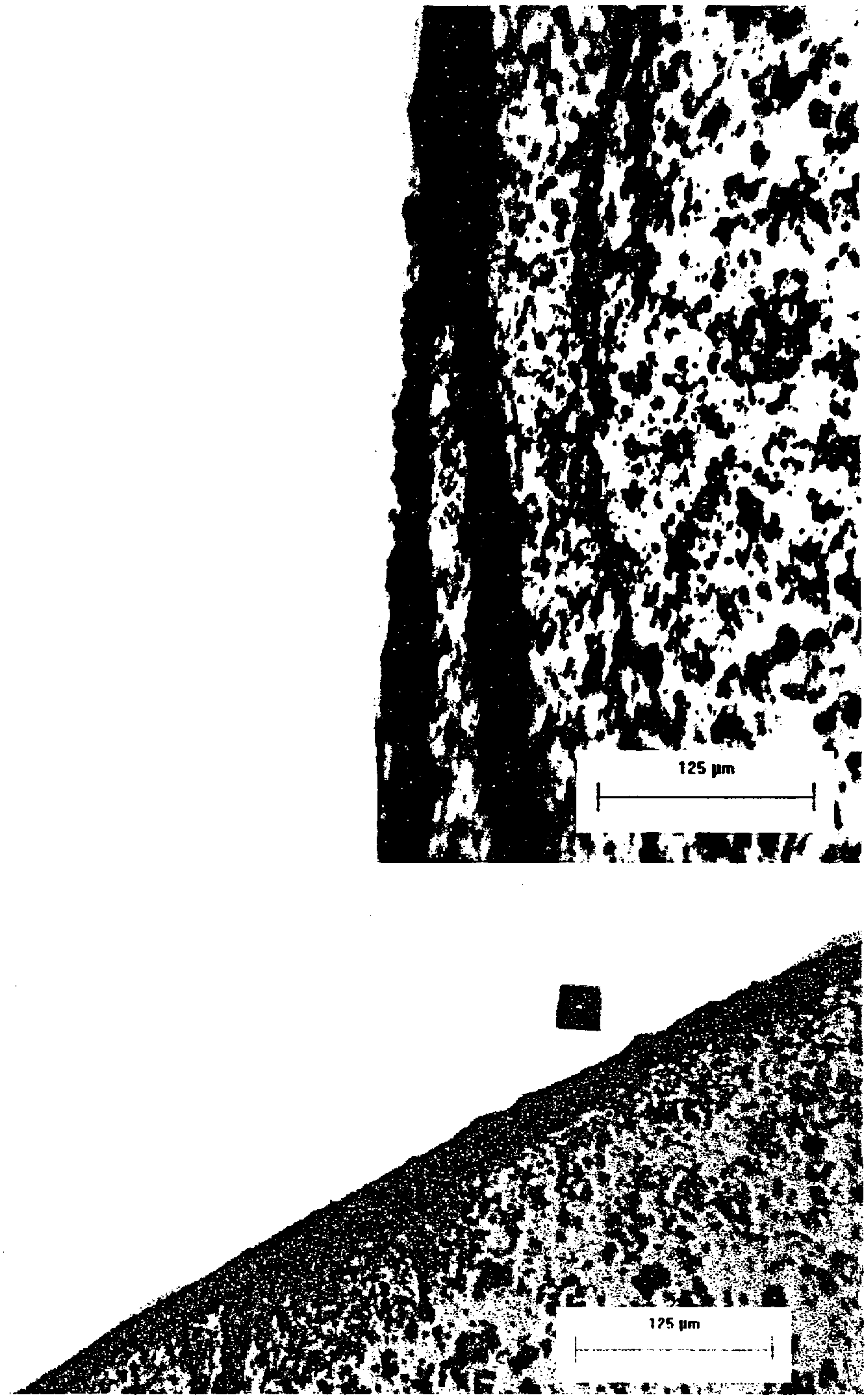

Fig. D.9 Cross-sectional view of Rod H9 fuel-cladding interface at two azimuthal positions ≈1000 mm above the fuel midplane (areas 6, 8). Scale marker = 125 µm. JPG file = 591B2 ID Oxide Areas 6,8. ET702573, ET702574

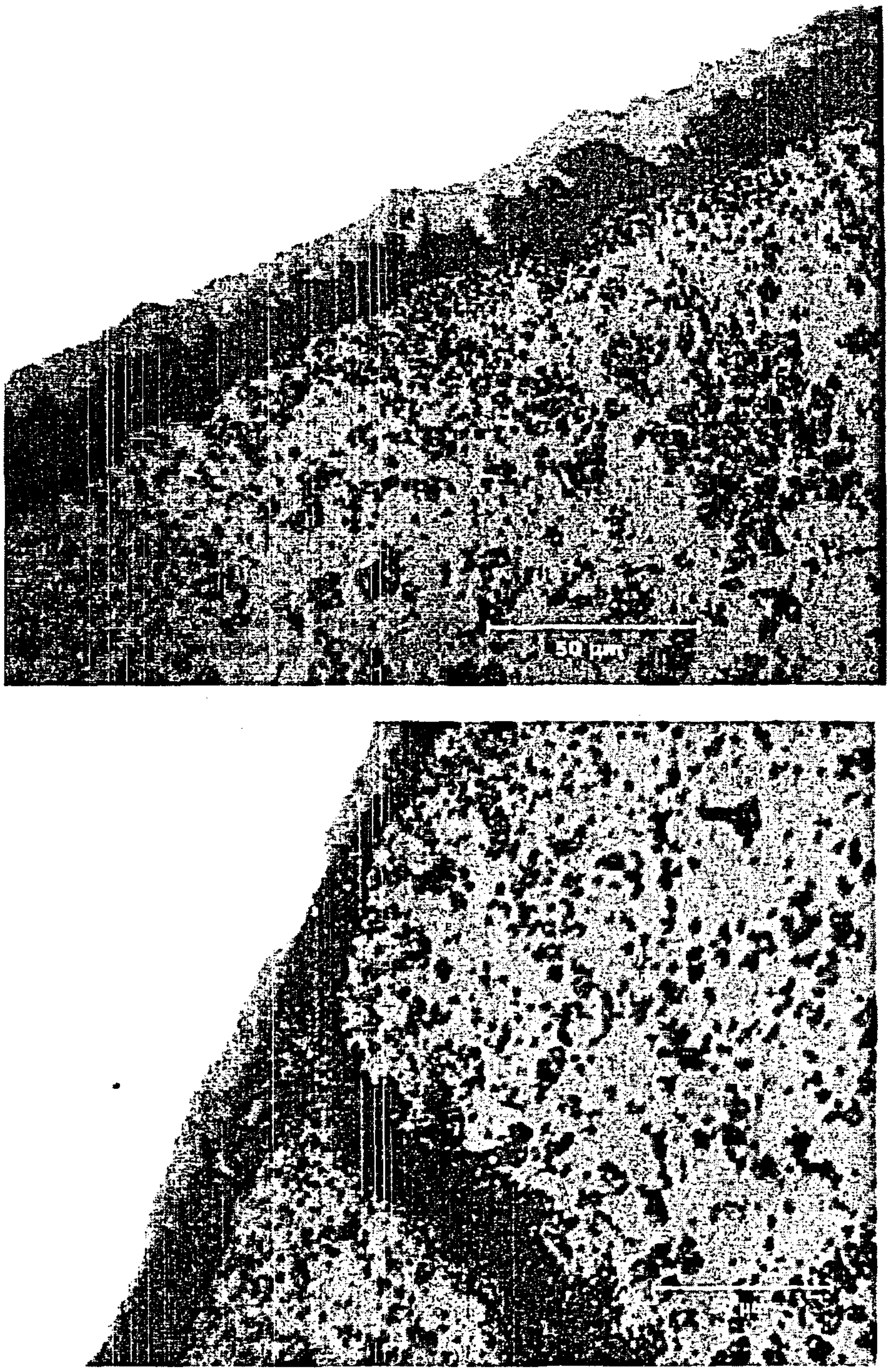

Fig. D.10 Cross-sectional view of Rod G6 fuel-cladding interface and cladding inner-surface oxide layer at two azimuthal positions located at the approximate fuel midplane (areas 1-2). Scale marker = 50 µm.
JPG file = 592C4 ID Oxide Areas 1, 2. ET703240, ET703241

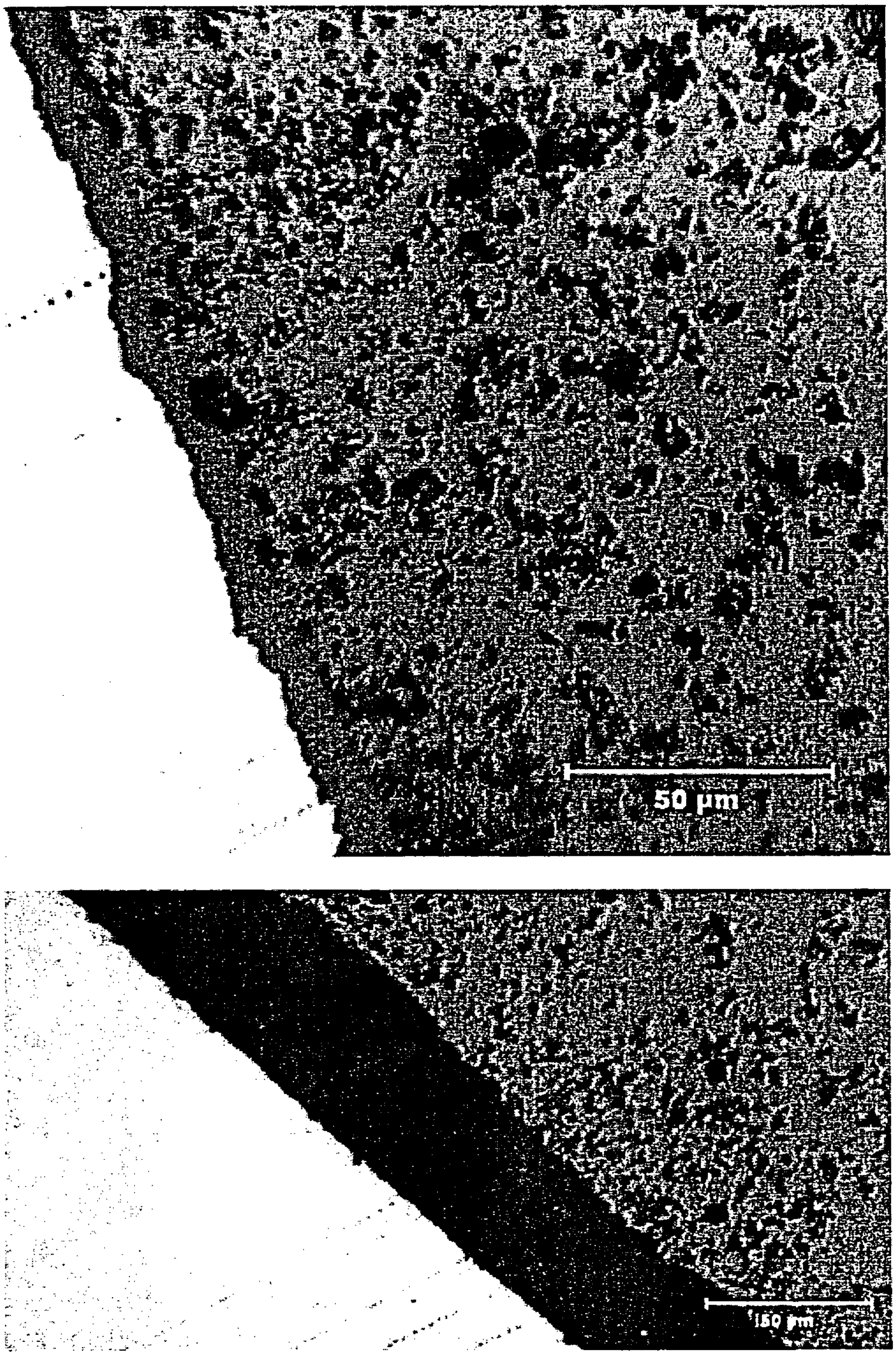

Fig. D.11 Cross-sectional view of Rod G6 fuel-cladding interface and cladding inner-surface oxide layer at two azimuthal positions at the approximate fuel midplane (areas 3-4). Scale marker = 50 µm.
JPG file = 592C4 ID Oxide Areas 3,4. ET703242, ET703243

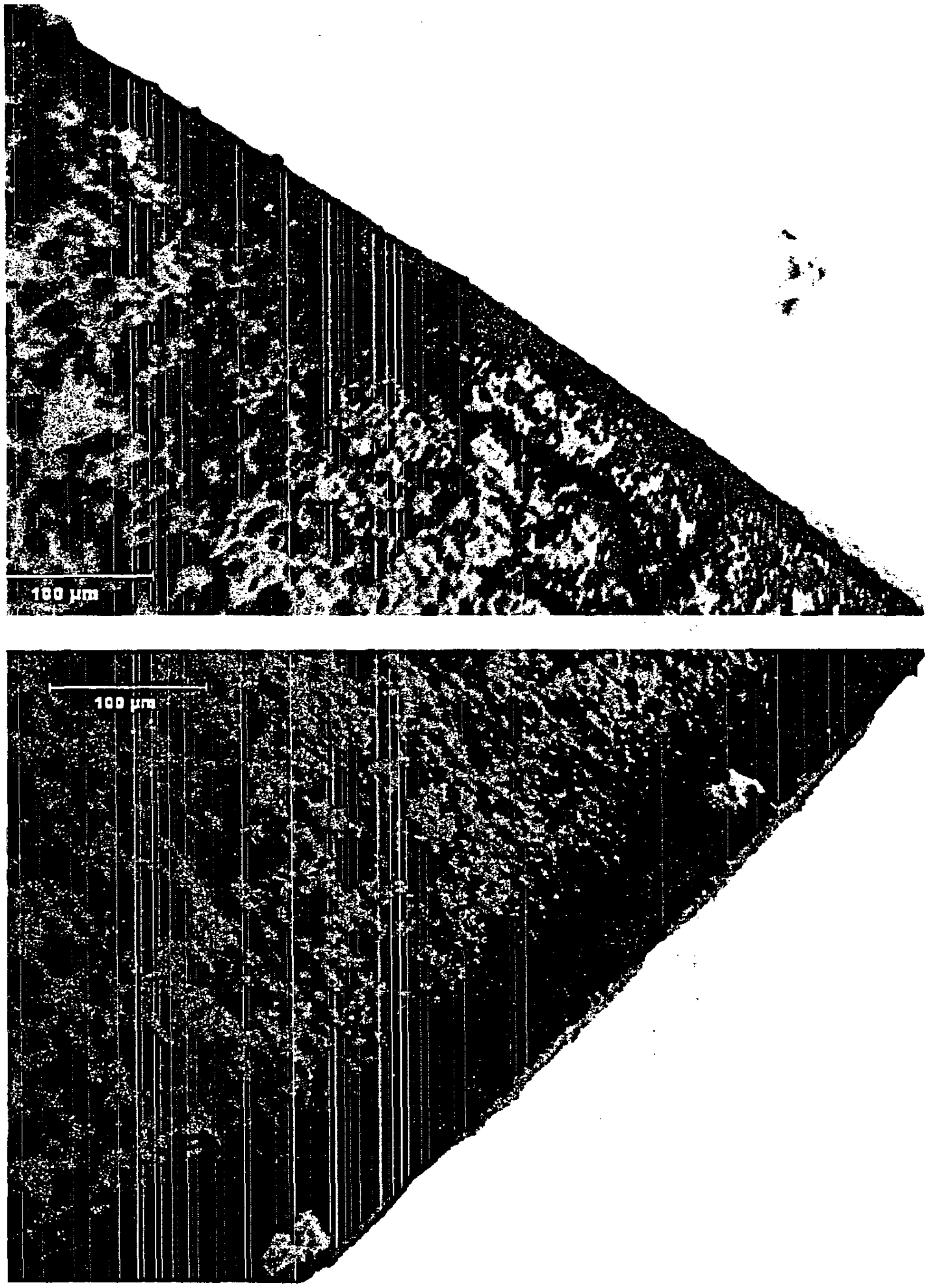

Fig. D.12 Cross-sectional view of Rod G6 fuel-cladding interface and/or cladding inner surface oxide layer at two azimuthal positions located at ≈500 mm above the fuel midplane (areas 2-4). Scale marker = 100 µm.
JPG file = 592C12 ID Oxide Areas 2,4. ET703111, ET703117

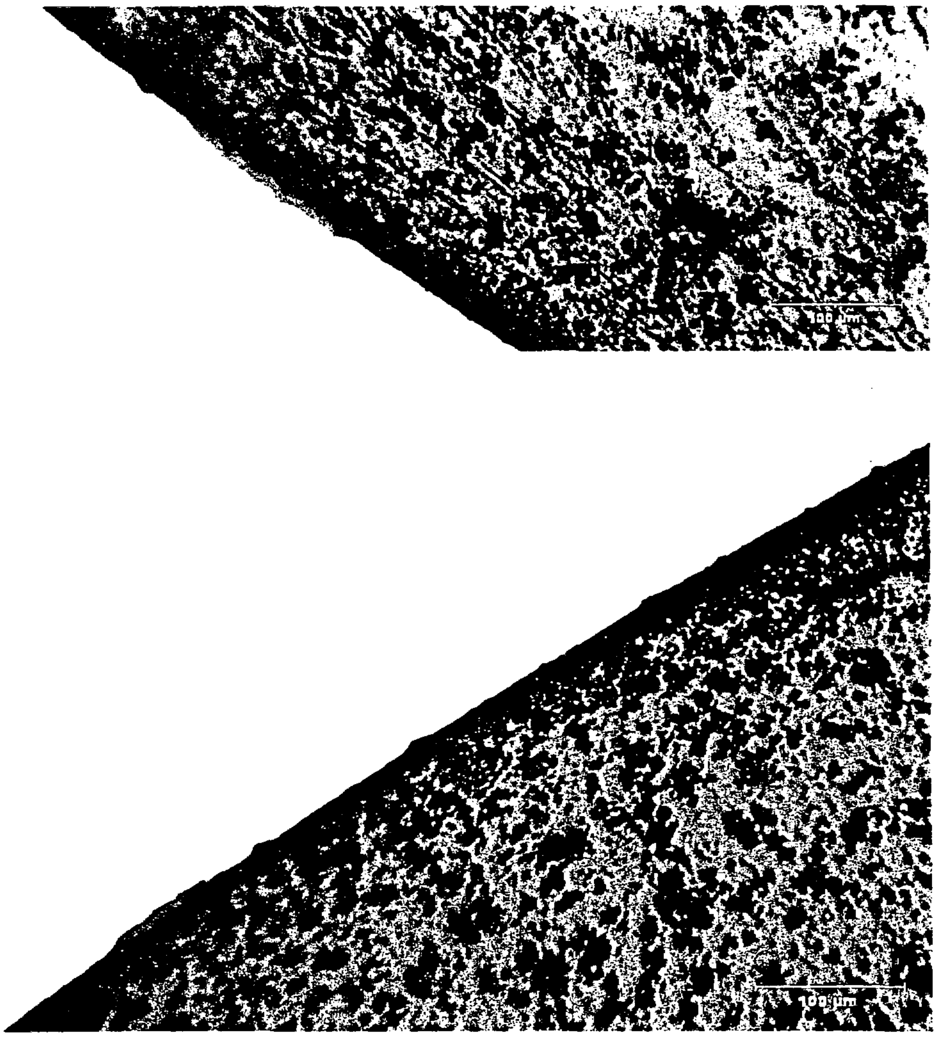

Fig. D.13 Cross-sectional view of Rod G6 fuel-cladding interface and cladding inner-surface oxide layer at two azimuthal positions located at ≈500 mm above the fuel midplane (areas 6-8). Scale marker = 100 μm.
JPG file = 592C12 ID Oxide Areas 6,8. ET703123, ET703129

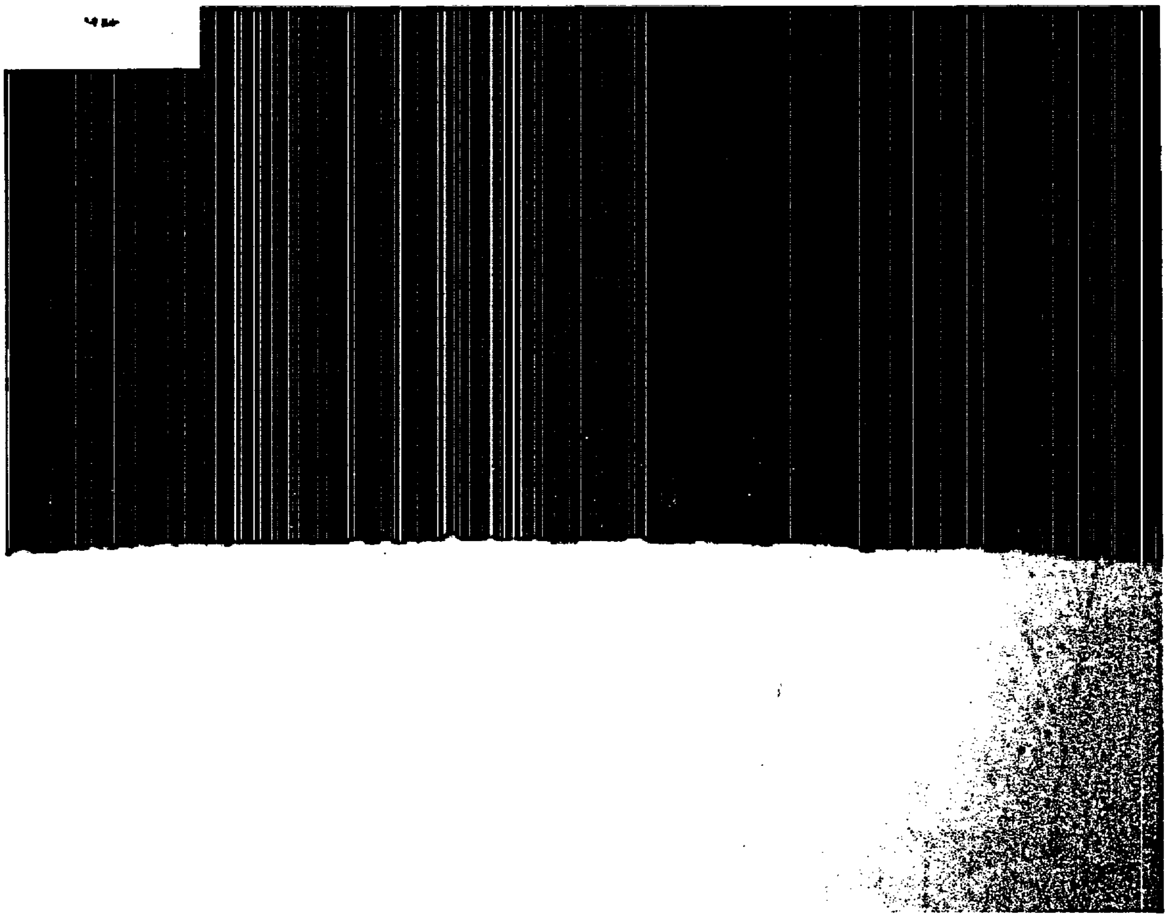

Fig. D.14 Cross-sectional view of Rod H9 cladding outer-surface oxide layer at the approximate fuel midplane (area 1). Scale marker = 50 µm. JPG file = 591C4 OD Oxide Area 1.

Fig. D.15 Cross-sectional view of Rod H9 cladding outer-surface oxide layer at the approximate fuel midplane (area 2). Scale marker = 50 μm.
JPG file = 591C4 OD Oxide Area 2.

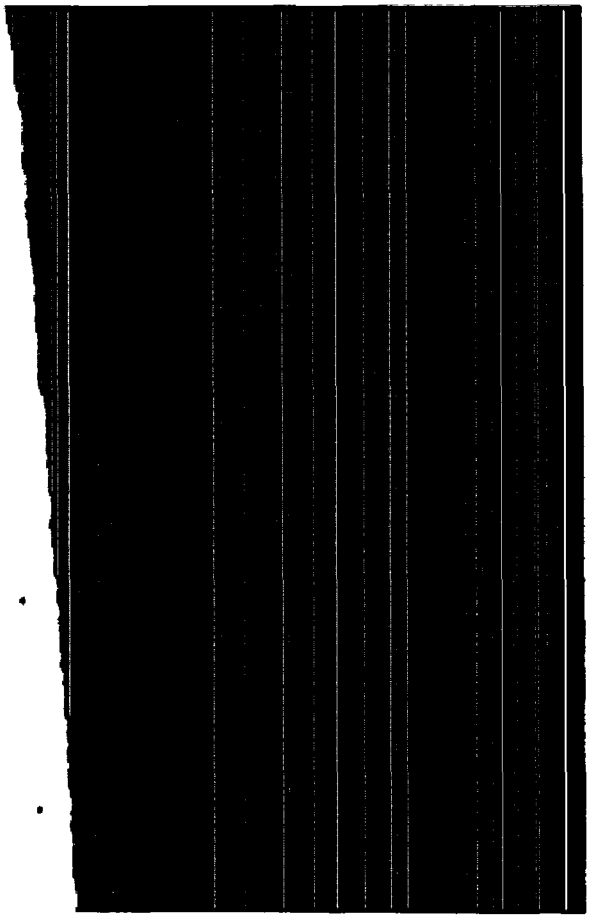

Fig. D.16 Cross-sectional view of Rod H9 cladding outer-surface oxide layer at the approximate fuel midplane (area 3). Scale marker = 50 µm.
JPG file = 591C4 OD Oxide Area 3.

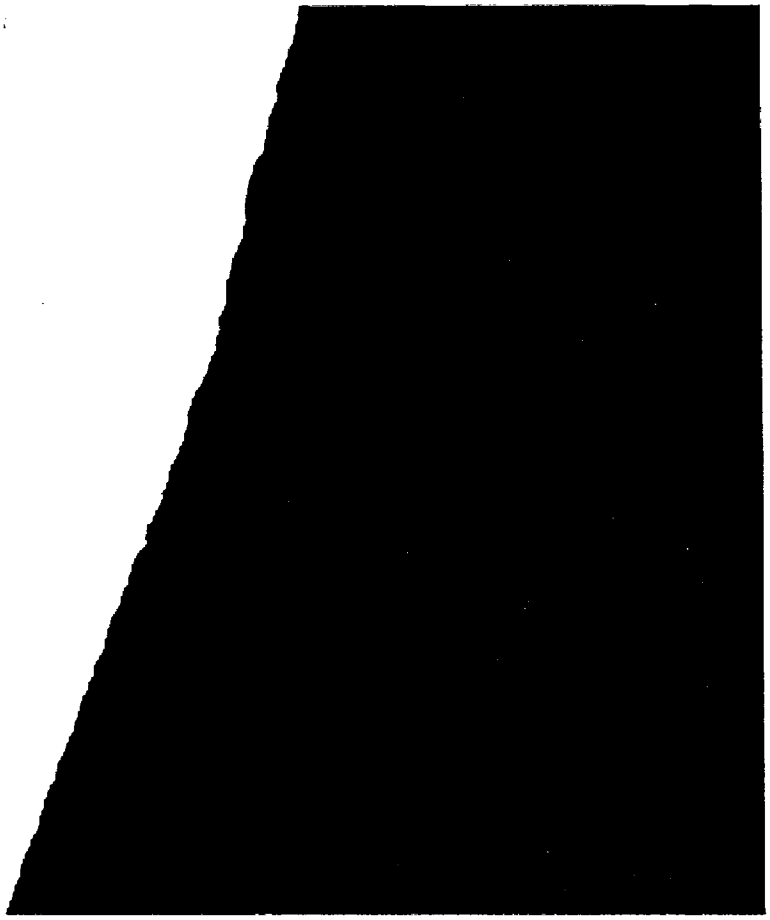

Fig. D.17 Cross-sectional view of the Rod H9 cladding outer-surface oxide layer at the approximate fuel midplane (area 4). Scale marker = 50 µm.
JPG file = 591C4 OD Oxide Area 4.

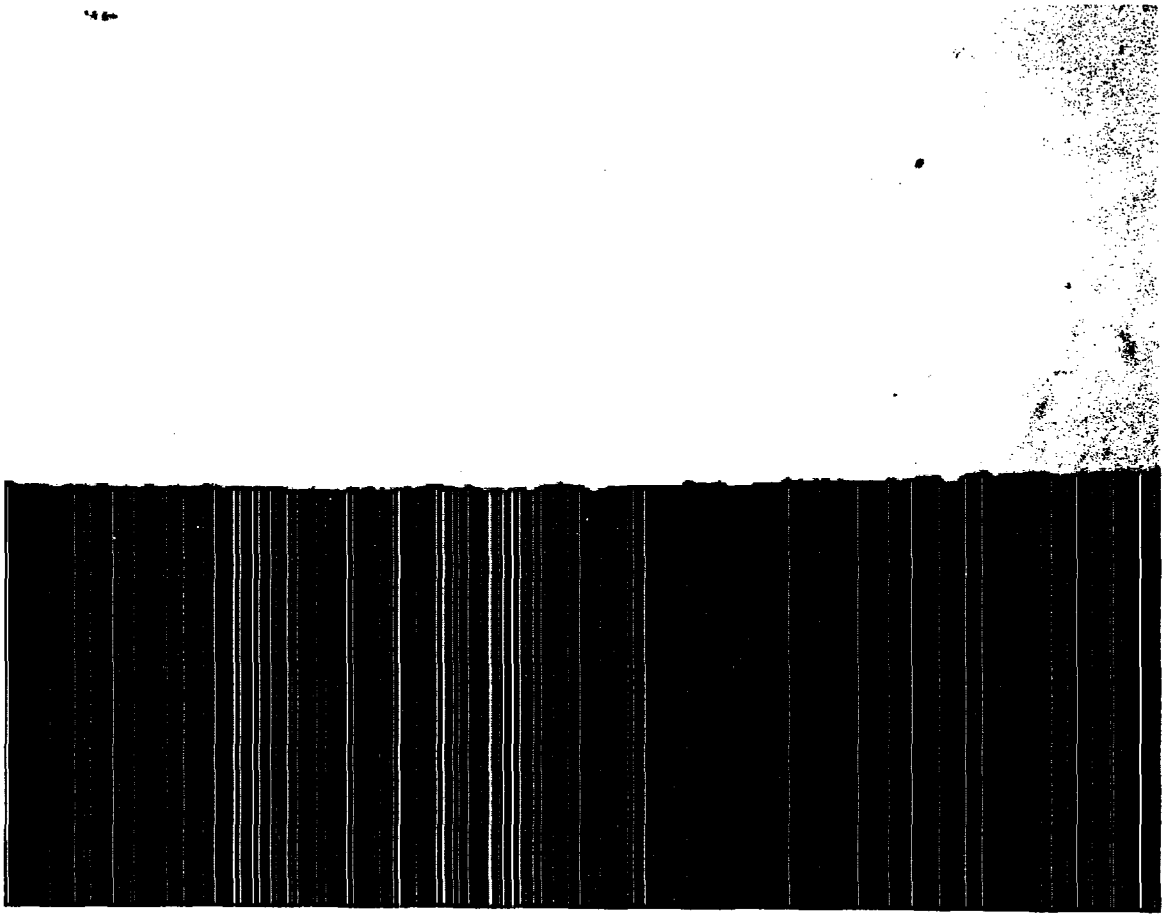

Fig. D.18 Cross-sectional view of Rod H9 cladding outer-surface oxide layer at the approximate fuel midplane (area 5). Scale marker = 50 μm.
JPG file = 591C4 OD Oxide Area 5.

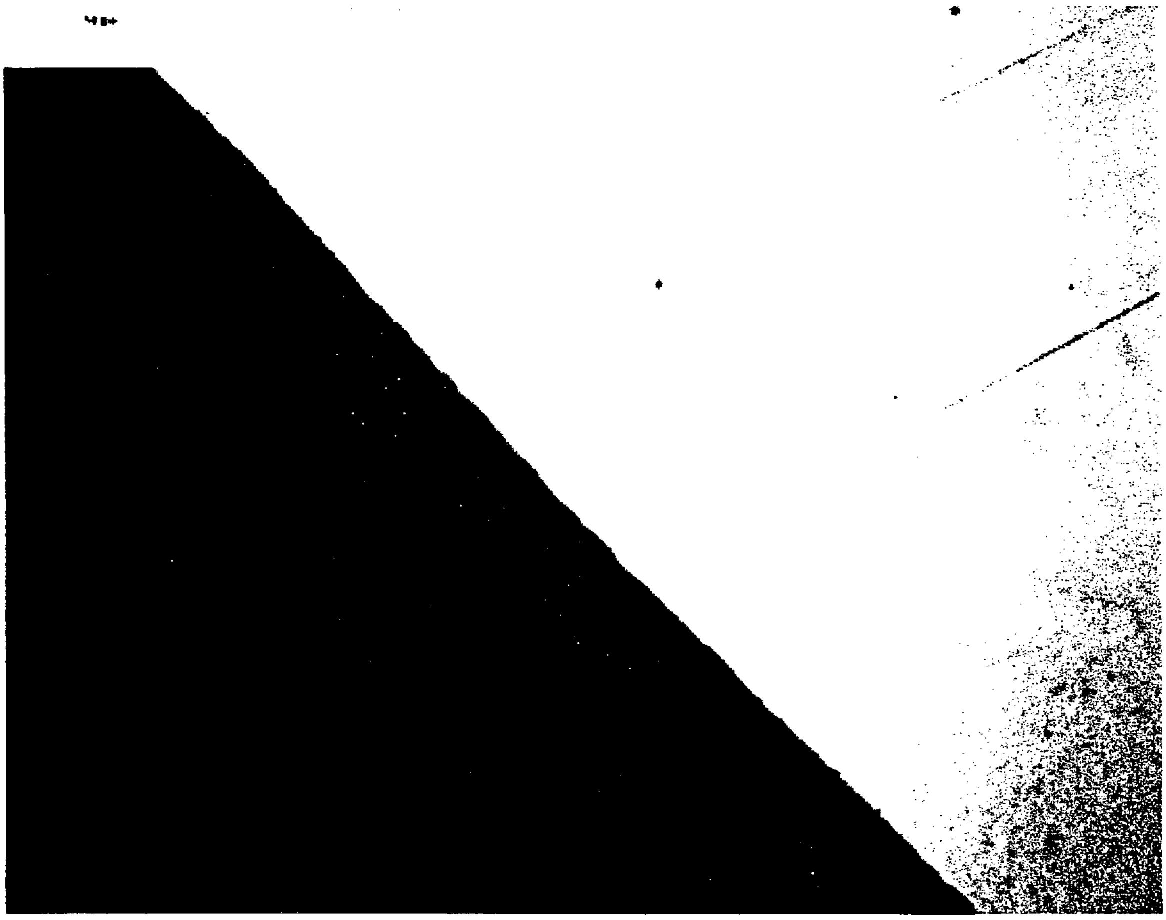

Fig. D.19 Cross-sectional view of Rod H9 cladding outer-surface oxide layer at the approximate fuel midplane (area 6). Scale marker = 50 µm.
JPG file = 591C4 OD Oxide Area 6.

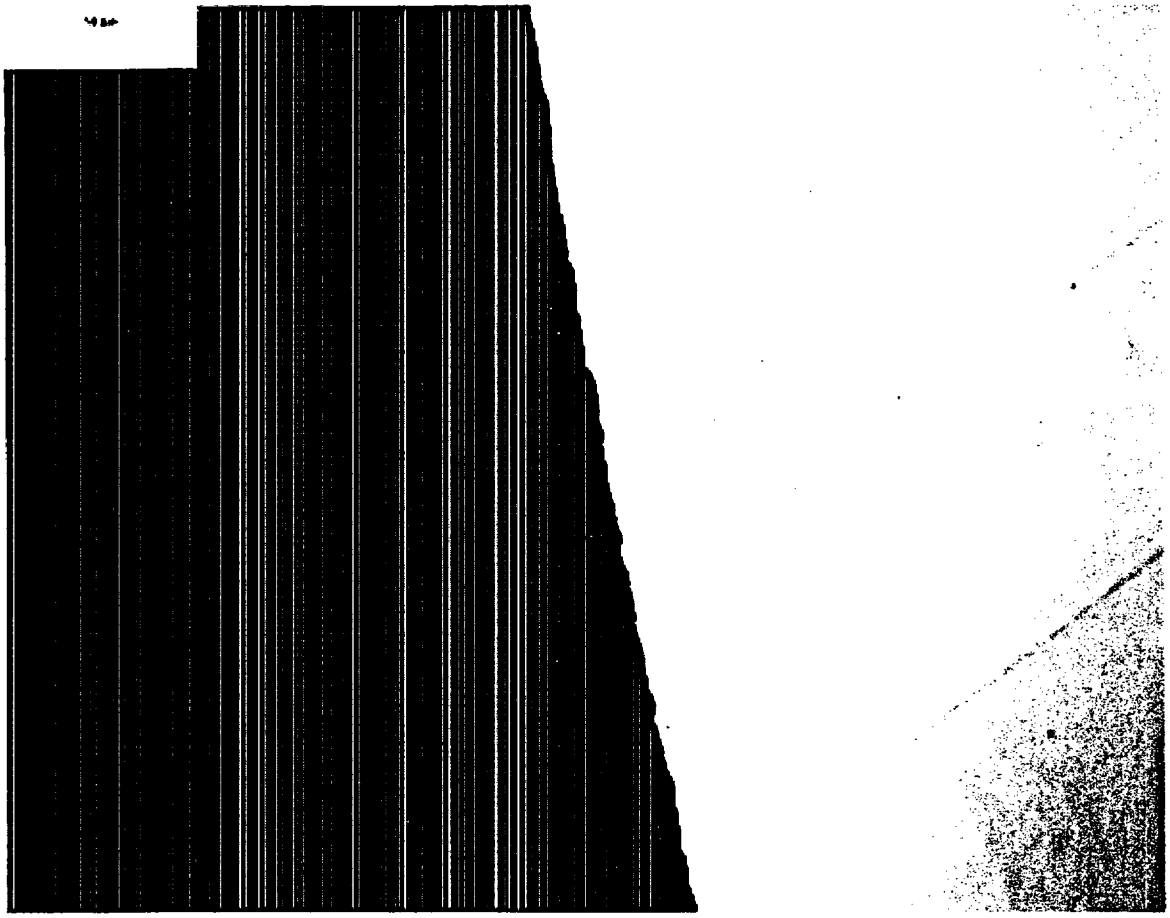

Fig. D.20 Cross-sectional view of Rod H9 cladding outer-surface oxide layer at the approximate fuel midplane (area 7). Scale marker = 50 μm.
JPG file = 591C4 OD Oxide Area 7.

Fig. D.21 Cross-sectional view of Rod H9 cladding outer-surface oxide layer at the approximate fuel midplane (area 8). Scale marker = 50 μm.
JPG file = 591C4 OD Oxide Area 8.

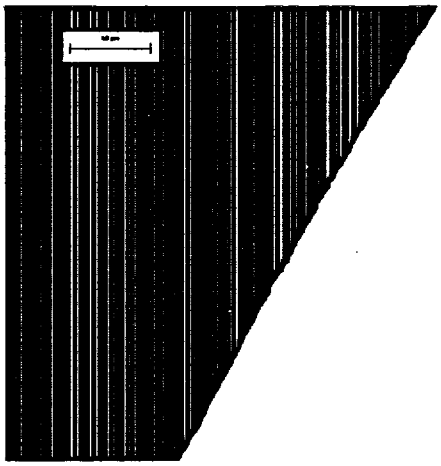

ET-701837

ET-701834

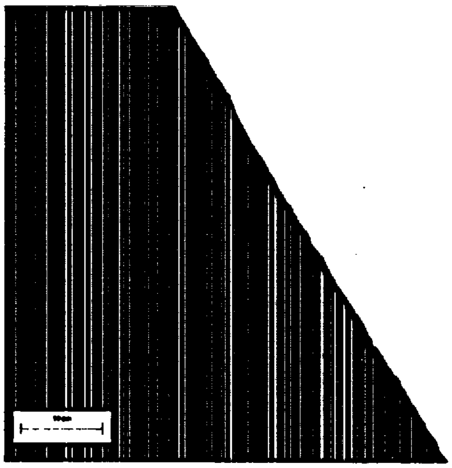

ET-701831

Fig. D.22 Cross-sectional view of Rod H9 cladding outer-surface oxide layer at ≈500 mm above the fuel midplane (areas 1-3). Scale marker = 50 µm. JPG file = 591C12 OD Oxide Area 1-3.

Fig. D.23 Cross-sectional view of Rod H9 cladding outer-surface oxide layer at ≈500 mm above the fuel midplane (areas 4-6). Scale marker = 50 μm.
JPG file = 591C12 OD Oxide Area 4-6.

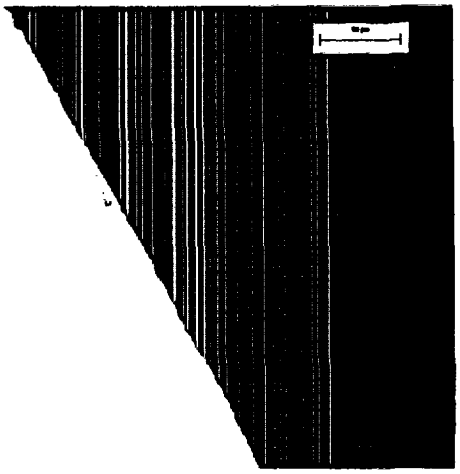

ET-701812

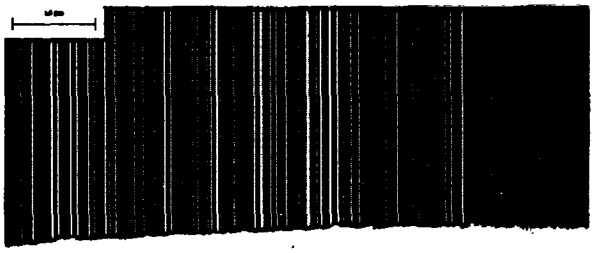

ET-701816

Fig. D.24 Cross-sectional view of Rod H9 cladding outer-surface oxide layer at ≈500 mm above the fuel midplane (areas 7-8). Scale marker = 50 μm.
JPG file = 591C12 OD Oxide Area 7-8.

Fig. D.25 Cross-sectional view of Rod H9 cladding outer-surface oxide layer at ≈1000 mm above the fuel midplane (area 1). Scale marker = 50 μm. JPG file = 591B2 OD Oxide Area 1. ET702544.

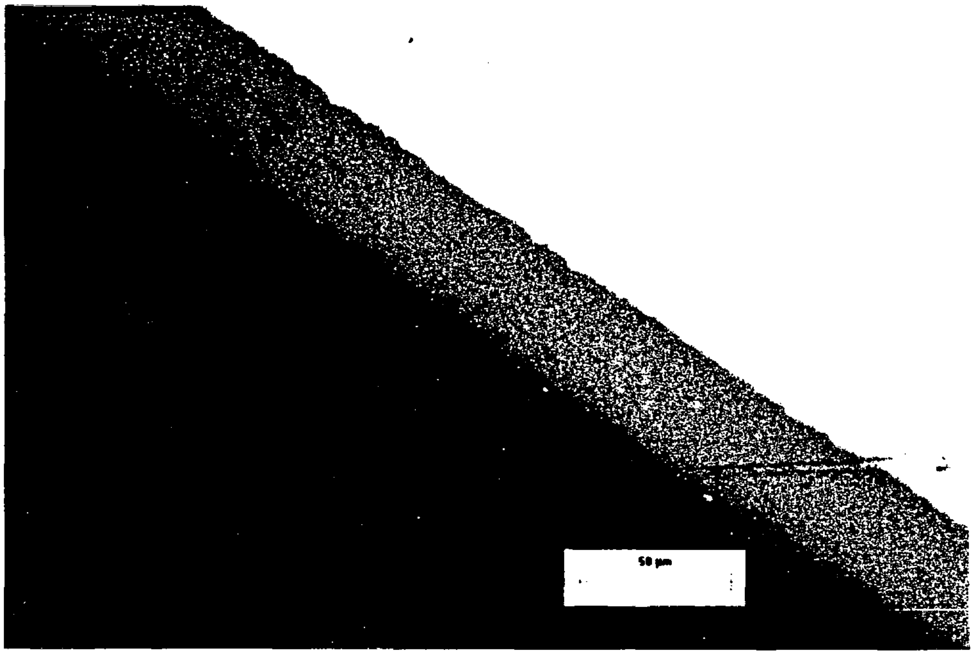

Fig. D.26 Cross-sectional view of Rod H9 cladding outer-surface oxide layer at ≈1000 mm above the fuel midplane (area 2). Scale marker = 50 μm. JPG file = 591B2 OD Oxide Area 2. ET702545.

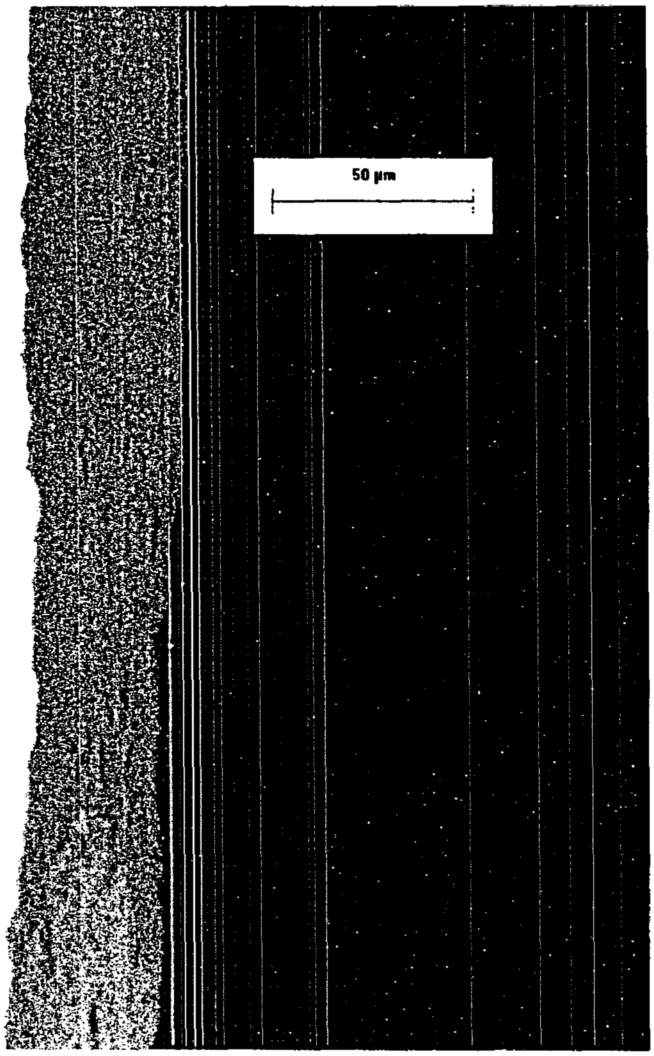

Fig. D.27 Cross-sectional view of Rod H9 cladding outer-surface oxide layer at ≈1000 mm above the fuel midplane (area 3). Scale marker = 50 µm.
JPG file = 591B2 OD Oxide Area 3. ET702546.

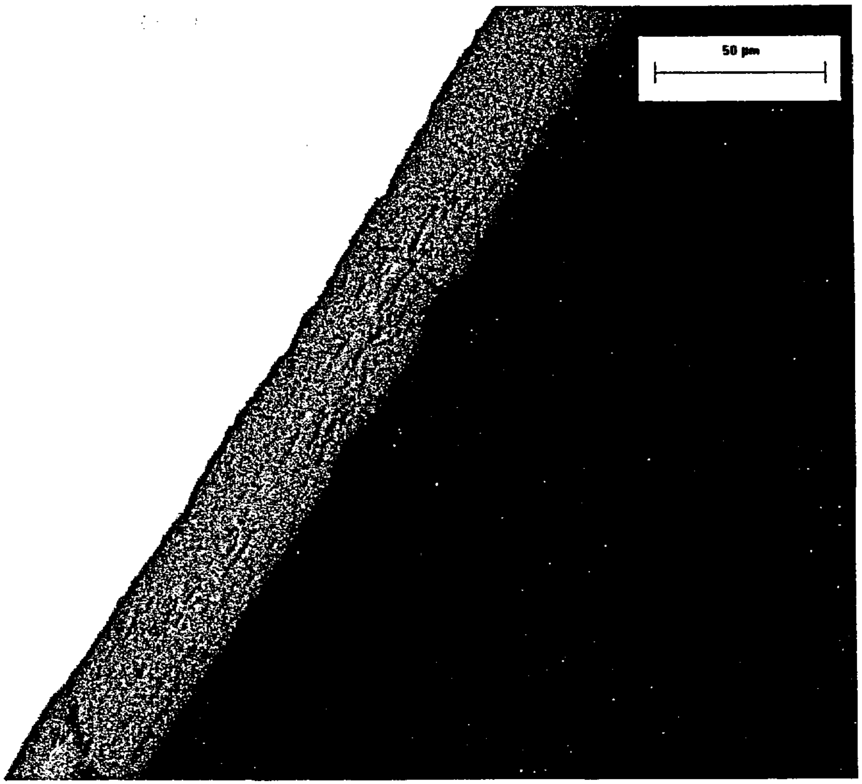

Fig. D.28 Cross-sectional view of Rod H9 cladding outer-surface oxide layer at ≈1000 mm above the fuel midplane (area 4). Scale marker = 50 µm. JPG file = 591B2 OD Oxide Area 4. ET702547.

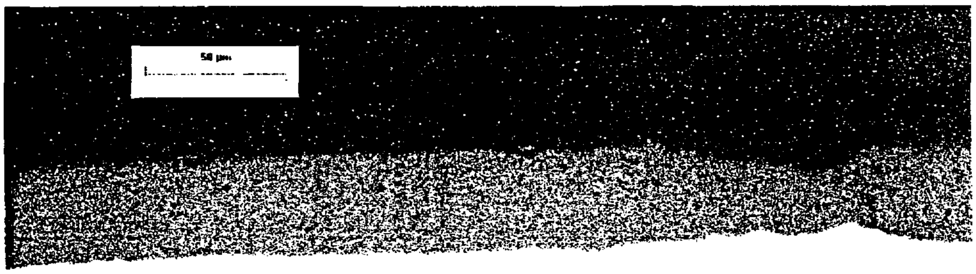

Fig. D.29 Cross-sectional view of Rod H9 cladding outer-surface oxide layer at ≈1000 mm above the fuel midplane (area 5). Scale marker = 50 µm. JPG file = 591B2 OD Oxide Area 5. ET702548.

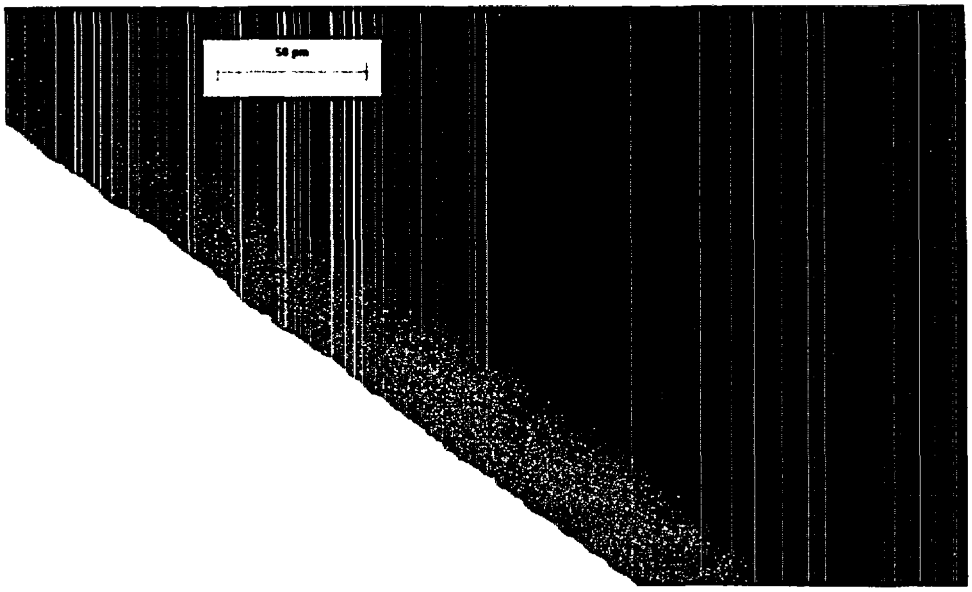

Fig. D.30 Cross-sectional view of Rod H9 cladding outer-surface oxide layer at ≈1000 mm above the fuel midplane (area 6). Scale marker = 50 µm.
JPG file = 591B2 OD Oxide Area 6. ET70254.

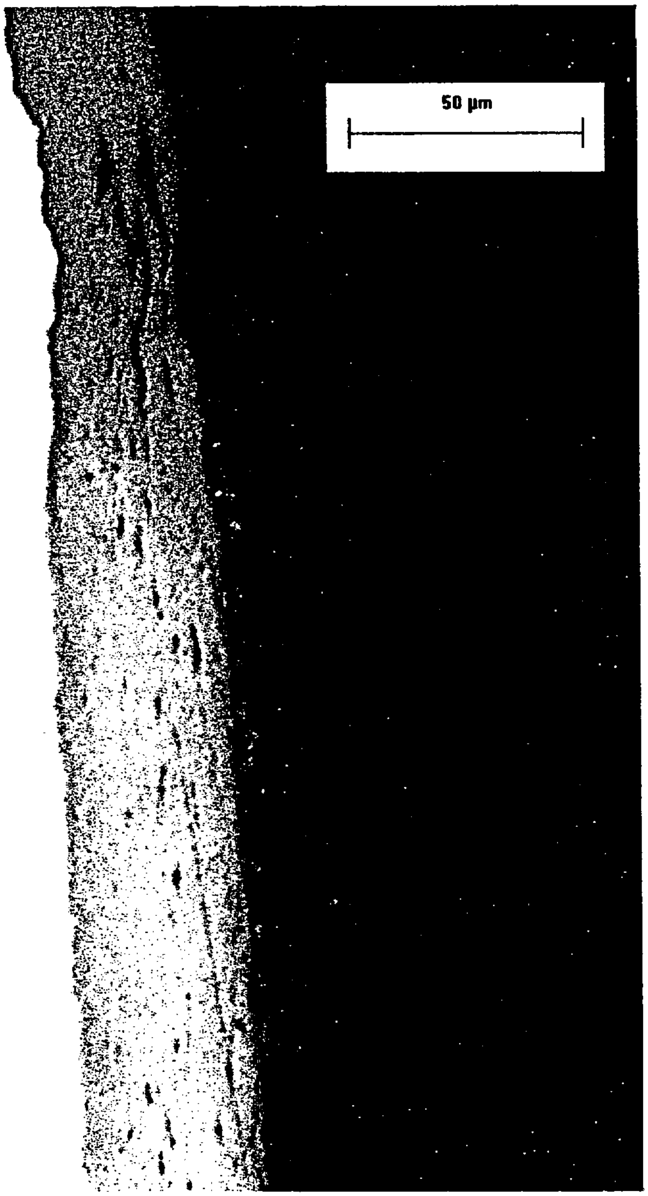

Fig. D.31 Cross-sectional view of rod H9 cladding outer-surface oxide layer at ≈1000 mm above the fuel midplane (area 7). Scale marker = 50 µm.
JPG file = 591B2 OD Oxide Area 7. ET702550.

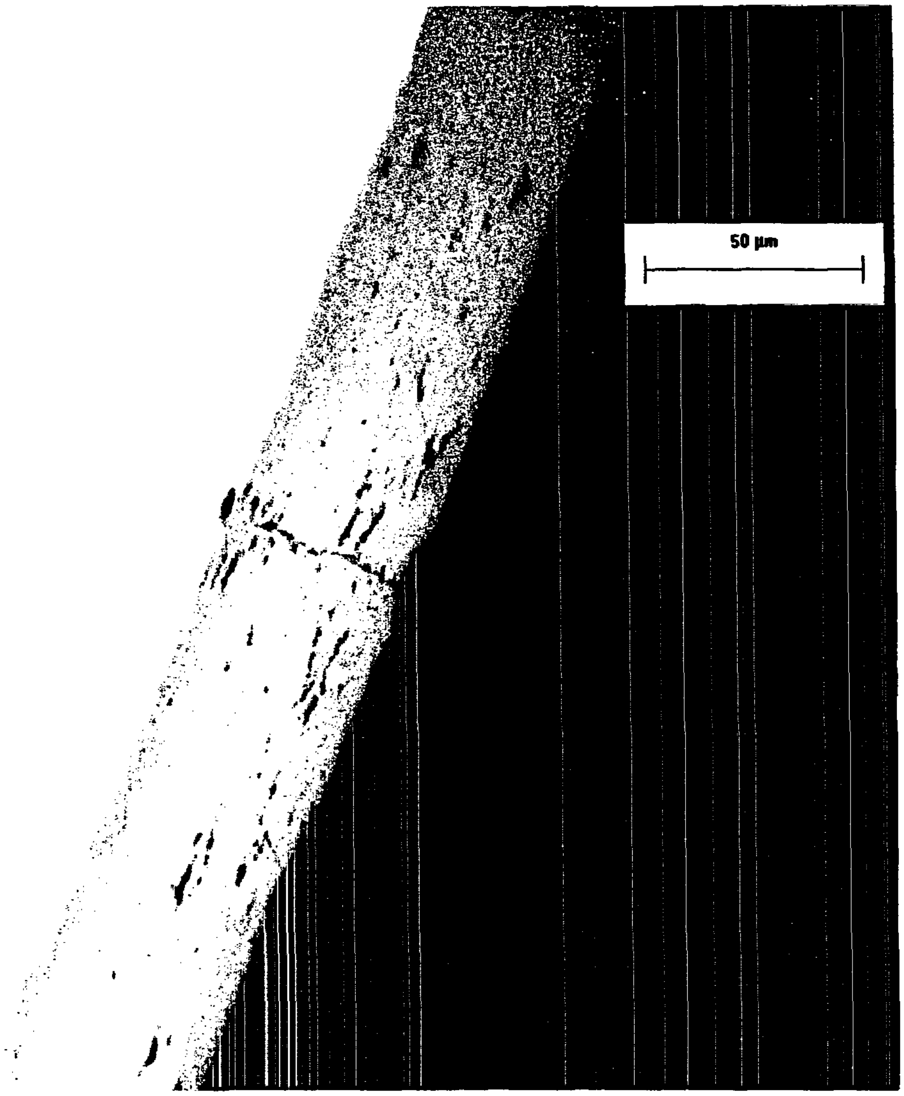

Fig. D.32 Cross-sectional view of Rod H9 cladding outer-surface oxide layer at ≈1000 mm above the fuel midplane (area 8). Scale marker = 50 µm.
JPG file = 591B2 OD Oxide Area 8. ET702551.

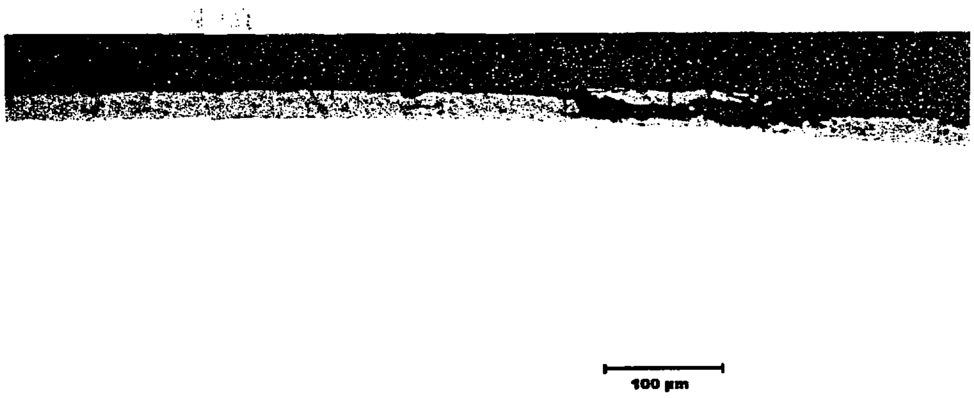

Fig. D.33 Cross-sectional view of Rod G6 cladding outer-surface oxide layer at the approximate fuel midplane (area 1). Scale marker = 100 µm. JPG file = 592C4 OD Oxide Area 1. ET703148.

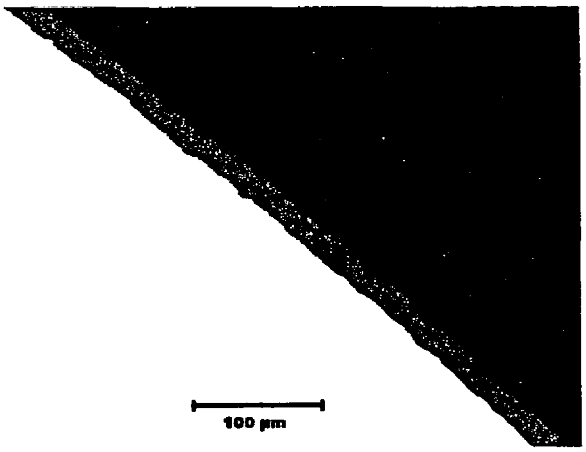

Fig. D.34 Cross-sectional view of Rod G6 cladding outer-surface oxide layer at the approximate fuel midplane (area 2). Scale marker = 100 µm. JPG file = 592C4 OD Oxide Area 2. ET703151.

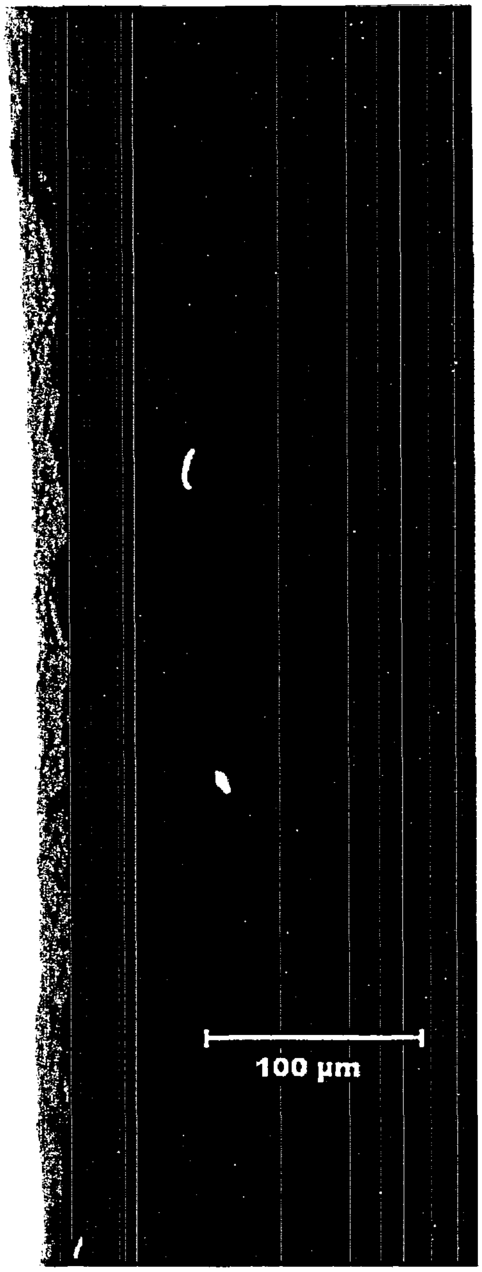

Fig. D.35 Cross-sectional view of Rod G6 cladding outer-surface oxide layer at the approximate fuel midplane (area 3). Scale marker = 100 μm. JPG file = 592C4 OD Oxide Area 3. ET703154.

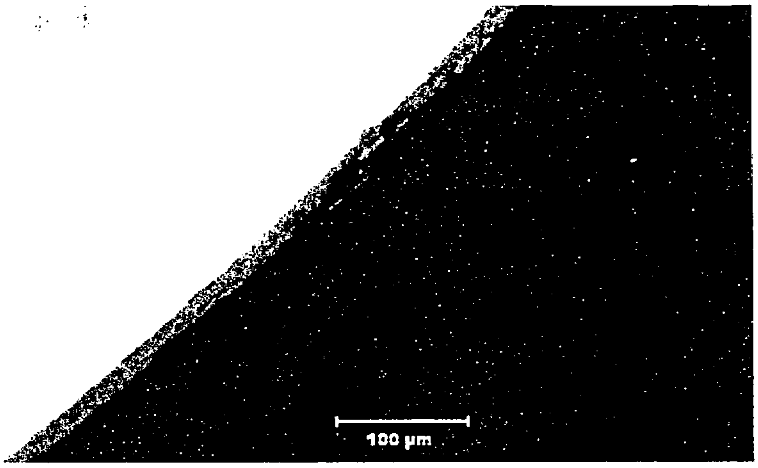

Fig. D.36 Cross-sectional view of Rod G6 cladding outer-surface oxide layer at the approximate fuel midplane (area 4). Scale marker = 100 µm. JPG file = 592C4 OD Oxide Area 4. ET703157.

Fig. D.37 Cross-sectional view of Rod G6 cladding outer-surface oxide layer at the approximate fuel midplane (area 5). Scale marker = 100 µm. JPG file = 592C4 OD Oxide Area 5. ET703160.

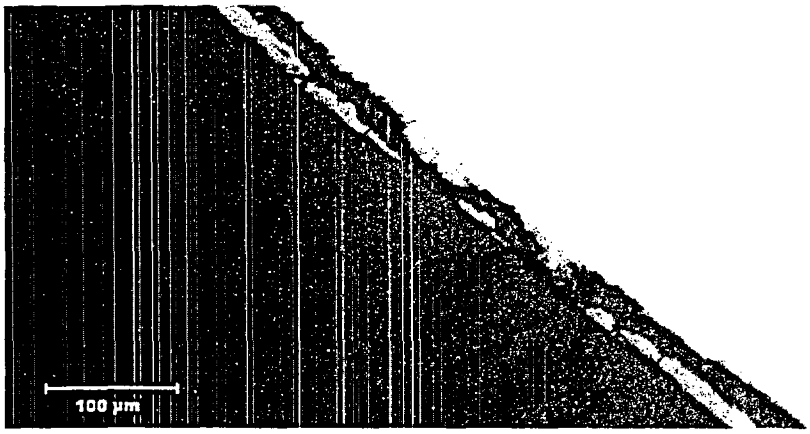

Fig. D.38 Cross-sectional view of Rod G6 cladding outer-surface oxide layer at the approximate fuel midplane (area 6). Scale marker = 100 µm. JPG file = 592C4 OD Oxide Area 6. ET703163.

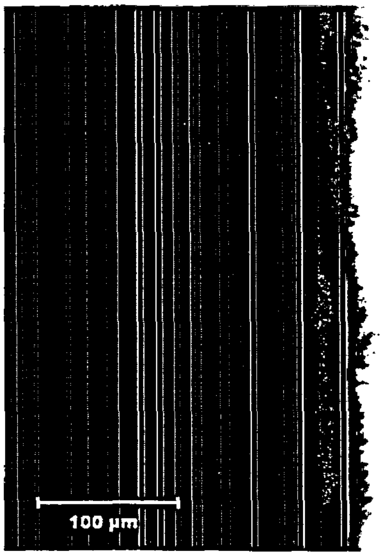

Fig. D.39 Cross-sectional view of Rod G6 cladding outer-surface oxide layer at the approximate fuel midplane (area 7). Scale marker = 100 µm. JPG file = 592C4 OD Oxide Area 7. ET703166.

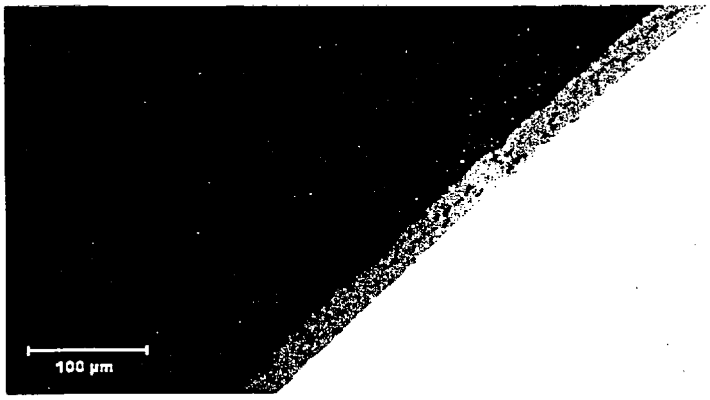

Fig. D.40 Cross-sectional view of Rod G6 cladding outer-surface oxide layer at the approximate fuel midplane (area 8). Scale marker = 100 µm.
JPG file = 592C4 OD Oxide Area 8. ET703169.

Fig. D.41 Cross-sectional view of Rod G6 cladding outer-surface oxide layer at ≈500 mm above the fuel midplane (area 1). Scale marker = 100 µm.
JPG file = 592C12 OD Oxide Area 1. ET703107.

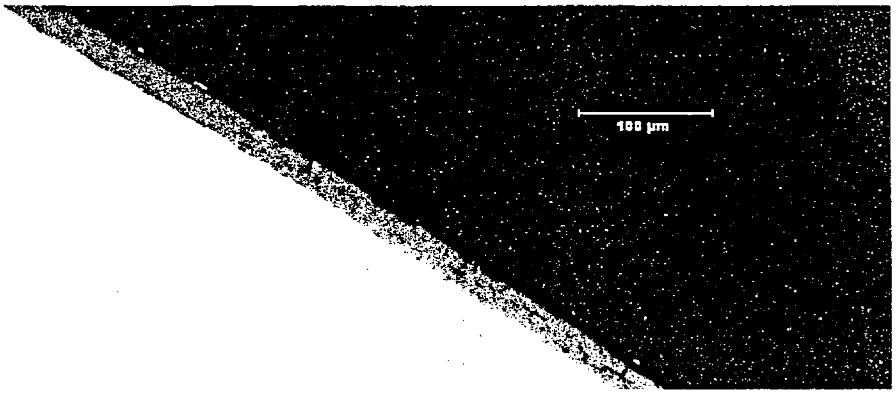

Fig. D.42 Cross-sectional view of Rod G6 cladding outer-surface oxide layer at ≈500 mm above the fuel midplane (area 2). Scale marker = 100 µm.
JPG file = 592C12 OD Oxide Area 2. ET703110.

Fig. D.43 Cross-sectional view of Rod G6 cladding outer-surface oxide layer at ≈500 mm above the fuel midplane (area 3). Scale marker = 100 µm. JPG file = 592C12 OD Oxide Area 3. ET703113.

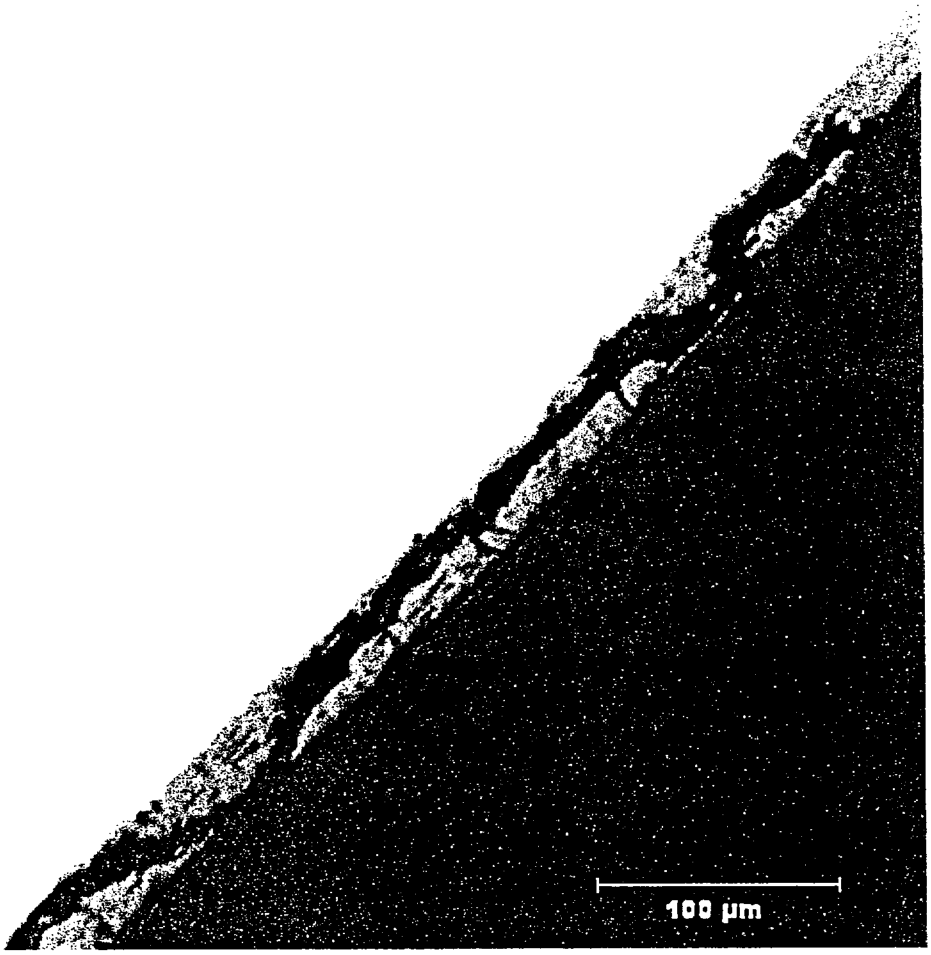

Fig. D.44 Cross-sectional view of Rod G6 cladding outer-surface oxide layer at ≈500 mm above the fuel midplane (area 4). Scale marker = 100 μm. JPG file = 592C12 OD Oxide Area 4. ET703116.

Fig. D.45 Cross-sectional view of Rod G6 cladding outer-surface oxide layer at ≈ 500 mm above the fuel midplane (area 5). Scale marker = 100 μm. JPG file = 592C12 OD Oxide Area 5. ET703119

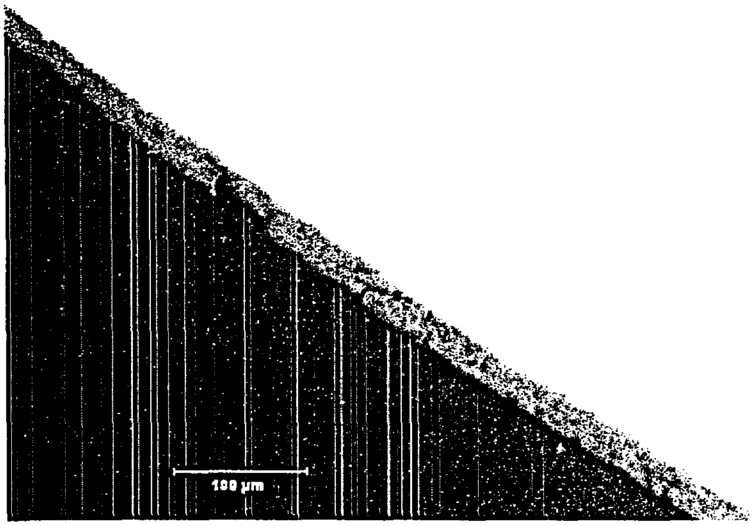

Fig. D.46 Cross-sectional view of Rod G6 cladding outer-surface oxide layer at ≈500 mm above the fuel midplane (area 6). Scale marker = 100 µm. JPG file = 592C12 OD Oxide Area 6. ET703122

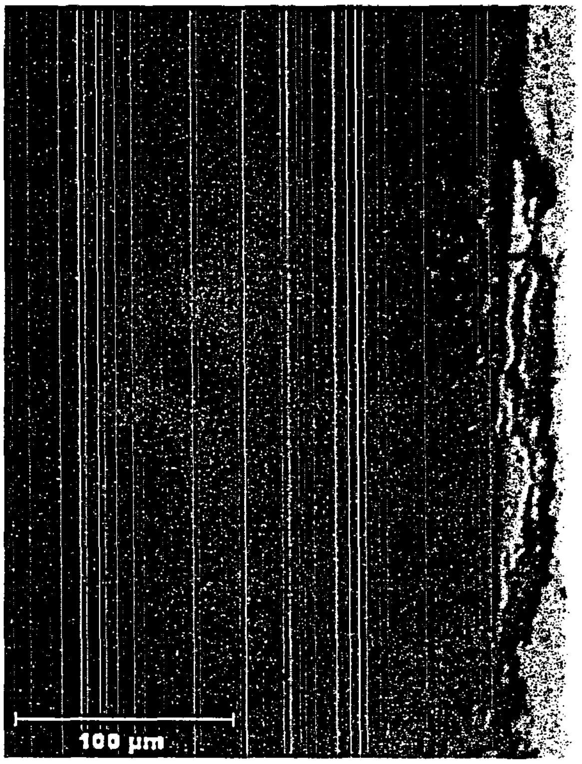

Fig. D.47 Cross-sectional view of Rod G6 cladding outer-surface oxide layer at ≈500 mm above the fuel midplane. Scale marker = 100 µm. JPG file = 592C12 OD Oxide Area 7. ET703125

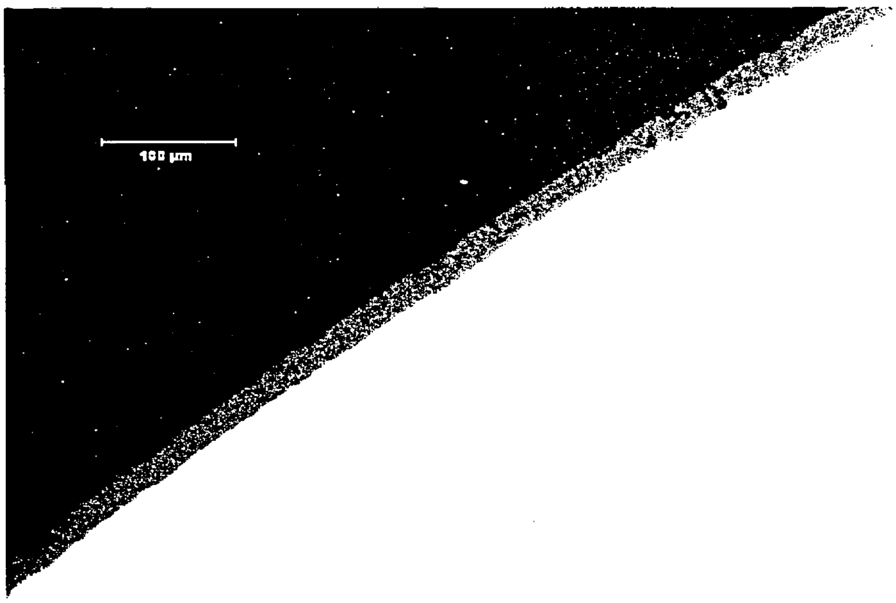

Fig. D.48 Cross-sectional view of Rod G6 cladding outer-surface oxide layer at ≈500 mm above the fuel midplane (area 8). Scale marker = 100 µm. JPG file = 592C12 OD Oxide Area 8. ET703128.

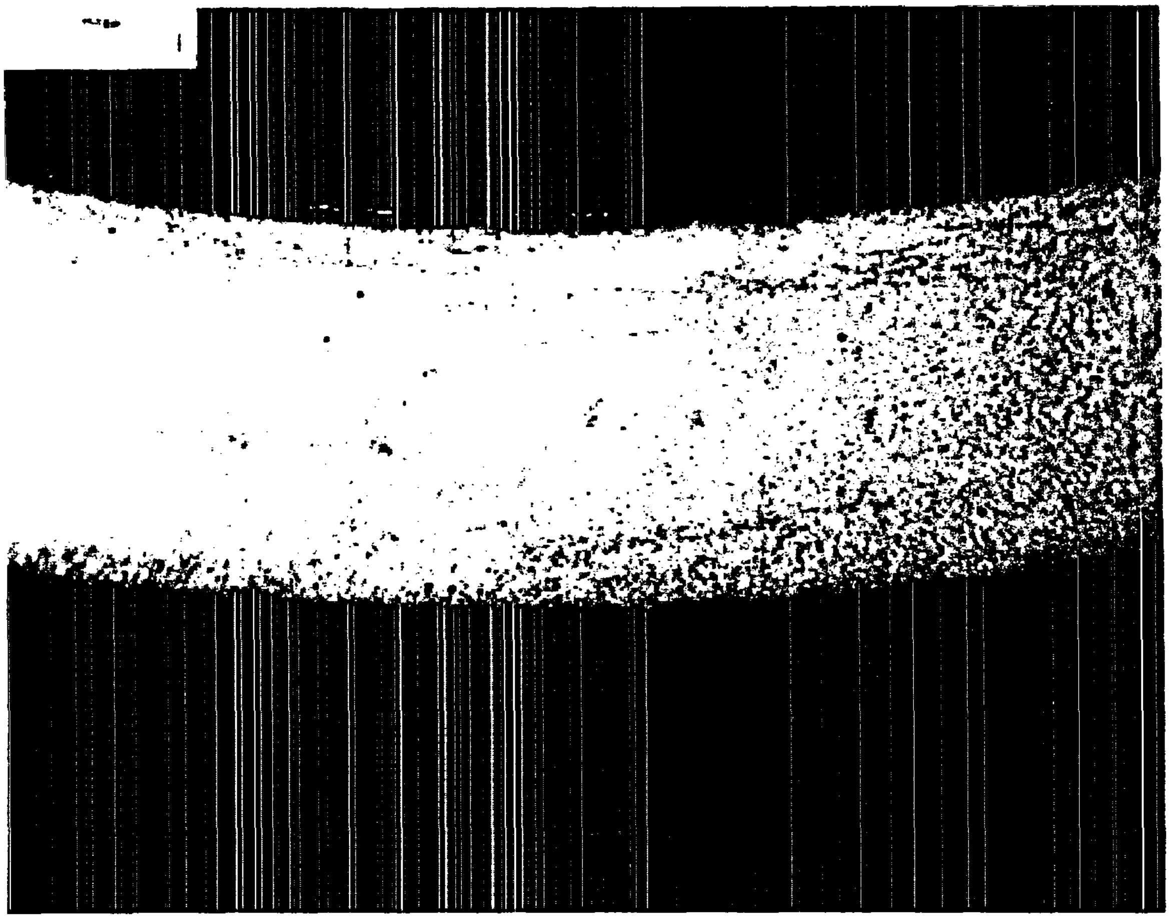

Fig. D.49 Cross-sectional view of Rod H9 cladding hydride morphology at fuel midplane (area 1). Scale marker = 250 μm.
JPG file = 591C4 Hydrides Area 1.

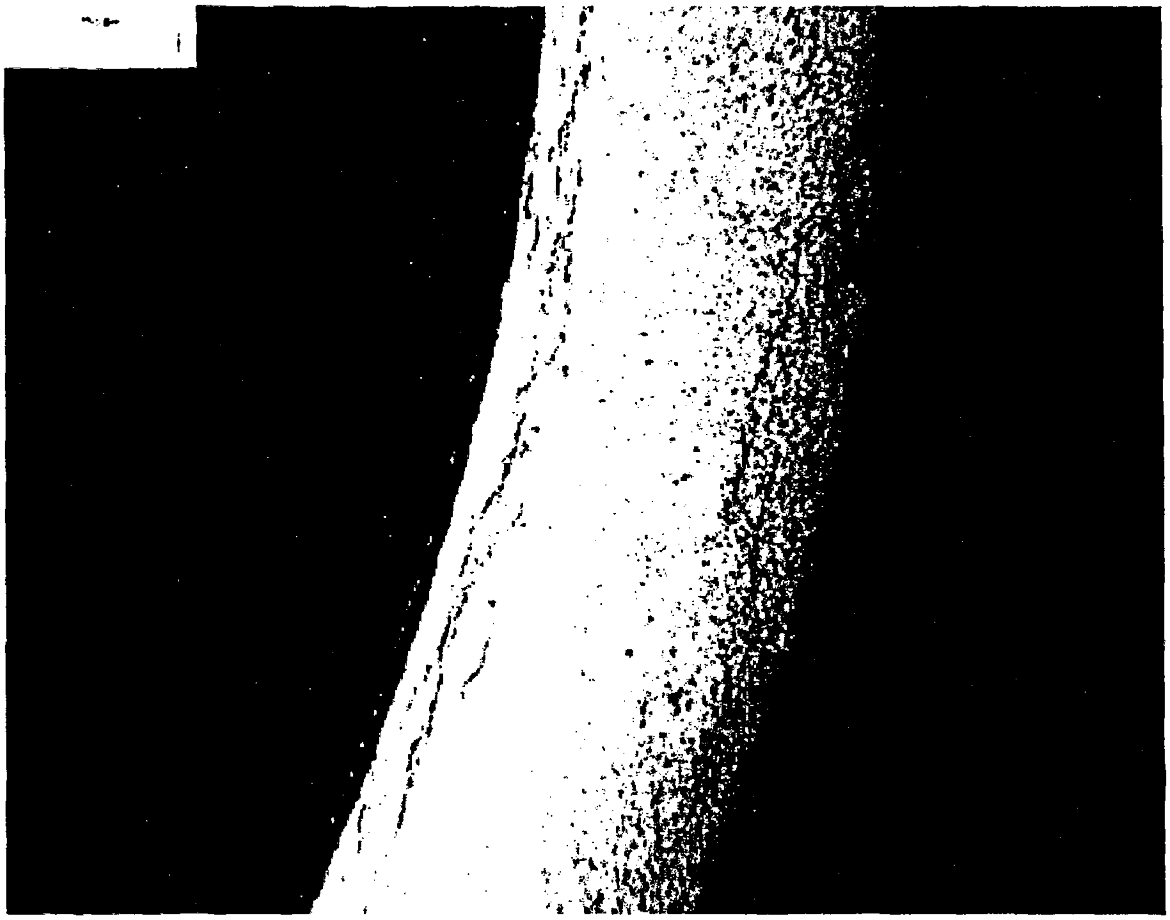

Fig. D.50 Cross-sectional view of Rod H9 cladding hydride morphology at approximate fuel midplane (area 2). Scale marker = 250 µm.
JPG file = 591C4 Hydrides Area 2.

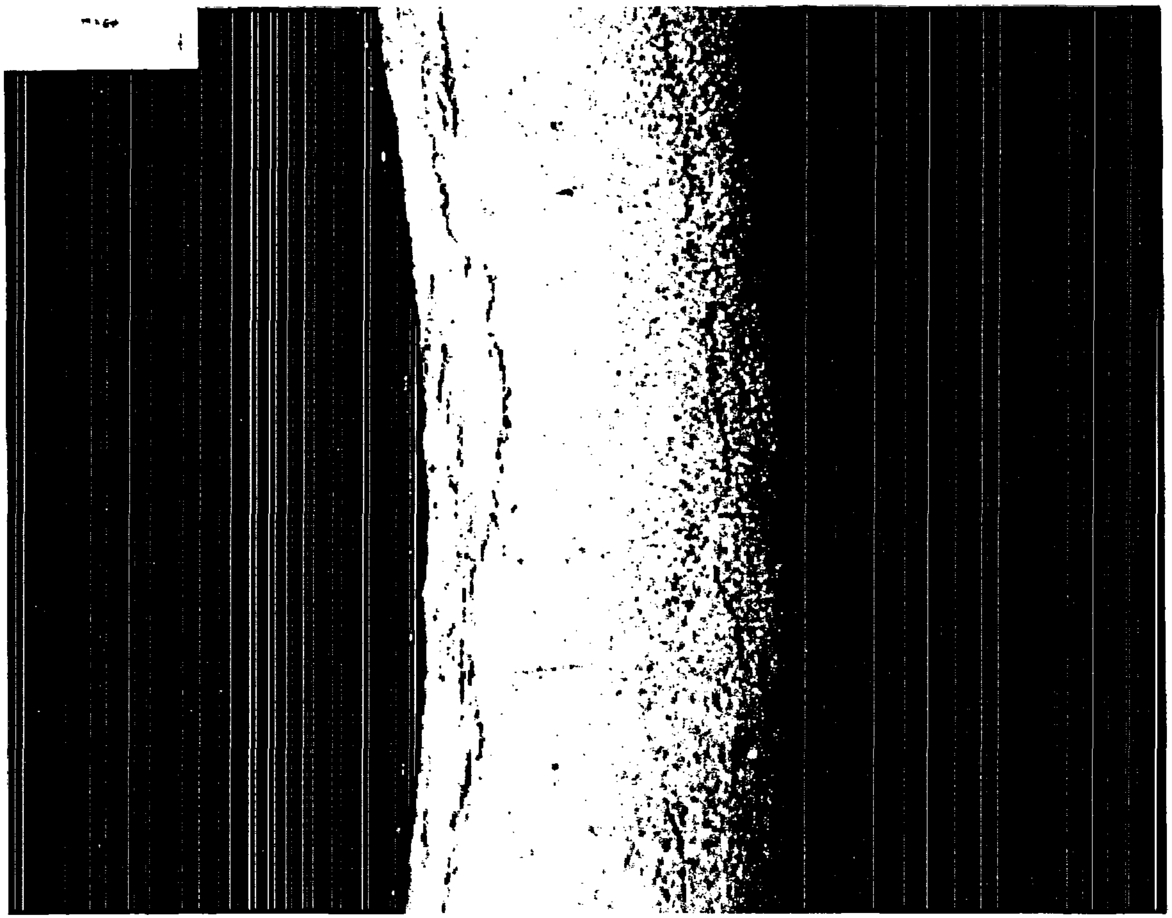

Fig. D.51 Cross-sectional view of Rod H9 cladding hydride morphology at approximate fuel midplane (area 3). Scale marker = 250 μm.
JPG file = 591C4 Hydrides Area 3.

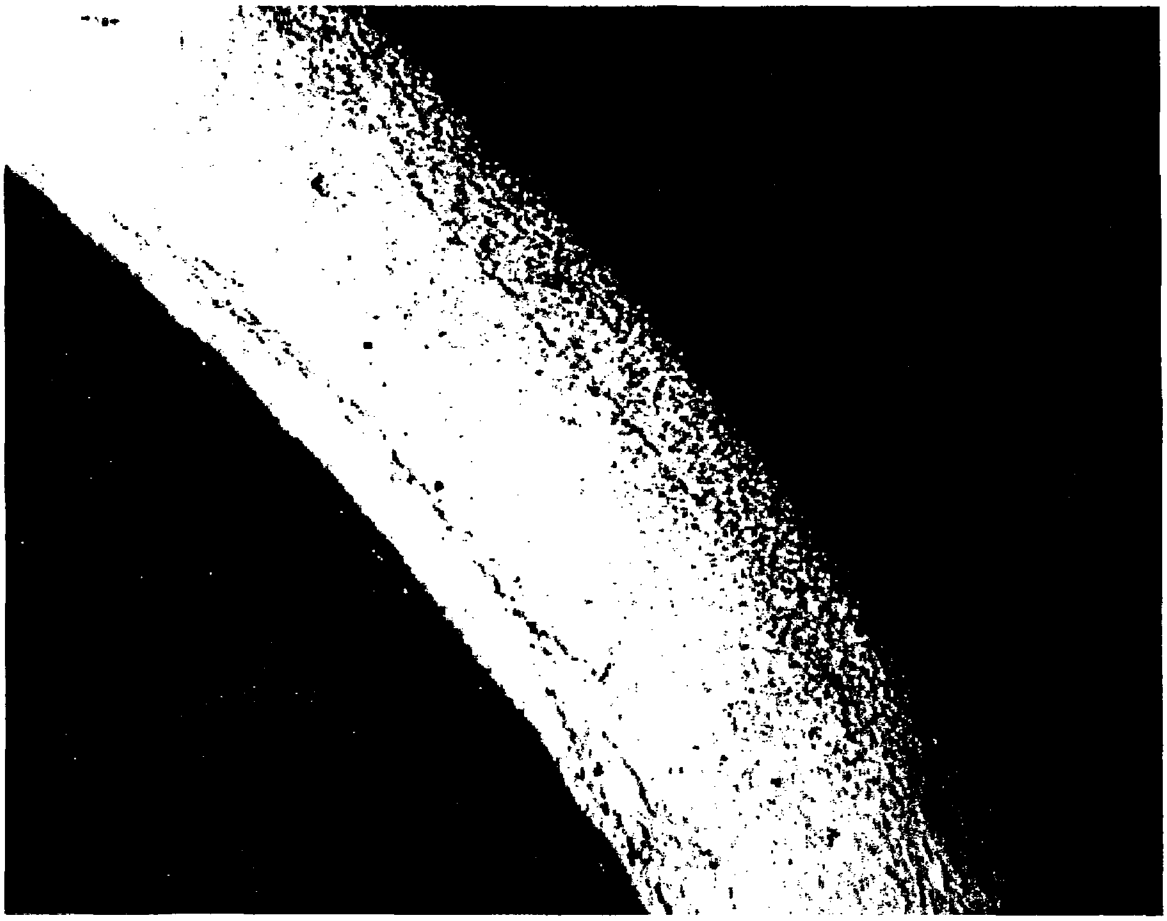

Fig. D.52 Cross-sectional view of Rod H9 cladding hydride morphology at approximate fuel midplane (area 4). Scale marker = 250 µm.
JPG file = 591C4 Hydrides Area 4.

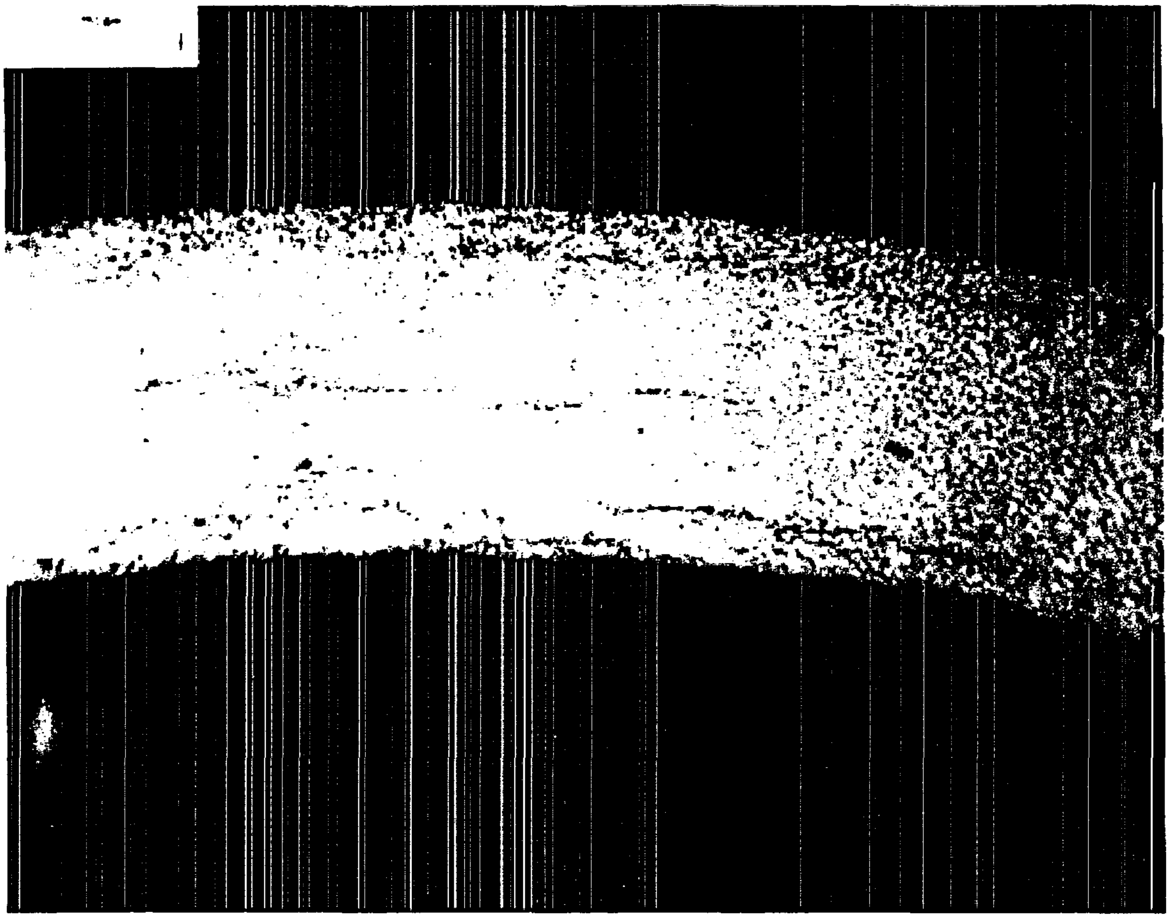

Fig. D.53 Cross-sectional view of Rod H9 cladding hydride morphology at approximate fuel midplane (area 5). Scale marker = 250 μm.
JPG file = 591C4 Hydrides Area 5.

Fig. D.54 Cross-sectional view of Rod H9 cladding hydride morphology at approximate fuel midplane (area 6). Scale marker = 250 µm.
JPG file = 591C4 Hydrides Area 6.

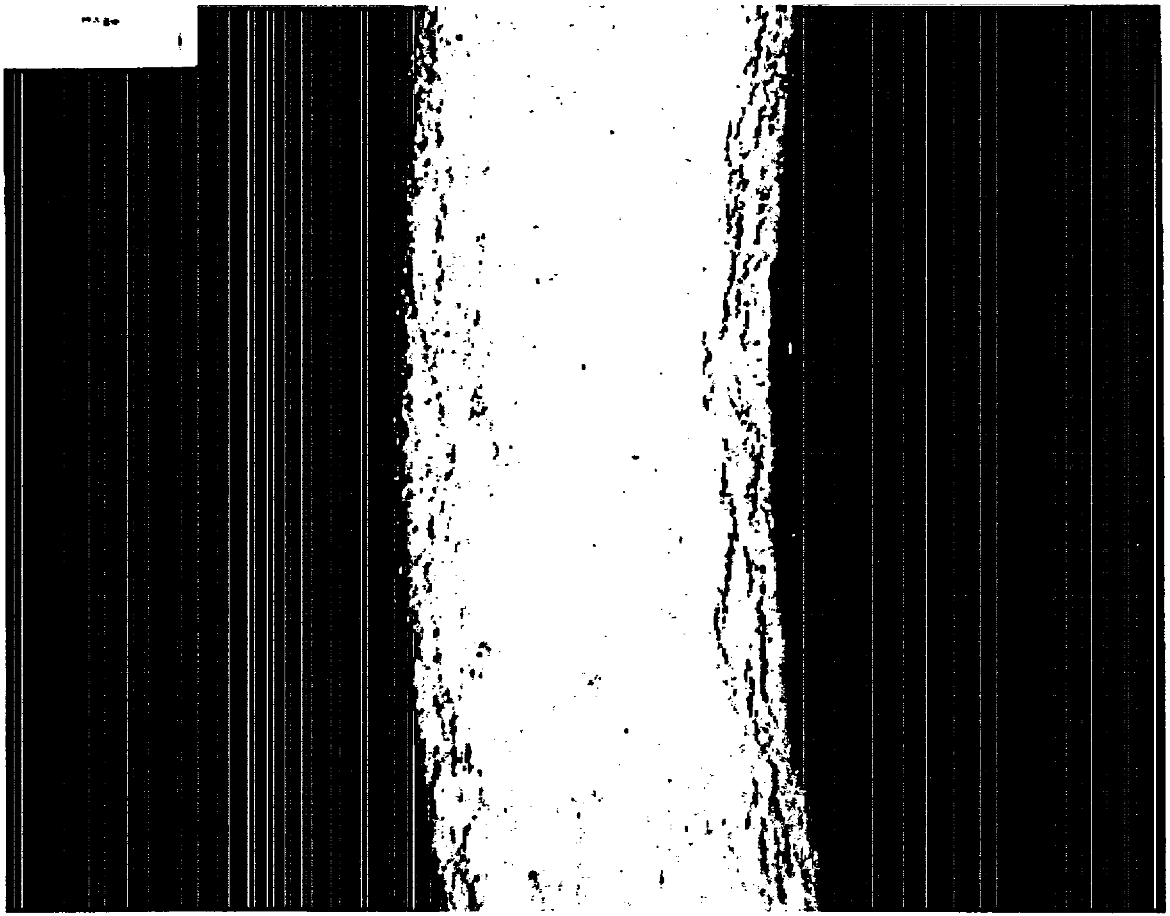

Fig. D.55 Cross-sectional view of Rod H9 cladding hydride morphology at approximate fuel midplane (area 7). Scale marker = 250 µm.
JPG file = 591C4 Hydrides Area 7.

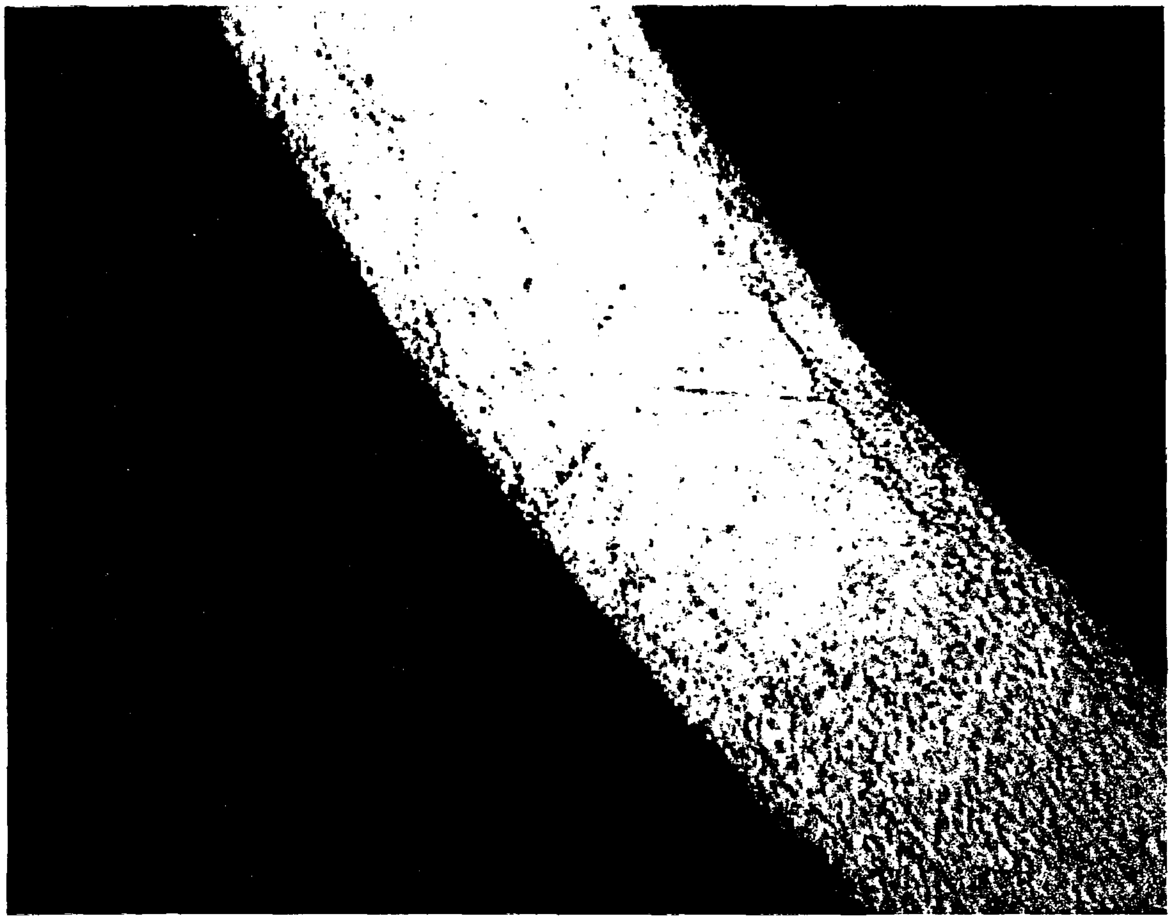

Fig. D.56 Cross-sectional view of Rod H9 cladding hydride morphology at approximate fuel midplane (area 8).
JPG file = 591C4 Hydrides Area 8.

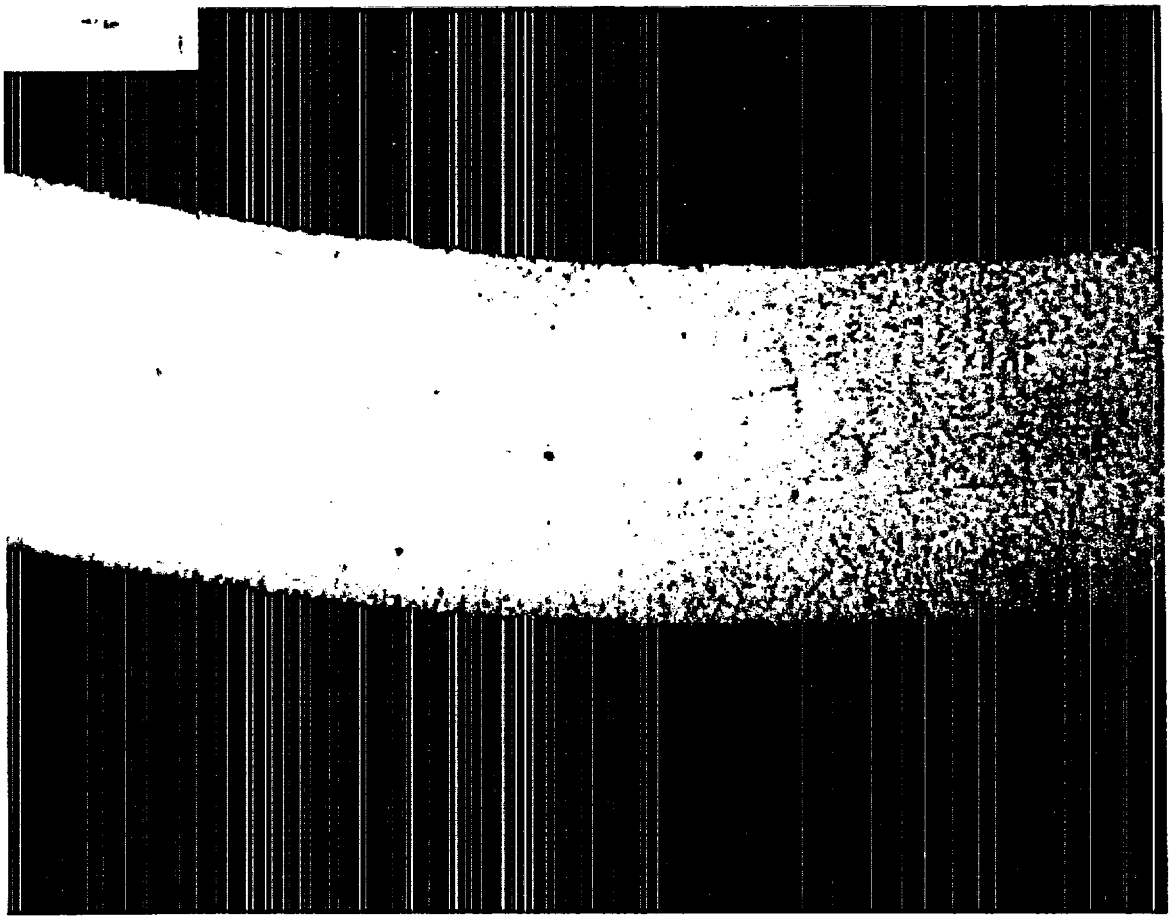

Fig. D.57 Cross-sectional view of Rod H9 cladding hydride morphology at ≈500 mm above fuel midplane (area 1). Scale marker = 250 μm.
JPG file = 591C12 Hydrides Area 1.

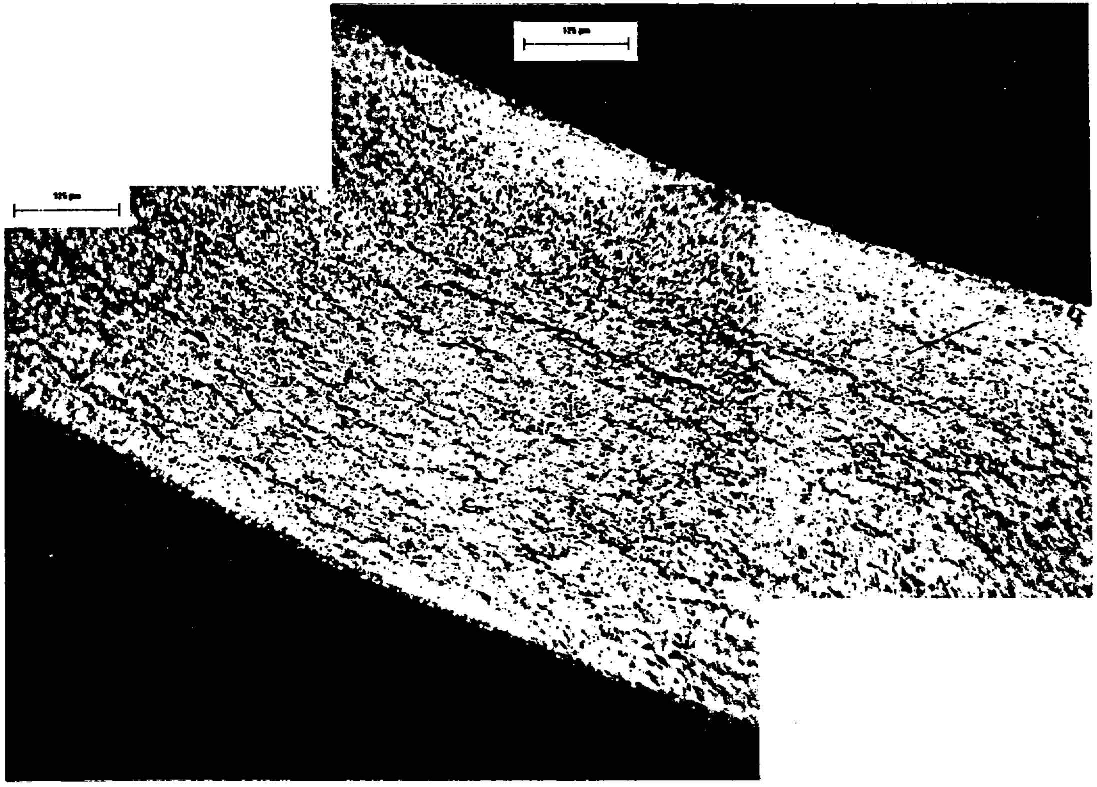

ET-701863, 864

Fig. D.58 Cross-sectional view of Rod H9 cladding hydride morphology at ≈500 mm above fuel midplane (area 2). Scale marker = 125 μm.
JPG file = 591C12 Hydrides Area 2.

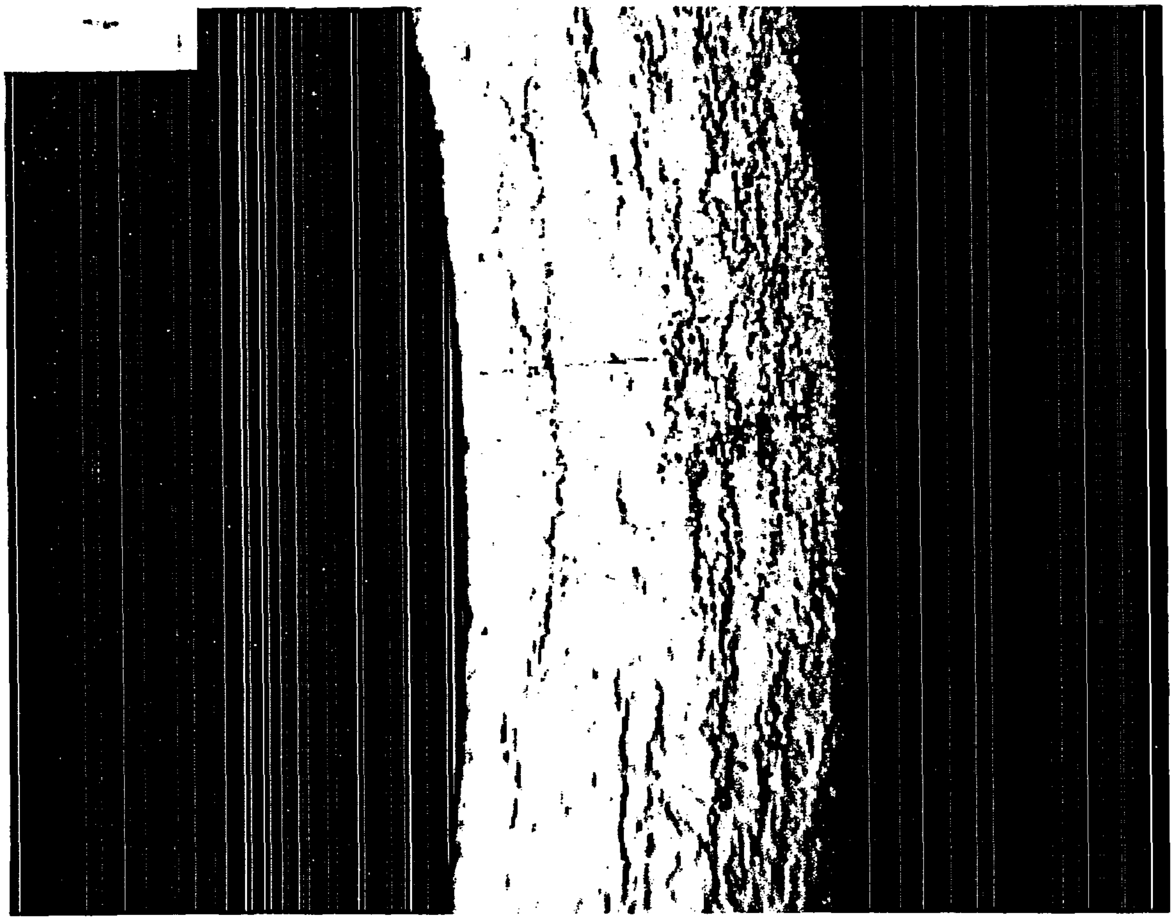

Fig. D.59 Cross-sectional view of Rod H9 cladding hydride morphology at ≈500 mm above fuel midplane (area 3). Scale marker = 250 μm.
JPG file = 591C12 Hydrides Area 3.

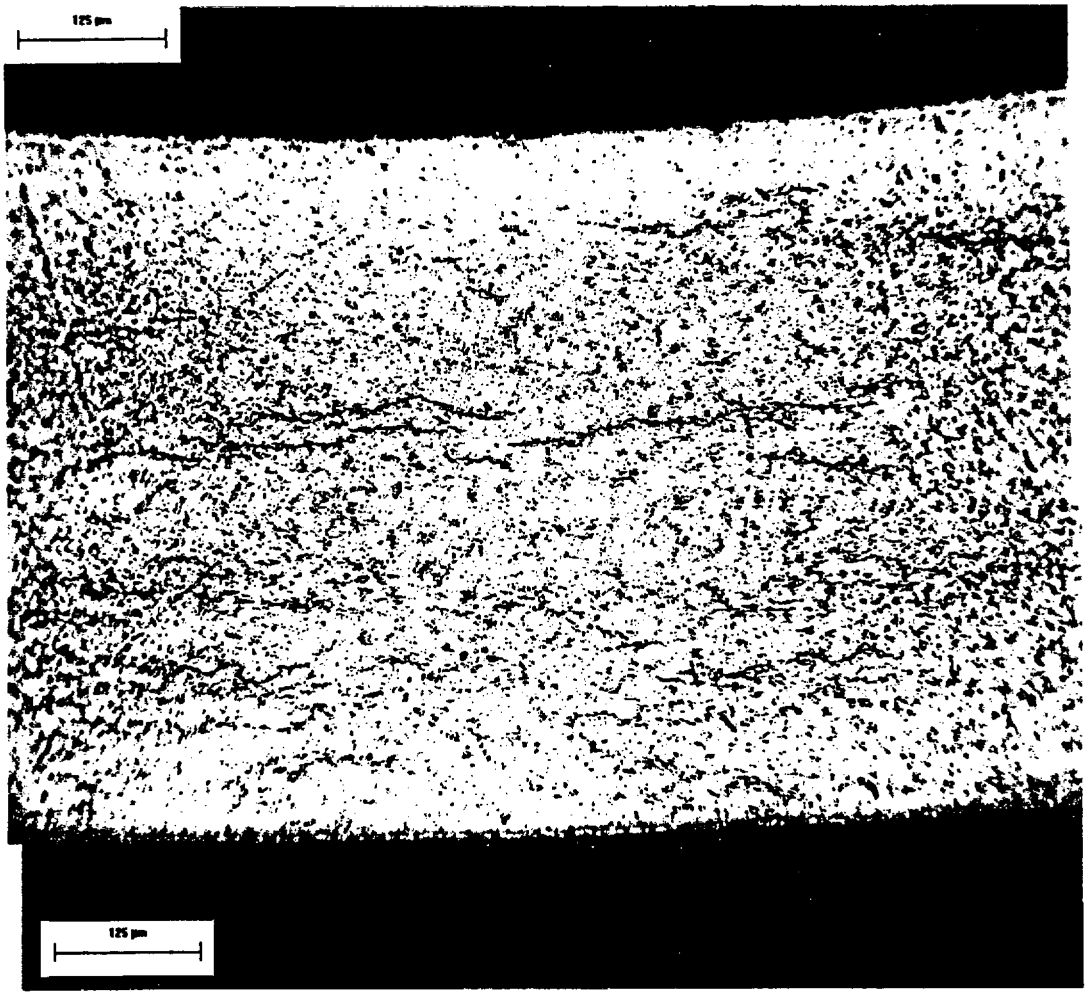

ET-701853, 854

Fig. D.60 Cross-sectional view of Rod H9 cladding hydride morphology at ≈500 mm above fuel midplane (area 4). Scale marker = 125 µm.
JPG file = 591C12 Hydrides Area 4.

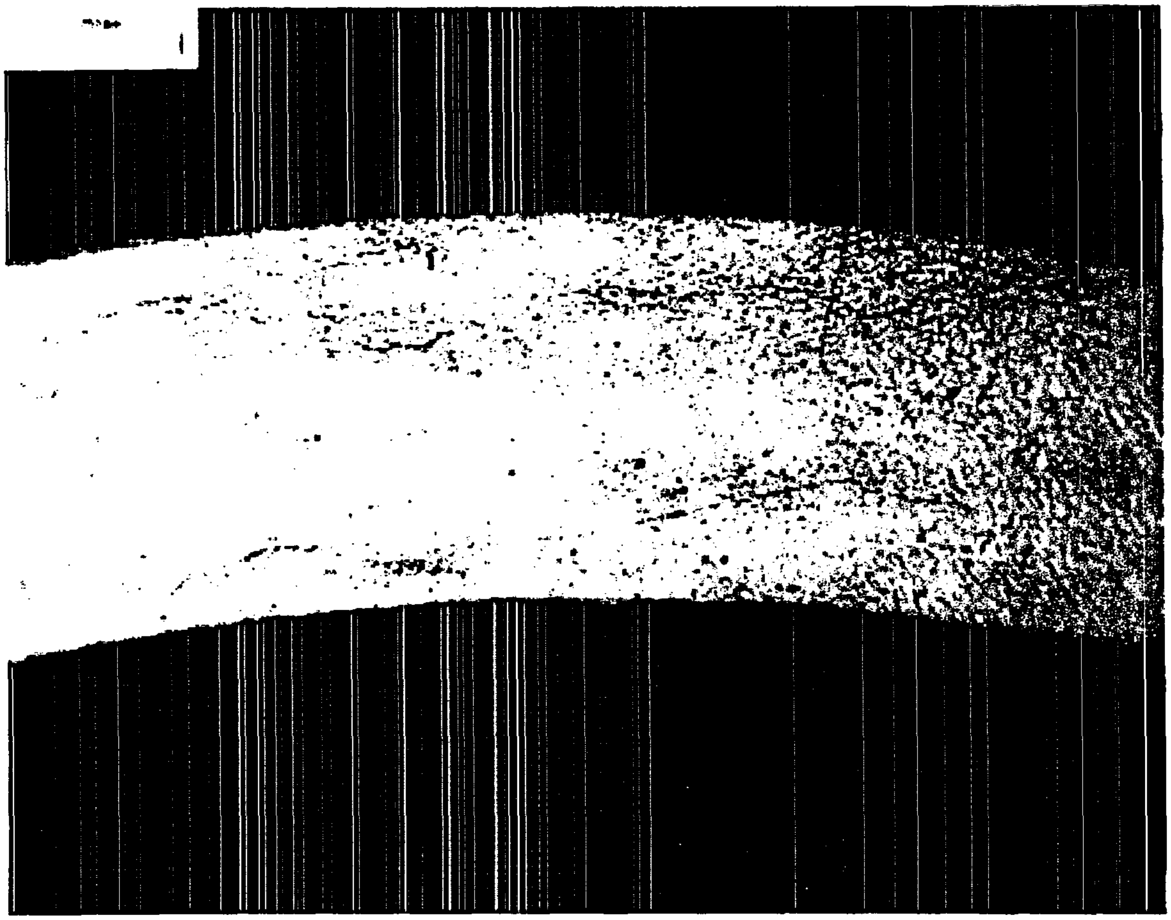

Fig. D.61 Cross-sectional view of Rod H9 cladding hydride morphology at ≈500 mm above fuel midplane (area 5). Scale marker = 250 μm.
JPG file = 591C12 Hydrides Area 5.

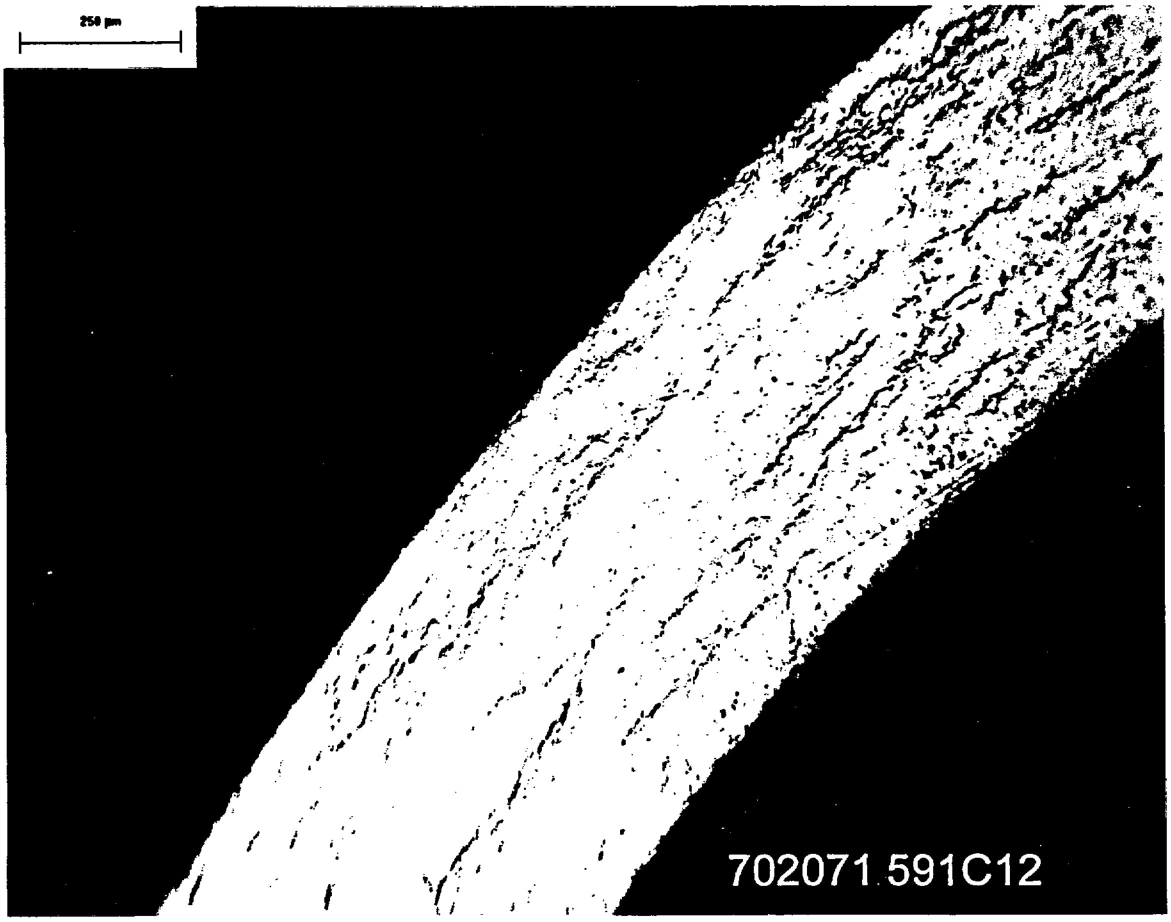

Fig. D.62 Cross-sectional view of Rod H9 cladding hydride morphology at ≈500 mm above fuel midplane (area 6). Scale marker = 250 µm.
JPG file = 591C12 Hydrides Area 6.

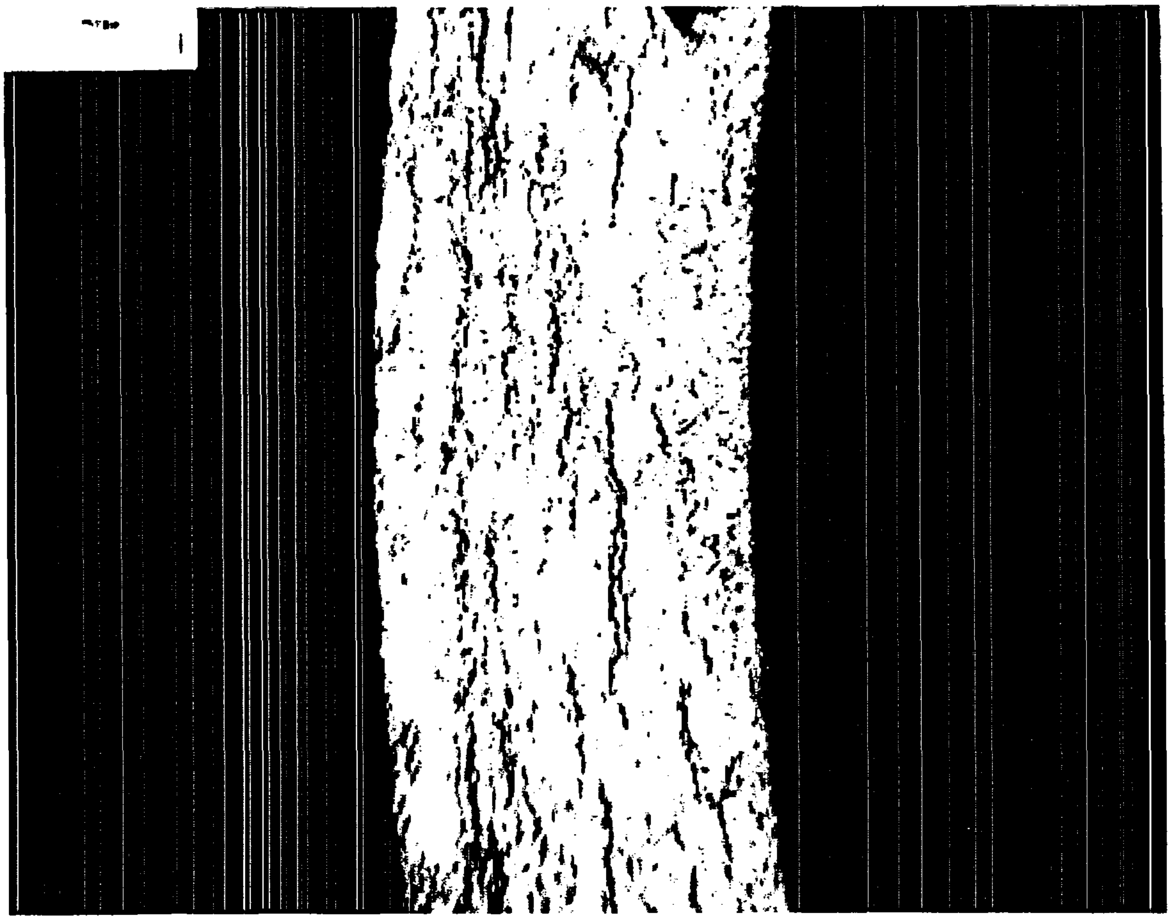

Fig. D.63 Cross-sectional view of Rod H9 cladding hydride morphology at ≈500 mm above fuel midplane (area 7). Scale marker = 250 μm.
JPG file = 591C12 Hydrides Area 7.

Fig. D.64 Cross-sectional view of Rod H9 cladding hydride morphology at ≈500 mm above fuel midplane (area 8). Scale marker = 250 µm.
JPG file = 591C12 Hydrides Area 8.

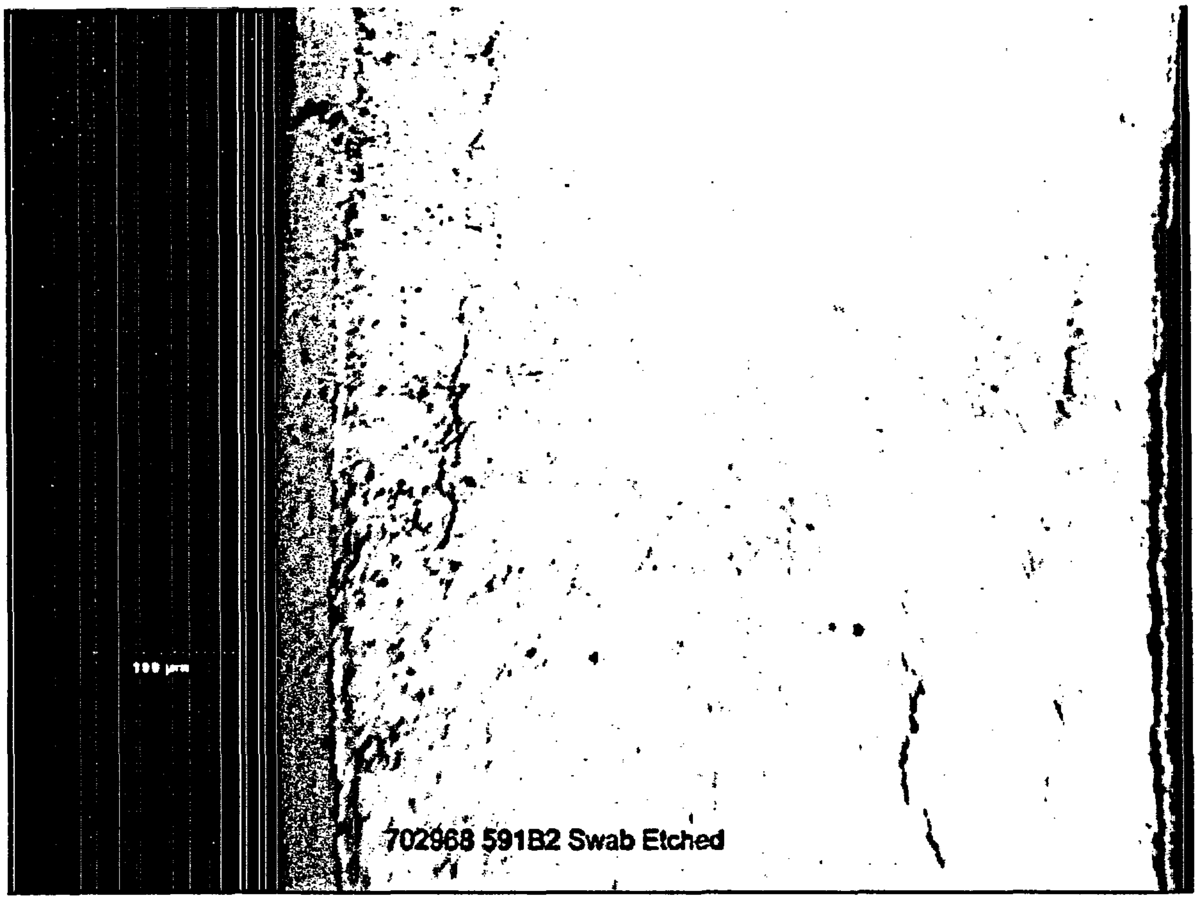

Fig. D.65 Cross-sectional view of Rod H9 cladding hydride morphology at ≈1000 mm above fuel midplane (area 1). Scale marker = 100 µm.
JPG file = 591B2 Hydrides Area 1.

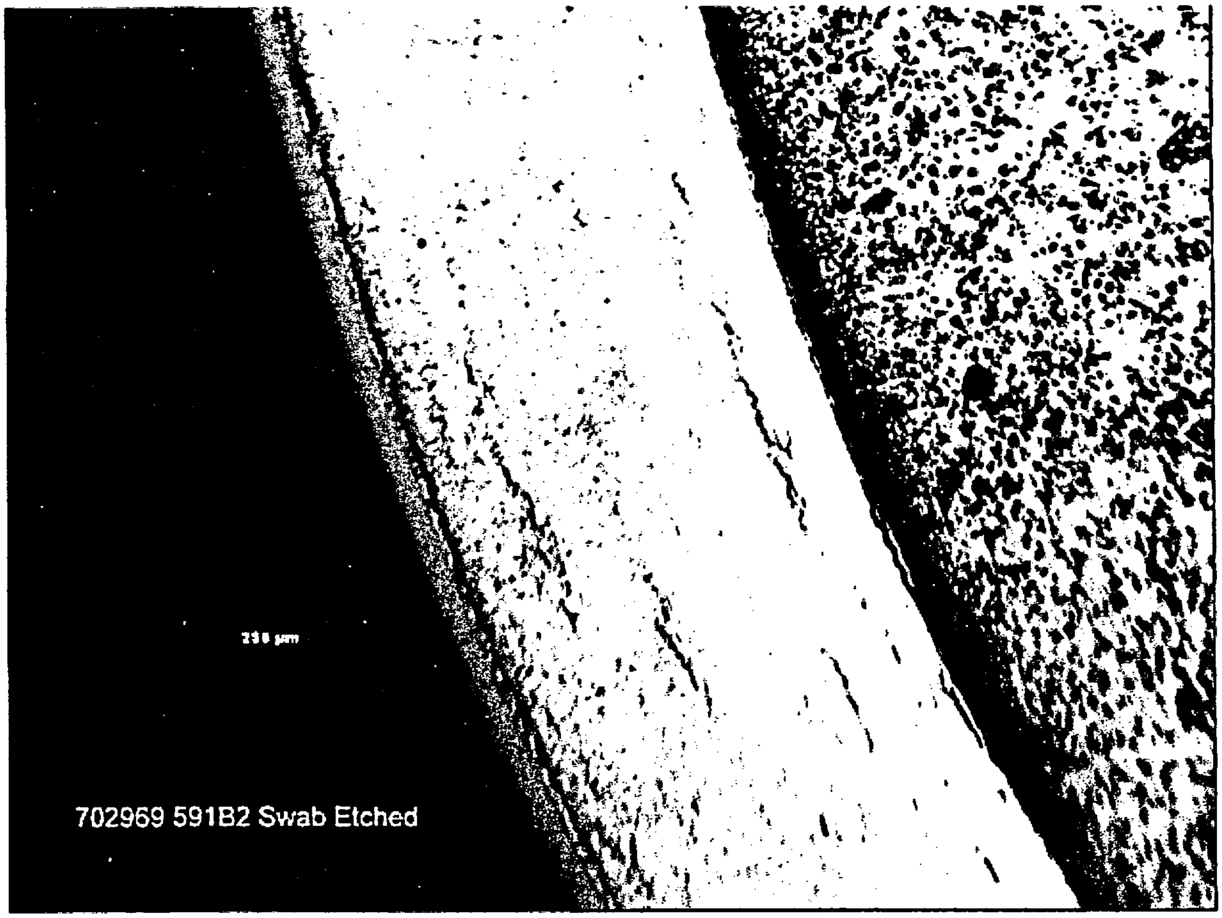

Fig. D.66 Cross-sectional view of Rod H9 cladding hydride morphology at ≈1000 mm above fuel midplane (area 2). Scale marker = 250 μm.
JPG file = 591B2 Hydrides Area 2.

Fig. D.67 Cross-sectional view of Rod H9 cladding hydride morphology at ≈1000 mm above fuel midplane (area 3). Scale marker = 250 µm.
JPG file = 591B2 Hydrides Area 3.

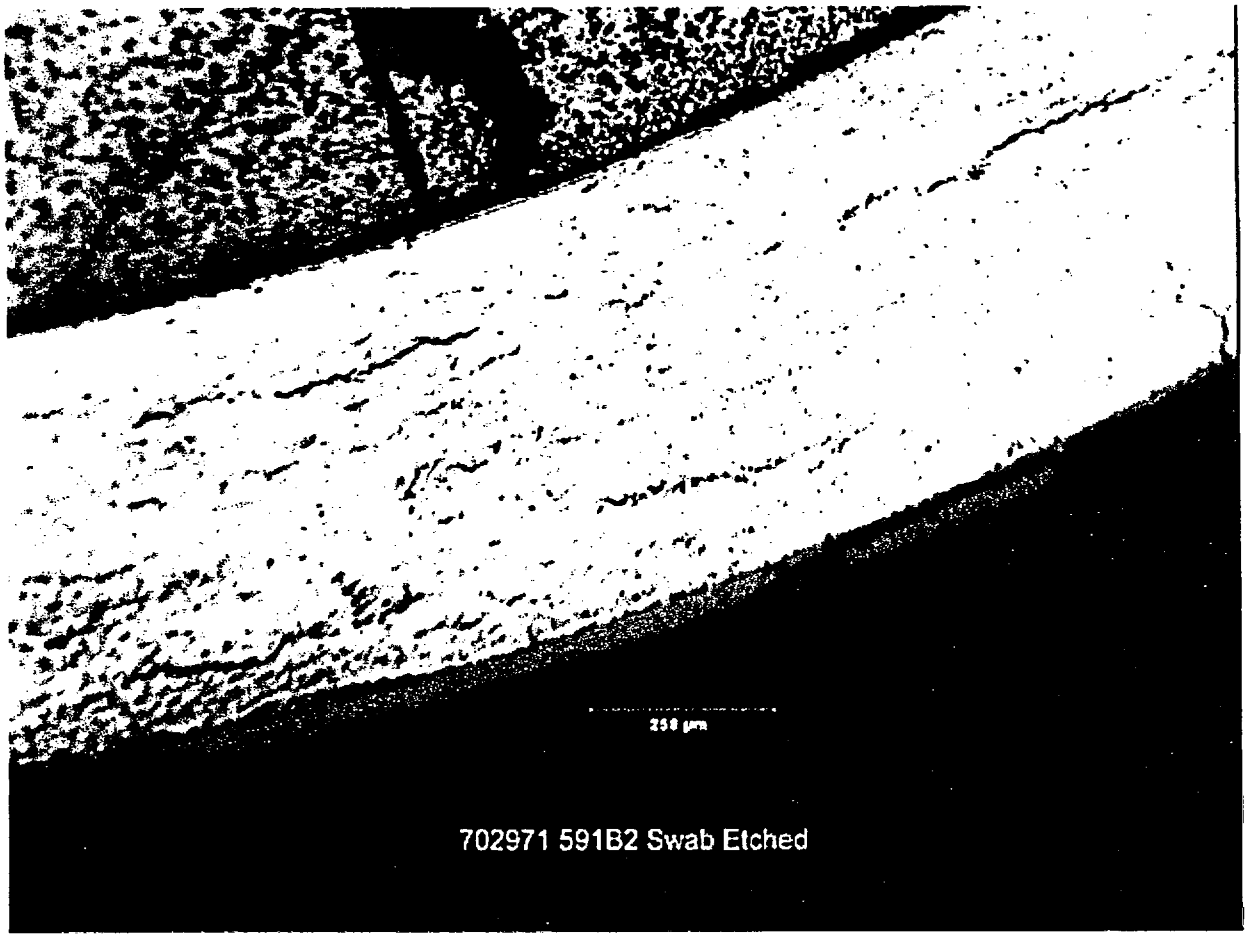

Fig. D.68 Cross-sectional view of Rod H9 cladding hydride morphology at ≈1000 mm above fuel midplane (area 4). Scale marker = 250 µm.
JPG file = 591B2 Hydrides Area 4.

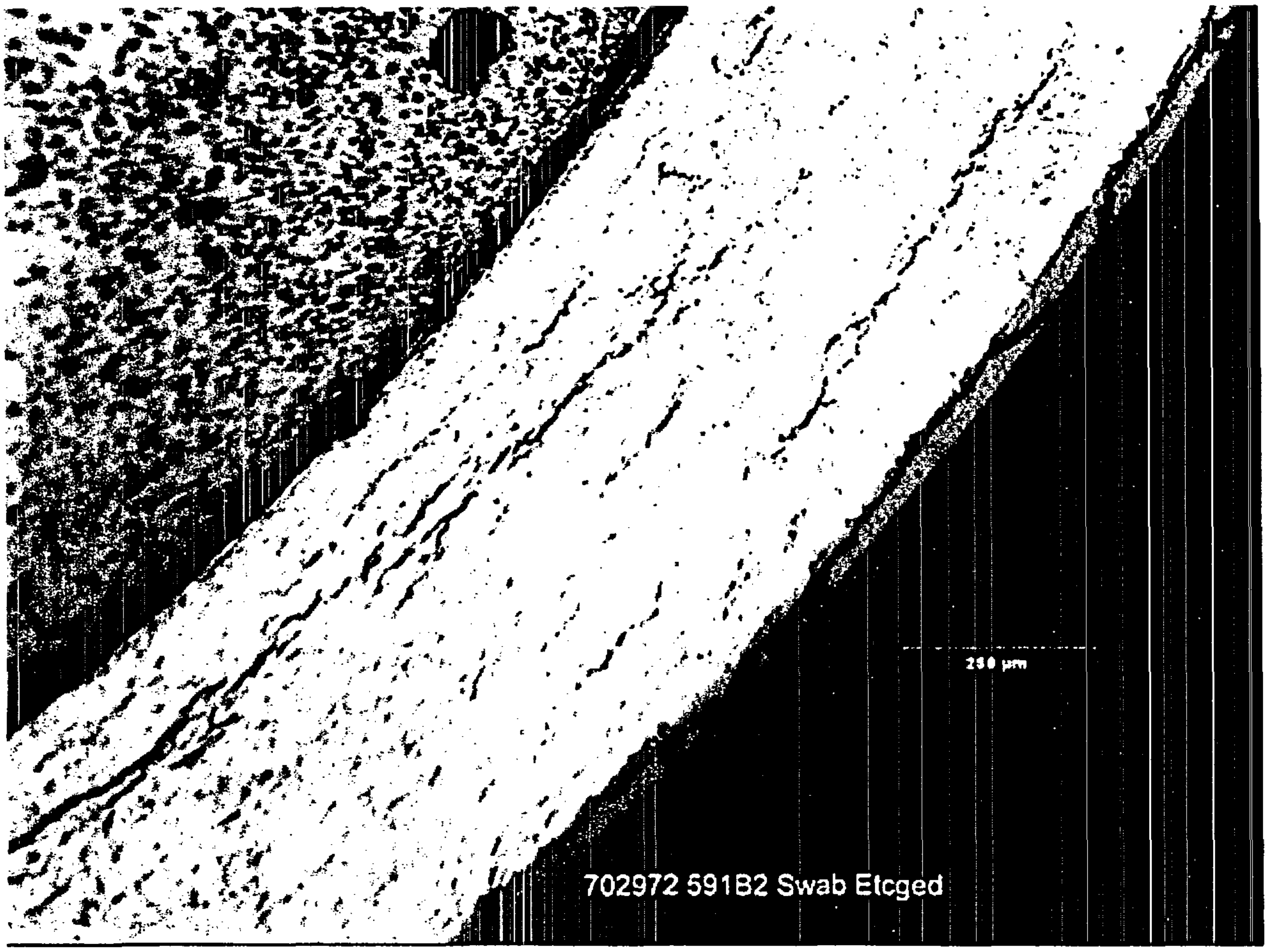

Fig. D.69 Cross-sectional view of Rod H9 cladding hydride morphology at ≈1000 mm above fuel midplane (area 5). Scale marker = 250 µm.
JPG file = 591B2 Hydrides Area 5.

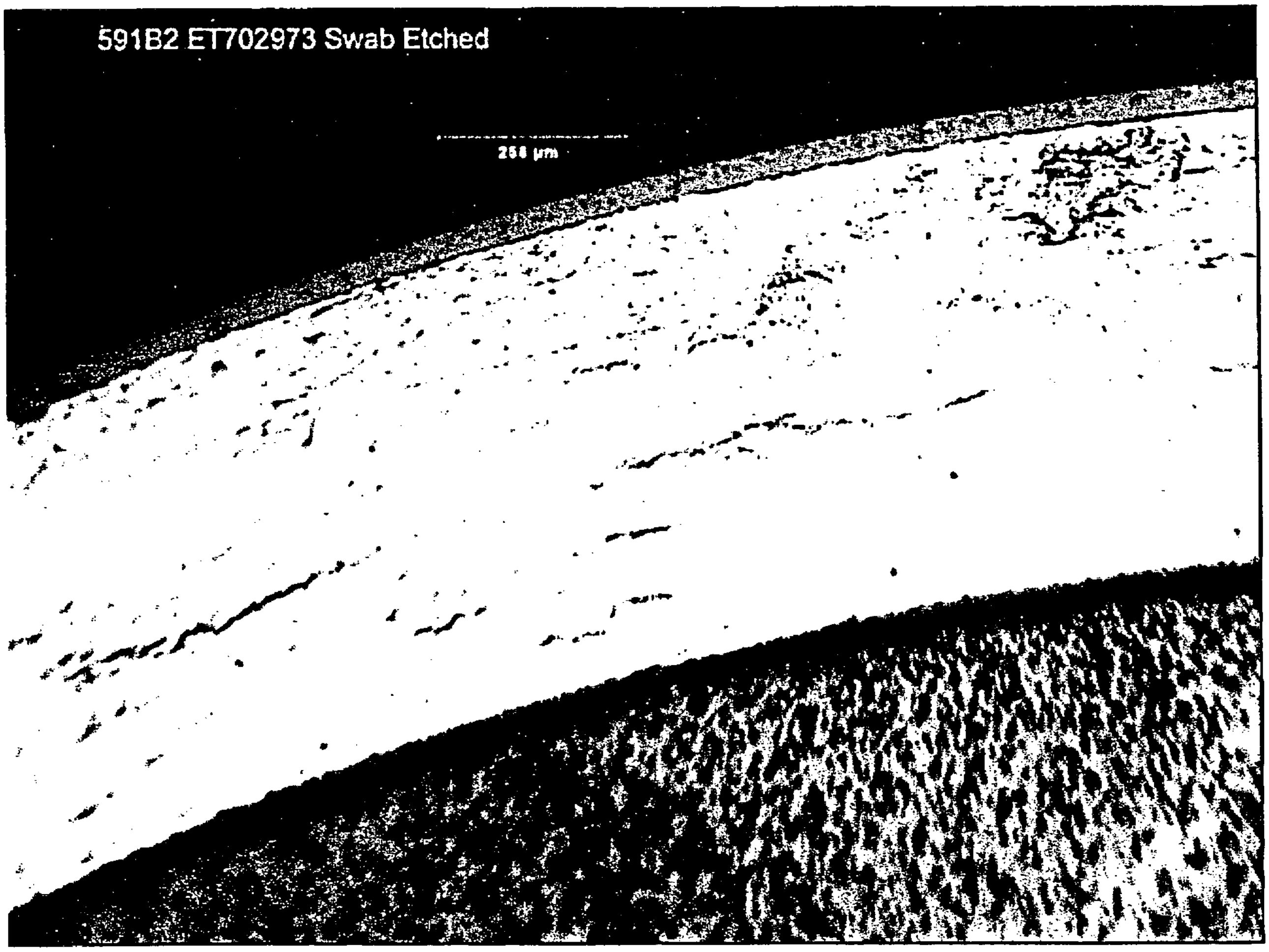

Fig. D.70 Cross-sectional view of Rod H9 cladding hydride morphology at ≈1000 mm above fuel midplane (area 6). Scale marker = 250 µm.
JPG file = 591B2 Hydrides Area 6.

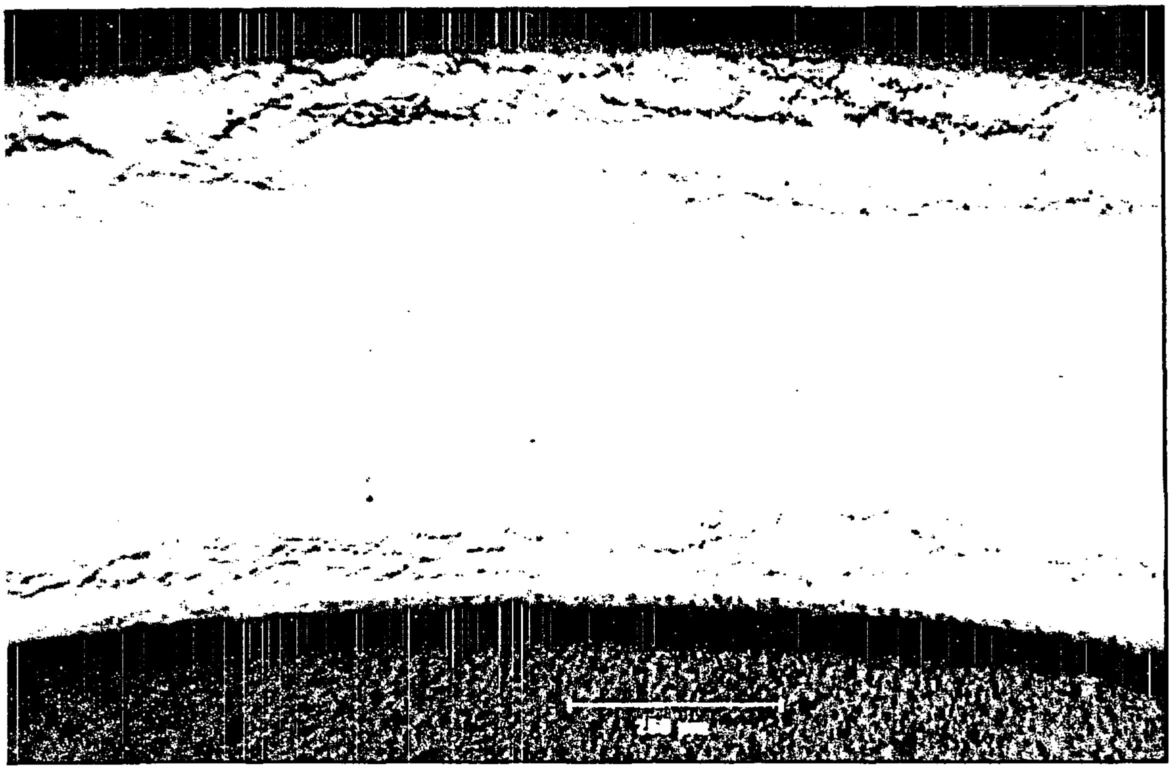

Fig. D.71 Cross-sectional view of Rod G6 cladding hydride morphology at the approximate fuel midplane (area 1). Scale marker = 250 μm. JPG file = 592C4 Hydrides Area 1. ET703343.

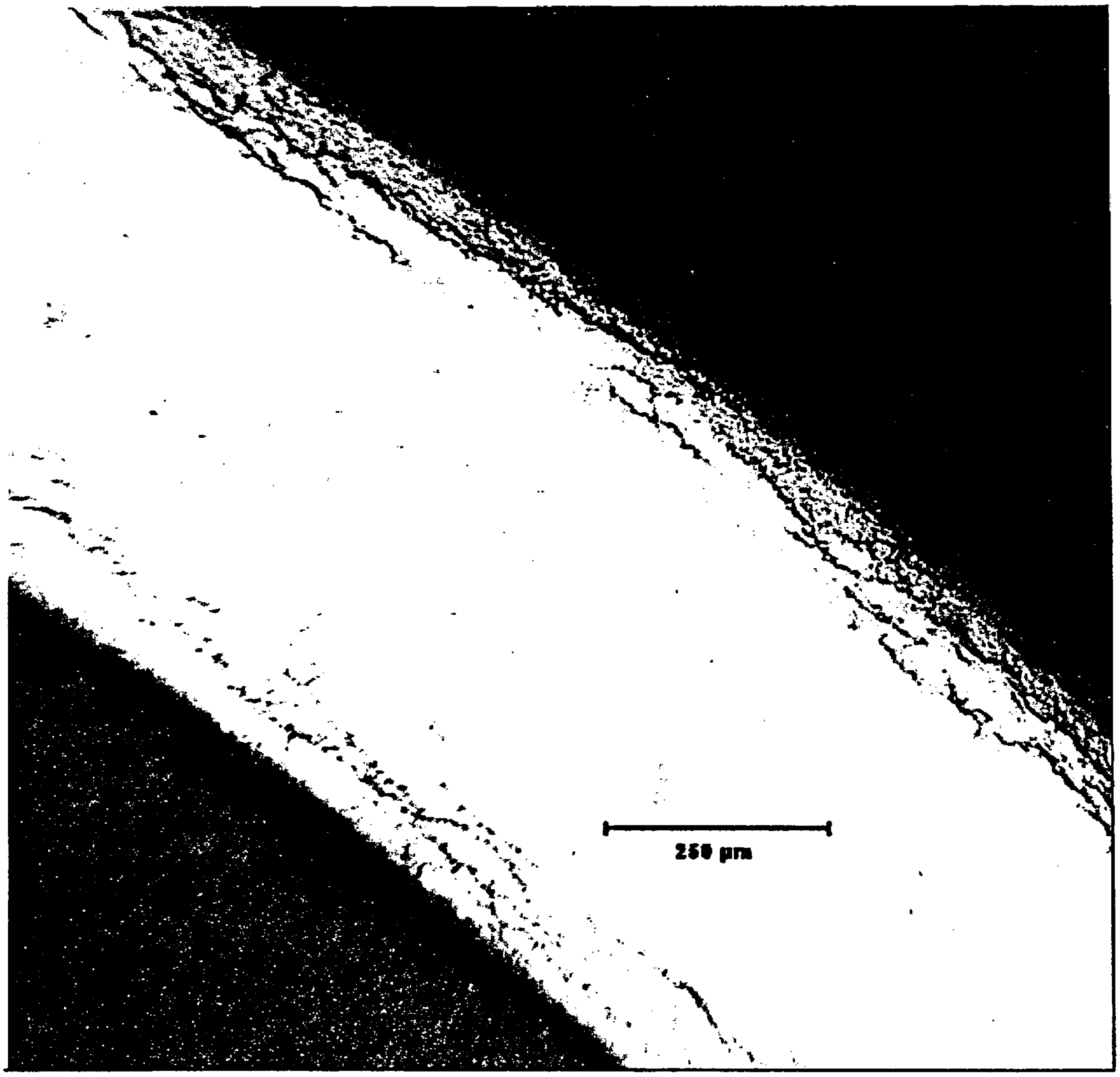

Fig. D.72 Cross-sectional view of Rod G6 cladding hydride morphology at the approximate fuel midplane (area 2). Scale marker = 250 μm. JPG file = 592C4 Hydrides Area 2. ET703344.

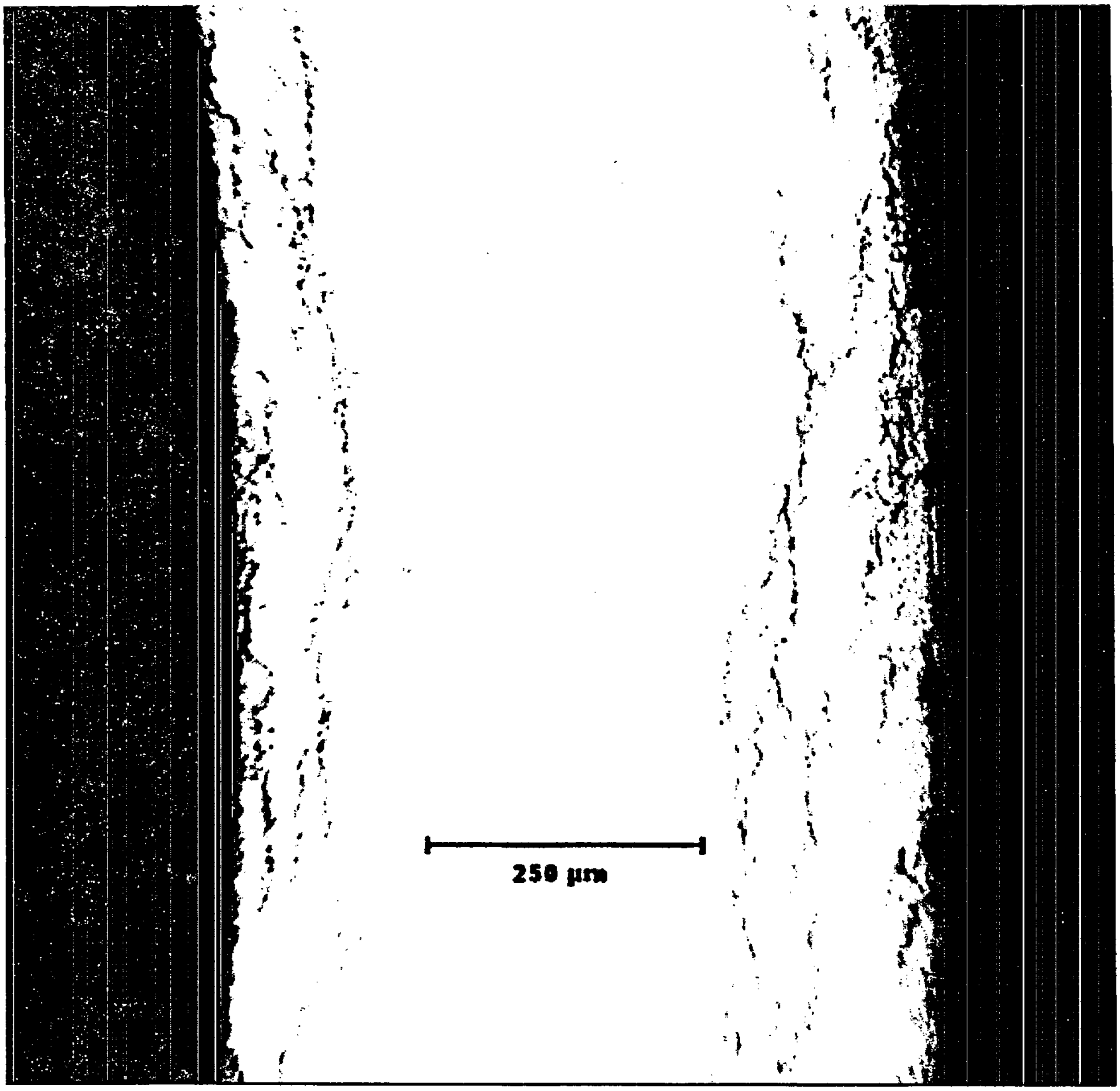

Fig. D.73 Cross-sectional view of Rod G6 cladding hydride morphology at approximate fuel midplane (area 3). Scale marker = 250 µm.
JPG file = 592C4 Hydrides Area 3. ET703345.

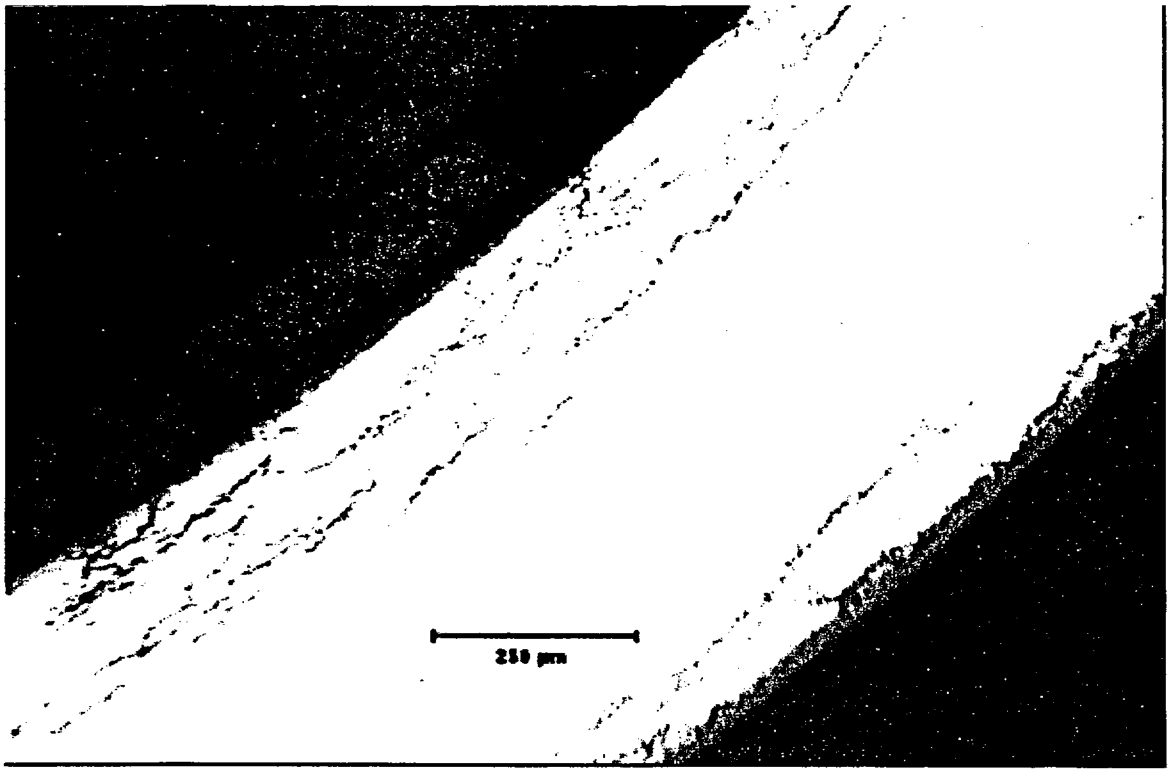

Fig. D.74 Cross-sectional view of Rod G6 cladding hydride morphology at approximate fuel midplane (area 4). Scale marker = 250 μm.
JPG file = 592C4 Hydrides Area 4. ET703346.

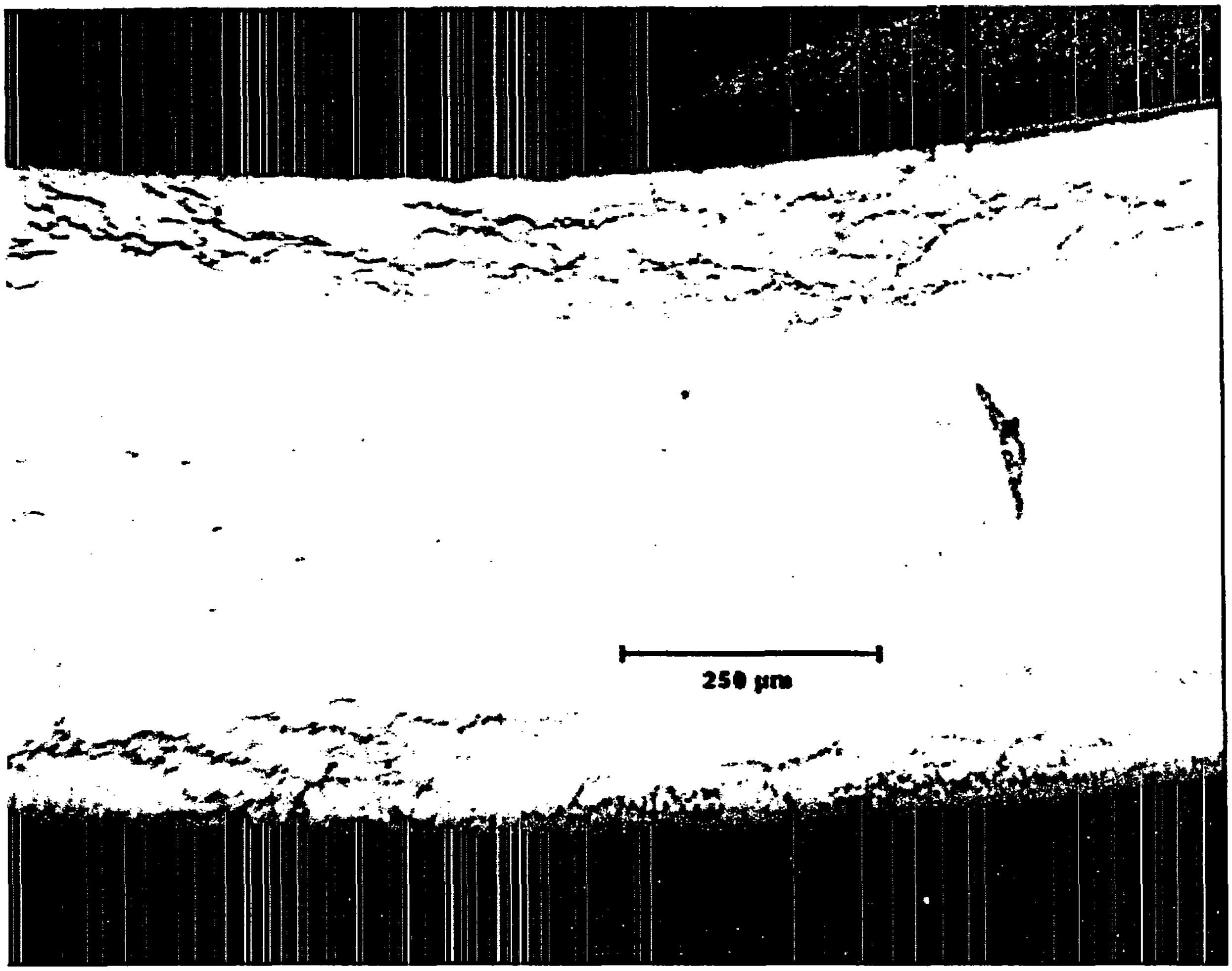

Fig. D.75 Cross-sectional view of Rod G6 cladding hydride morphology at approximate fuel midplane (area 5). Scale marker = 250 μm. JPG file = 592C4 Hydrides Area 5. ET703347.

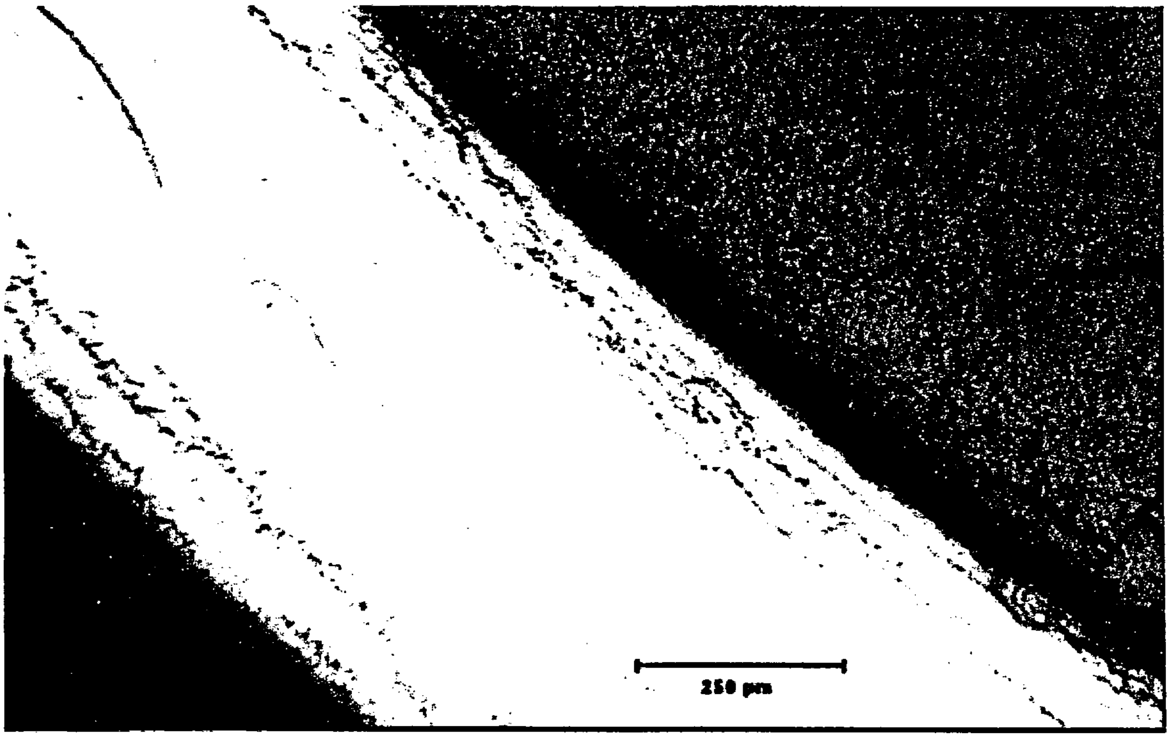

Fig. D.76 Cross-sectional view of Rod G6 cladding hydride morphology at approximate fuel midplane (area 6). Scale marker = 250 µm. JPG file = 592C4 Hydrides Area 6. ET703348.

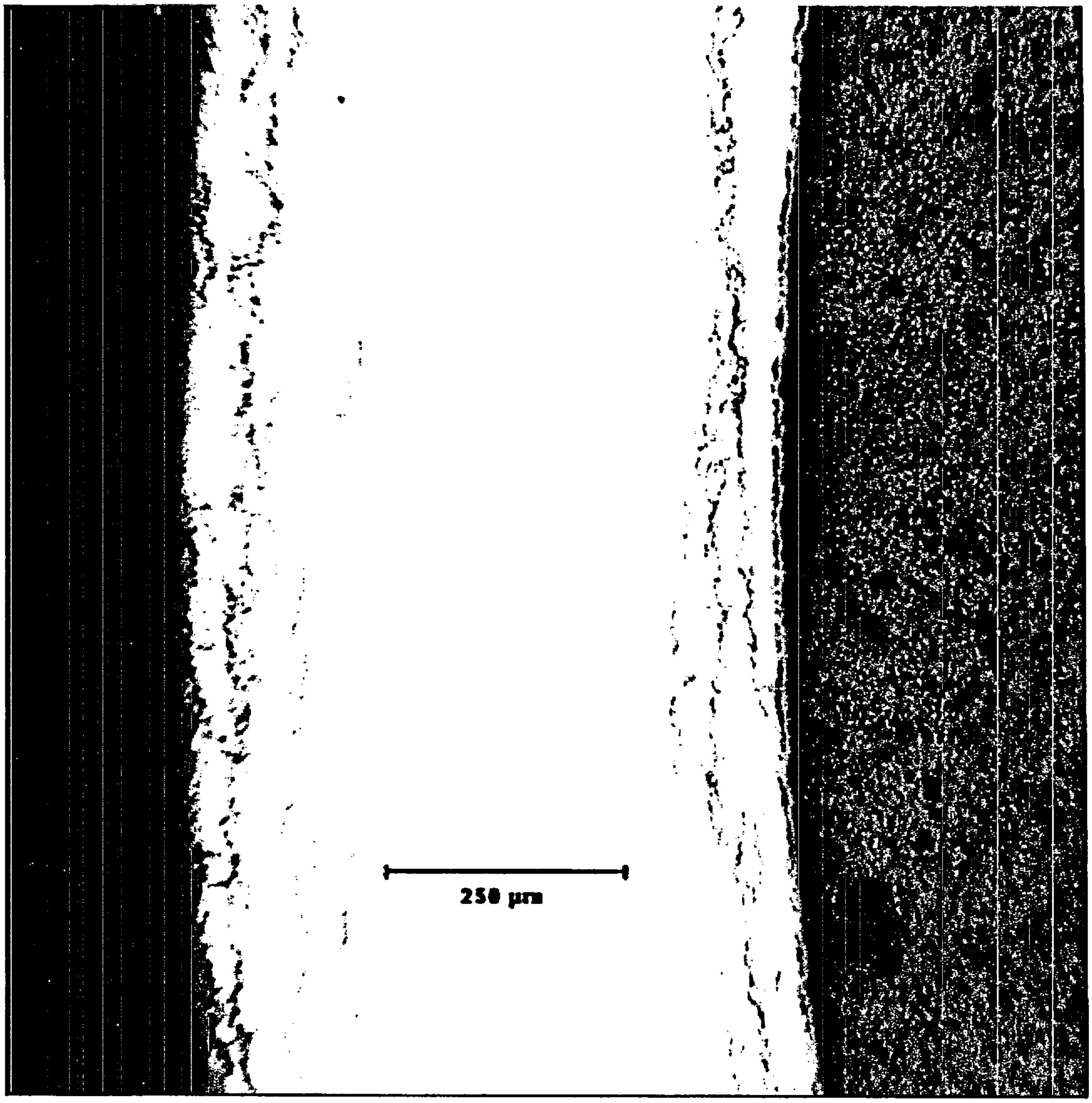

Fig. D.77 Cross-sectional view of Rod G6 cladding hydride morphology at approximate fuel midplane (area 7). Scale marker = 250 µm. JPG file = 592C4 Hydrides Area 7. ET703349.

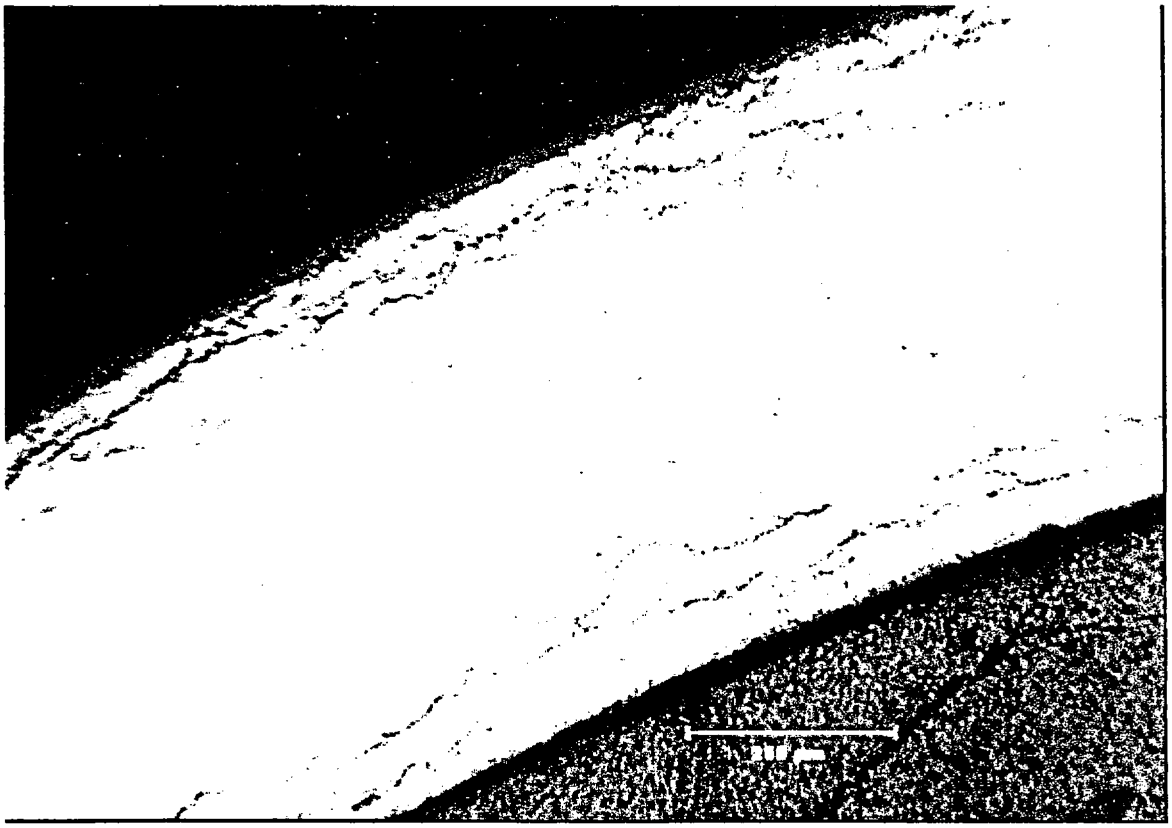

Fig. D.78 Cross-sectional view of Rod G6 cladding hydride morphology at approximate fuel midplane (area 8). Scale marker = 250 µm. JPG file = 592C4 Hydrides Area 8. ET703350.

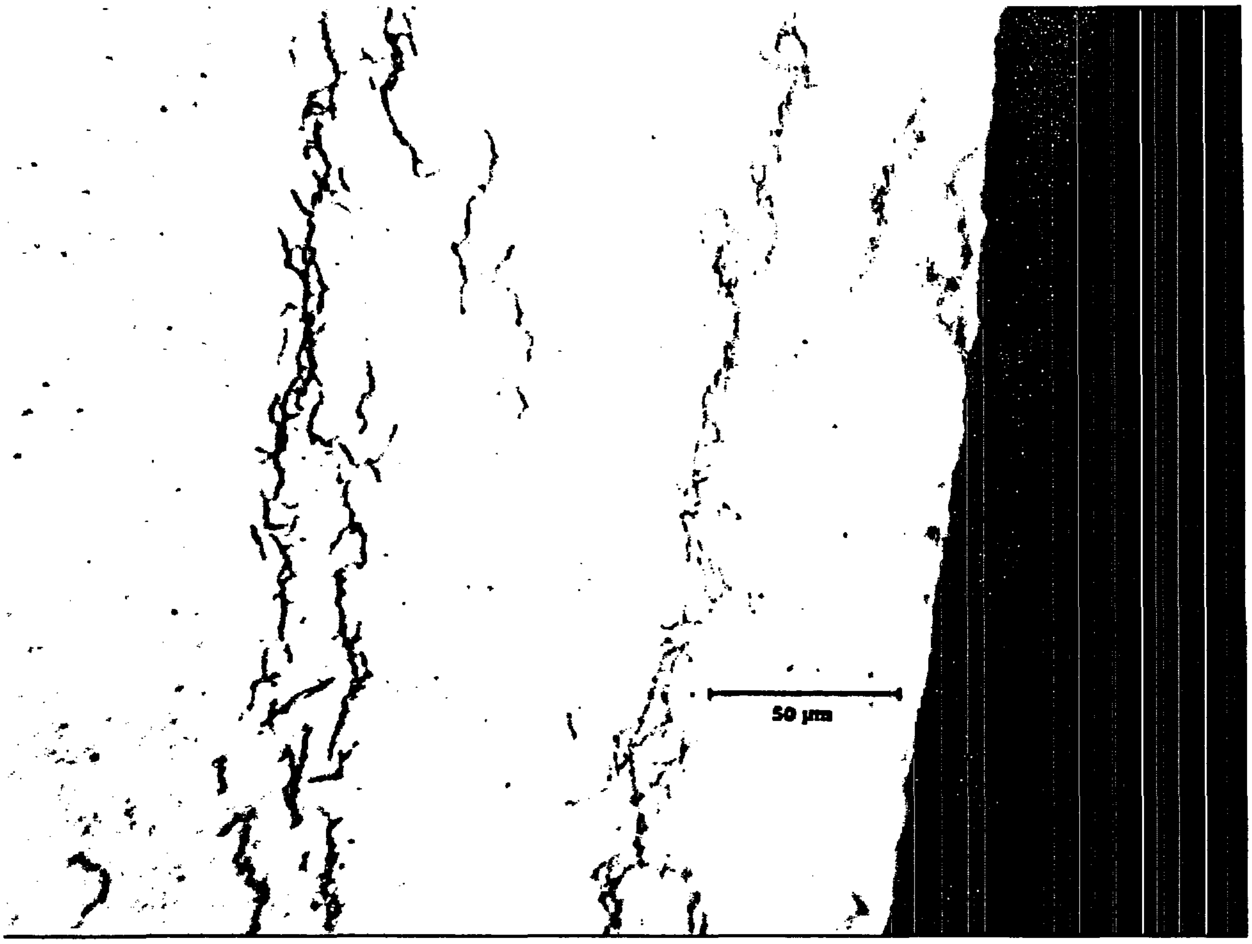

Fig. D.79a Hydride orientation/distribution at area 5 within Rod G6 cladding at the approximate fuel midplane position. High magnification photomicrograph near the cladding outer surface.
JPG file = 592C4 etched OD hydrides. ET703374.

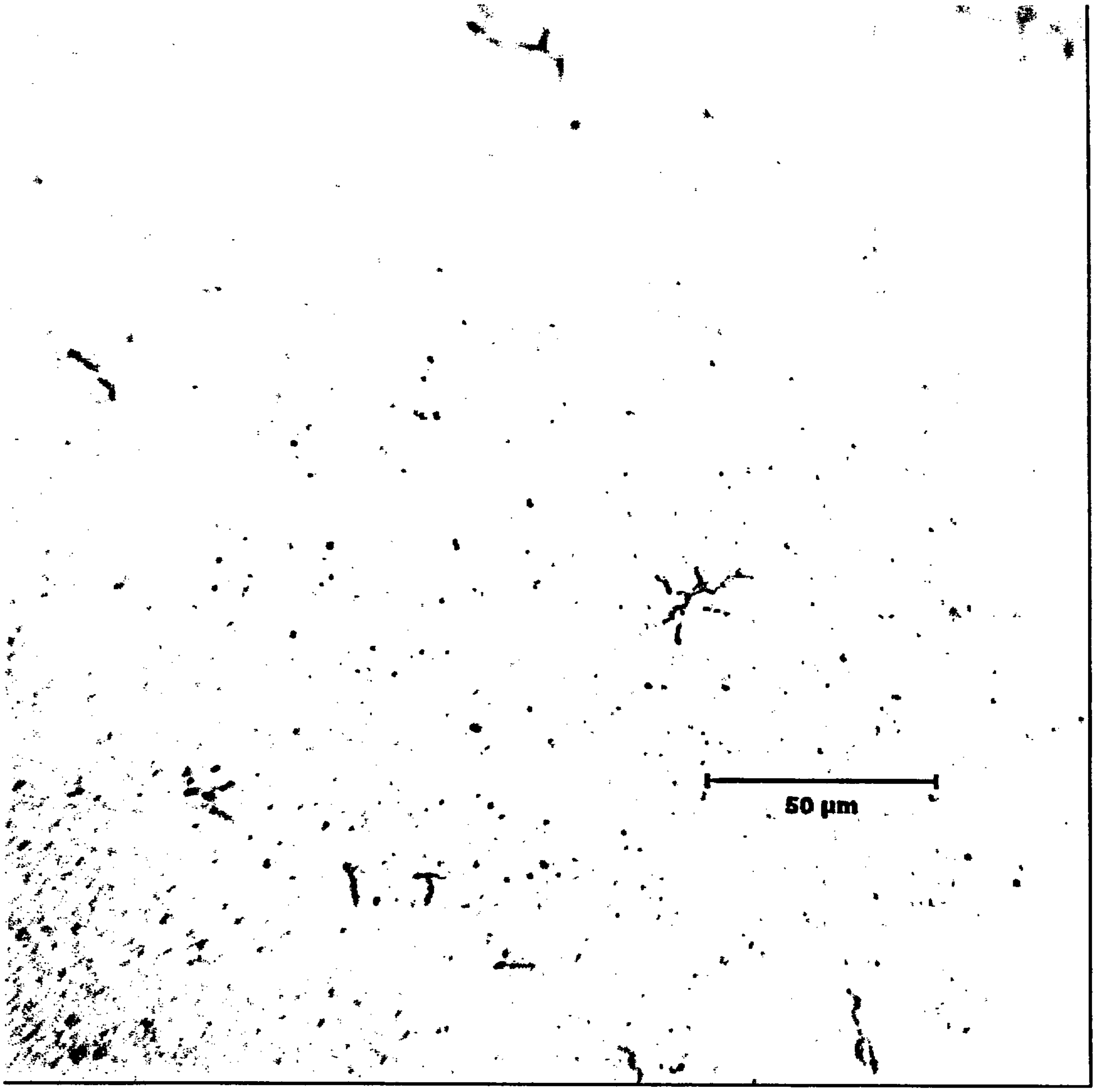

Fig. D.79b. Hydride orientation/distribution within Rod G6 cladding at the approximate fuel midplane position. High magnification photomicrograph near the cladding middle surface.
JPG file = 592C4 etched crowfeet1. ET703367.

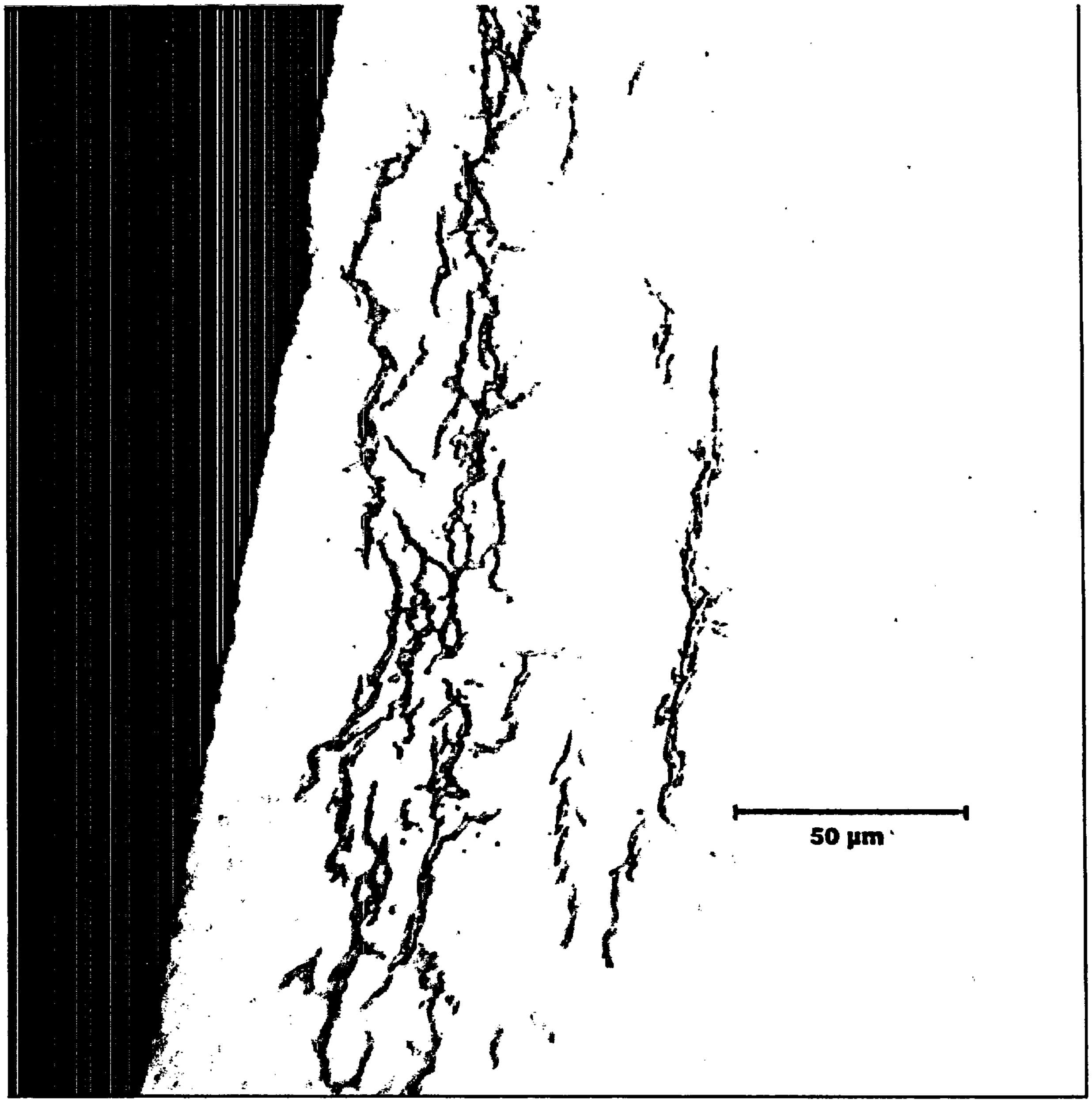

Fig. D.79c. Hydride orientation/distribution within Rod G6 cladding at the approximate fuel midplane (area 5). High magnification photomicrograph near the cladding inner surface.
JPG file = 592C4 etched ID hydrides. ET703373.

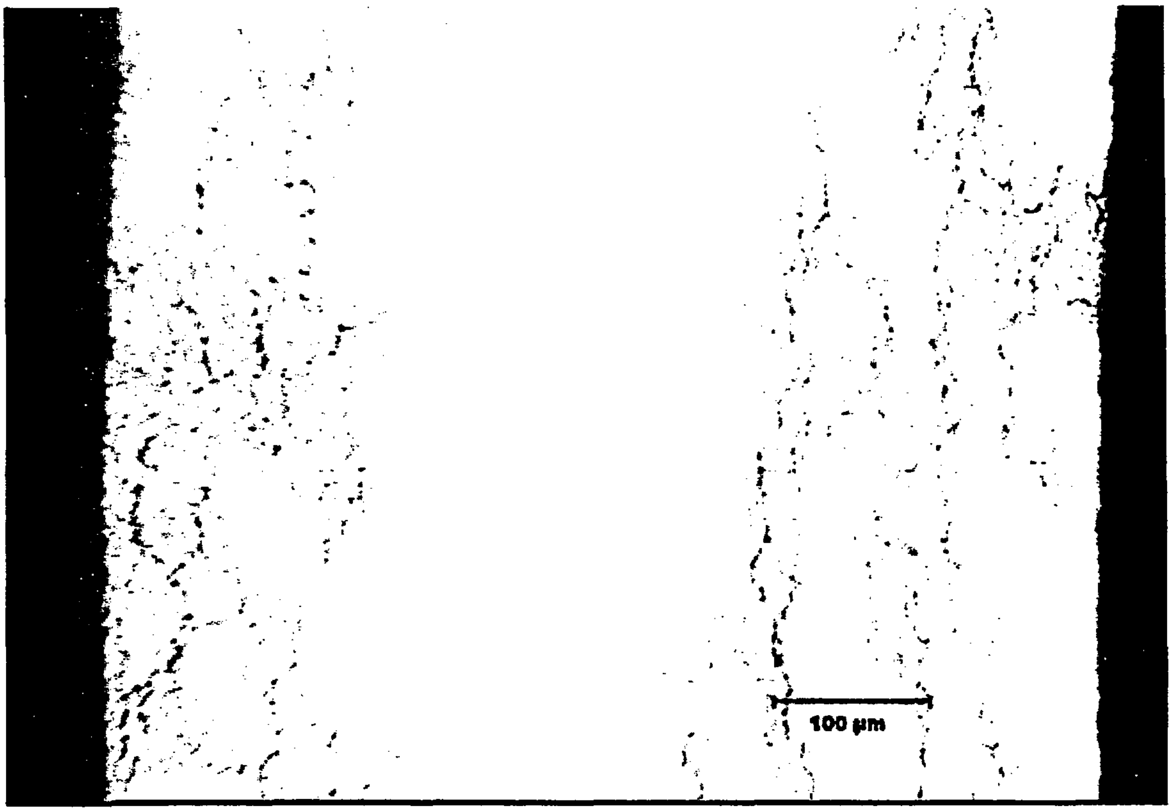

Fig. D.80 Cross-sectional view of Rod G6 cladding hydride morphology at ≈ 500 mm above fuel midplane (area 1). Scale marker = 100 μm.
JPG file = 592C12 Hydrides Area 1. ET703257.

Fig. D.81 Cross-sectional view of Rod G6 cladding hydride morphology at ≈500 mm above fuel midplane (area 2). Scale marker = 100 μm.
JPG file = 592C12 Hydrides Area 2. ET703260.

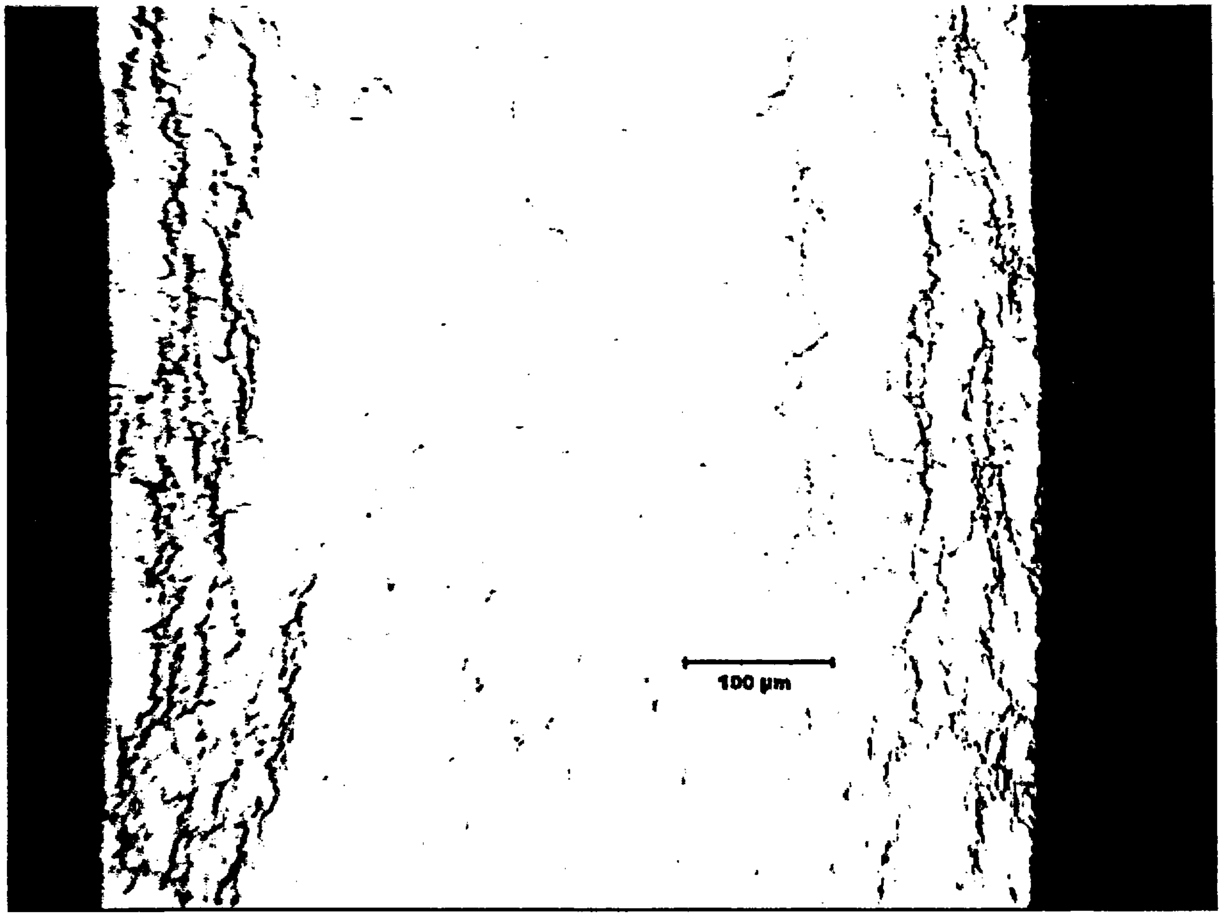

Fig. D.82 Cross-sectional view of Rod G6 cladding hydride morphology at ≈500 mm above fuel midplane (area 3). Scale marker = 100 µm.
JPG file = 592C12 Hydrides Area 3. ET703263.

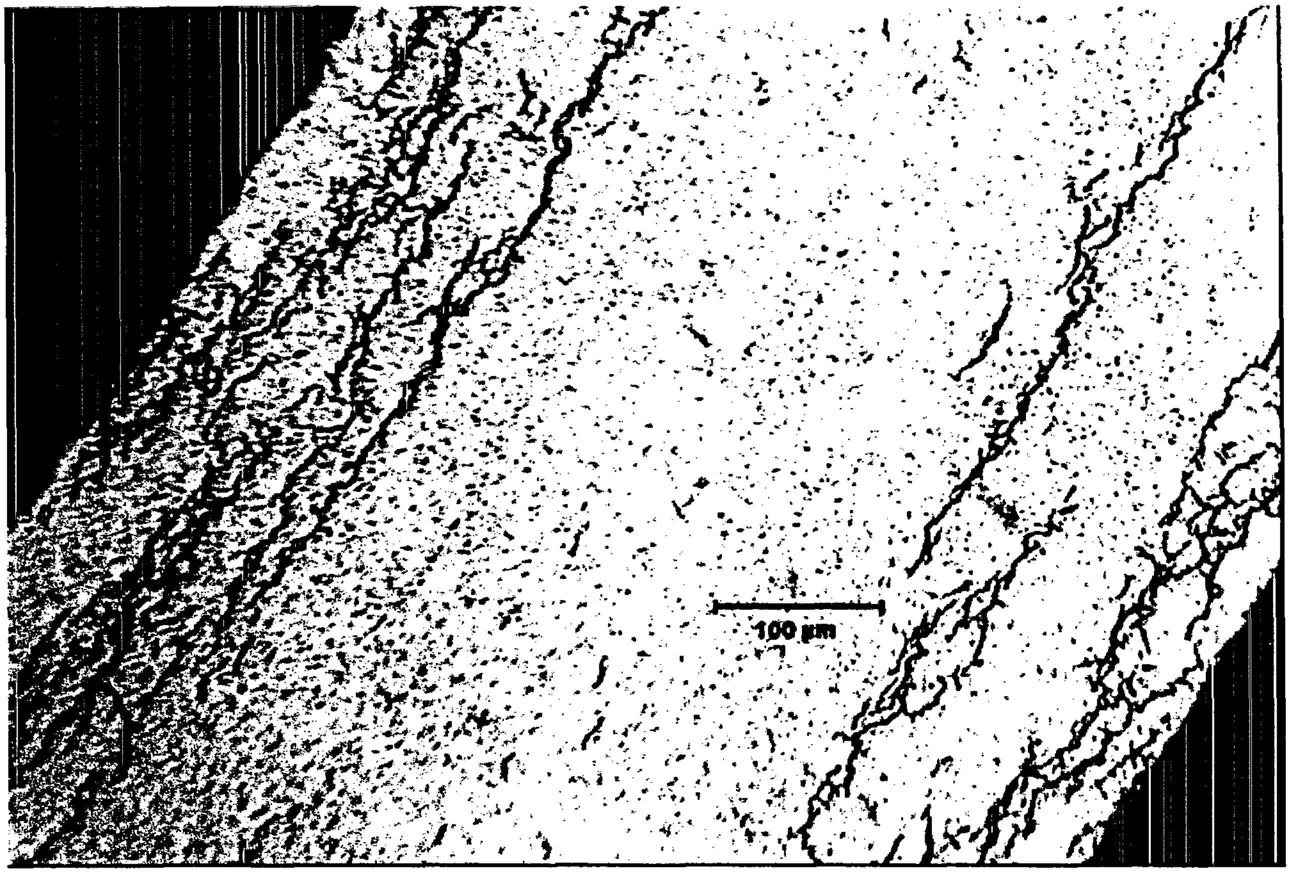

Fig. D.83 Cross-sectional view of Rod G6 cladding hydride morphology at ≈500 mm above fuel midplane (area 4). Scale marker = 100 µm.
JPG file = 592C12 Hydrides Area 4. ET703266.

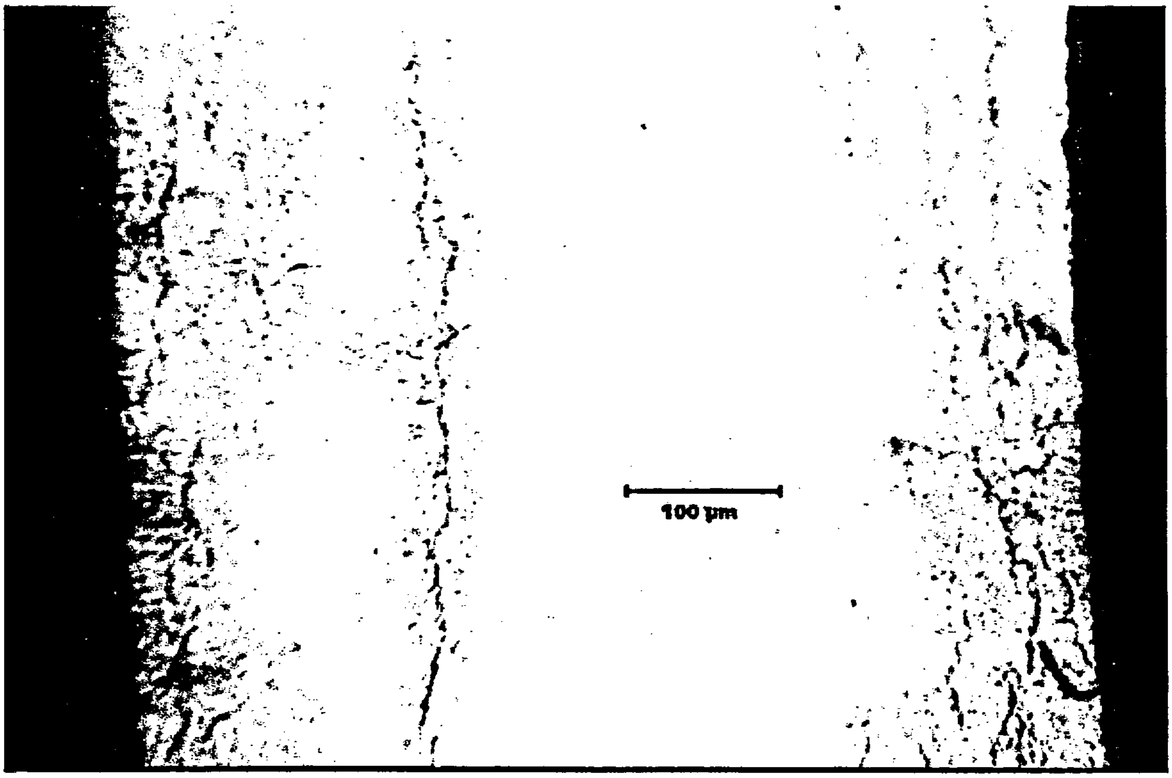

Fig. D.84 Cross-sectional view of Rod G6 cladding hydride morphology at ≈500 mm above fuel midplane (area 5). Scale marker = 100 µm.
JPG file = 592C12 Hydrides Area 5. ET703269.

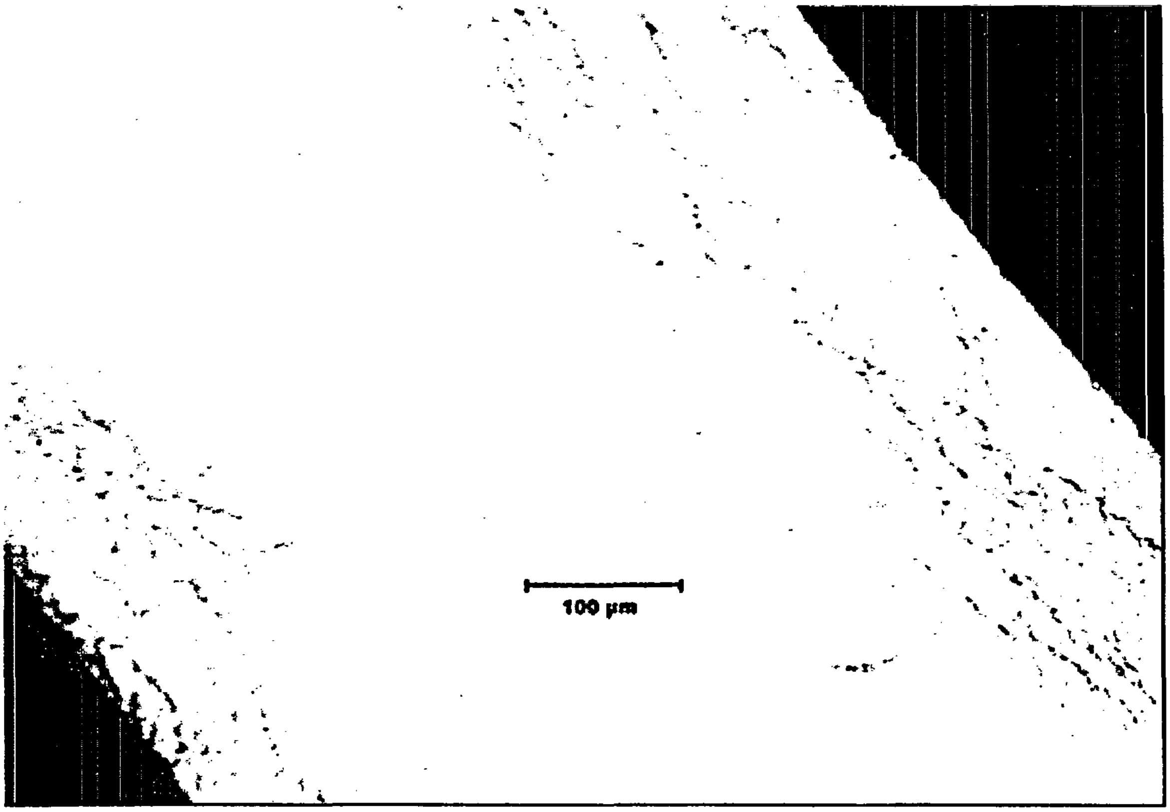

Fig. D.85 Cross-sectional view of Rod G6 cladding hydride morphology at ≈500 mm above fuel midplane (area 6). Scale marker = 100 µm.
JPG file = 592C12 Hydrides Area 6. ET703272.

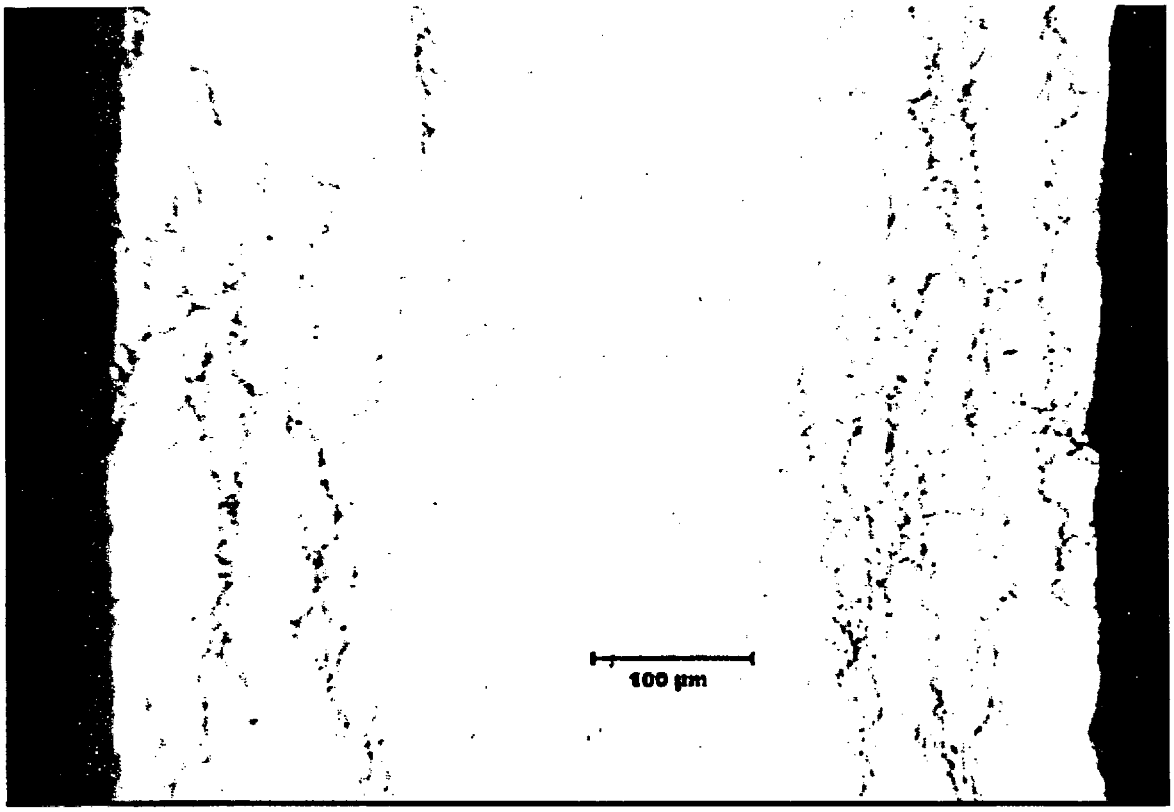

Fig. D.86 Cross-sectional view of Rod G6 cladding hydride morphology at ≈500 mm above fuel midplane (area 7). Scale marker = 100 μm.
JPG file = 592C12 Hydrides Area 7. ET703275.

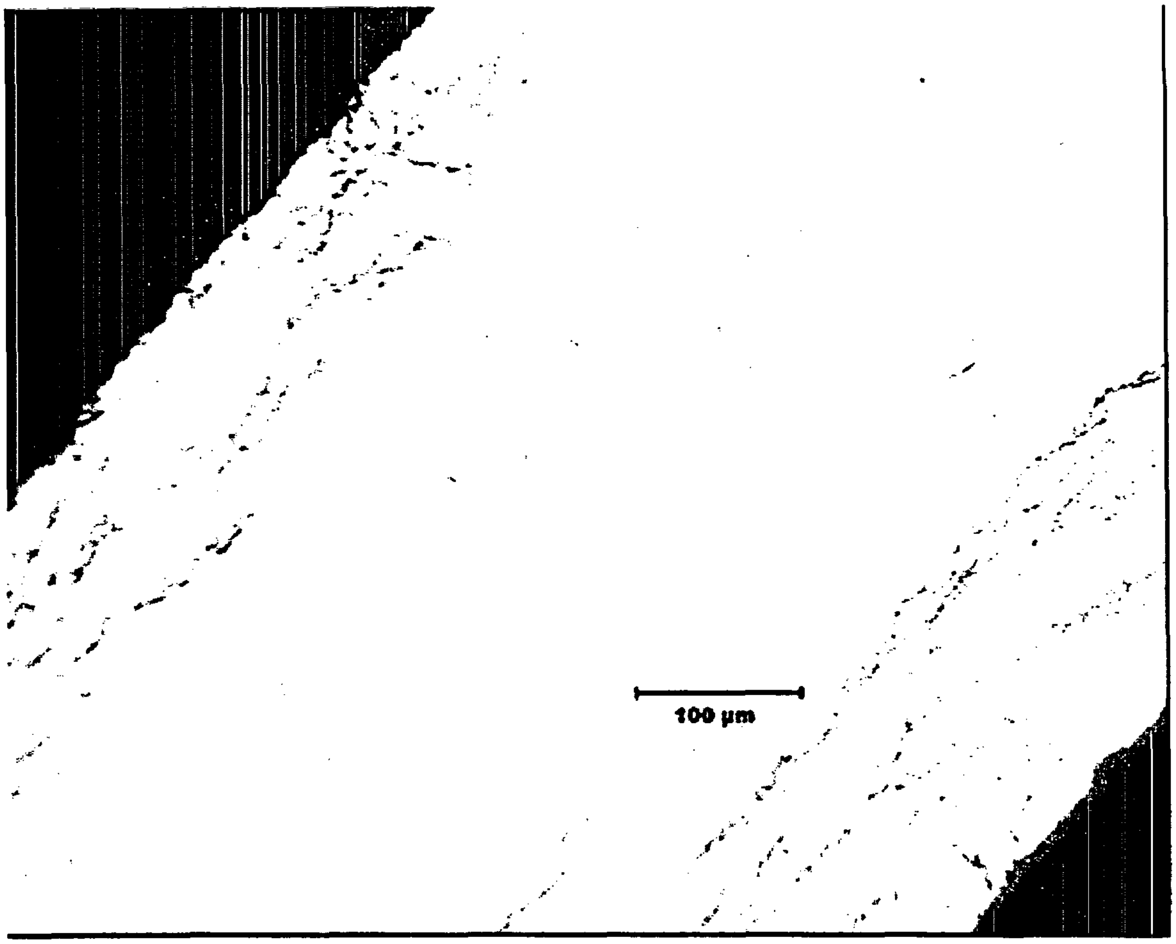

Fig. D.87 Cross-sectional view of Rod G6 cladding hydride morphology at ≈500 mm above fuel midplane (area 8). Scale marker = 100 µm.
JPG file = 592C12 Hydrides Area 8. ET703278.

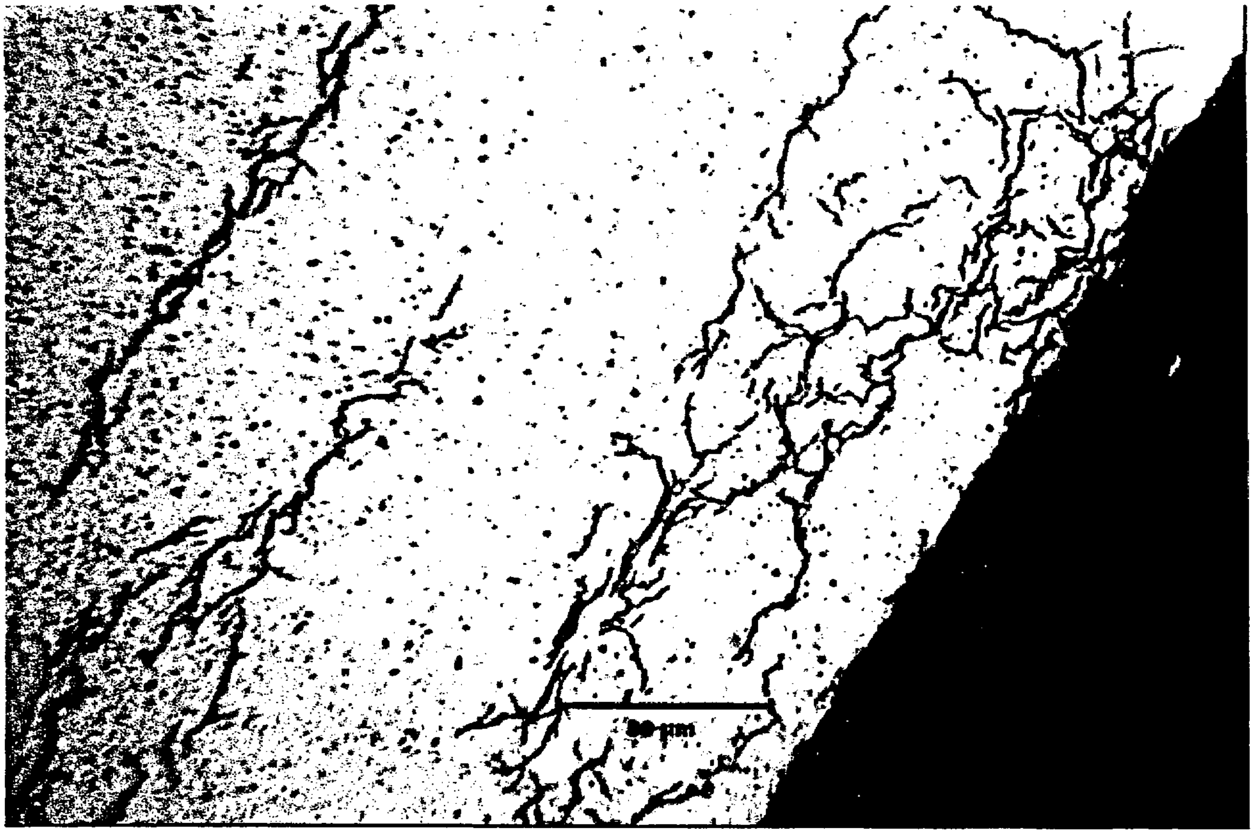

Fig. D.88a. High magnification of hydride orientation/distribution near the outer surface ≈500 mm above the fuel midplane (area 4) within Rod G6 cladding.
JPG file = 592C12 etched area 4 outer. ET703267.

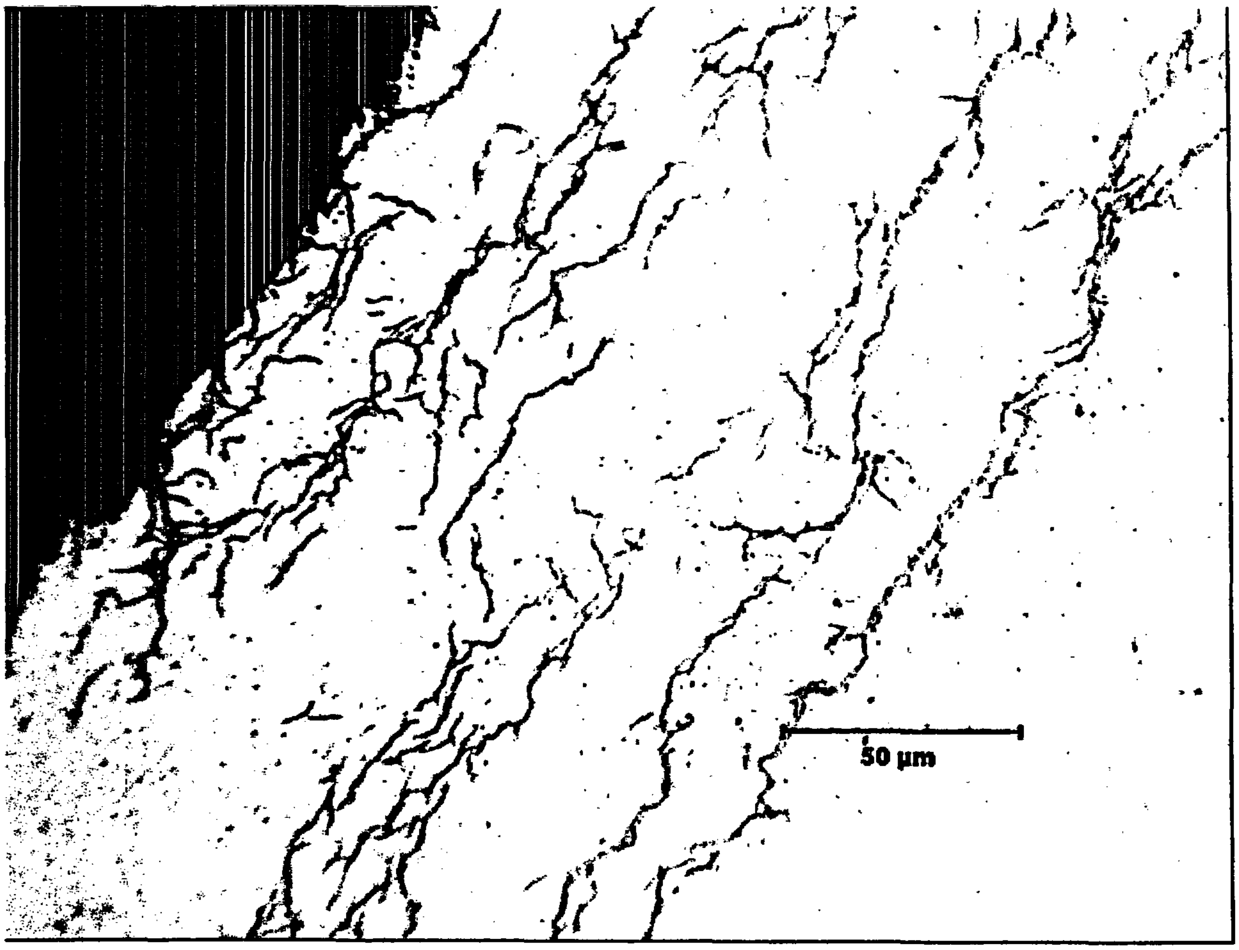

Fig. D.88b. High magnification of hydride orientation/distribution near the inner surface ≈500 mm above the fuel midplane (area 4) within Rod G6 cladding. JPG file = 592C12 etched area 4 inner. ET703268.

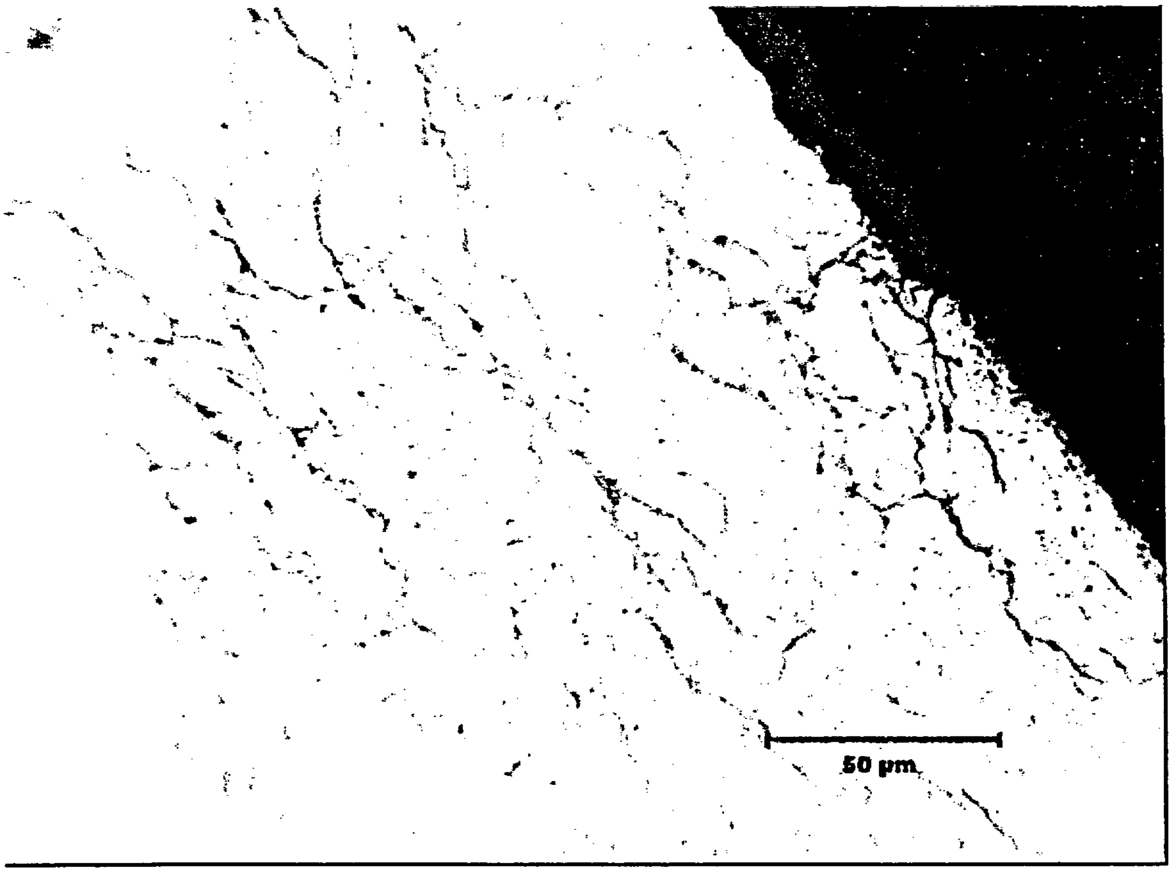

Fig. D.89a. High magnification of hydride orientation/distribution near the inner surface ≈500 mm above the fuel midplane (area 6) within Rod G6 cladding. Note the fine precipitates around the hydrides.
JPG file = 592C12 etched area 6 inner. ET 703274.

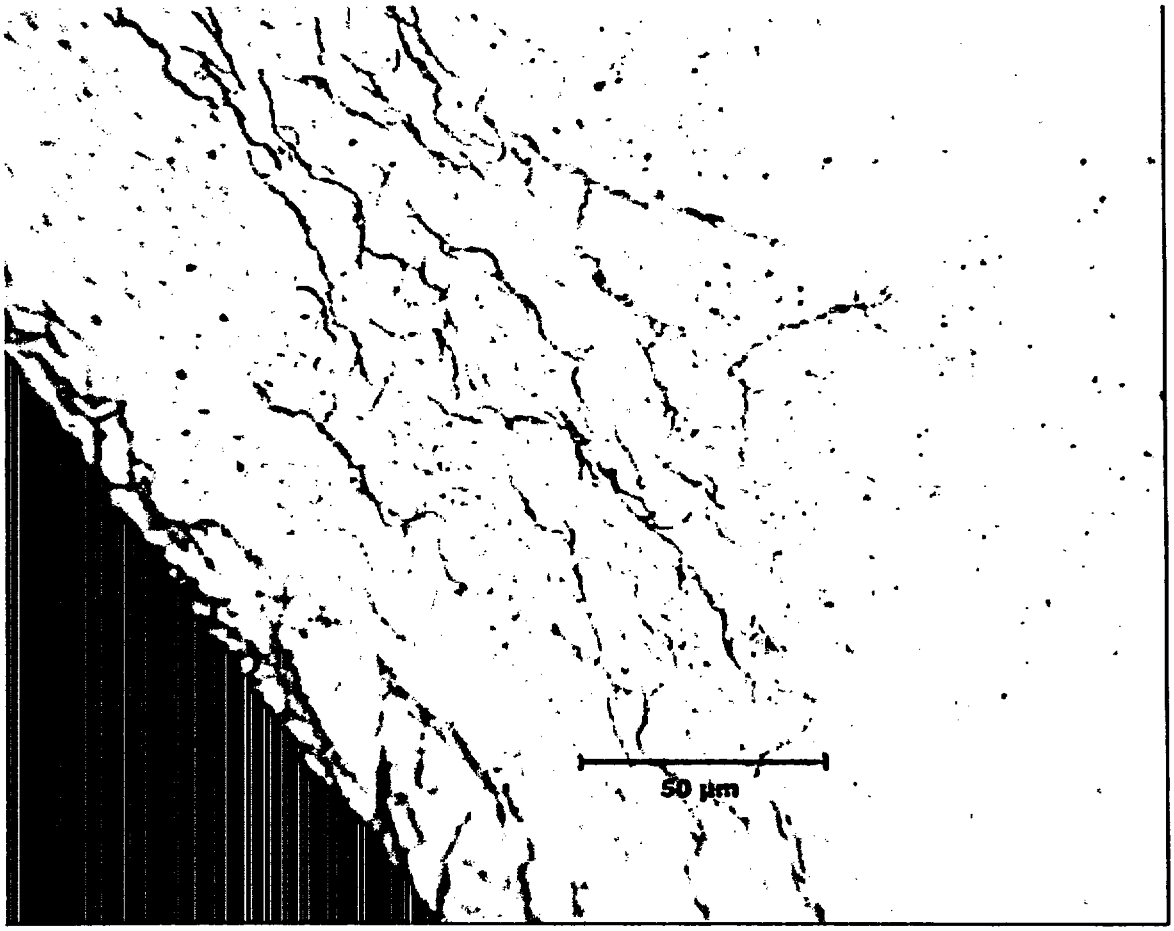

Fig. D.89b. High magnification of hydride orientation/distribution near the outer surface ≈500 mm above the fuel midplane (area 6) within Rod G6 cladding. Note the fine precipitates around the hydrides.
JPG file = 592C12 etched area 6 outer. ET 703273.

APPENDIX E

BASELINE COMPARATIVE DATA

Tables

E.1 Turkey Point Rod Diameter (inches) at an Elevation 2-3 m from the Bottom of the Rods. E-2

E.2 Gas Composition of Surry Rods After 15 years Dry Storage with Rods from Two 3-Cycle Turkey Point Assemblies D01, and D04....E-4

E.3 Isotopic Composition of Fission Gas From Four Surry Rods After 15 Years of Dry Storage and Rods in Turkey Point Assemblies D01 and D04....E-4

Figures

E.1 Cladding OD Oxide Layers for Three-Cycle Turkey Point PWR Rods....E-3

E.2 Cladding Thicknesses (μ-inch) for Three-Cycle Turkey Point PWR Rods....E-3

E.3 Hydrogen Contents for Three-Cycle Turkey Point (D01 and D04) Fuel Rods....E-5

Table E.1 Turkey Point Rod Diameter (inches) at an Elevation 2-3 m from the Bottom of the Rods. (Refs E.1 and E.2)

Rod	Maximum, in.	Average, in.	Minimum, in.
D01-F7	.4212	.4204	.4195
-F8	.4218	.4205	.4200
-F9	.4210	.4203	.4191
-G6	.4220	.4205	.4195
-G7	.4233	.4202	.4190
-G8	.4238	.4205	.4190
-G9	.4226	.4198	.4183
-G10	.4228	.4210	.4198
-H6	.4202	.4194	.4188
-H7	.4218	.4210	.4195
-H9	.4230	.4205	.4199
-I6	.4222	.4202	.4192
-I7	.4210	.4200	.4195
-I8	.4218	.4205	.4198
-I9	.4225	.4202	.4190
-J7	.4216	.4205	.4192
-J8	.4215	.4205	.4195
-J9	.4228	.4210	.4192
D04-G9	.4222	.4205	.4188
-G10	.4225	.4210	.4192
In Inches			
	Maximum	**Average**	**Minimum**
Global	.4238	--	.4188
Average	.4221	.4204	.4193
In mm			
Global	10.765	--	10.638
Average	10.721	10.678	10.650

Oxide Thickness (μ inches)

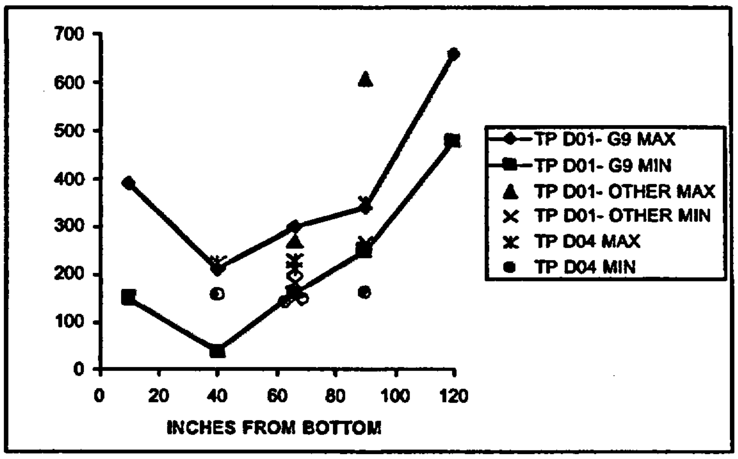

Fig. E.1 Cladding OD Oxide Layers for Three-Cycle Turkey Point PWR Rods. (Refs. E.1 and E.2).

Cladding Thickness

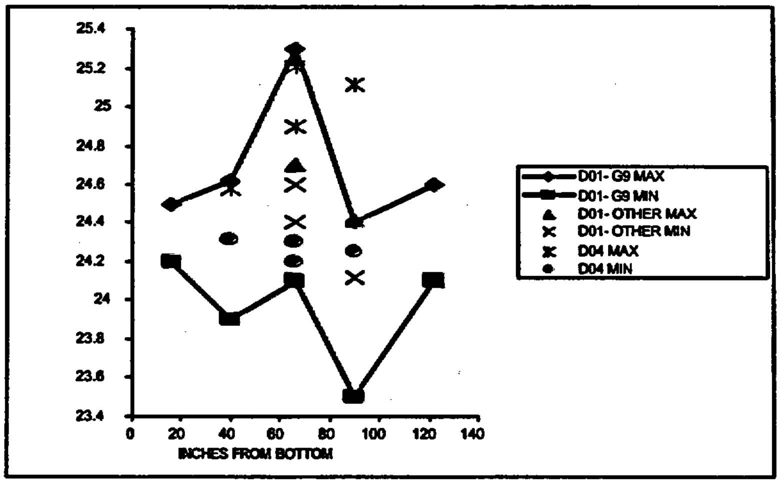

Fig. E.2 Cladding Thicknesses (μ-inch) for Three-Cycle Turkey Point PWR Rods. (Refs. E.1 and E.2).

Table E.2 Gas Composition of Surry Rods After 15 years Dry Storage with Rods from Two 3-Cycle Turkey Point Assemblies D01, and D04 (Refs. E.1 and E.2)

	Gas Composition (%)		
	Turkey Point D01	Turkey Point D04	Surry
He	99.4	98.3-98.9	96.1-98.3
H_2	NM	NM	<0.01-0.01
N_2	0-0.01	<0.01-0.43	0.01-0.03
O_2	<0.01	<0.01-0.12	<0.01-0.01
Ar	0.07-0.13	0.58-0.72	0.25-0.33
CO_2	NM	NM	0.01
Xe	0.43-0.48	0.44-0.49	1.3-3.3
Kr	0.05	0.05	0.11-.036
Xe/Kr ratio	8.6-9.0	8.8-9.8	9.0-11.4
NM = not measured			

Table E.3 Isotopic Composition of Fission Gas From Four Surry Rods After 15 Years of Dry Storage and Rods in Turkey Point Assemblies D01 and D04 (Refs. E.1 and E.2)

	Isotopic Composition (at. %)		
Isotope	Turkey Point DO1	Turkey Point DO4	Surry
Kr-83	12	12	11-11.5
Kr-84	32	32-33	≈33.3
K4-85	4-5	4	≈2.1
Kr-86	51-52	51-52	53-54
Xe-131	8	8-9	7-7.5
Xe-132	20-21	21	≈22
Xe-134	28	38	≈28
Xe-136	43-44	42-43	42-42.2

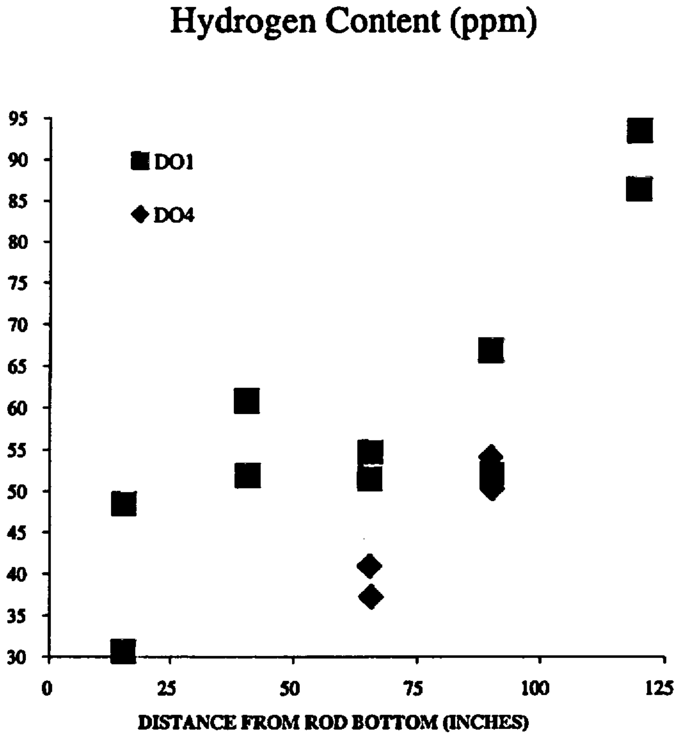

Fig. E.3. Hydrogen Contents for Three-Cycle Turkey Point (D01 and D04) Fuel Rods (Refs. E.1 and E.2)

References

E.1 Davis, R. B. "Pre-Test Nondestructive Examination Data Summary Report on Turkey Point Spent Fuel Assemblies D01, D04, and D06 for the Climax – Spent Fuel Test." HEDL-TME 80-83, UC-70, Hanford Engineering Development Laboratory: Richland, WA. January 1981

E.2 Atkin, S. D. "Destructive Examination of 3-Cycle LWR Fuel Rods from Turkey Point Unit 3 for the Climax – Spent Fuel Test." HEDL-TME 80-89, UC-70, Hanford Engineering Development Laboratory: Richland, WA. June 1981

APPENDIX F

THERMAL CREEP TESTS

F.1 Test Apparatus....F-4

F.1.1 Sample Preparation....F-4

F.1.2 Test Chambers....F-5

F.1.3 Furnaces....F-5

F.1.4 Pressurization Systems....F-7

F.1.5 Profilometer....F-9

F.2 Test Conduct....F-10

F.3 Surry Post-storage Thermal Creep Tests....F-15

F.3.1 Pressure and Temperature Histories....F-15

F.3.2 Summary Creep Results....F-16

Figures

Fig. F.1 Configuration of Surry Creep Sample.... F-5

Fig. F.2 Actual End-Fitting Closure Welds.... F-5

Fig. F.3 Test Chamber and Creep Sample Assembly....F-6

Fig. F.4 Crucible Furnaces Holding the Test Chambers....F-6

Fig. F.5 Schematic Diagram of the Creep Pressurization System.... F-7

Fig. F.6 Pressurization Systems for the Surry Thermal Creep Tests....F-8

Fig. F.7 Laser Profilometer for Measuring Surry Sample Diameter and Length......... F-9

Fig. F.8 Cross-Sectional Profile of the C8 Sample at the Axial Midplane prior to the Thermal Creep Test........F-11

Fig. F.9 Outside Diameter of the C8 Sample as a Function of Axial Location............ F-12

Fig. F.10 Profiling of the Lower End Fitting of the C8 Sample for Determination of a Possible Change in Sample Length due to Creep Anisotropy............... F-12

Fig. F.11 Pressure and Temperature History of the C8 Test in the First Run Segment..... F-13

Fig. F.12 Diameter Profile of the C8 Sample at the Axial Midplane before and after the First Run Segment........ F-13

Fig. F.13 Outside Diameter of the C8 Sample before and after the First Run Segment... F-14

Fig. F.14 Pre- and Post-Run Profiles of the C8 Bottom End Fitting. Overlapping suggests there was no sample length change........F-14

Fig. F.15 Strain vs. Time Plot for the C8 Sample after the First Run Segment............ F-15

Fig. F.16 Pressure and Temperature Histories for the Initial 1873 h Operation of the C9 Test........ F-17

Fig. F.17 Expanded Scales of Fig. F.16 Showing the Operating Range of the Pressure Controller/Regulator for the C9 Test. F-17

Fig. F.18 Deformation History of Sample C3 Operated Nominally at 220 MPa and 360°C for 3305 h........ F-18

Fig. F.19 Deformation History of Sample C6 Operated Nominally at 190 MPa and 380°C for 2348 h........ F-18

Fig. F.20 Deformation History of Sample C8 Operated Nominally at 220 MPa and 380°C for 2182 h........ F-19

Fig. F.21 Deformation History of Sample C9 Operated Nominally at 190 MPa and 400°C for 1873 h and Subsequently at 250 MPa and 400°C for 693 h....... F-19

Fig. F.22 Cross-Section Profiles of the C3 Sample at the Axial Midplane before and after the Test........F-20

Fig. F.23 Cross-Section Profiles of the C6 Sample at the Axial Midplane before and after the Test........F-20

Fig. F.24 Cross-Section Profiles of the C8 Sample at the Axial Midplane before and after the Test....F-21

Fig. F.25 Cross-Section Profiles of the C9 Sample at the Axial Midplane before and after the Test....F-21

Fig. F.26 Pre and Post-Run Profiles of the Lower End Fitting of Sample C9 .... F-22

Tables

Table F.1 Surry Post-Storage Thermal Creep Samples.... F-4

Table F.2 Achieved and Target Conditions for Surry Thermal Creep F-16

Table F.3 Second Creep Rate for Surry Post-Storage Cladding....F-22

F.1 Test Apparatus

F.1.1 Sample Preparation

Post-storage thermal creep tests were performed with sections of defueled Surry rod cladding internally pressurized with an inert gas and with the pressure actively regulated during the tests. Periodically, the samples were depressurized and removed from the furnace for diametral and length measurements. The measurements were made at room temperature.

Test samples were prepared from two Surry rods (H9 and G6) with identical design and comparable irradiation/storage histories. Each sample was 75 mm (3 in.) long. Sample identities and the estimated oxide layer thickness (23-30 μm), and hydrogen content (230-265 wppm) are shown in Table F.1. The estimates were made by interpolation and extrapolation of measurement data from nearby sibling samples. All samples were from the flat-power region of the rods just above and below Grid Spacer No. 4. By selecting samples from close proximity to each other, the intent is to minimize sample-to-sample variation in the tests.

The samples were defueled by dissolution with nitric acid and cleansed with alcohol and water in an ultrasonic cleaner. To minimize the volume of pressurized gas in the system, the inside of the cladding sample was filled with slightly undersized Zr-702 pellets. The end fittings were attached remotely with a tungsten-inert-gas (TIG) welder with a rotary head in the hot cell. Figure F.1 shows a mockup sample, and Fig. F.2 shows the closure welds of an actual sample. While the bottom end fitting was a solid plug, the top end fitting was a single machined piece with a thick-wall extension tube. The extension allowed the mechanical ("Swagelok") connection to the pressurization system to be made outside the heating zone for improved hermeticity. Both end fittings were made of Zr-702 material for compatibility with the Surry's Zircaloy-4 cladding.

Table F.1 Surry Post-Storage Thermal Creep Samples

Sample	from	Axial Location(1) (mm)	Oxide Thickness (μm)(2)	H content (wppm)(2)
C3	Rod H9	-38	23	230
C6	Rod H9	76	25	240
C8	Rod G6	254	23	260
C9	Rod H9	330	30	265

(1) Above fuel column midplane measured from center of the sample.

(2) Estimated based on sibling sample characterization data.

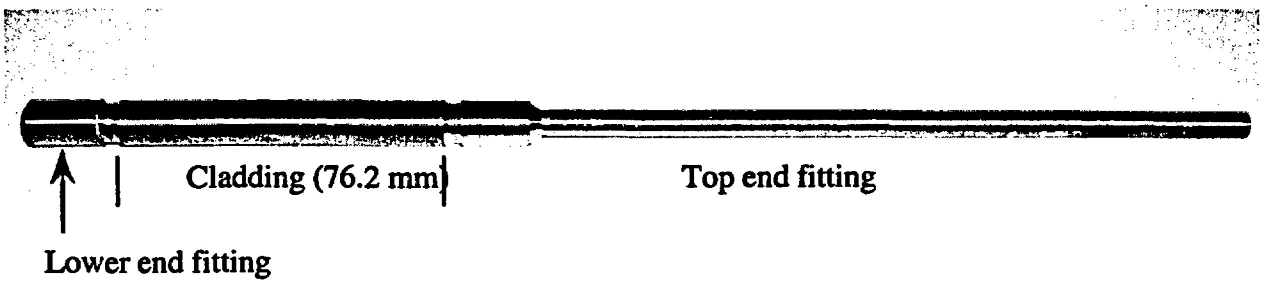

Fig. F.1 Configuration of Surry Creep Sample. End fittings were welded to cladding.

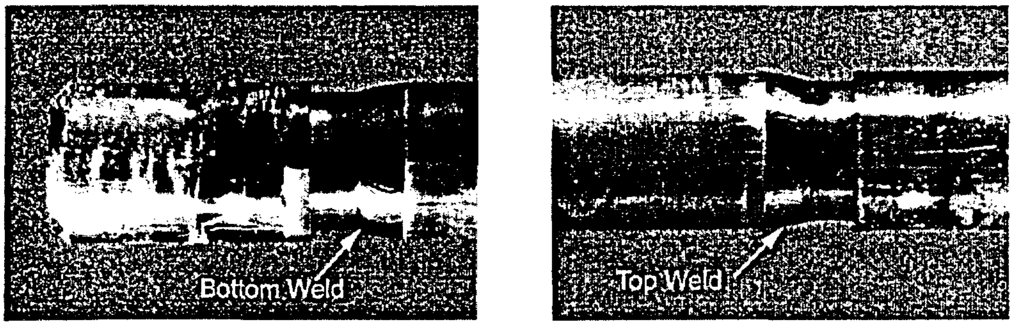

Fig. F.2 Actual End-Fitting Closure Welds.

Because welding softened the cladding immediately adjacent to the weld, hose clamps were applied to the ends of the cladding to preclude possible localized deformation during the test. The clamps were lined with collars made of Zr-702 material for compatibility with the Zircaloy-4 cladding. The width of the collar is 10 mm. Once installed, the collar/clamp assembly stayed on the sample until the end of the test.

F.1.2 Test Chambers

To mitigate sample oxidation and possible spread of contamination in case of a sample rupture, argon-purged test chambers were used. The exit end of the purge from the chamber was fitted with a high-efficiency-particulate filter for contamination control. Three chambers were built – two small units containing one sample each and a large unit containing up to three samples. Figure F.3 shows the single-sample test chamber.

Each of the small chambers was equipped with two thermocouples, and the larger chamber with three. The thermocouples were Type K with sheathed-and-ungrounded hot junctions positioned near the midplane of the sample but not touching. The thermocouples and the temperature recording systems were calibrated against standards traceable to NIST prior to the start of the tests.

F.1.3 Furnaces

Three insulated crucible furnaces (Fig. F.4) were used to provide the test temperatures required. The test chambers fit snugly inside the furnaces.

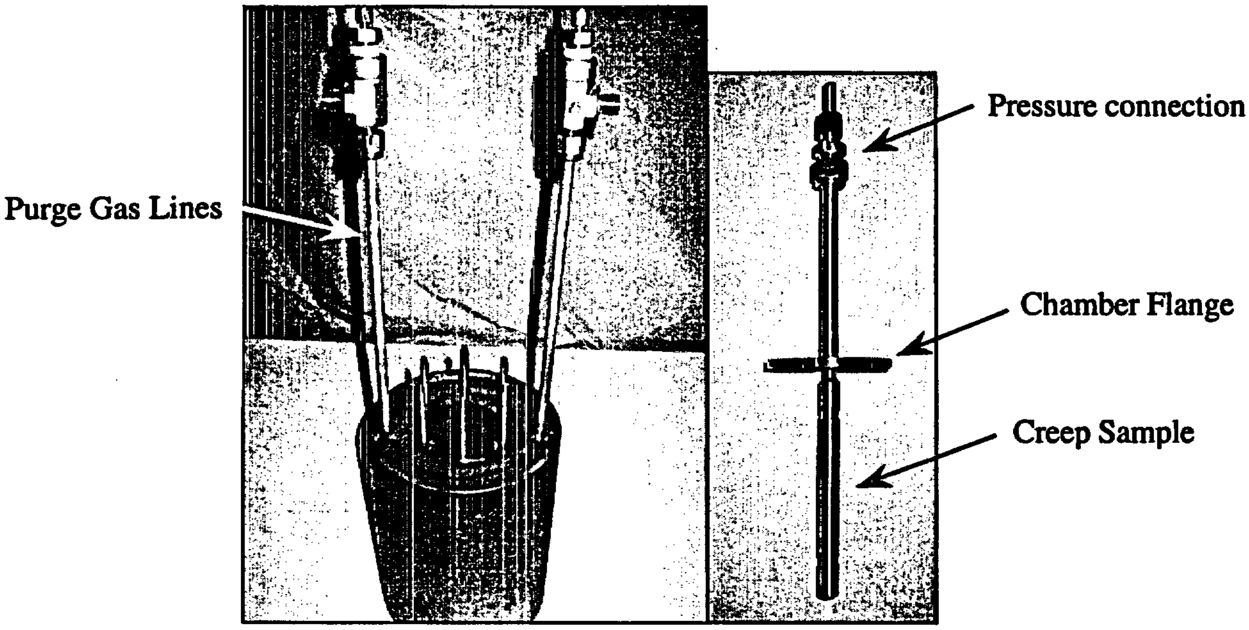

Fig. F.3 Test Chamber (left) and Creep Sample Assembly (right). The purge-gas lines in the test chamber served also as penetrations for thermocouples as seen in Fig. F.4.

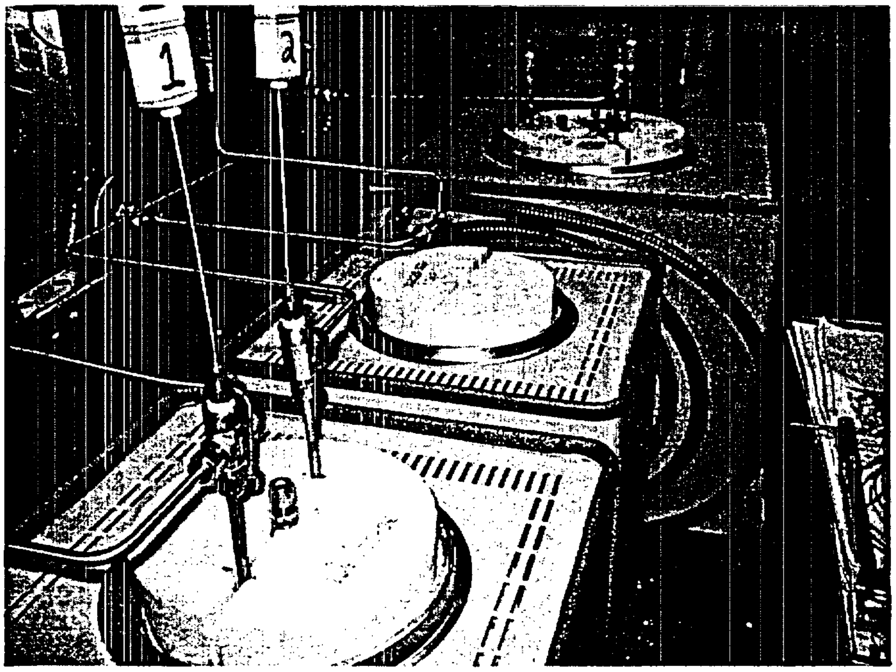

Fig. F.4 Crucible Furnaces Holding the Test Chambers.

F.1.4 Pressurization Systems

Five pressurization systems were constructed for the Surry post-storage creep tests. Instead of the conventional pump and accumulator approach, microprocessor-based pressure controller and regulators were employed to maintain the sample pressure steady during the tests. The pressure source was specialty cylinders with a 41 MPa (6000 psi) maximum pressure charge (corresponds to ≈320 MPa hoop stress in the Surry cladding). Each system contained a solenoid valve, which, in case of a sample rupture, would close and isolate the sample from the pressure source. Figure F.5 shows the schematic diagram of the systems, and Fig. F.6 shows the actual construction.

The pressure transducers and the associated measurement and recording systems were calibrated against standards traceable to NIST by an accredited metrology firm prior to the tests.

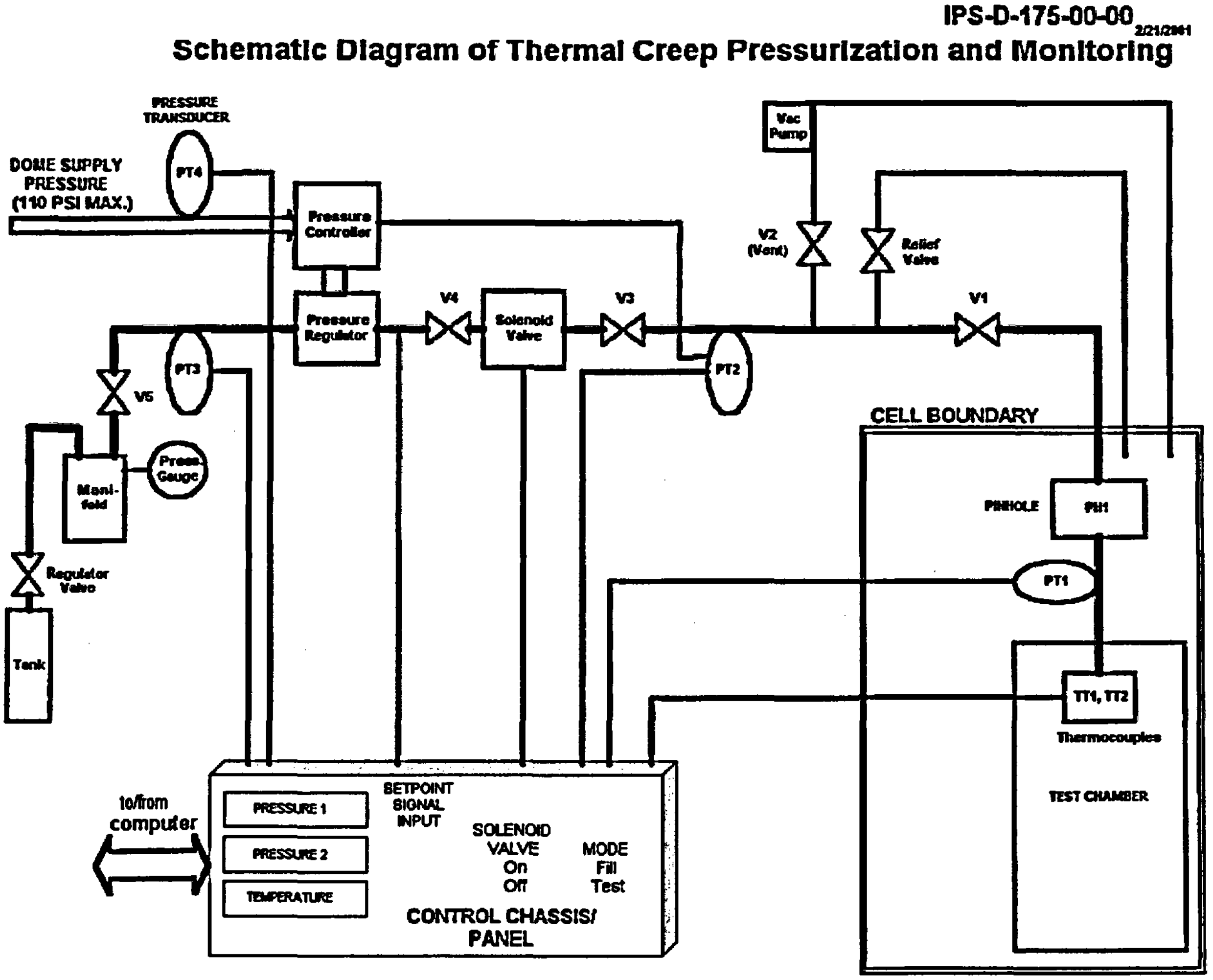

Fig. F.5 Schematic Diagram of the Creep Pressurization System.

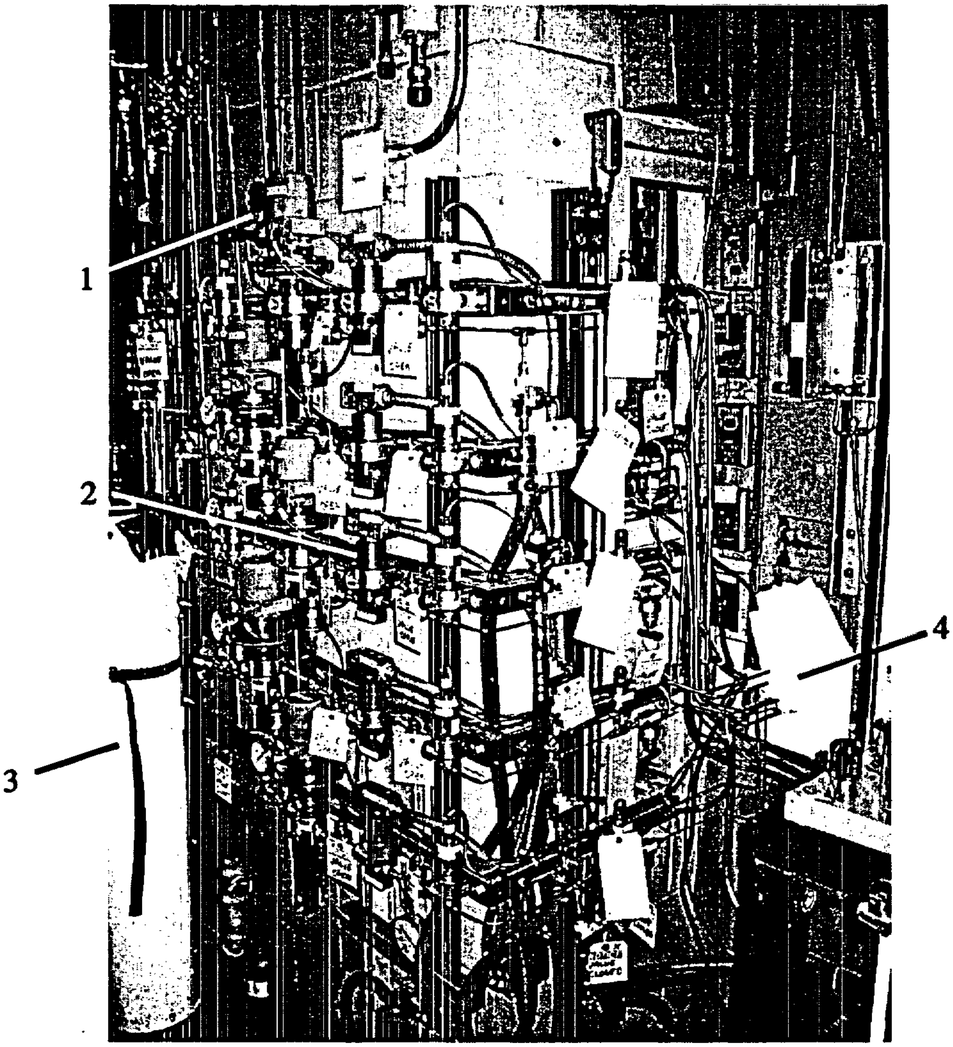

Fig. F.6 Pressurization Systems for the Surry Thermal Creep Tests. 1) pressure controllers/regulators; 2) solenoid valves; 3) pressure source [41 MPa (6000 psi) argon cylinders]; and 4) line penetrations into the hot cell.

F.1.5 Profilometer

A laser profilometer (Fig. F.7) was used to measure the sample diameter and length before the test and after each run. (Each test consisted of multiple runs.) The measurements were performed at room temperature with the sample discharged from the furnace. The stage mechanism of the profilometer provided accurate rotational and linear positioning capability to allow repeated measurements of sample dimensions at the same locations after every run. The diametral measurement accuracy is ≈5 x 10^{-4} mm (2 x 10^{-5} in.), corresponding to a strain accuracy of ≈0.005% for the Surry samples.

The sample diameters were measured every 9° azimuthal at 7.6-mm (0.3-in.) longitudinal intervals. The 20 azimuthal readings were averaged to yield the sample outside diameter (OD) for that axial location. The ODs of the middle 5 axial locations were then averaged to yield the sample OD for strain determinations.

The length of the sample was measured by profiling the lower end plug from a fixed top-end reference position. A shifting of the profile would be an indication of sample length change.

The accuracy of the profilometer was routinely verified against a NIST-traceable plug gauge.

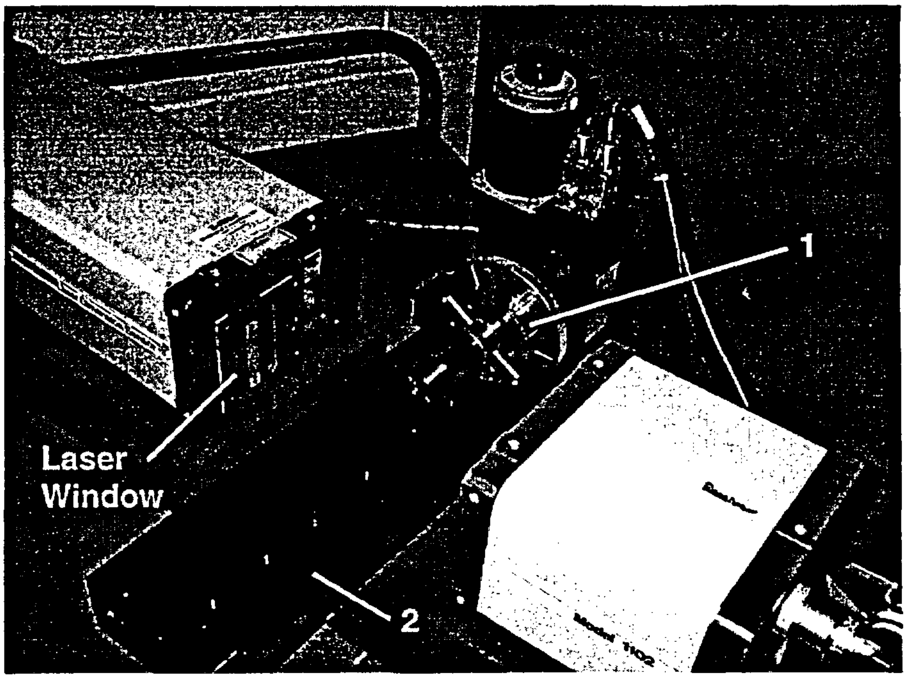

Fig. F.7. Laser Profilometer for Measuring Surry Sample Diameter and Length. The sample is mounted in the chuck (1), which permitted the rotational movement, and the slide (2) permitted the linear movement.

F.2 Test Conduct

The conduct of a thermal creep test is illustrated in this section using the C8 test as an example.

Before the test, the diameters of the C8 sample were measured with the laser profilometer. The resultant cross-sectional profile of the sample at the axial midplane is shown in a radial plot in Fig. F.8. From these 19-position azimuthal measurements, the average diameter at this axial location was determined to be 10.6492 mm (0.41926 in.). (Note: The out-of-roundness of the sample is exaggerated by the expanded plotting scale in Fig. F.8.)

The identical process was performed for the other axial locations, and the resultant average diameter profile is shown in Fig. F.9. The readings from the middle five axial positions were then averaged to yield the average OD of the sample 10.6497 mm (0.41928 in.).

To determine possible sample length changes due to creep anisotropy, the bottom end fitting of the sample was profiled from a fixed reference position at the top, as shown in Fig. F.10. A shift of the profile later would be an indication of a possible change in sample length.

After the pretest profilometry was completed and judged to be satisfactory, the C8 sample was loaded into the test chamber and connected to the pressurization system.

At room temperature, the C8 sample was pressurized to 6.85 MPa-gauge (≈50 MPa hoop cladding stress) and isolated from the rest of the pressurization system for a pressure-decay leak check. After observing no discernible pressure drop in the prescribed 180 s period, the pressure was reduced to 0.68 MPa (100 psi), the nominal holding position.

To expel trapped air in the sample from the initial installation, the pressurization system was evacuated and backfilled several times with argon gas. Afterwards, the system was returned to its holding pressure of 0.68 MPa (100 psig).

The furnace was then turned on to achieve the desired temperature of 380°C for the C8 test. Temperature overshoot was typically small, approximately several degrees Celsius. The pressure in the sample was maintained at 0.68 MPa (100 psig) during the heatup. Once the steady temperature was attained, the pressure-decay leak test was repeated to verify hermeticity at temperature. Again, the C8 sample was found to be leak-tight.

The sample was then pressurized to the target 27.9 MPa (4070 psig), corresponding to a wall-average hoop stress of 220 MPa after taking into account actual sample diameter and (metal) wall thickness.

The first run segment of the C8 test had a 335-h duration. The measured pressure and temperature profiles during the run are shown in Fig. F.11. Both pressure and temperature were steady and on target. The time-averaged pressure and temperature were 27.9 MPa (4071 psig) and 380.7°C, respectively.

At the end of the first run segment, the sample was depressurized from 27.9 MPa (4070 psig) to the holding pressure of 0.68 MPa (100 psig). The furnace was then turned off to allow the sample to cool to room temperature. This shutdown sequence is designed to preclude possible stress-induced reorientation of hydrides in the cladding during cool-down.

Profilometry of the C8 sample was repeated in a manner identical to pretest profilometry. The plots showing the pre- and post-run comparisons of cross-sectional profile at the axial midplane, the average diameter over the sample length, and the profile of the bottom end plug are given in Figs. F.12, F.13, and F.14, respectively.

In Figure F.14, the diameter of the lower end plug (Zr-702) was found to be the same before and after the run. Since the end plug was stress-free and not deforming, this result indicated that the purge chamber was effective, and that there was no discernible oxidation of the C8 cladding.

The calculated OD hoop strain (based on the middle five axial readings) was 0.232%. The wall-average hoop strain, taking into account the post-storage cladding dimension and oxide thickness, is 1.13 times higher, or 0.262%. The resultant strain vs. time plot after the first run for the C8 test is shown in Fig. F.15. The above procedure was repeated after every run for the C8 test.

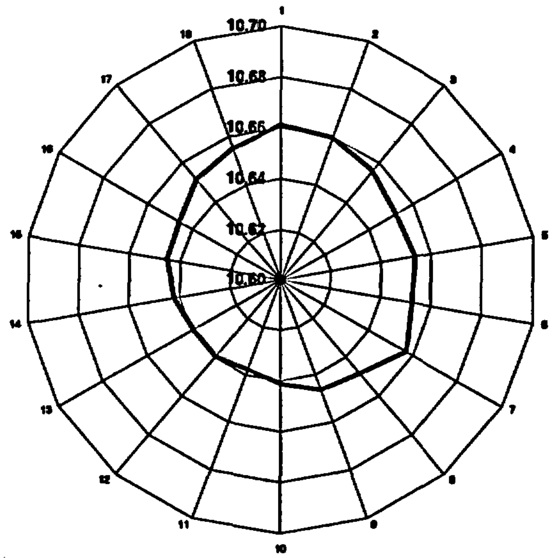

Fig. F.8 Cross-Sectional Profile of the C8 Sample at the Axial Midplane prior to the Thermal Creep Test. The reference diameter for creep measurements is 10.6492 mm

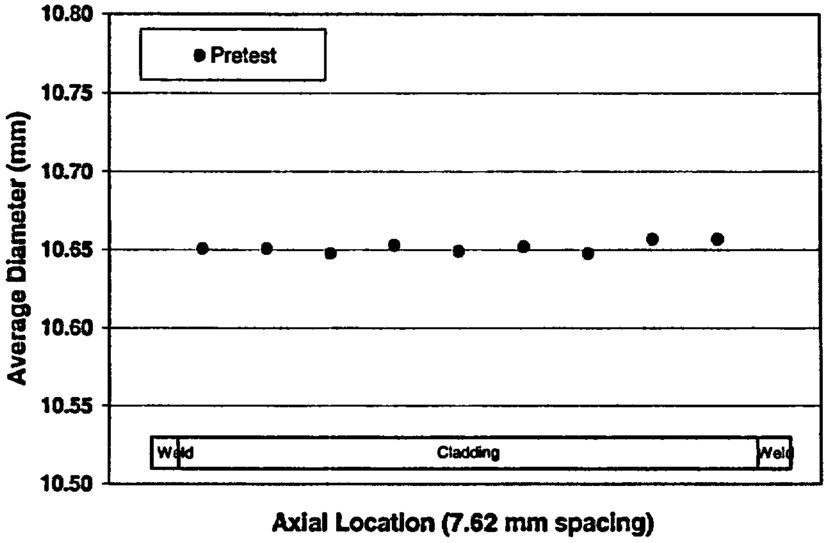

Fig. F.9 Outer Diameter of the C8 Sample as a Function of Axial Location. The middle five readings were averaged to yield the average OD (10.6497 mm =0.41928 in.) of the sample.

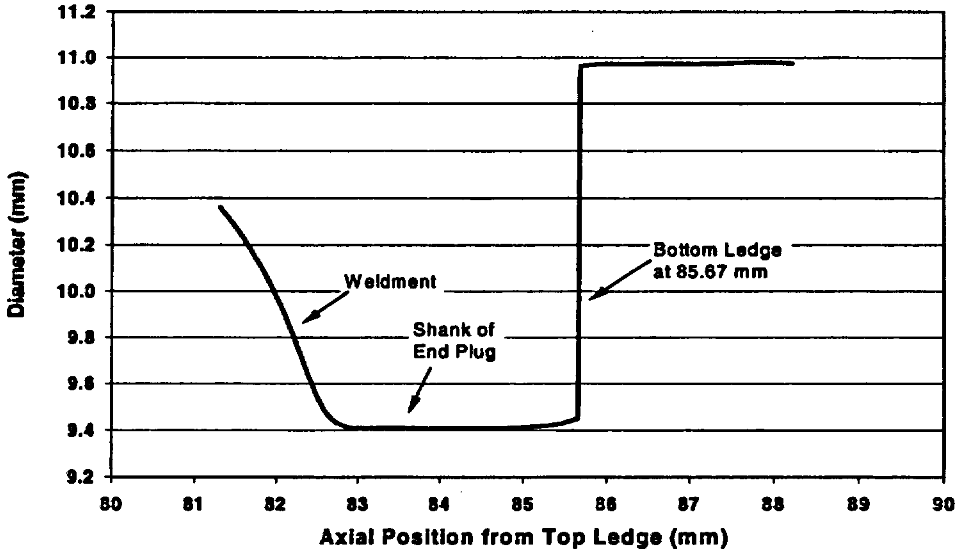

Fig. F.10 Profiling of the Lower End Fitting of the C8 Sample for Determination of a Possible Change in Sample Length due to Creep Anisotropy.

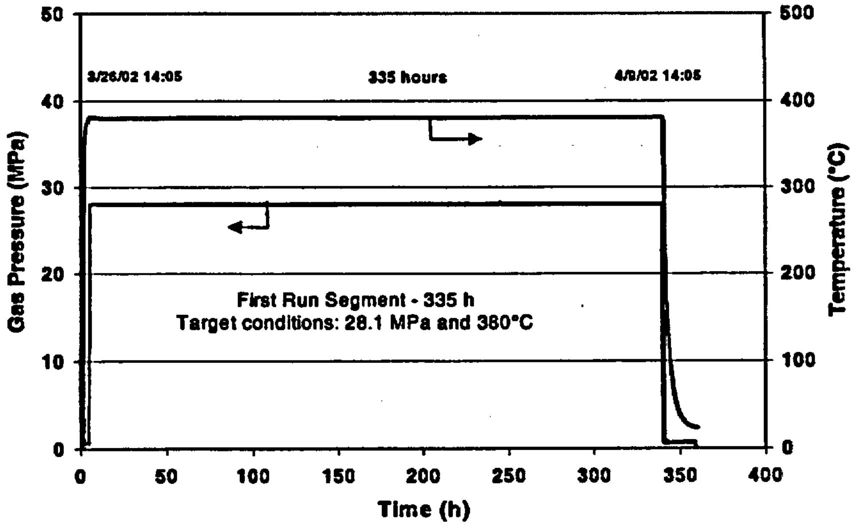

Fig. F.11 Pressure and Temperature History of the C8 Test in the First Run Segment.

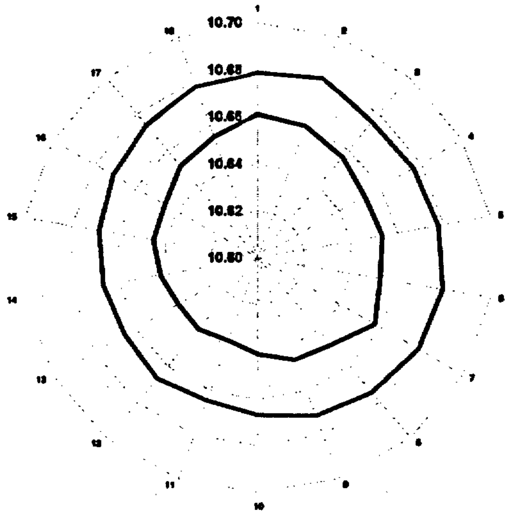

Fig. F.12 Diameter Profile of the C8 Sample at the Axial Midplane before and after the First Run Segment.

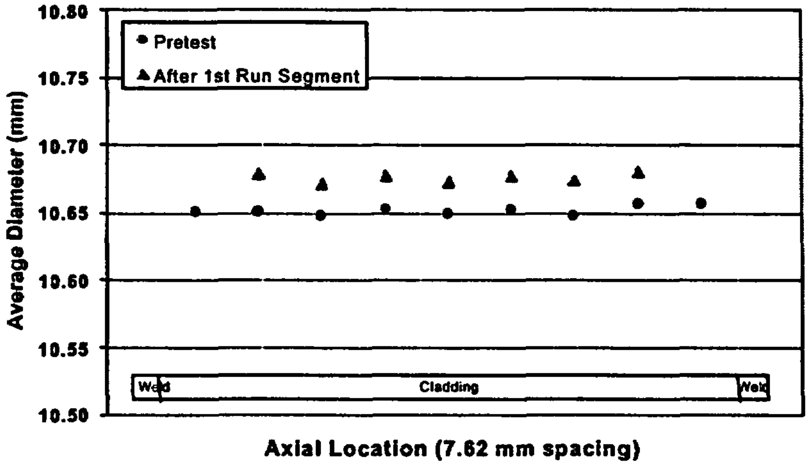

Fig. F.13 Outer Diameter of the C8 Sample before and after the First Run Segment. The two readings near the ends became unavailable due to the hose clamping of the cladding near the welds.

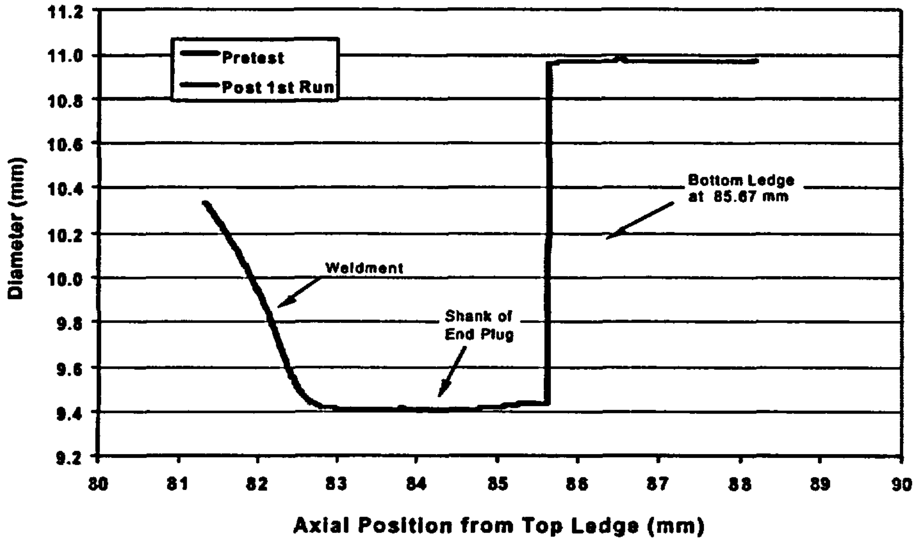

Fig. F.14 Pre- and Post-Run Profiles of the C8 Bottom End Fitting. Overlapping suggests no sample length change.

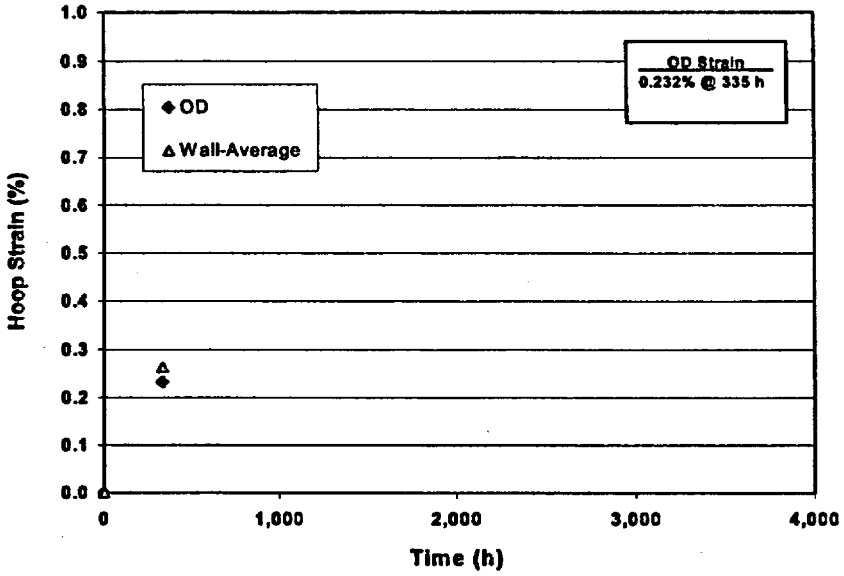

Fig. F.15 Strain vs. Time Plot for the C8 Sample after the First Run Segment. The calculated wall-average hoop strain is 1.13 times that of the OD hoop strain.

F.3 Surry Post-Storage Thermal Creep Tests

At the end of the tests, all four samples were found to have measurable strains and confirmed to be intact.

F.3.1 Pressure and Temperature Histories

Summary pressure and temperature histories for the C3, C6, C8 and C9 tests are shown in Table F.2 along with the target conditions. As noted before, the C9 test had two stress settings – the initial 1873 h was 190 MPa, and the subsequent 693 h was 250 MPa. Also shown in the table are the wall-average hoop strains at the end of the test durations.

It should be noted that the reported stresses are engineering hoop stresses, not true stresses. No efforts were made to adjust the gas pressure to keep the hoop stress constant to account for wall thinning. In all tests, the internal pressure was maintained constant over the entire test duration.

All four tests were completed satisfactorily, and the composite pressure and temperature histories for one of the tests, C9 for the initial 1873-h operation, are illustrated in Fig. F.16. In this plot, the pressure trace appears to be a band with a thickness of ≈ 0.1 MPa (14 psig). At a higher resolution (Fig. F.17), it can be seen that the "band" reflects the working range of the pressure controller/regulator. The periodicity of the cycles (when the regulator opened momentarily to replenish the loss of pressure due to leakage) was ≈6 h. The ≈±0.05 MPa (7 psig) pressure range translates into a ±0.2% range on sample hoop stress.

F.3.2 Summary Creep Results

Creep deformations as a function of time are shown in Figs. F.18, F.19, F.20, and F.21 for Samples C3, C6, C8, and C9, respectively. In each plot, both the OD strain and the calculated wall-average strain are shown. The OD strain is multiplied by 1.13 to obtain the wall-average strain.

The radial plots of the sample cross section may be useful to detect localized bulging which may indicate non-uniform wall thinning or impending burst rupture. These data were evaluated after every run. All results indicate the deformation to be azimuthally uniform, even for the C9 sample with a wall-average hoop strain of 5.83% at the end of test. Figs. F.22, F.23, F.24, and F.25 show, respectively, the cladding cross-sectional profiles of the C3, C6, C8 and C9 samples (at the axial midplane) before and after the tests.

At the time of test termination, the C3, C6 and C8 samples were evidently in the secondary (steady-state) creep regime. This also appears to be the case for the C9 sample at the end of the 190 MPa test. Steady-state creep rates were calculated for the tests, and the results are summarized in Table F.3.

There were no discernible sample length changes in any of the tests. Figure. F.26 shows the result for the C9 sample. The fact that the end fitting had the same diameter as before the test showed there was little oxidation of the sample.

Table F.2 Achieved and Target Conditions for Surry Thermal Creep Test

Sample	Time-Avg. Temp. (°C)		Time-Avg. Pressure (MPa)		Time-Avg. Hoop Stress (MPa)		Test Duration (h)	Wall-Avg. Hoop Strain (%)
	Actual	Target	Actual	Target	Actual	Target		
C3	360.4	360	27.99	28.06	219.4	220	3305	0.22
C6	381.0	380	24.23	24.23	190.4	190	2348	0.35
C8	381.0	380	28.06	28.06	220.2	220	2180	1.10
C9	399.6	400	24.23	24.23	189.8	190	1873	1.04
	399.5	400	31.88	31.88	249.4	250	693	5.83(a)

a. At the end of the 693 incremental hours.

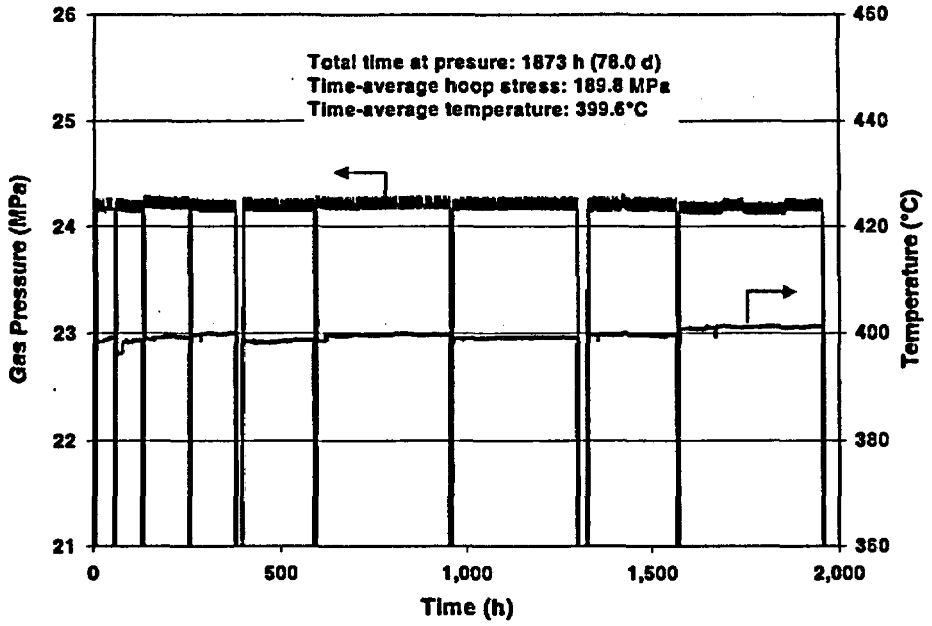

Fig. F.16 Pressure and Temperature Histories for the Initial 1873-h Operation of the C9 Test. The test was interrupted nine times for profilometry measurements.

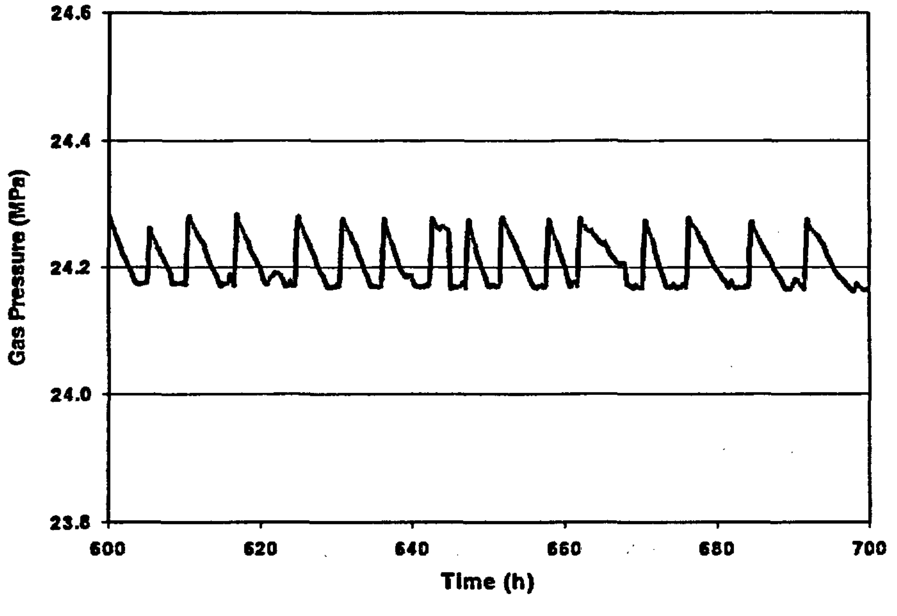

Fig. F.17 Expanded Scales of Fig. F.16 Showing the Operating Range of the Pressure Controller/Regulator for the C9 Test. The periodicity was about 6 h.

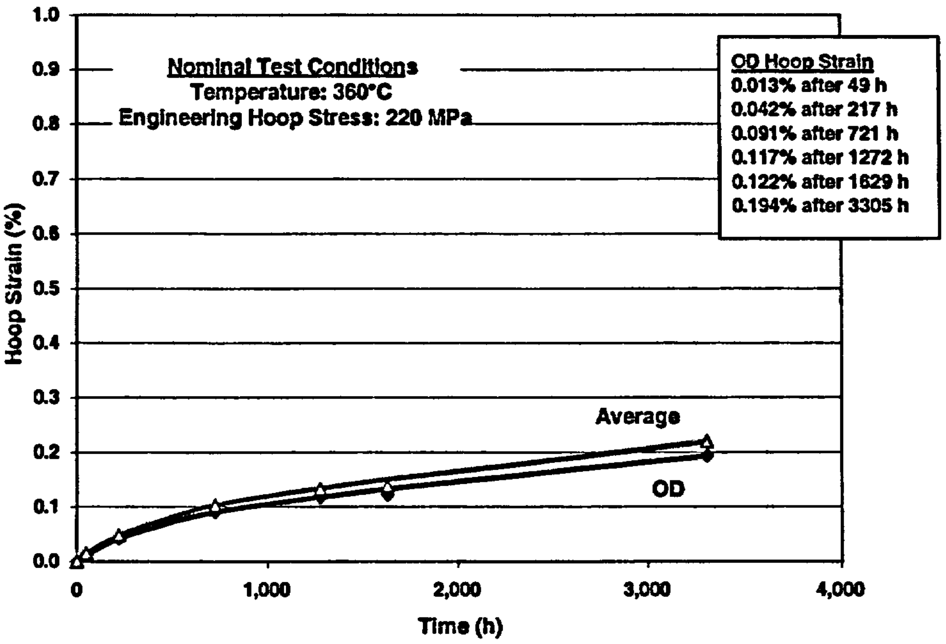

Fig. F.18 Deformation History of Sample C3 Operated Nominally at 220 MPa and 360°C for 3305 h.

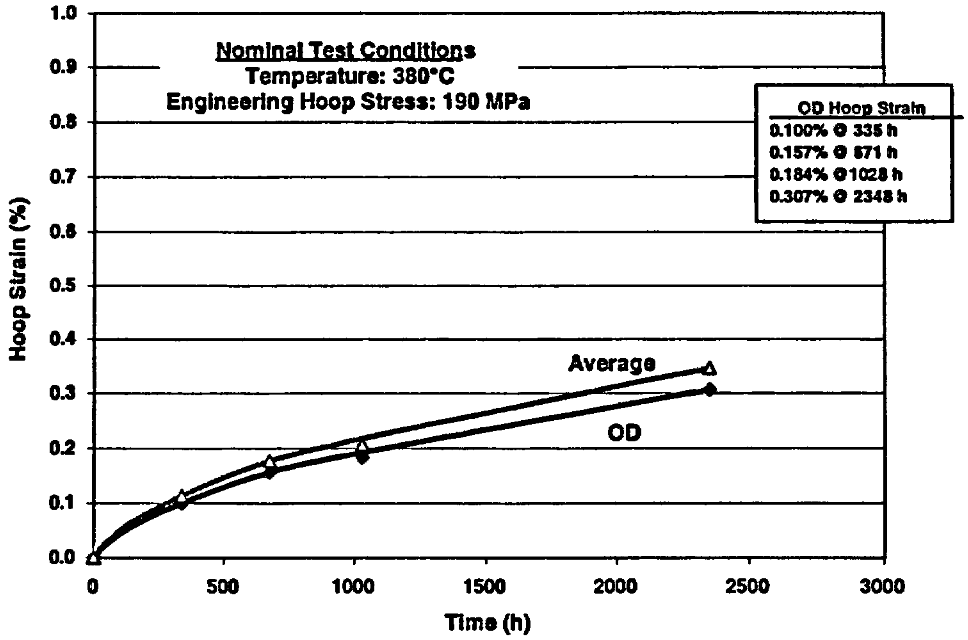

Fig. F.19 Deformation History of Sample C6 Operated Nominally at 190 MPa and 380°C for 2348 h.

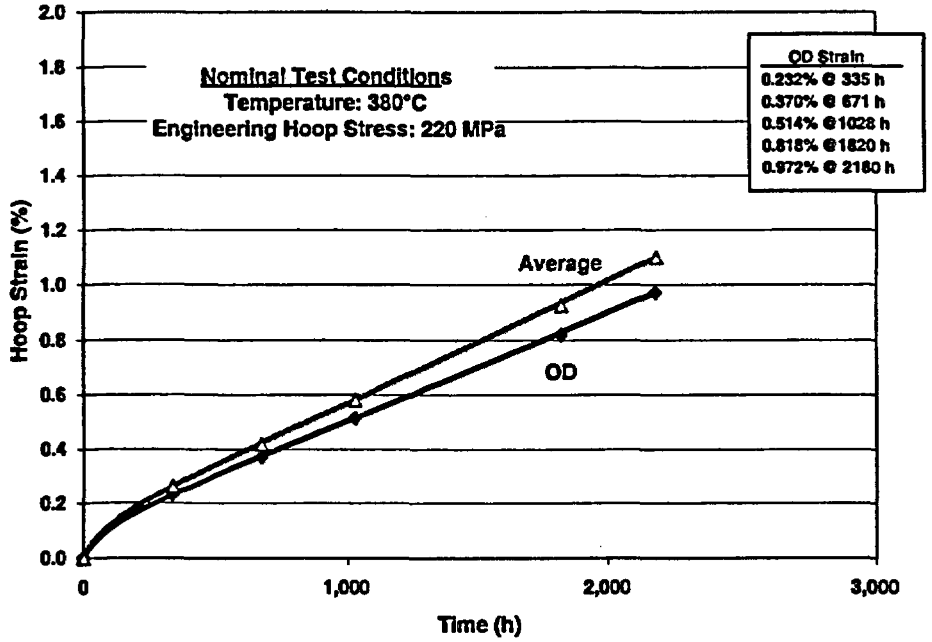

Fig. F.20 Deformation History of Sample C8 Operated Nominally at 220 MPa and 380°C for 2182 h.

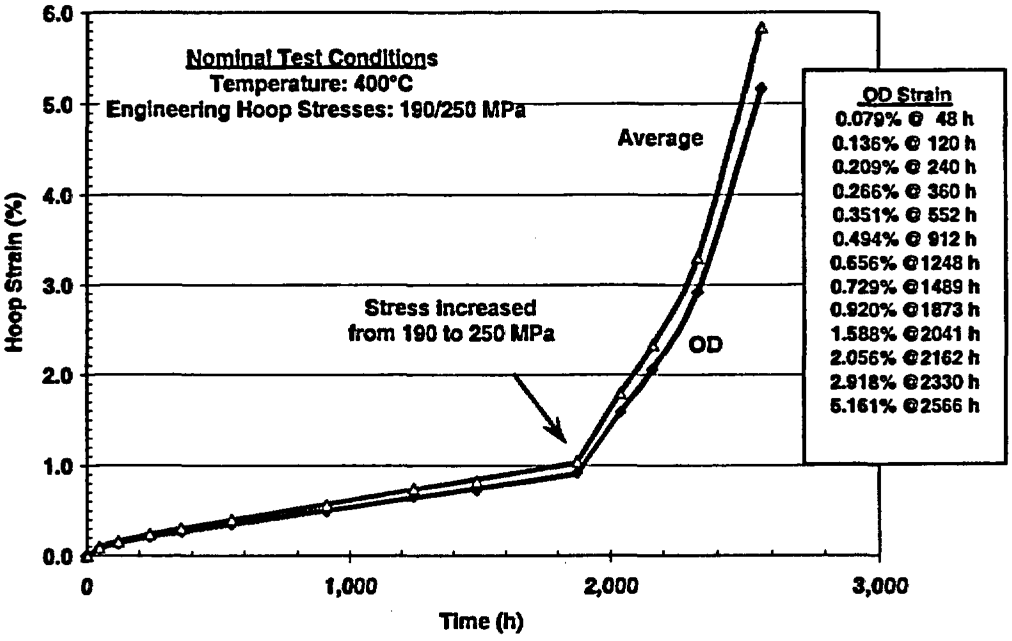

Fig. F.21 Deformation History of Sample C9 Operated Nominally at 190 MPa and 400°C for 1873 h and Subsequently at 250 MPa and 400°C for 693 h.

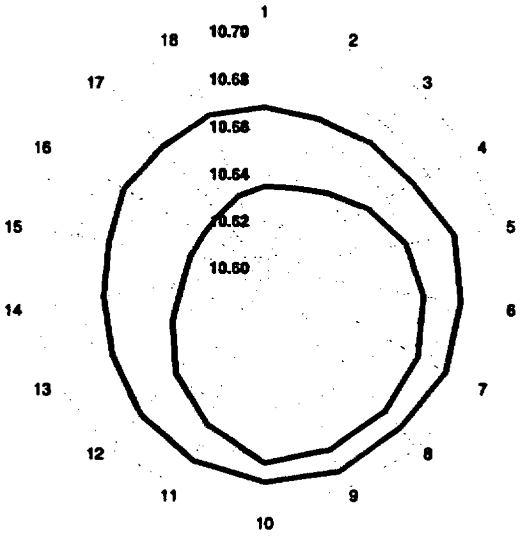

Fig. F.22 Cross-Section Profiles of the C3 Sample at the Axial Midplane before and after the Test.

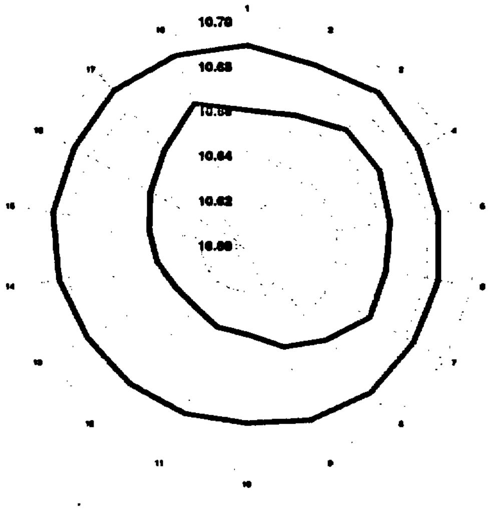

Fig. F.23 Cross-Section Profiles of the C6 Sample at the Axial Midplane before and after the Test.

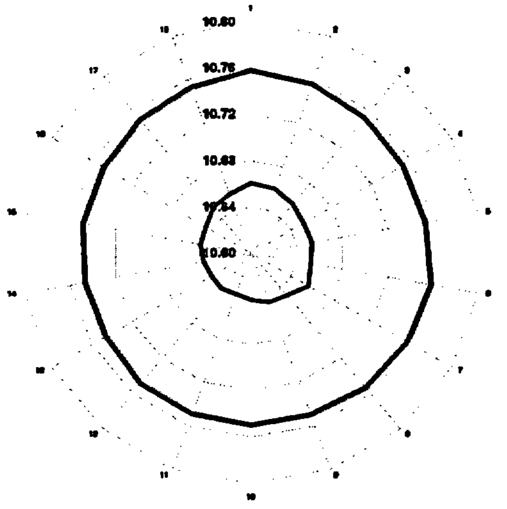

Fig. F.24 Cross-Section Profiles of the C8 Sample at the Axial Midplane before and after the Test.

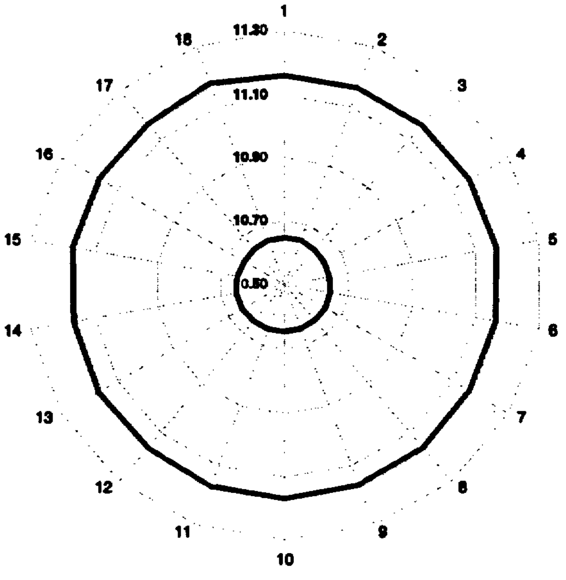

Fig. F.25 Cross-Section Profiles of the C9 Sample at the Axial Midplane before and after the Test.

Table F.3 Secondary Creep Rate for Surry Post-Storage Cladding

Sample	Nominal Temp. (°C)	Nominal Hoop Stress (MPa)	Secondary Creep Rate (%/h)
C3	360	220	4.2×10^{-5}
C6	380	190	8.8×10^{-5}
C8	380	220	4.5×10^{-4}
C9	400	190	4.9×10^{-4}
C9	400	250	$>4.9 \times 10^{-3}$

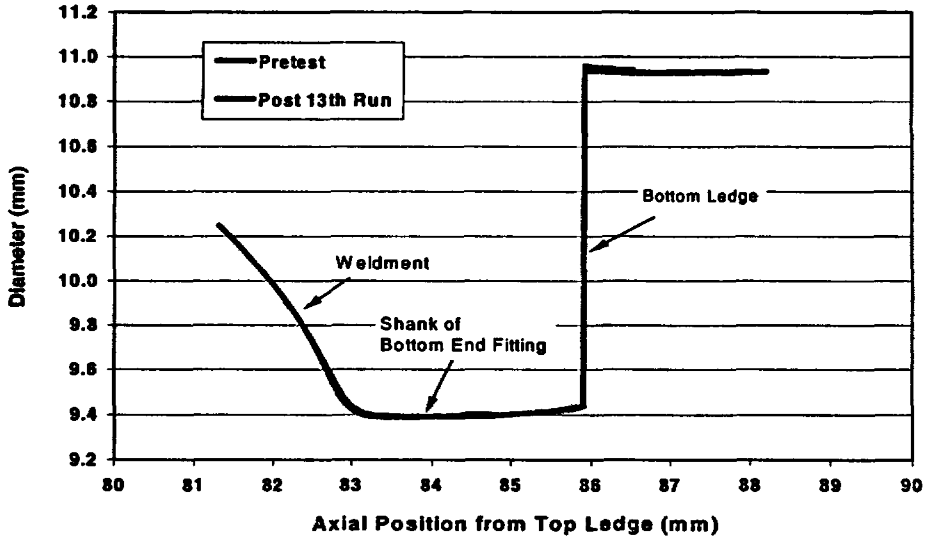

Fig. F.26 Pre- and Post-run Profiles of the Lower End Fitting of the C9 sample (as measured from the top of the sample). Near identical position of curves indicates no change in the sample length.

NRC FORM 335
(2-89)
NRCM 1102,
3201, 3202

U.S. NUCLEAR REGULATORY COMMISSION

BIBLIOGRAPHIC DATA SHEET

(See instructions on the reverse)

1. REPORT NUMBER
(Assigned by NRC, Add Vol., Supp., Rev., and Addendum Numbers, if any.)

NUREG/CR-6831

2. TITLE AND SUBTITLE

Examination of Spent PWR Fuel Rods after 15 Years in Dry Storage

3. DATE REPORT PUBLISHED

MONTH	YEAR
September	2003

4. FIN OR GRANT NUMBER

Y6248

5. AUTHOR(S)

R. E. Einziger, H. Tsai, M. C. Billone, and B. A. Hilton

6. TYPE OF REPORT

Technical

7. PERIOD COVERED *(Inclusive Dates)*

11/01/2000 - 09/30/2003

8. PERFORMING ORGANIZATION - NAME AND ADDRESS *(If NRC, provide Division, Office or Region, U.S. Nuclear Regulatory Commission, and mailing address; if contractor, provide name and mailing address.)*

Argonne National Laboratory
9700 South Cass Avenue
Argonne, IL 60439

9. SPONSORING ORGANIZATION - NAME AND ADDRESS *(If NRC, type "Same as above"; if contractor, provide NRC Division, Office or Region, U.S. Nuclear Regulatory Commission, and mailing address.)*

Division of Systems Analysis and Regulatory Effectiveness
Office of Nuclear Regulatory Research
U.S. Nuclear Regulatory Commission
Washington, D.C. 20555-0001

10. SUPPLEMENTARY NOTES

NRC Project Manager: S. Basu

11. ABSTRACT *(200 words or less)*

15 x 15 PWR fuel (35.7 GWd/MTU) was stored in a dry inert atmosphere Castor V/21 cask for ~15 years as peak cladding temperatures decreased from about 350°C to 150°C. Prior to the storage, the loaded cask was subjected to extensive thermal benchmark tests during which time the peak temperatures were in excess of 400°C. The cask was opened to examine the fuel rods for degradation and to determine if they were suitable for extended storage. Little or no cladding creep occurred during thermal benchmark testing and 15 years of dry storage. Post-storage creep testing indicated that the cladding retains significant creep ductility after the dry cask storage. It is anticipated that the creep would not increase significantly during additional storage due to the low temperature after 15 years. In the central region of the fuel column, the measured hydrogen content in the cladding is consistent with the thickness of the oxide layer. At higher elevations, there is less hydrogen than would be expected from the oxide thickness. Migration of hydrogen to the cooler ends of the rod probably occurred during dry storage. The volume of hydrides varies azimuthally around the cladding, but all of the hydrides appear to have retained the circumferential orientation, suggesting the clad ductility was retained. Hydrides result from clad oxidation during in-reactor operation and contribute to a loss of clad ductility if oriented in large quantities in cladding.

12. KEY WORDS/DESCRIPTORS *(List words or phrases that will assist researchers in locating the report.)*

Spent Fuel Storage
Castor Cask
Creep Strain Measurements
Irradiated Fuel Performance
Hydrides
Zircaloy

13. AVAILABILITY STATEMENT

unlimited

14. SECURITY CLASSIFICATION

(This Page)

unclassified

(This Report)

unclassified

15. NUMBER OF PAGES

16. PRICE

NRC FORM 335 (2-89)

This form was electronically produced by Elite Federal Forms, Inc.

UNITED STATES
NUCLEAR REGULATORY COMMISSION
WASHINGTON, DC 20555-0001

OFFICIAL BUSINESS